March 2019

The Non-linear Dynamics of Barred Galaxy Evolution in LCDM

Michael Petersen

THE NON-LINEAR DYNAMICS OF BARRED GALAXY EVOLUTION IN ΛCDM

A Dissertation Presented

by

MICHAEL S. PETERSEN

Submitted to the Graduate School of the
University of Massachusetts Amherst in partial fulfillment
of the requirements for the degree of

DOCTOR OF PHILOSOPHY

February 2019

Astronomy

THE NON-LINEAR DYNAMICS OF BARRED GALAXY EVOLUTION IN ΛCDM

A Dissertation Presented

by

MICHAEL S. PETERSEN

Approved as to style and content by:

_____

Martin D. Weinberg, Chair

_____

Neal Katz, Member

_____

Mauro Giavalisco, Member

_____

Lorenzo Sorbo, Member

_____

Daniela Calzetti, Department Chair
Astronomy

ACKNOWLEDGMENTS

I would like to thank my advisors, Martin D. Weinberg and Neal Katz, for patiently working with me to develop my research program. They have let me grow according to my abilities and explore research unfettered, supporting and encouraging me through slow phases and crunch times. I appreciate everything they have done to nurture my curiosity and help me grow as a scientist—both reining me in and letting me engage in Mierenneuken as appropriate. I would also like to thank Mauro Giavalisco and Lorenzo Sorbo, the other members of my thesis committee, for encouragement in this research, as well as helpful comments and suggestions.

I wish to thank the Five College Astronomy department, and in particular Suzan Edwards, James Lowenthal, Anne Jaskot, and Kim Ward-Duong, for the opportunity to work as a Teaching Assistant for a truly innovative observational astronomy class that kept me grounded and inspired about research questions far afield from the work I present in this thesis. I would also like to extend a thank you to Rob Gutermuth, who persuaded me to continue pushing myself on research that could never end up in this dissertation, but taught me how to manage projects.

I would also like to thank everyone who has been affiliated with the University of Massachusetts Amherst Astronomy department during the years that I have been here, and in particular my fellow graduate students. The department has been a vibrant organization that I have been proud to be a part of.

A special thank you to my family and friends, too many to list, who have supported me while I have worked on this project, and in particular completing this document.

ABSTRACT

THE NON-LINEAR DYNAMICS OF BARRED GALAXY EVOLUTION IN ΛCDM

FEBRUARY 2019

MICHAEL S. PETERSEN

B.A., COLGATE UNIVERSITY

M.Sc., UNIVERSITY OF MASSACHUSETTS AT AMHERST

Ph.D., UNIVERSITY OF MASSACHUSETTS AMHERST

Directed by: Professor Martin D. Weinberg

The study of barred galaxy dynamics has had many successes explaining observed phenomena in barred galaxies both locally and distant, including our own Milky Way, a barred galaxy. However, the majority of this knowledge arises from either (a) analytic linear theory, which by definition cannot inform nonlinear processes, or (b) simulations which are subject to an unconstrained host of evolutionary mechanisms, including 'real' dynamical processes and 'artificial' numerical processes, and are thus difficult to interpret. This work chooses a path which attempts to take the best of both techniques, employing n-body simulations in the Λ cold dark matter paradigm designed to isolate dynamical mechanisms responsible for the evolution and observed features of barred galaxies. We develop techniques to analyze the simulations: (1) an algorithm to classify orbit families in an evolving system, (2) a method to compute the area of orbit trajectories, (3) a technique to measure

the angular momentum flow through specific channels, and (4) a parameterization of bar evolutionary phases based on harmonic decompositions. Using these simulations, we elucidate a wide range of dynamical processes important for barred galaxy evolution including (1) the shadow bar, which inhibits angular momentum transfer between the disc and the dark matter halo and may reduce the amount of angular momentum transferred by a factor of three, (2) the presence specific orbit families that support the growth of the bar whose role had not been previously understood, (3) harmonic–locking, which alters and/or stalls the evolution of the bar pattern, and (4) the role of the dark matter halo relative to the disc in determining the evolution. We present observational diagnostics including (1) a method to measure the dynamical length of the bar including descriptions of how traditional metrics overestimate the bar length, (2) predictions for the rate of radial mixing and the mechanisms responsible, (3) predictions for the mechanisms important for bulge formation, such that bulges with may form solely through secular processes, and (4) predictions for the flux of dark matter density at the solar radius for direct-detection experiments, where the flux may double from the naive model typically used.

TABLE OF CONTENTS

LIST OF TABLES

LIST OF FIGURES

Figure **Page**

INTRODUCTION

Galactic bars are some of the most arresting features in galaxy morphology. Since the initial classification and coining of the term by Edwin Hubble in 1926, and the initial dynamical work by titans of dynamics such as Jeans, Oort, and Lindblad, bars have been the subject of continual study. New technologies have continued to enable advancements in the study of barred, from more powerful telescopes resolving barred galaxies to higher and higher redshift to high-resolution spectroscopy from integral field units (IFUs) that now provide resolved velocity maps for a sample of nearby barred galaxies. This document contains dynamical research undertaken to carry on the tradition of barred galaxy dynamics, with an eye to the future of high redshift observations and the new capabilities of IFUs.

Two of the chapters (Chapter 1; Chapter 2) have been published previously. The remaining five chapters are the result of an in-depth look at a suite of models, and in particular two simulations which were used to develop analysis techniques (Chapter 3; Chapter 4; Chapter 5). Much of this dissertation is in pursuit of examining lore about barred galaxy dynamics that has been taken for granted and identifying both where it accurate and where it falls short, or has missed critical mechanisms.

We offer an overview of the dissertation here in the form of chapter abstracts, highlighting specific sections that are of particular interest to observational astronomers or dynamicists, as well as new algorithms that enable physical insight.

In Chapter 1, we investigate the complex interactions between the stellar disc and the dark-matter halo during bar formation and evolution using n-body simulations with fine temporal resolution and optimally chosen spatial resolution. We find that the forming stellar bar traps dark matter in the vicinity of the stellar bar into bar-supporting orbits. We call

this feature the *shadow bar*. The shadow bar modifies both the location and magnitude of the angular momentum transfer between the disc and dark matter halo and adds 10 per cent to the mass of the stellar bar over 4 Gyr. The shadow bar is potentially observable by its density and velocity signature in spheroid stars and by direct dark matter detection experiments. Numerical tests demonstrate that the shadow bar can diminish the rate of angular momentum transport from the bar to the dark matter halo by more than a factor of three over the rate predicted by dynamical friction with an untrapped dark halo, and thus provides a possible physical explanation for the observed prevalence of fast bars in nature.

In Chapter 2, we use the simulations of Chapter 1 to make predictions for dark matter direct detection. Over a handful of rotation periods, dynamical processes in barred galaxies induce non-axisymmetric structure in dark matter halos. Using n-body simulations of a Milky Way-like barred galaxy, we identify both the trapped dark-matter component and a strong response wake in the dark-matter distribution that affects the predicted dark-matter detection rates for current experiments. The presence of a baryonic disk together with well-known dynamical processes (e.g. spiral structure and bar instabilities) increase the dark matter density in the disk plane. We find that the magnitude of the combined stellar and shadow bar evolution, when isolated from the effect of the axisymmetric gravitational potential of the disk, accounts for $>30\%$ of this overall increase in disk-plane density. This is significantly larger that of previously claimed deviations from the standard halo model. The dark-matter density and kinematic wakes driven by the Milky Way bar increase the detectability of dark matter overall, especially for the experiments with higher v_{min}. These astrophysical features increase the detection rate by more than a factor of two when compared to the standard halo model and by a factor of ten for experiments with high minimum recoil energy thresholds. These same features increase (decrease) the annual modulation for low (high) minimum recoil energy experiments. We present physical arguments for why these dynamics are generic for barred galaxies such as the Milky Way rather than contingent on a specific galaxy model.

In Chapter 3, we interpret barred galaxy evolution through orbit morphology, introducing a new geometric algorithm (Section 3.2.5) that rapidly isolates commensurate (resonant) orbits, identifying regions occupied by different orbital families. Compared to spectral methods, the geometric algorithm can identify resonant orbits within a few dynamical periods, crucial for understanding a realistic evolving galaxy model. The flexible methodology accepts arbitrary potentials, enabling detailed descriptions of the orbital structure. We apply the machinery to four different potential models, including two barred models, fully characterizing the orbital membership. We identify key differences in orbital structures, including orbit families whose presence can be used as an indicator of the bar evolutionary state and the shape of the dark matter halo. We use the characterization of orbits to investigate the shortcomings of analytic and self-consistent studies, comparing our findings to the evolutionary epochs in self-consistent barred galaxy simulations. We present a new observational metric (Section 3.4) to apply to galaxies that may reveal signatures of commensurabilities and allow for differentiation between halo models.

In Chapter 4, we use the n-body simulations of Chapter 3 to understand the dynamical mechanisms responsible for the evolution of the bar-disc-dark matter halo system. We find evidence for three distinct phases of barred galaxy evolution: assembly, secular growth, and steady-state equilibrium (Section 4.3). Using an ensemble decomposition of the disc into orbital families, we track gross metrics for the bar through time and correlate the quantities with the phases of evolution. We thoroughly account for the angular momentum transfer between particles and identify the channels responsible for the angular momentum transfer, finding that the halo in a high-central-density halo model mediates the assembly and growth of the bar, while the outer disc mediates the assembly and growth of the bar in a low-central-density halo model. Both galaxies exhibit a steady-state equilibrium where the bar is neither lengthening nor slowing. We identify the cause of the steady-state equilibrium observed in the model galaxie: the balancing of torque between particles that are gaining and losing angular momentum. We propose observational metrics for barred galaxies that

can be used to help determine the evolutionary phase of a barred galaxy (Section 4.3.1), and discuss the implications of the phases for galaxy evolution as a whole.

In Chapter 5, we study the evolutionary paths of bar formation in the simulations of Chapter 3 and Chapter 4 using harmonic function expansion analysis to characterize the dynamical mechanisms in bar evolution. We correlate orbit families with the empirical orthogonal functions that form the gravitational potential basis with phases of bar evolution. In both models we find evidence for three phases in evolution from the harmonic expansion. We recover known analytic results, such as bar slowdown owing to angular momentum transfer. We also find new dynamical mechanisms for bar evolution, including a steady-state equilibrium configuration and harmonic interaction resulting in harmonic locking (Section 5.4.3.1). Additionally, we find that ellipse fitting may severely bias measurements of the bar length relative to the measurements based on orbits that comprise the true backbone supporting the bar feature (Section 5.5.1). The bias will lead to overestimates of both bar mass and bar pattern speed, affecting inferences about the evolution of bars in the real universe. We propose a direct observational technique to compute the radial extent of trapped orbits and determine a dynamical length for the bar in Section 5.5.2.

In Chapter 6, we study the radial density profiles of disc galaxies in a model first presented in Chapter 3, inferring possible dynamical mechanisms responsible the creation of the radial metallicity gradient in the Milky Way and the creation of the bulge from disc material. We study the interaction of several known stellar mixing mechanisms found in a self-consistent n-body model galaxy that resembles the Milky Way, including a strong bar, finding that the bar alone (without any spiral pattern) is an efficient driver of radial mixing, and easily drives continued secular bulge formation. A bulge forms that is prominent in both face-on appearance and edge-on profile, though we demonstrate that standard photometric decomposition methods would not recover dynamically-relevant components for the bar and bulge in all cases. We offer strategies to recover better estimates of the bar profile. We find that orbits never move outward to larger apocenter radii from inside the bar

radius, but resonance passage as orbits join the bar and heteroclinic motion (family switching) within the bar results in net inward radial motion (Section 6.4). Interaction with the bar produces the majority of the orbits which reside above the plane of the galaxy, through a combination of resonant trapping and incomplete resonance passages.

In Chapter 7, we present suite of model disc galaxies embedded in dark matter halos with the aim of identifying the generic mechanisms that control bar formation and evolution. Using techniques designed to isolate physical mechanisms from Chapter 3, Chapter 4, and Chapter 5, we analyze the orbital structure, angular momentum content, and harmonic decomposition evolution and describe phases of bar evolution and the conditions under which they take place. Isophotal and harmonic analysis reveals that despite their apparent photometric similarity, the ratio of different harmonic orders (e.g. the quadrupole to the monopole) can be different by up to 50 per cent (Section 7.3.1). We identify thresholds for bar formation in the mutual phase-space structure of the disc and halo, including configurations where the disc will remain stable without forming a bar for the age of the universe, as well as initially axisymmetric configurations which are so unstable to bar formation as to be unphysical representations of bar evolution. Between the thresholds for realistic bar formation we find a sweet spot for growing a secular bar and identify the mechanisms which allow the bar to grow to its largest amplitude. We find evidence for model parameters which control the timescales for evolution, namely the velocity dispersion and geometry of the stellar component. We discuss the implications of the mechanisms found to be important for bar formation and evolution for galaxy evolution as a whole.

CHAPTER 1

DARK MATTER TRAPPING BY STELLAR BARS: THE SHADOW BAR

1.1 Introduction

Galactic bars change the internal structure of disc galaxies by rearranging the angular momenta and energy of orbits that would otherwise be conserved. As many as two-thirds of local galaxies show bar features in the infrared (Sheth et al., 2008). Bars have been suggested to affect both structural properties such as bulge structure (Kormendy & Kennicutt, 2004; Laurikainen et al., 2014) and stellar breaks (Muñoz-Mateos et al., 2013; Kim et al., 2014), as well as evolutionary properties such as star formation rates (Masters et al., 2012; Cheung et al., 2013) and metallicity gradients (Williams et al., 2012). Weinberg & Katz (2002) also showed that bars can affect the central profiles of dark matter haloes. Bars are the strongest of the persistent disc asymmetries and, therefore, provide a dynamical laboratory for understanding the long-term evolution of galaxies.

For simplicity of analysis, many previous theoretical works have adopted a component-by-component analysis of angular momentum transport by adopting a fixed halo potential, a rigid bar, or both. However, the baryonic disc and dark matter halo comprise a single system that shares the same dynamics as a consequence of their mutually generated gravitational field. Therefore, some fraction of the dark-matter orbital elements will overlap with those in the disc and, thus, there is little reason not to suspect that some of the dark matter halo will respond similarly to the stellar disc. The dynamical interplay between these components is of considerable interest in developing a comprehensive understanding of the disc-halo system.

In this paper, we present a time-dependent analysis of trapped stellar and halo orbits in a fully self-consistent simulation. We find evidence for the formation and subsequent secular evolution of a trapped population of halo orbits, a *shadow bar*, that arises in response to the same collective dynamics that make the classic stellar bar. The shadow bar fundamentally changes the orbital structure of the halo in the vicinity of the bar. These same orbits, when unperturbed by the bar, would contribute strongly to the disc-halo torque responsible for slowing the bar, which can be understood in the context of simple perturbation theory models. We investigate and document the magnitude of halo trapping, finding that the trapping affects both the dark-matter density and velocity structure.

A well-studied consequence of angular momentum transport in barred galaxies is the tension between the theorised slowing of the bar pattern speed (Tremaine & Weinberg, 1984b; Weinberg, 1985) and observations that do not show a slowing pattern speed (e.g. Aguerri et al. 2015). This is often interpreted as evidence for only small amounts of dark matter at the centre of galaxies (Debattista & Sellwood, 2000; Sellwood & Debattista, 2006; Villa-Vargas et al., 2009) or as a motivation for changing the law of gravity (Tiret & Combes, 2007). However, the dark-matter orbits trapped by the bar are unavailable for secular evolution, significantly reducing the halo torque on the bar.

For our own Milky Way (MW)—a barred galaxy—several experiments may detect the influence of a shadow-bar modified dark matter density and velocity distribution. These include ongoing analysis of stellar surveys such as RAVE (Steinmetz et al., 2006), GAIA (Gilmore et al., 2012), and APOGEE (Allende Prieto et al., 2008) since halo stars might have similar orbits to dark matter particles. Some of these studies have already seen suggestions of rotation in a bulge-bar component (Rojas-Arriagada et al. 2014, Soto et al. 2014). Signs of a shadow bar could also affect the interpretation of tentative signals from direct dark matter detection experiments, e.g. CoGeNT (Aalseth et al., 2013), CDMS II (Agnese et al., 2013), and DAMA/LIBRA (Bernabei et al., 2014).

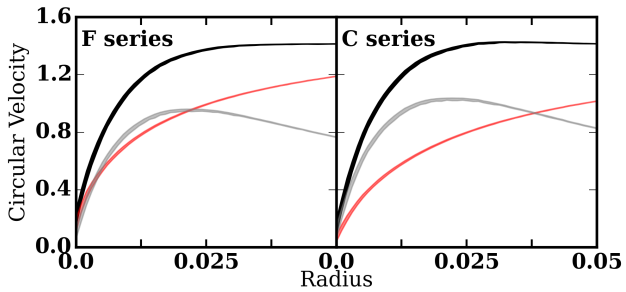

Figure 1.1. Initial circular velocity curves for the F-series cusp models (left panel) and C-series cored models (right panel). The circular velocity from $p = 0.2$ to $p = 0.8$ is shown in black where p is the quantile value for the rank-ordered circular velocities. The $p = 0.2$ to $p = 0.8$ contributions from the disc (grey line) and halo (red line) have been separated to demonstrate the maximality of the disc. Radius and circular velocity are in virial units (see Section 2.2.1), where a radius of 0.01 coresponds to 3 kpc and a circular velocity of 1.0 corresponds to 150 km s^{-1} when scaled to a Milky Way mass galaxy.

This paper is organised as follows: the next section describes the initial conditions for our fiducial simulation (section 1.2.1.1), a series of simulations with varying halo properties (section 1.2.1.2), and the details of our N-body solver (section 6.2.1). We include two idealised numerical experiments with modifications to the bar perturbation to better understand the importance of the bar growth rate on halo orbit trapping and halo structure. Our results are presented in section 3.3. We examine the fiducial simulation in detail, beginning with an overall summary picture of the fiducial simulation in section 1.3.1, followed by studies of the disc and halo orbit morphologies in sections 1.3.2.1 and 1.3.2.2, respectively. These analyses reveal that in addition to the stellar bar, a significant mass fraction of the halo within a bar length is trapped into the bar potential. The dynamical properties of the entire trapped orbit population are discussed in section 1.3.3 and contextualised using perturbation theory. This is followed by an exploration of the overall dynamical consequences of the shadow bar itself in section 1.3.4. Section 7.5 connects with previous work by using a suite of experiments motivated by published models and further demonstrates the robust nature of the shadow bar. We conclude with a summary and discussion of the stellar disc–dark matter halo relationship and our detailed orbital analysis in section 7.6.

1.2 Methods

1.2.1 Initial conditions

This section motivates our mass models and describes the realisation of the initial conditions. We begin with the details of our fiducial simulation. The phase space is realised using a methodology that closely follows Holley-Bockelmann et al. (2005), hereafter HB05. We then discuss model variants that (1) address typical literature treatments; (2) seek to model physical processes in the universe; and (3) verify the theorised dynamical implications of the fiducial experiment. Our key simulations are summarised in Table 1.1.

In all the simulations presented here, the number of disc particles and halo particles are $N_{\rm disc} = 10^6$ and $N_{\rm halo} = 10^7$, respectively. The disc particles have equal mass. The halo particles have a number density $n_{\rm halo} \propto r^{-\alpha}$, where $\alpha = 2.5$. This steep power law better resolves the inner halo in the vicinity of the disc bar, our subject of interest. The particle's masses are assigned to simultaneously reproduce the desired halo mass density and the number density. In practice, the halo resolution is improved by a factor of 100 within a disc scale length ($M_{r<R_d} = 0.005 M_{\rm vir}$, $N_{r<R_d} = 5 \times 10^5$) compared to using a fixed halo particle mass. The effective halo particle number within all disc-relevant radii is then $N_{\rm halo} \sim 10^9$, more than satisfying the criteria of Weinberg & Katz (2007b) for an adequate treatment of resonant dynamics.

All units are scaled to so-called *virial* units with $G = 1$ that describe the mass and radius of the halo at the point of halo collapse in the cold-dark-matter scenario. For comparison to the MW, we follow the estimated halo mass of Boylan-Kolchin et al. (2013) such that $M_{\rm vir} = 1.6 \times 10^{12}$ M$_\odot$, making $R_{\rm vir} = 1.0$ correspond to 300 kpc, a velocity of 1.0 equivalent to 150 km s^{-1}, and a time of 1.0 equivalent to 2.0 Gyr. The system is constructed such that $M(R_{\rm vir}) = 1.0$.

1.2.1.1 Fiducial simulation

We follow the now standard prescription for producing a strong bar in an N-body simulation by choosing a fiducial model with a slowly rising rotation curve. This simulation is labelled F in Table 1.1, using the initial rotation curve shown by the F-series rotation curve in Fig. 1.1 (left panel). The contributions from the individual components are derived by calculating the radial force contributions from each component separately: $v^2_{c,\mathrm{disc}} = rF_{r,\mathrm{disc}}$ and $v^2_{c,\mathrm{halo}} = rF_{r,\mathrm{halo}}$ where r is the radius of the particle, and F_r is the radial force contribution from the corresponding component at the particle's position. The slowly rising rotation curve minimises the bar-damping effect of the initial inner Lindblad resonance and allows the region inside of corotation to act as a "resonant cavity" for bar formation (Sellwood & Wilkinson, 1993). For a rising rotation curve, one can show using first-order perturbation theory that the response of a nearly circular orbit to the bar perturbation is to slow and even reverse its apse precession rate (the so-called "donkey effect" of Lynden-Bell & Kalnajs 1972, see Binney & Tremaine 2008). This results in the orbit lingering near the position angle of the bar, causing the effective bar strength, the quadrupole perturbation strength specifically, to increase. This growth extends the reach of the perturbation, inducing more orbits to slow or reverse their precession rate, resulting in an exponential growth for the bar. The fiducial simulation is analysed in section 3.3.

The fiducial simulation has an initially exponentially-distributed stellar disc embedded in a fully self-consistent non-rotating $c = R_{\mathrm{vir}}/r_s \approx 15$ NFW dark-matter halo (Navarro et al., 1997) where r_s is the scale radius, and R_{vir} is the virial radius:

$$\rho(r) = \frac{\rho_0 r_s^3}{(r + r_c)(r + r_s)^2} \tag{1.1}$$

where ρ_0 is set by the chosen mass and $r_c = 0$ is the core radius for the fiducial model. The dynamical implications of a core produced by early evolutionary processes (Weinberg & Katz 2002, Sellwood & Debattista 2009) will be explored in section 3.3 and 7.5 by comparison to simulations with non-zero values of r_c. The halo velocities are realised from the

distribution function produced by an Eddington inversion of $\rho(r)$ (see Binney & Tremaine 2008). Eddington inversion provides an isotropic distribution, roughly consistent with the observed distributions in dark-matter only ΛCDM simulations. This method naturally results in a non-rotating halo; we will describe realising rotating haloes in section 1.2.1.2.

For all the simulations here, we adopt an exponential radial stellar disc profile with an isothermal vertical distribution:

$$\rho_d(R,z) = \frac{M_{\rm d}}{8\pi z_0 R_d^2} e^{-R/R_d} {\rm sech}^2(z/z_0) \tag{1.2}$$

where M_d is the disc mass, R_d is the disc scale length, and z_0 is the disc scale height. We set $M_d = 0.025$, $R_d = 0.01$, and $z_0 = 0.001$ throughout. All simulations in this work have a disc:halo mass ratio of 1:40 inside of its virial radius[1]; while a comparatively low mass ratio for studies in the literature (e.g. contrasting with Debattista & Sellwood 2000; Athanassoula & Misiriotis 2002; Saha et al. 2012), we choose this mass ratio to mimic the mass ratio for the $z = 0$ MW, as determined through simulations (Vogelsberger et al., 2014), abundance matching (Kravtsov 2013; Moster et al. 2013), and stellar kinematics (Bovy & Rix, 2013). The disc parameter values are consistent with the MW values of Bovy & Rix (2013), who found $M_\star \approx 4.6 \times 10^{10}$, or $0.029\ M_{\rm vir}$ (again using the scaling from Boylan-Kolchin et al. 2013); $R_d = 2.15$ kpc and $z_0 = 370$ pc, which are reasonably similar to our values. We do not include a bulge due to the uncertainty in its phase-space distribution, but this should not limit the application of our models to the observed universe since the dynamical mechanisms governing bar formation and evolution are dominated by the graviatational potential outside the bar region. Similarly for the thick disc, although we will address the dynamical effects of a thick disc in a later paper. We additionally do not include a gas component. In the present-day, gas is a tracer component in the MW;

[1]To preserve equilibrium, the halo extends beyond a virial radius, where it is truncated, but here we consider the mass within a virial radius for this ratio calculation.

while the gas fraction may have been higher in the past, this quantity is highly uncertain. Literature results have demonstrated scenarios where gas accretion can destroy and re-form the bar over a cosmological (Bournaud & Combes, 2002; Bournaud et al., 2005). However, other simulations including gas as part of the initial conditions (Villa-Vargas et al., 2010; Athanassoula et al., 2013) do not show signs of bar destruction, though the bars resulting from gas-rich simulations may be weaker. While including gas as part of the initial conditions may slow the rate at which bars form, the presence of a gas component does not fundamentally alter the dynamics. In light of this, we suggest that our models are adequate for learning about the dynamical mechanism of DM trapping, and believe that the results presented here would remain largely unchanged in the presence of a collisional component with present-day parameters.

The F-series rotation curve has a disc fraction $f_D \equiv V_{c,\star}/V_{c,\mathrm{tot}} = 0.71$ at $R = 2.2R_d$, the radius at which the exponential disc reaches the maximum circular velocity[2]. Martinsson et al. (2013) found that for typical spiral galaxies, $f_D = 0.4 - 0.7$, with $\langle f_D \rangle = 0.57$, making our disc more maximal than the typical spiral. Piffl et al. (2014) measured $f_D = 0.63$ for the MW, in agreement with the findings of Martinsson et al. (2013). However, Bovy & Rix (2013) suggested that the MW may be nearer to a maximal disc, with $f_D = 0.83$. All methods to observationally determine f_D rely on assumptions about the parameters to describe the disc, as well as the structure of the dark matter halo, hence we believe that within the uncertainties, our fiducial model represents a realistic galaxy. The purpose of the simulation was not to create an exact MW analogue, but to make a cosmologically realistic galaxy.

Disc velocities are chosen by solving the Jeans' equations in cylindrical coordinates in the combined disc–halo potential. We set the radial velocity dispersion from the Toomre

[2]The parameter f_D is often called the 'maximality'. By the nature of our simulations, f_D only measures the contribution of the stellar component rather than the total baryonic component, so we quote literature results which are able to isolate stellar contributions from the full baryonic contributions.

stability equation,

$$\sigma_r(R) = Q\frac{3.36G\Sigma(R)}{\kappa(R)}, \tag{1.3}$$

where $G = 1$, $\Sigma(R)$ is the stellar surface density, and κ, the epicyclic frequency (also sometimes written as Ω_r), is given by

$$\kappa^2(R) = R\frac{d\Omega(R)^2}{dR} + 4\Omega(R)^2 \tag{1.4}$$

where Ω is the azimuthal frequency (sometimes explicitly written as Ω_ϕ in cylindrical coordinates). We choose $Q = 0.9$ to facilitate comparisons to the literature (e.g. Athanassoula & Misiriotis 2002) and to ensure the relatively rapid growth of a bar[3]. This departs from our previous choice in HB05 of a *warm* disc with $Q = 1.4$. Also, we replace the axisymmetric velocity ellipsoid generated from the epicyclic approximation in the disc plane used in HB05 by the Schwarzschild velocity ellipsoid (Binney & Tremaine, 2008). In practice, this latter velocity ellipsoid improves the initial equilibrium by using the second moment of the cylindrical collisionless Boltzmann equation with an asymmetric drift correction:

$$\sigma_\phi^2 = \left(\frac{\sigma_r\kappa(R)}{2\Omega(R)}\right)^2. \tag{1.5}$$

As in HB05, the vertical velocity dispersion σ_z is

$$\sigma_z^2(R) = \frac{1}{\rho_d(R,z)}\int_z^\infty \rho_d(R,z)\frac{\partial\Phi_{\rm tot}}{\partial z}dz. \tag{1.6}$$

From a dynamical standpoint, our relatively low disc-to-halo mass ratio accomplishes two additional goals: (1) it decreases the strength of local instabilities that allows us to focus on secular dynamics; and (2) it enables the exploration of the *slow mode* of bar growth

[3]In the absence of a dark matter halo, $Q = 0.9$ is formally unstable; in the presence of the dark matter halo, this value results in a locally stable disc that forms a bar in several dynamical times.

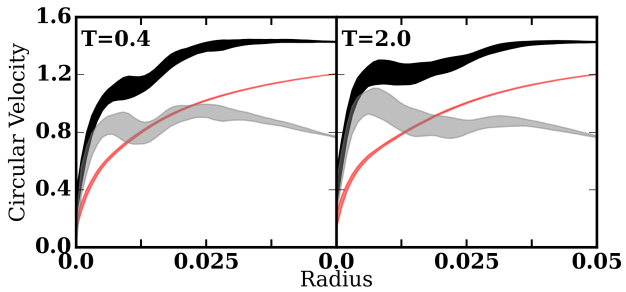

Figure 1.2. Circular velocity curves for the fiducial model at system time T=0.4 (left panel) and T=2.0 (right panel). The circular velocity from $p = 0.2$ to $p = 0.8$ is shown in black. The $p = 0.2$ to $p = 0.8$ contributions from the disc (grey line) and halo (red line), where p is the quantile value for the rank-ordered circular velocities, have been calculated separately to demonstrate the evolution of each component. Radius and circular velocity are in virial units, as in Figure 1.1. System time is also given in virial units, where T=1.0 corresponds to 2.0 Gyr when scaled to the MW.

(Polyachenko & Polyachenko, 1996), seemingly not achievable given *maximal* discs. We examine the former in this paper and will explore the latter in more detail in a forthcoming paper.

1.2.1.2 Halo model variants

We investigate two additional classes of halo models based on our fiducial one: (1) halo models with a cored central profile instead of a cusp[4]; and (2) rotating haloes. These variants are inspired both by cosmological hydrodynamic simulations (Bullock et al., 2001), and a desire to connect with previous literature choices.

We construct cored haloes by setting $r_c = 0.02$ in equation (7.3). The halo mass is matched between the cusp and core model haloes at the virial radius to maintain the disc:halo mass ratio within the virial radius. This model uses the C-series rotation curve (the right panel of Figure 1.1). The overall rotation curves for the F- and C-series models are within 5 per cent at any given radius, despite the relative contributions from each

[4]A cored central profile satisfies $\rho(r) \propto r^{-\alpha}$ where $\alpha \to 0$ as $r \to 0$; the unmodified NFW has a cuspy central profile with $\alpha = 1$.

Simulation	scale length (R_d)	scale height (h)	disc mass	halo profile	Notes
F	0.01	0.001	0.025	cusp	
Fr	0.01	0.001	0.025	cusp, $\lambda = 0.03$	
C	0.01	0.001	0.025	cored, $r_c = 0.02$	
Cr	0.01	0.001	0.025	cored, $r_c = 0.02$, $\lambda = 0.03$	
Ff	0.01	0.001	0.025	cusp	fixed disc potential
Fs	0.01	0.001	0.025	cusp	shuffled halo

Table 1.1. List of simulations.

component being appreciably different. The C-series rotation curves have $f_D = 0.81$ at $R = 2.2R_d$. As we shall see, the resonant dynamics are quite different, as the phase-space gradient of the distribution function is the controlling parameter of the resonant density (see Sellwood 2014 for a review). In a cored halo, the flattening of the central density profile creates a harmonic core, i.e. orbits at small radii would execute simple harmonic motion in the absence of a stellar disc. For this model series, the relatively low halo density near the centre of the simulation leads to a well-known buckling instability (see Sellwood 2014 for a review). The differences between the fiducial and variant halo models are discussed in section 1.4.1.

We construct rotating haloes consistent with the cumulative mass distribution M for specific angular momentum $j(M)$ in a spherical shell as proposed by Bullock et al. (2001),

$$j(M) \propto M^{1.3}, \tag{1.7}$$

normalised such that

$$\lambda = \frac{\sum_i m_i \vec{r_i} \times \vec{v_i}}{\sqrt{2} M_{\rm vir} V_{\rm vir} R_{\rm vir}} = 0.03. \tag{1.8}$$

The value $\lambda = 0.03$ is roughly the median value in the distribution compiled from cosmological simulations by Bullock et al. (2001). We realise a distribution that satisfies equations (1.7) and (1.8) as follows. First, we begin with a phase space for the initially nonrotating spherical halo as described in section 1.2.1.1. We randomly sample the phase space of the initially nonrotating halo by mass as described in section 1.2.1.1 and choose particles from the distribution $M(r)$ by rejection. Then, we change the direction of rotation for orbits with $L_z < 0$ from the probability distribution determined from equation (1.7) by changing the sign of L_z until the desired value of λ is obtained. For our $N = 10^7$ haloes, this results in a deviation from the desired $\lambda = 0.03$ of less than 1 per cent. Changing the sign of any component of the angular momentum of a particular orbit remains a valid solution to the collisionless Boltzmann equation, preserving the initial equilibrium of the

system. Large values of λ may result in an unstable halo (Kuijken & Dubinski, 1994), but this is not observed for the modest λ selected here, unsurprising given the results of Barnes et al. (1986) and Weinberg (1991). The initial rotation curves for Fr and Cr (see Table 1.1) are the F and C series respectively (Figure 1.1).

1.2.1.3 Two tests of the dynamical mechanism

In addition to the halo model variants, we examine two additional modifications to the fiducial model designed to test our physical understanding of the dynamical processes. Such restricted simulations do not have analogues in the real universe, but can illuminate specific processes.

In the first experiment, Ff in Table 1.1, we exploit the separate Poisson-equation solutions for the stellar disc and dark matter halo in EXP (see below for a description of this N-body code) by allowing the dark matter halo potential to self-consistently evolve while disallowing changes to the stellar disc potential. This allows us to investigate the adiabatic compression of the initially spherical dark matter halo in response to the stellar disc potential. The results are compared to that of the fiducial simulation in section 1.3.2.2 to isolate the effect of non-axisymmetric disc evolution on the global halo properties.

In the second experiment, Fs in Table 1.1, we artificially eliminate the trapping that leads to the shadow bar by shuffling the azimuth of halo particles in the fiducial simulation. The shuffling interval for an individual orbit i is chosen following a Poisson distribution with an average value of $2P_{\phi,i}$ where $P_{\phi,i} \equiv 2\pi/\Omega_{\phi,i}$ is the azimuthal period for orbit i. This technique preserves the radial structure of the halo and produces minimal disturbances to the equilibrium. The results of this experiment are used to quantify the effect of trapping on classical dynamical friction torque and to corroborate our hypothesis of the shadow bar's effect on the angular momentum transport between the disc and halo in section 1.3.4.

We verify that the shuffling process effectively eliminates trapping by attempting to detect a trapped component using the methodology that will be described in 1.3.2, finding

that <0.1 per cent of the orbits demonstrate a trapped signal, consistent with uncertainties owing to resolution. Both models use the F-series initial rotation curve (Figure 1.1)

1.2.2 N-body simulations

We perform the system evolution using EXP (Weinberg, 1999). This code is designed to represent the gravitational field for multiple galaxy components by a rapidly converging series of functions. EXP is advantageous for secular dynamics problems owing to its absence of high-frequency noise and its high-efficiency relative to fully adaptive Poisson solvers such as direct summation or tree gravity algorithms.

These series of functions are the eigenfunctions of the Laplacian. For conic coordinate systems, the Laplacian is a special case of the Sturm-Liouville (SL) equation,

$$\frac{d}{dx}\left[p(x)\frac{d\Phi(x)}{dx}\right] - q(x)\Phi(x) = \lambda\omega(x)\Phi(x) \tag{1.9}$$

where λ is a constant and $\omega(x)$ is a known function, called either the density or weighting function. These eigenfunctions have many useful properties. For systems with a finite domain, the eigenvalues are real, discrete, and bounded from below; their corresponding eigenfunctions are mutually orthogonal, and oscillate more rapidly with increasing eigenvalue. We will assume that the functions are indexed in order of increasing eigenvalue. For example, the eigenfunctions of the Laplacian over a periodic finite interval are sines and cosines; in cylindrical coordinates, they are Bessel functions. For a spherical geometry, the eigenfunctions satisfy Poisson's equation such that

$$\frac{1}{4\pi G}\int drr^2 d_k^*(r)u_j(r) = \delta_{jk} \tag{1.10}$$

where d_k is the density and u_j is the potential that together form a biorthogonal pair. A variety of analytic biorthgonal pairs are available (Clutton-Brock 1973, Clutton-Brock et al. 1977, Hernquist & Ostriker 1992, Earn 1996). Here, we follow Weinberg (1999) and

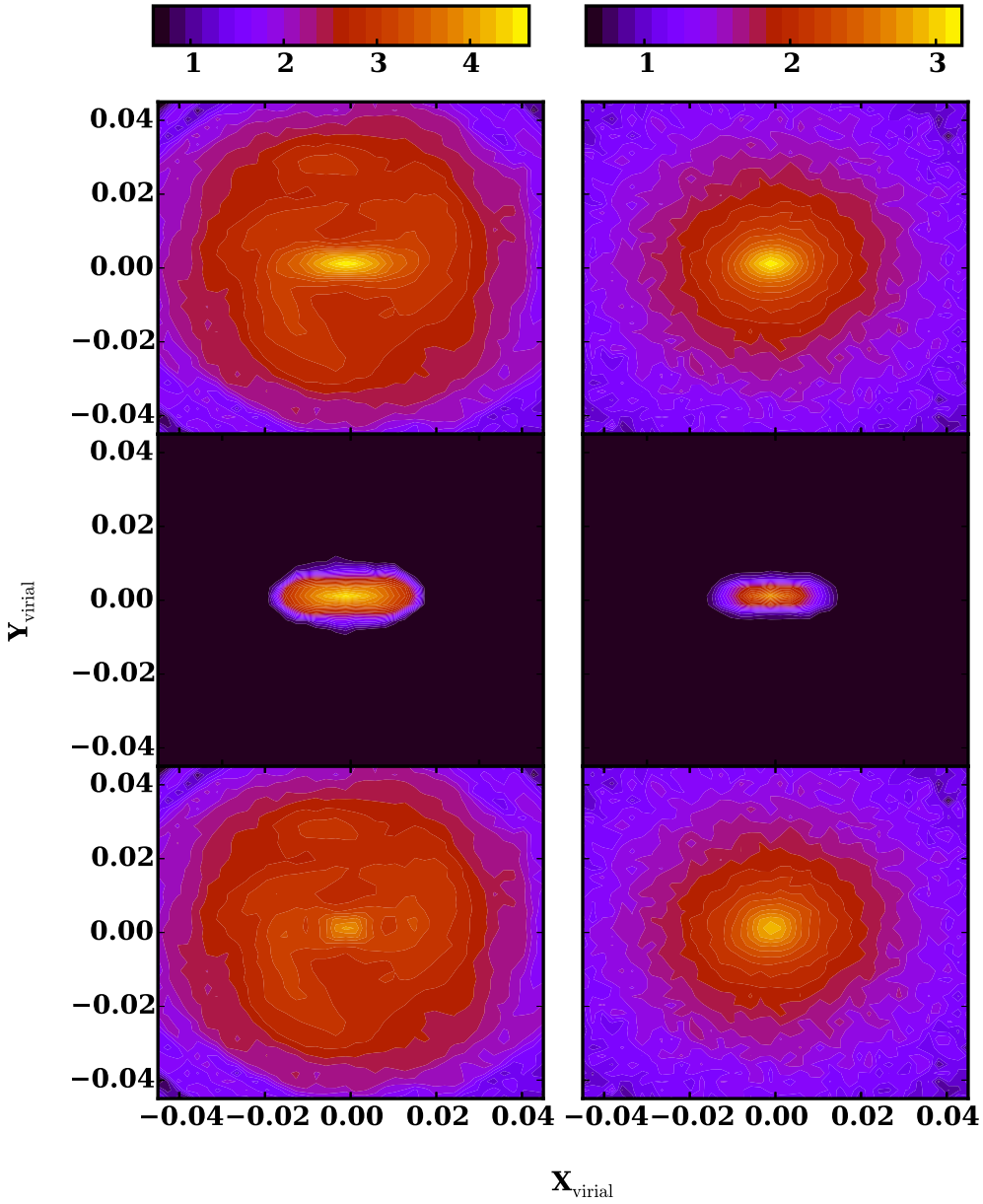

Figure 1.3. The surface density of the fiducial simulation for the stellar disc (left panels) and the dark matter halo (right panels). The upper panels show the in-plane density ($|z| < 0.003$, ≈ 1 kpc for MW-like scalings), the middle panels show the in-plane density of the trapped component (the stellar bar on the left and the shadow bar on the right), and the lower panels show the in-plane density of the untrapped component, at T=2.0 (4 Gyr for MW-like scalings). Positions are given in virial units, as in Fig. 1.1, discussed in section 2.2.1.

numerically solve equation (1.9) to obtain a basis whose lowest-order pair ($n = 0$, $l = m = 0$) matches the equilibrium profile of the initial conditions. Higher-order terms then represent deviations about this profile with successive higher spatial frequency, which can account for the evolution of the system.

The overall power owing to discreteness noise scales as $1/N$, and we may limit small-scale fluctuations by truncating the series, effectively providing a low-pass spatial filter that removes high-frequency noise from the discrete particle distribution (Weinberg, 1998). Although it is possible to derive an analogous three-dimensional basis from the cylindrical Laplacian, the boundary conditions are complex and difficult to match to the approximately spherical domain of the halo. After much trial and error, we found that a empirical orthogonal function decomposition of a high-dimensional spherical basis produces better results. Weinberg (1999) and HB05 describe this method in detail. The field approach is also advantageous as it enables a direct comparison with perturbation theory. However, we are aware of two significant disadvantages of the field approach as well: 1) the technique cannot be fully adaptive and limit high frequencies simultaneously; and 2) it can be susceptible to $m = 1$ (dipole) modes induced by unphysical 'sloshing' of the expansion centre against the centre-of-mass. While our simulations show nonzero $m = 1$ power, we verify that the expansion centre deviates from the centre-of-mass by less than $0.1z_0$ at all times. We also note that $m = 1$ modes are theoretically predicted (Weinberg, 1994) and appear in real galaxies (e.g. Zaritsky et al. 2013) and hence do not necessarily indicate a numerical fault. We will investigate these phenomena further in a future paper.

For this class of Poisson solver, the computational effort scales linearly with particle number, making low-noise simulations with high N possible. A number of basis terms are kept to allow for astronomically realistic perturbations to the equilibrium profile while minimising the linear least-squares fit to a Monte Carlo realisation of the initial particle positions. We retain terms in the halo basis up to $l = m = 6$, and a maximum radial index of $n = 20$ corresponding to the largest eigenvalues for the spherical harmonics of the halo.

For the disc, we select $m = 6$, $n = 12$ for the empirical orthogonal functions. This basis selection allows for variations of $0.1R_d$ (300 pc for a MW-sized galaxy) in the vicinity of the bar, decreasing to 5×10^{-5} (15 pc for a MW-sized galaxy) near the centre. This solver naturally suppresses the small scales that may lead to anomolous diffusion, which can lead to unphysically rapid evolution, without adding spatial resolution on the scales of interest[5]. While possible, we do not recondition the basis on the evolving equilibrium during simulations, relying instead on the initial Poisson variance to allow for sufficient degrees of freedom.

Particles are advanced using a leapfrog integrator with an adaptive time step algorithm. Briefly, we begin by partitioning phase space s ways such that each partition contains n_j particles that require a time step $\delta t = 2^{-j}\delta T$, where δT is the largest time step and $j = 0, \ldots, s-1$. The time step for $j = s-1$ corresponds to a single time-step simulation. Since the total cost of a time step is proportional to the number of force evaluations, the speed up factor is given by: $\mathcal{S} = \sum_{j=0}^{s-1} n_j / \sum_{j=0}^{s-1} n_j 2^{-j}$. For a $c = 15$ NFW dark-matter profile with $N = 10^7$ multimass particles as described in section 1.2.1.1, we find that $s = 8$ and $\mathcal{S} \approx 30$, an enormous speed up! Forces in our algorithm depend on the basis coefficients and the leap frog algorithm requires linear interpolation of these coefficients to maintain second-order error accuracy per step. The expansion coefficients are partially accumulated and interpolated at each level j to preserve continuity as required by the numerical integration scheme for finer time steps. This interpolation and the bookkeeping required for the successive bisection of the time interval is straightforward. The symmetric structure of the leap-frog algorithm allows the coefficient values to be interpolated rather than extrapolated. This algorithm will be discussed in more detail in a forthcoming paper.

To motivate our choice of timesteps, we first define a characteristic force scale as $d_i \equiv \Phi_i / |\partial \Phi_i / \partial \mathbf{x}_i|$ where Φ_i is the current scalar potential of the particle. The time step

[5]Note that this method does not remove all the relaxation from fluctuations in the basis; this method will only remove relaxation on resolution scales smaller than those probed by the basis.

level, j, for each orbit is then assigned by the minimum of three criteria: (1) v_i/a_i, the characteristic force timescale, (2) d_i/v_i, the characteristic work timescale, and (3) $\sqrt{d_i/a_i}$, the characteristic escape timescale. The quantity v_i is the current scalar velocity of the particle and a_i is the current scalar acceleration of the particle. The criteria have prefactors $\epsilon_f,\ \epsilon_w,\ \epsilon_e$, respectively, which can be tuned to achieve the desired time resolution. Using the initial distribution of particles in the fiducial model, we tune the ratios of the prefactors based on the mean of the ratio of the calculated timescales for all the disc particles. We find that $\epsilon_f/\epsilon_w \approx 10$, and $\epsilon_w/\epsilon_e \approx 2.5$.

Weinberg & Katz (2007a) use numerical perturbation theory to determine a scaling for particle timestep criteria, finding that 1/100 of the period of oscillation appropriately recovers the resonant dynamics. Weinberg & Katz (2007a) defined particle number and time-step criteria to help ensure that the dynamics in the vicinity of the homoclinic trajectory are accurate for a very slowly evolving system. The formal requirement of a slowly evolving system is implicit in the time ordering that enables the perturbative analytic estimates that underpin secular evolution. In this standard formulation of secular evolution (e.g. dynamical friction), changes in otherwise conserved actions occur during their homoclinic passage. For strong (typically low-order) resonances, these regions are large and the criteria are easily satisfied. For weaker (typically higher-order) resonances, large particle numbers are required. Conversely, for more rapidly evolving systems, a smaller particle number may suffice. We choose to err on the side prudence by satisfying the slow-evolution criteria. Using the fiducial model, we find that at a scale height, $r = 0.001$, the appropriate timestep is $h \leq 1.8 \times 10^{-4}$, similar to the timestep chosen in HB05, $h = 2 \times 10^{-4}$. To comply with the findings of Weinberg & Katz (2007a), we set the smallest timestep to be $h = 1.25 \times 10^{-4}$. We then tune the prefactors such that nearly all the disc particles (> 99.5 per cent) as well as halo particles in the vicinity of the disc reside in this level, while allowing other halo particles to occupy larger timestep levels to take advantage of the computational speedup. We allow for four multistep levels ($s = 5$) so that the maximum

timestep is 16 times larger than the minimum time step ($h_{\max} = 2 \times 10^{-3}$). We note that while many halo particles at large radii do not even require $h = 2 \times 10^{-3}$ for 1/100$^{\rm th}$ of an oscillation, we truncate the multistep levels to match the output frequency, $\delta T = 0.002$. While this decreases the speed up factor, we find that with $s = 5$, $S \approx 5$, still a considerable speed up.

1.3 Results from the fiducial simulation

This section characterises the fiducial simulation. We begin with a description of the structure and long-term evolution of the bar profile and pattern speed in section 1.3.1. We then motivate a new time-dependent tool for characterising orbits trapped into resonance and apply this tool in section 1.3.2.1 and 1.3.2.2 to the disc and halo populations, respectively. We show that the evolution of a stellar bar in the presence of a dark-matter halo traps a large fraction of dark matter orbits in the vicinity of the bar, resulting in a shadow bar. The implications and dynamical consequences of this trapping on the evolution of the galaxy are presented in section 1.3.3. This is followed by a discussion of the observational consequences of the shadow bar in section 1.3.4.

1.3.1 Formation and evolution of the bar

Figure 1.2 shows the rotation curves determined by rank ordering the force-derived circular velocities (as in Figure 1.1, $v_c^2 = rF_r$, calculated separately for each component) of particles in a narrow annulus at each radius R and selecting quantile values from $p = 0.2 - 0.8$. We display the resulting curves for two characteristic times: immediately after initial bar formation ($T = 0.4$) while the bar is still rapidly growing, and well-after bar formation ($T = 2.0$). We display the range of circular velocities spanned by the $p = 0.2 - 0.8$ quantile values to demonstrate the non-axisymmetric nature of the circular velocity field (particularly for radii $R < R_{\rm bar} \approx 0.01$), i.e. the minor axis of the bar will have appreciably higher circular velocity than the major axis of the bar. The bounding $p = 0.2, 0.8$ quantiles

are chosen to be representative of the approximate values along the major and minor axes, respectively. The bulk of our analyses focus on the evolution after a discernible bar feature has formed, i.e. $T > 0.4$. The rotation curve continues to evolve after bar formation, as evidenced by the comparison between the panels of Figure 1.2. In particular, the disc contribution responds strongly to the formation and continued evolution of the bar, though the halo contribution also changes by up to 25 per cent at small radii ($R < R_{\rm bar}$).

Initially, the ratio of dark matter mass to stellar mass inside of one disc scale length is $M_{\rm dm}/M_{\star}(R < 0.01) = 0.757$. Although the gravitational potential in the disc plane is dominated by the stellar contribution, the dark matter provides an important channel for secular evolution, changing its phase-space distribution by trapping has important dynamical consequences that we will outline below[6].

In Figure 1.3, we plot the surface density of the disc and halo at a late time ($T = 2.0$), well after the bar has formed. An in-plane density slice of the halo reveals an approximately elliptical distribution aligned with the stellar bar, up to a maximum ellipticity of $e = 0.3$ in the fiducial model. Because the disc bar dominates the gravitational potential at these radii, by itself, this is not particularly surprising (e.g. Colín et al. 2006; Athanassoula 2007; Debattista et al. 2008). However, as we shall see in section 1.3.2.2, a large fraction of this dark matter is dynamically trapped in the bar potential; i.e. it now part of the bar! The dynamical nature of this halo feature and its evolutionary implications has not been identified previously. Additionally, a three-dimensional analysis of the disc shows that the initially spherical halo has, at late times, been flattened by the presence of the disc potential particularly at $R < 0.01$ (see section 1.3.2.2 for additional discussion).

We first describe the stellar bar by fitting ellipses to the projected disc surface density at each time. The bar changes appreciably with time, both elongating and slowing over the course of the simulation. In the upper panel of Figure 1.4, we plot the pattern speed of the

[6]At late times, $T = 2.0$, $M_{\rm dm}/M_{\star}(R < 0.01) = 0.595$, owing to an increase of stellar mass at small radii–a consequence of bar formation.

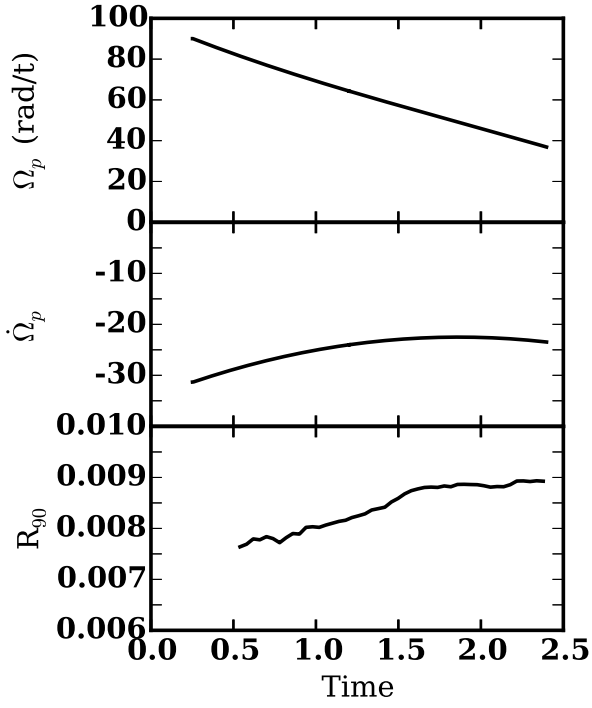

Figure 1.4. Upper panel: the pattern speed of the stellar bar as a function of time for the fiducial simulation. Middle panel: the rate of change in the pattern speed as a function of time. Bottom panel: the characteristic radius of the bar that encloses 90 per cent of the trapped stellar orbits (R_{90}) determined by k-means analysis. The bar slows nearly linearly at all times while the bar lengthens. Radius and time are given in virial units.

bar, Ω_p as a function of time. The pattern speed monotonically decreases with time, nearly linearly as $\dot{\Omega}_p$ changes only slightly (middle panel).

This global, phenomenological view of bar evolution does not reveal the underlying dynamical details and their implications for the long-term evolution of galaxies. Advancing beyond the traditional ellipse and Fourier determinations of the bar is possible in N-body simulations, albeit difficult. The centrepiece of our analysis below is the ability to accurately examine the dynamical characteristics of individual orbits to construct a more nuanced understanding of bar-disc-halo dynamics.

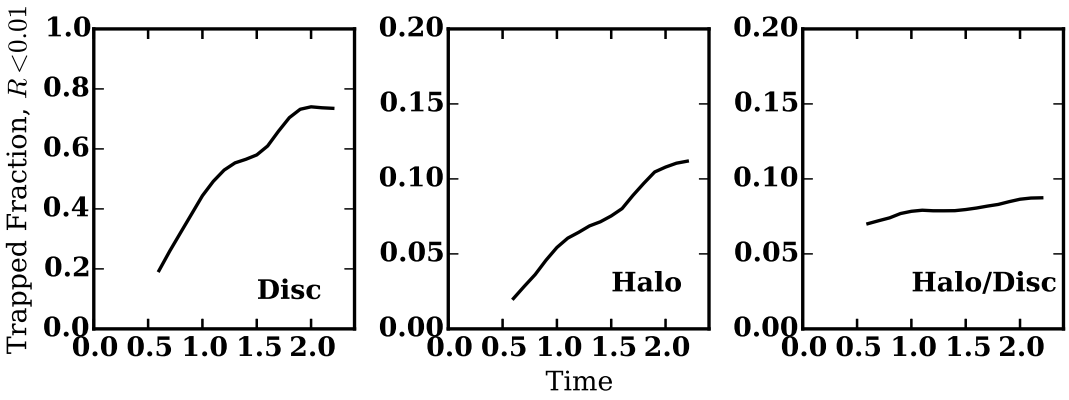

Figure 1.5. Trapped populations by fraction of mass interior to $R = 0.01$ (the initial scale length), as determined by k-means power, for the fiducial simulation. Left panel: disc trapping as a function of time. Middle panel: halo trapping as a function of time. The trapped halo fraction (the shadow bar) monotonically increases at all times. Right panel: The ratio of the shadow bar to stellar bar (by total mass) as a function of time. The halo is trapping at a faster rate than the disc, owing to the consistent increase in the reservoir of untrapped matter as the halo contracts in response to the bar growth. Time is given in virial units.

1.3.2 Orbit taxonomy

Orbits mediate the transfer of angular momentum between large-scale components (e.g. the disc and halo). For systems dominated by regular orbits for which the derivatives of the potential can be computed exactly (i.e. separable and regular systems), Fourier transformations of particle coordinates can determine the orthogonal frequencies of orbits in cylindrical coordinates ($\Omega_r,\ \Omega_\phi,\ \Omega_z$) and these frequencies allow for rapid and unambiguous determination of orbits trapped into potential features. The most obvious of these features are resonances, commensurabilities of frequencies with the pattern speed of the bar that satisfy the relation

$$l_r\Omega_r + l_\phi\Omega_\phi = m\Omega_p. \tag{1.11}$$

Previous studies have analysed N-body simulations by fixing or 'freezing' the gravitational potential after a period of self-consistent evolution and characterise the time-independent orbital structure (e.g. Binney & Spergel 1982, Martinez-Valpuesta et al. 2006a, Saha et al.

2012). If the rate of bar evolution is sufficiently small compared to the time required to cross the resonance zone ($\dot{\Omega}_p = \mathcal{O}(\epsilon)$ and $\dot{I}_{\rm bar} = \mathcal{O}(\epsilon)$ as $\epsilon \to 0$, where $\dot{I}_{\rm bar}$ is the time derivative of the moment of inertia of the bar), the dynamics will be approximately described by secular theory (e.g. Tremaine & Weinberg 1984b, Weinberg 1985, Hernquist & Weinberg 1992). However, realistic potentials are continuously evolving, so one must attempt a finite-time analysis of secular processes to investigate the nonlinear effects. In other words, one must devise techniques that characterise orbits while the bar pattern speed and geometry change. To this end, we have developed a k-means classifier for orbits, which quickly and accurately decomposes particles into orbital components classified by their commensurabilities. Briefly, the k-means technique (Lloyd, 1982) iteratively sorts a collection of points into k clusters given a distance metric. For our application, we use a time series in the r and θ (azimuthal angle) positions of apsides (radial turning points, $r_{\rm max}$) for a given orbit to determine its membership in the bar. As a first application of the method in this work, we limit our analysis to $k = 2$.

In a frame corotating with the bar, the apsides of orbits trapped by the bar do not precess through 2π. That is, the azimuthal position of outer turning points for trapped orbits oscillate about some fixed position angle in the bar frame of reference. We exploit these slowly changing apse positions for trapped orbits to identify coherent bar-supporting orbits over a finite time period. Specifically, we define $\delta\theta_{\parallel}$ to be the absolute value of the difference in azimuthal angle between the outer turning point of a particular orbit and the bar position angle. Let $\langle\delta\theta_{\parallel}\rangle_{20}$ be the average value of $\delta\theta_{\parallel}$ in 20 azimuthal periods for a given orbit. We use the k-means technique to identify orbits with $\langle\delta\theta_{\parallel}\rangle_{20} < \pi/8$. Orbits that are periodic and aligned with the bar in its corotating frame have $\langle\delta\theta_{\parallel}\rangle_{20} = 0$ while those with no correlation have $\langle\delta\theta_{\parallel}\rangle_{20} = \pi/4$. Additionally, relevant resonances trap orbital apsides perpendicular to the bar. In this case, we define an analogous $\delta\theta_{\perp}$. In practice, this technique allows for rapid determinations of bar membership over time windows that

are too brief for frequency determinations using Fourier techniques. In many cases, the bar evolution is so rapid that an analysis in a frozen potential would not be relevant.

After testing a range of period windows, the choice of 20 azimuthal periods was chosen as a balance between minimizing sampling noise while retaining temporal resolution of the evolutionary time scale. Our method is applicable to all but the most extremely centrally confined particles whose azimuthal periods are too small to satisfy an approximate Nyquist criterion. For the simulations here, this critical azimuthal period is $T_\theta = 0.004$ and affects approximately 0.1 per cent of the orbits. As a simple verification test, we analysed the fixed disc potential simulation (i.e. non-axisymmetric disc evolution is disallowed, Ff in Table 1.1), finding a bar signal of $<$0.1 per cent, demonstrating that the method is very robust against false positives.

For this paper, we will abbreviate our discussion by assuming that all orbits trapped by the bar potential are 2:1 orbits–those that exhibit two radial periods in every azimuthal period, identified by $k = 2$. In reality, the primary resonance bifurcates into 4:1 and 2:1 orbits at high bar strength near the ends of the bar (Athanassoula, 1992). An in-depth discussion of the k-means identifier and its application to orbital family determination will be presented in a later paper.

1.3.2.1 Disc orbits

Since our understanding of secular evolution is informed by perturbation theory, we describe the orbital behaviour in the disc by conserved quantities; here we choose energy and the in-plane angular momentum, E and L_z. At radii larger than the corotation radius (hereafter, CR)[7], orbits have low ellipticity ($e < 0.1$). Inside of CR, the ellipticity increases owing to the bar. The bar-parenting orbit family ($\mathbf{x}_1$ in the notation of Contopoulos & Papayannopoulos 1980) is an orbit family whose outer turning points align. These arise

[7]The CR resonance has $m = l_\phi = 2,\ l_r = 0$ in the notation of equation 7.2. The CR radius is ≈ 0.02 in the fiducial simulation at $T = 2.0$.

from the inner Lindblad resonance (ILR)[8] in perturbation theory. Such orbits are easily identified with the k-means identifier.

As a first application of the k-means method, we identify the radius that encloses 90 per cent of the bar-trapped disc orbits as the characteristic bar radius, R_{90}. The bottom panel of Figure 1.4 shows that the radius of trapped orbits increases monotonically with time, corroborating previous works indicating the lengthening of bars over time. The trapped fraction of disc orbits satisfying $R < 0.01$ is an explicit measure of the bar mass and, therefore, the bar potential (see the left-hand panel of Figure 1.5). The fiducial simulation exhibits a monotonic increase in the trapped fraction with time. Further, the growth of the bar can be roughly divided into three phases: formation, fast growth, and slow growth. The first, formation ($T < 0.5$ in Figure 1.5), is not studied in this work. We instead begin our study of orbits at times after which the bar can be detected through ellipse fitting, the fast growth phase[9]. In this phase ($0.5 < T < 1.2$), the bar rapidly gains mass and significant $m = 2, 4, 6$ patterns are observed beyond R_d. In the third phase ($T > 1.2$), the bar continues to add mass (albeit at a diminished rate), but the disc is relatively devoid of other $m \neq 2$ features.

1.3.2.2 Halo orbits

The structure of the dark matter distribution in the stellar disc has recently been debated, with particular discussion regarding the creation of a co-rotating 'dark disc' (Read et al., 2008; Bruch et al., 2009; Read et al., 2009; Purcell et al., 2009; Pillepich et al., 2014). This dark disc is formed by the accretion of satellites that settle into a rotating structure through dynamical friction, affecting the local dark matter density by contributing up to 60 per cent in some simulations (Ling et al., 2010), but very little in others (Pillepich et al., 2014).

[8]The ILR resonance has $m = l_\phi = 2,\ l_r = -1$ in the notation of equation 7.2

[9]The trend at $0.5 < T < 1.0$ cannot be extrapolated to T=0.0, suggesting that the growth rate at $0.0 < T < 0.5$ is more rapid than in the range $0.5 < T < 1.0$. However, this cannot be determined through the k-means technique due to time resolution limits.

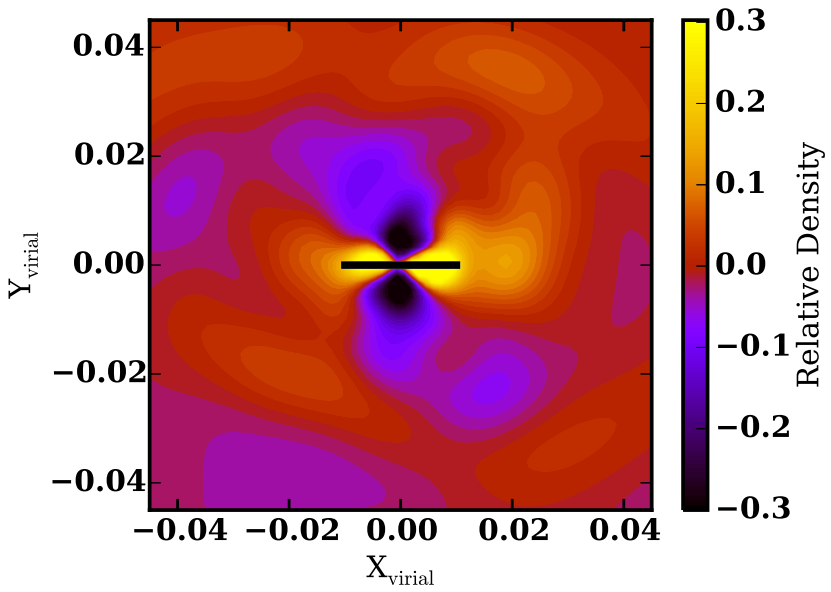

Figure 1.6. The halo wake ($(m > 0) + (m = 0, n \neq 0)$, filled colour) with the bar position and length indicated as the thick black line. The wake lags behind the bar (rotating clockwise) at $R > 0.5R_d$, but is generally aligned with the bar within $0.5R_d$, where we observe significant trapping (see Fig. 1.5). Note the resemblance to the untrapped component of the disc in Fig. 1.3. Positions are given in virial units, as in Fig. 1.3.

Additionally, the halo is shown to be prolate at small radii in the presence of a stellar bar, referred to as the 'halo bar' or 'dark matter bar' (Colín et al., 2006; Athanassoula, 2007; Athanassoula et al., 2013; Saha & Naab, 2013), though Debattista et al. (2008) demonstrated that if the disc were evaporated, the prolate inner region of the halo would recover its initially spherical shape.

In our fiducial simulation, the dark-matter halo becomes oblate near the disc at late times. We also refer to this as the 'dark disc', while noting the difference in formation mechanism from previous authors. This dark disc is a necessary consequence of the gravitational potential of the disc instead of depending on accretion. We, therefore, expect this dark matter feature to be a generic consequence of stellar discs. At $T = 2.0$, long after the bar has formed, and at $R = 0.03$, approximately the radius where the disc and halo contributions to the rotation curves are equal, a determination of the ellipsoidal shape of the halo following the method of Allgood et al. (2006) finds $S \equiv c/a = 0.45$ (as well as $Q \equiv b/a = 0.8$), where a, b, and c are the lengths of the major, intermediate, and minor axes, respectively. While some of this flattening is attributable to adiabatic compression of the halo in response to the presence of the stellar disc, a test simulation that allows the halo to achieve equilibrium while holding the initial disc potential fixed demonstrates that adiabatic compression alone, which gives $S = 0.6$ and $Q > 0.99$, cannot account for their deviation from the initially spherical distribution. In the plane of the disc, the effect is even more pronounced; at $R = 0.03$ for all $T > 1.0$, the azimuthal average of the density in the disc plane is >30 per cent larger than the initially spherical distribution[10].

Examining the evolution of the halo flattening in the fiducial simulation reveals that the initial response of the halo to the presence of the disc is complete by $T = 0.3$, in the midst of bar formation; at $T = 0.3$ and $R = 0.03$ in the fully self-consistent simulation we find

[10]The density along the polar axis at all times is nearly equal to the initial distribution at $R > 0.01$. At $R < 0.01$, the potential of the disc causes spherical adiabatic contraction such that the halo density along the polar axis is also enhanced relative to the initial distribution.

that $S = 0.6$ and $Q = 0.95$. The similarity of these values to that of the settled halo in the fixed disc potential test at late times suggests that the evolution of the disc is responsible for the continued compression and the move to triaxiality. Furthermore, the continued evolution of the halo shape suggests that simply including adiabatic compression in halo models is insufficient to recover the dynamics of the stellar disc and halo.

The distribution of $\cos\beta \equiv L_z/L$ also illuminates the flattening of the halo[11]. A perfectly spherical halo will exhibit uniform coverage in $\cos\beta$ owing to the random orientations of the orbital planes. However, at high binding energy (small radii), where the disc dominates the potential, the halo shows enhanced populations at $\cos\beta \approx 1$. Taken together, the continued flattening of the halo and the distribution of $\cos\beta$ suggest that the continued deposition of angular momentum into the halo owing to secular torques from the bar causes the formation of the dark disc in our simulations.

Clearly, the perturbative effect of the stellar bar on the halo cannot be ignored. To investigate the secular response of the halo orbits to the bar, we apply the k-means analysis to these orbits as well and find a class of 2:1 orbits that respond similarly to the bar as their disc analogues. In other words, the presence of the stellar disc traps initially spherical halo orbits into not only planar orbits, but into bar-supporting orbits that we call the *shadow bar*. We emphasise that this result is qualitatively different from those of Debattista et al. (2008), whose orbits are necessarily untrapped if they retain their box-like nature relative to the triaxial halo upon evaporation of the disc. We cannot comment on the likelihood of a similar box orbit-retaining outcome for other studies that point out a bar-like feature in the halo (Colín et al., 2006; Athanassoula, 2007; Athanassoula et al., 2013).

The growth rate of trapped halo orbits also follows that of the stellar bar, albeit with a smaller fraction of the halo mass available for trapping at $R < 0.01$ (the middle panel of

[11]The definition of $\cos\beta$ means that an orbit in the disc plane will have $\cos\beta = 1$, such that $\beta = 0°$. Throughout the work, we will make use of the limit $\cos\beta > 0.9$, which corresponds to $\beta < 26°$, to define halo orbits at low inclination relative to the disc angular momentum plane.

Figure 1.5). The continued growth of the trapped fraction during the simulation corroborates that halo trapping is secular and not merely a result of the initial settling of the halo in response to the stellar disc. In the rightmost panel of Figure 1.5, we plot the ratio of dark matter trapped mass to stellar trapped mass (the total for the simulation rather than that scaled to the mass interior to R_d). This also rises monotonically throughout the simulation, owing to both the presence of a larger reservoir of planar material as the dark disc grows with time and the increasing strength of the bar potential with time. The result is that the shadow bar grows at a faster rate than the stellar bar.

Overall, the trapped halo orbits exhibit the same behaviour as their trapped disc counterparts: bar-supporting orbits are found at larger radii through time. The trapped orbits in the halo are 5-10 per cent of the trapped mass of disc orbits, and 3-5 per cent of the total trapped angular momentum. That is, the shadow bar is not a large contributor to the mass of the visible stellar bar. However, the existence of shadow bar modifies the rate and location of angular momentum exchange between the bar and halo. Simple perturbation theory calculations following the model presented in Weinberg (1985) demonstrate that the halo orbits that accept L_z from the disc are preferentially located near $\cos\beta = 1$ and these orbits are the ones that are efficiently trapped into the shadow bar. If we bin the halo orbits by $\cos\beta$, we find that at $T = 2.0$, approximately 45 per cent of the orbits satisfying $\cos\beta > 0.9$ in the annulus $0.003 < R < 0.01$ are trapped[12], compared to 12 per cent for all dark matter at $R < 0.01$ (see Figure 1.5). Preferential trapping of orbits with $\cos\beta > 0.9$ suggests that the shadow bar will decrease the angular momentum transport from the bar to the halo relative to that predicted by dynamical friction theory. We will estimate the magnitude of these effects in section 1.3.4. In the case of a dark disc formed through satellite accretion, whose distribution would be concentrated near $\cos\beta = 1$ rather than evenly distributed in $\cos\beta$, we would expect to observe enhanced trapping relative to what is presented here.

[12]The lower bound, $R = 0.003$, is selected to avoid the inner region of the halo where the z-dimension oscillations of the orbit, even if the orbit has net rotation (nonzero L_z), confuse the calculation of $\cos\beta$.

Moreover, the overall contribution of the dark matter wake has a very long reach. To see additional effects of the shadow bar on the halo at large scales, we plot the in-plane wake (as in Weinberg & Katz 2007a) at $T = 2.0$ in Figure 1.6. Here, we define the halo wake as the response of the *untrapped* halo to the non-axisymmetric bar. We find the halo wake by removing all the trapped orbits as found by the k-means analysis and comparing the resulting distribution to the lowest order axisymmetric density profile. To accomplish this, we constructed a new basis using only the untrapped orbits (as described in section 6.2.1) and then removed the lowest order ($m = 0,\ n = 0$) component to find the wake[13]. Despite removing the trapped orbits, we observe a strong quadrupole feature that follows the stellar bar (along the x-axis) and extends to the end of the stellar bar (the extent of the stellar bar is shown as the black line). Beyond the extent of the bar, an $m = 2$ pattern is observed, a direct result of the secular evolution detailed in Weinberg (1985). If the disc scale length of the simulation is scaled to that of the MW, this wake extends out to the Solar circle at approximately the 10 per cent level. This scaling of the simulation may not be the most appropriate due to the apparent disagreement between the bar length-scale length relationship in our simulation and the MW. If the simulation is instead scaled to the bar length of Wegg et al. (2015), 4.6 kpc, the density enhancement from the wake may be as large as 25 per cent!

1.3.3 Dynamical properties of orbits

To understand the dynamics of the trapped halo orbits, we investigate the distribution of conserved quantities in the various orbit populations. We characterise the orbits by energy E, an isolating integral for all regular orbits, and $L_z/L_{\max}(R)$, where we normalise the angular momentum perpendicular to the disc, L_z, by the angular momentum of a circular

[13]Note that in addition to the non-axisymmetric $m \neq 0$ components, we include $m = 0,\ n \neq 0$ terms in the wake calculation.

orbit with the same energy, $L_{\max}$[14]. Figure 1.7 shows the distribution of $\langle \delta\theta_{\parallel} \rangle_{20}$ for stellar orbits from the fiducial simulation at $T = 2.0$. Orbits with $\langle \delta\theta_{\parallel} \rangle_{20} < \pi/8$ reliably indicate bar-trapped orbits. As expected, the strongest signal comes from mildly elliptical orbits with $L_z/L_{\max}(R) = 0.5$ near the end of the bar with $E = -9.5$ ($R = 0.01$). Many of the orbits within a characteristic radius of the bar are trapped (exhibiting $\langle \delta\theta_{\parallel} \rangle_{20} < \pi/8$), though Figure 1.5 indicates that not all orbits within $R = 0.01$ are trapped.

A similar exercise performed for the halo (Fig. 1.8) reveals that trapped halo orbits occupy the same region in $E - L_z$ parameter space as the trapped disc orbits. Because the fiducial halo is initially isotropic the quantity $L_z/L_{z,\max}(R)$ can have values from -1 to 1. The shadow bar reveals itself by the prominent $\langle \delta\theta_{\parallel} \rangle_{20} < \pi/8$ feature in the upper left corner of Figure 1.8 at $E < -9$ ($R < 0.01$). This reinforces our finding that both dark-matter and stellar orbits are trapped by their mutual gravitational potential, and that the disc and the halo cannot be treated as distinct dynamical components.

In addition to the shadow bar, Figure 1.8 reveals two planar retrograde families exhibiting $\langle \delta\theta_{\parallel} \rangle_{20} > \pi/3$ (or equivalently $\langle \delta\theta_{\perp} \rangle_{20} < \pi/6$), which correlate with overdensities in Figure 1.6 and are associated with the ILR and CR resonances. Similarly, we observe the outer Lindblad resonance (OLR, $m = l_\phi = 2,\ l_r = 1$ in the notation of equation 7.2) as a prograde planar family at $E = -6.5$ ($R = 0.04$), observable as an overdense region with $\langle \delta\theta_{\parallel} \rangle_{20} > \pi/3$ in Figure 1.6. The approximate position of the resonances were located by using the monopole potential field of the disc and halo from the basis so that equation 7.2 could be solved numerically as a function of E and κ when combined with the instantaneous pattern speed of the bar (see Figure 1.4)[15]. We further confirmed the resonant nature of orbits in these $E - \kappa$ regions by examining individual orbits.

---

[14]The quantity, $L_z/L_{\max}$, is equivalent to $(\cos\beta)\,\kappa$, where $\cos\beta \equiv L_z/L$ and $\kappa \equiv L/L_{\max}$, as defined in the literature (e.g. Tremaine & Weinberg 1984b).

[15]Owing to the choice of a spherically symmetric system for the resonance determination, the tilt of the rotation plane, and thus our approximation for the location of resonances, does not depend on $\cos\beta$.

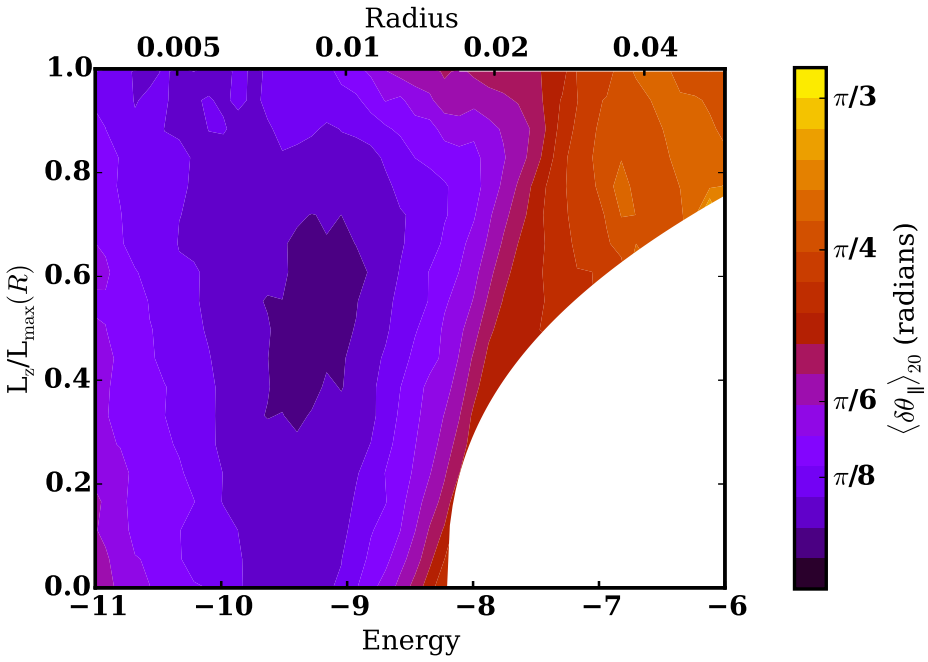

Figure 1.7. The distribution of $\langle \delta\theta_{\parallel} \rangle_{20}$ as a function of energy, E, vs. scaled angular momentum, $L_z/L\max(R)$, at $T = 2.0$ for the stellar disc. At each radius, L_z and E are calculated for a circular planar orbit and used to determine the mapping between energy and radius, as well as the maximum L_z at a given radius. The quantity $L_z/L_{max}(R)$ is zero for a radial orbit and unity for a circular orbit. Nearly all disc orbits are prograde, $L_z/L_{max}(R) > 0$. The colours denote the average apse position relative to the position angle of the bar. The region in E-L_z space with insufficient density to obtain a reliable estimate is white. The disc is largely comprised of circular orbits at $R > 0.02$. The dark blue region indicates the stellar bar. Radius and energy are given in virial units, see Section 2.2.1.

To summarise the previous sections, the initially nearly isotropic dark matter halo evolves significantly in the presence of an evolving disc. The effects are three-fold: (1) the trapping of dark matter orbits into the shadow bar; these orbits subsequently behave just like stellar bar orbits; (2) the dark disc, a response to the presence of the stellar disc as well as secular torques from the stellar and shadow bar; these orbits do not resemble the stellar disc per se, but more importantly do not resemble initial halo orbits; and (3) the dark matter wake, created by the influx of L_z from the stellar disc.

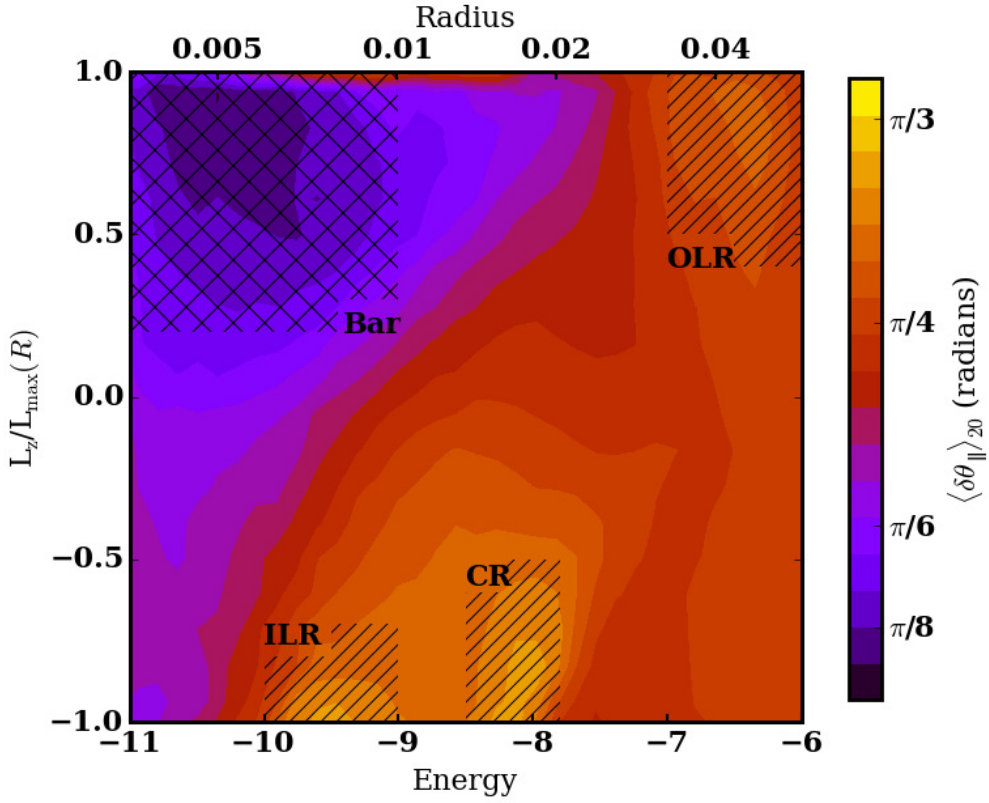

Figure 1.8. As in Fig. 1.7 but for the dark matter halo. Retrograde orbits are now present and the $L_{\rm z}/L_{\rm max}(R)$ axis now runs from -1 to 1. The dark blue region in the upper left, with an x-hatched region overlaid, indicates orbits trapped into the shadow bar, which occupies the same region in $E - L_{\rm z}$ space as the stellar bar (compare to Fig. 1.7). Additional features from the k-means analysis are also seen, including two retrograde populations at $E = -9.5$ and $E = -8.2$ that are transiently moving through the ILR and the CR, respectively. A prograde population is observed at OLR, $E = -6.5$. These populations correspond to the wake overdensities in Fig. 1.6. As in Fig. 1.7, radius and energy are given in virial units.

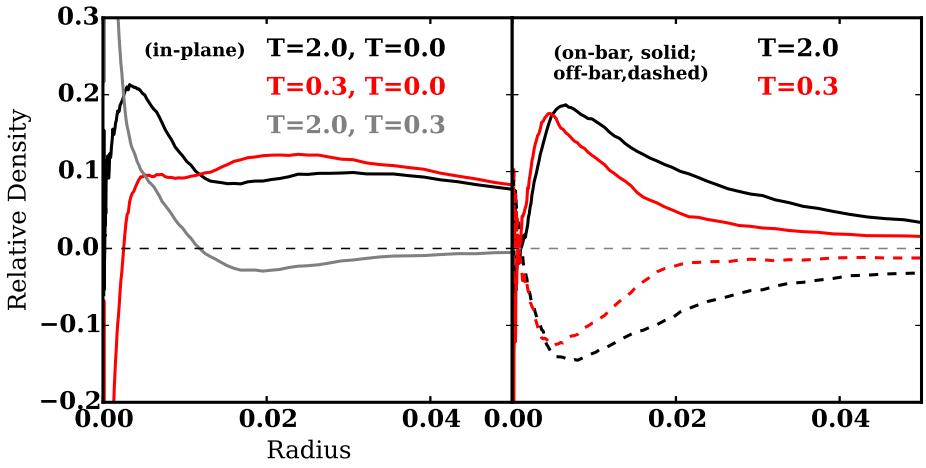

Figure 1.9. Left panel: the in-plane dark matter density ratio for axisymmetric density profiles at three pairs of times. The black line compares $T = 2.0$ with $T = 0.0$ (the total change in the profile during the simulation), the red line compares $T = 0.3$ to $T = 0.0$ (the change in the halo distribution induced by bar formation), and the grey line compares $T = 2.0$ to $T = 0.3$ (changes caused by secular evolution). The halo has dramatically redistributed its density in response to the presence of a stellar disc by $T = 0.3$, but continues to evolve secularly owing to the presence of the bar. Outside of $R = 0.05$, the fractional density difference rapidly falls to zero. Right panel: the in-plane fractional dark matter density ratio parallel to the bar and perpendicular to the bar, compared to the axisymmetrised profile, for two times. The on-bar radial cut shows an enhancement at a >5 per cent level within $R = 0.02$ following bar formation ($T = 0.3$), and a > 10 per cent enhancement within $R = 0.02$ after further evolution ($T = 2.0$). Radius and time are given in virial units, as in Fig. 1.2.

1.3.4 Observational consequences of the shadow bar

Although the trapped dark-matter mass fraction is small, even a small change in L_z for halo 2:1 orbits affects both the structure of the dark matter halo and the evolution of the stellar disc in our simulations, and these dynamics are reflected in observable properties of each. In this subsection, we discuss the global implications of several facets of the dark-matter halo response, focusing first on changes to the density and velocity structure, effects that might be traced by halo stars (e.g. observable by Gaia), and then turn to implications for the fast bar–slow bar formation scenarios.

1.3.4.1 Density and velocity structure

The bar changes the density and velocity structure of the dark matter halo. The dark disc in the fiducial simulation appears as an in-plane overdensity that grows with time. However, the non-axisymmetric structure of the shadow bar also contributes to density variations in the plane. Figure 1.9 demonstrates these two effects at play. In the left panel, we plot the axisymmetric density (azimuthally averaged) ratios for three pairs of times to directly explore the temporal evolution of the planar density without the shadow bar. Over the course of the entire simulation, from $T = 0$ to $T = 2$ ($\delta T = 4$ Gyr scaled to the MW; black curve), the in-plane density out to $R = 0.05$ (15 kpc for the MW) increases everywhere by > 8 per cent . Inside of $R = 0.01$, the density increases by up to 20 per cent. For comparison, the evolution from $T = 0$ to $T = 0.3$ is shown in red, demonstrating that the majority of the azimuthally averaged evolution at $R > 0.015$ (4.5 kpc for the MW) happens as the bar is forming. The evolution from $T = 0.3$ to $T = 2$ ($\delta T = 3.4$ Gyr for the MW), shown in grey, corroborates this, and shows that the in-plane density at $R < 0.015$ increases dramatically as the bar continues to grow.

The right-hand panel of Figure 1.9 examines the density on and off the bar axis, relative to the axisymmetric density, at two different times. The dark matter distribution is significantly non-axisymmetric at $T = 0.3$, in the midst of bar formation, including an enhancement of up to 17 per cent at $R = 0.005$ (1.5 kpc for the MW). At $T = 2.0$, the asymmetry is more pronounced enhancing the overdensity in the direction of the bar to 10 per cent out to $R = 0.02$ (6 kpc for the MW) and to 5 per cent out to $R = 0.035$ (10.5 kpc for the MW), as well as shifting the peak overdensity to a larger radius as compared to $T = 0.3$. Although the azimuthally averaged profile remains roughly unchanged at $R > 0.015$, the bar produces significant non-axisymmetric halo evolution at all relevant disc radii.

Further, the isotropic nature of the dark matter halo velocity in the plane of the disc has been significantly altered through an infusion of $L_{\rm z}$ from the disc. In the left panel of

Figure 1.10, we plot the tangential velocity distributions on- and off-bar for particles (black and red curves, respectively) near the end of the bar ($0.008 < R < 0.01$) at $T = 2$. For comparison, the dashed black line indicates a normal distribution with the same tangential velocity dispersion, centred at zero velocity. Along the bar axis, the peak of the tangential velocity (V_θ) distribution is shifted by $\delta V_\theta = 0.2$ (30 $\mathrm{km\ s^{-1}}$ for the MW). Even off the bar axis, the peak of the tangential velocity distribution has been shifted by $\delta V_\theta = 0.1$ (15 $\mathrm{km\ s^{-1}}$ for the MW). Additionally, the tails of both the on- and off-bar distributions are enhanced relative to a normal distribution owing to secular processes reshaping the halo.

In the right panel of Figure 1.10 we again plot the tangential velocity distribution for the on- and off-bar populations, but now compare it to the disc. We plot the on-bar disc distribution in the same annulus near the end of the bar as the solid grey line and the axisymmetric velocity distribution of velocities in the disc as the dashed grey line[16]. The on-bar disc particles are shifted to higher tangential velocities ($V_{\theta,\mathrm{bar}} = 0.8 = 120\ \mathrm{km\ s^{-1}}$ for the MW, including a shift between peaks of $\delta V_\theta = 0.5 = 75\ \mathrm{km\ s^{-1}}$ for the MW), which the halo reflects, albeit at a smaller δV (as discussed above). The on-bar disc distribution also shows an enhancement relative to the axisymmetric distribution at $V_\theta = 1.4$ that is mildly reflected in the halo. The particles trapped into the bar potential librate around the pattern speed as the flattening and trapping of dark matter particles correlate the velocities to create a non-zero mean velocity distribution that is particularly enhanced along the bar axis (in addition to the generic rotation seen in the off-bar population). In other words, the the L_z distribution has been modified, with the enhancement most clearly seen along the bar major axis. We make predictions for the net effect of the above considerations on dark matter direct detection experiments in Chapter 2.

Although our fiducial model is motivated by ΛCDM simulations (halo) and direct observations (disc), it represents a single realisation from a particular model family. We em-

[16] 5 per cent of the disc orbits at the end of the bar are retrograde, reflecting precession toward the bar that causes the tangential velocity in the inertial frame to be negative.

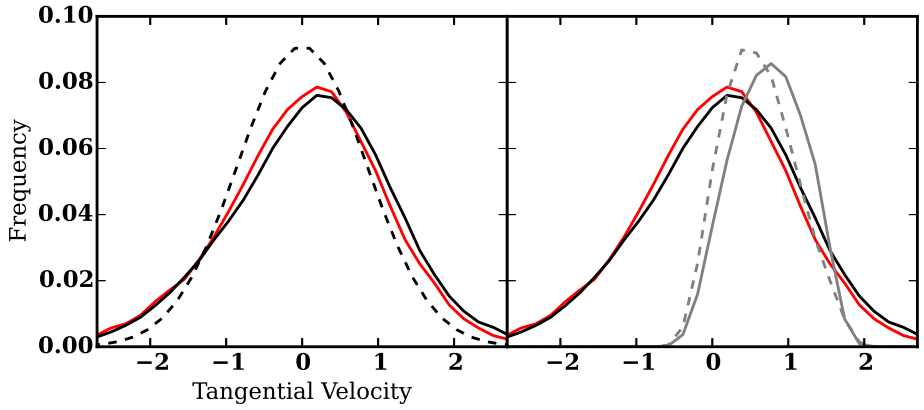

Figure 1.10. Left panel: Tangential velocity distributions at $T = 2.0$ on- (solid black) and off-bar (red) for the dark matter halo, at $R = 0.008$ (near the end of the bar). The dashed black line indicates a normal distribution. The tangential velocity distribution on the bar axis (solid black) shows both an enhancement centred near $V_c = 0.8(120\ \mathrm{km\ s^{-1}}$ for the MW), approximately the bar velocity at this radius, as well as a shift in the overall velocity peak. Both curves show enhanced tails relative to the normal distribution, at velocities $V_c < -1.5$. Right panel: The same dark halo tangential velocity distributions as the left panel are plotted, along with the disc on-bar distribution and axisymmetric distribution shown as the solid grey and dashed grey lines, respectively (scaled by 0.6). Tangential velocity is given in virial units, as in Fig. 1.1.

phasise that these observational conclusions are likely to vary even within a model family. However, we expect that the dynamical nature of the density and velocity differences driven by the shadow bar will be generic. To reduce the uncertainty of these simulation-derived quantities for application to Earth-based dark matter detection experiments, at least three additional pieces of information are critical. First, both the density and velocity signatures will be affected by the assumed length of the MW bar and its evolution as a function of time. Relative to the disc scale length, our bar is shorter than the observed MW bar (Wegg et al., 2015); also, the MW bar may have been longer in the past depending on its formation mechanism. Therefore, dark matter at the solar radius maybe have been influenced more readily. Secondly, we have demonstrated that the velocity structure depends on the position angle of the bar, so we need an accurate determination of the MW bar position angle. Finally, we need the formation time of the MW bar. The shadow bar continues to grow in time relative to the mass of the stellar bar. Therefore, an older MW bar would have more trapped dark matter material relative to the stellar bar. An older MW bar may also have a different velocity structure due to trapped dark matter orbits contributing to the torque on the untrapped halo component and the efficiency of L_z transfer from the enhanced mass of the shadow bar.

1.3.4.2 Angular momentum transport

The shadow bar contains a large fraction of the dark-matter orbits at low inclination: > 45 per cent of dark matter orbits satisfying $0.003 < R < 0.01$ and $0.9 < \cos\beta \leq 1$ are trapped, as discussed in section 1.3.2.2. The low inclination orbits are the same orbits responsible for accepting angular momentum and slowing the bar as determined by examining the model of Weinberg (1985). We expected that this would diminish the torque relative to the canonical perturbation theory results (e.g. Tremaine & Weinberg 1984b). We test this speculation by azimuthally shuffling the halo orbits as described in section 1.2.1.3. The purpose of this simulation is to prevent the shadow bar from forming and mimic the

standard dark-matter halo dynamical friction scenario. Figure 1.11 compares the results of the fiducial simulation to the azimuthally shuffled experiment. The azimuthally-shuffled halo is able to transfer angular momentum continuously, evident through the rapidly decreasing pattern speed during the evolution. Given the assumption that $\Delta L \approx \Delta\Omega_p$ for a stellar bar with the same geometry, we find that $\Delta\Omega_{p,\mathrm{shuffled}}/\Delta\Omega_{p,\mathrm{self-consistent}} \approx 3$, an appreciable increase in torque. Clearly, inhibiting the formation of the shadow bar results in a strong torque on the bar by the halo. We only present the results of the simulation for $T < 1.2$ because after this time the resultant stellar bars no longer qualitatively resemble each other ($I_{\mathrm{bar,shuffled}} \neq I_{\mathrm{bar,self-consistent}}$ where I is the moment of inertia of the bar), making the comparison of the simulations unfair.

The shadow bar does not eliminate the torque altogether, of course. A massive bar, enhanced by the dark matter, will couple more strongly to higher order resonances, even though these resonances are much weaker. The relative strength can be roughly approximated by considering the inverse of the largest winding number in the resonant equation (the maximum of $[m,\ l_\phi,\ l_r]$ in equation 7.2) for a particular resonance. For example, the 4:2:1 resonance will be approximately half as strong as the 2:2:1 resonance, and so on, for all realistic distribution functions (Binney & Tremaine, 2008). However, the primary (low-order) resonances are weakened by the reduction in available dark matter to accept angular momentum as more halo material becomes trapped. An enhanced dark disc, fed through satellite accretion, could act as a larger reservoir for material to trap, with presently unexplored implications for the torque.

1.4 Comparison between our fiducial and other models

1.4.1 Halo initial conditions

Our fiducial model is a simple representation of a disc galaxy in the ΛCDM formation scenario: a cuspy dark-matter halo profile with an exponential stellar disc. However, there are a variety of alternatives that are commonly explored in the literature. These include

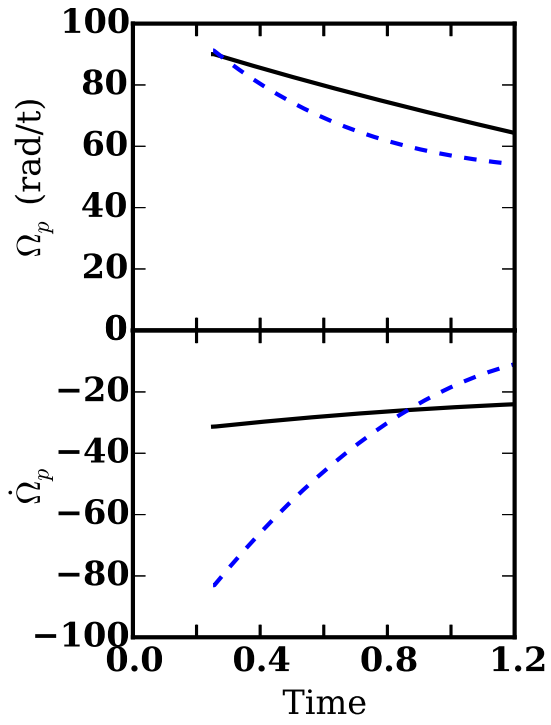

Figure 1.11. Upper panel: the pattern speed for the fiducial simulation (black) and an azimuthally-shuffled halo to suppress shadow bar formation (Fs; the dashed blue line). The simulation time is limited to $T < 1.2$ so that the stellar bars that form are still roughly equivalent. Lower panel: Change in pattern speed, following the same colour scheme. The shuffled simulation slows much more rapidly during the simulation, indicative of an increased L_z acceptance by the halo when there is no shadow bar. Time is given in virial units, as in Fig. 1.4.

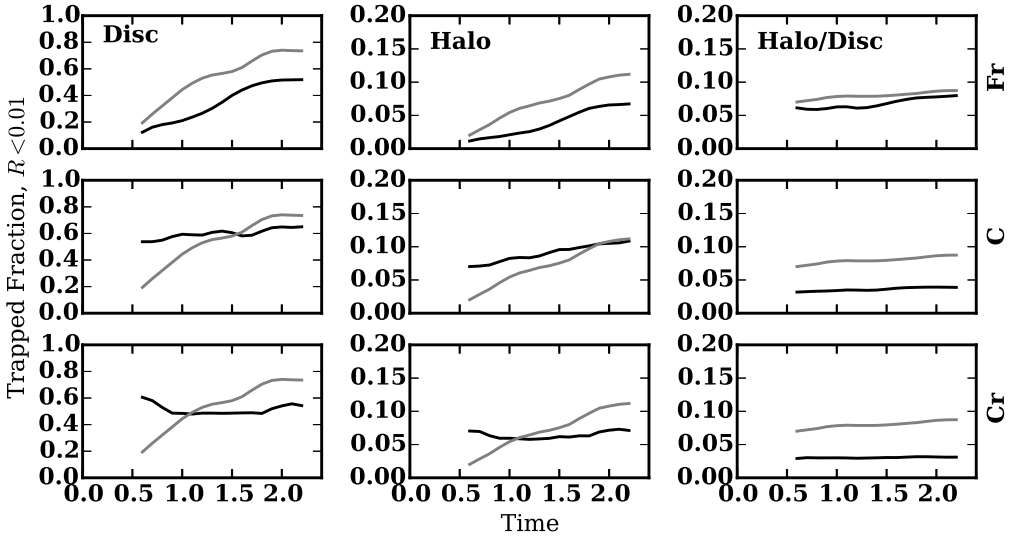

Figure 1.12. From left to right: stellar disc trapping, dark matter trapping, and the ratio of dark-matter halo to stellar disc trapping by the bar inside $R = 0.01$. Compare these to Fig. 1.5. From top to bottom the simulations are: the cusped rotating halo (Fr in Table 1.1), the cored nonrotating (C), and the cored rotating (Cr) models. Black lines indicate the total mass trapped scaled by the mass interior to $R = 0.01$ and grey lines indicate the corresponding curve for the fiducial model. Time is given in virial units, as in Fig. 1.5.

models whose density approaches a constant at some characteristic core radius r_c and rotating halo models (models with a non-zero value of L_z). The former, which have some observational (e.g. rotation curves, Breddels & Helmi 2013) and theoretical motivation (e.g. satellite accretion producing cores, black holes, and feedback from star formation or supernova; Tremaine & Ostriker 1999, Mashchenko et al. 2006, Governato et al. 2012) have often been used in N-body bar simulations (Athanassoula & Misiriotis 2002, Martinez-Valpuesta et al. 2006a, Saha et al. 2010). The latter are motivated by both evolutionary processes such as merging (Dekel et al., 2003) and the hierarchical formation process itself (Navarro et al. 1997, Bullock et al. 2001). In this section, we briefly summarise the variation in the properties of the disc and shadow bars for a representative member of each of these two model classes.

Table 1.1 describes the halo models we tested in addition to the fiducial cuspy nonrotating model. The resultant disc and shadow bar evolutions are shown in Figure 1.12, the analogue of Figure 1.5. The qualitative evolution is similar between all four simulations, suggesting that the results presented in section 3.3 are generally relevant. In particular, the shadow bar continues to grow relative to the stellar bar in all the simulations (the right panel of Figure 1.12). The fiducial model exhibits the strongest stellar and shadow bars at late times as a fraction of the available mass, but the trend in each model suggests that an equilibrium has not been reached at $T = 2.0$, the end of the simulations. (Recall that one system time unit is approximately 2 Gyr scaled to the MW, so that $T = 2.0$ is roughly 4 Gyr or 40 per cent of the age of the Galaxy.) The cored halo models exhibit a buckling instability at $T = 0.6$ in the cored nonrotating model, and at $T = 1.0$ in the cored rotating model. This instability releases disc orbits trapped during the bar formation phase, albeit a relatively small fraction, and does not appear to reduce the dark-matter fraction relative to the trapped disc fraction.

Overall, the differences in evolution between the models can be described as follows: (1) the cored halo increases the initial strength of the stellar bar through a stronger instabil-

ity (rapid growth at $T < 0.6$). However, the relative strength of the shadow bar is smaller and stagnant at late times owing to the reduced central density and, consequently, a smaller population of halo orbits that are available to trap; and (2) the increased rotation of a halo affects models by reducing the strength of the bar at early times (diminished the growth between $T = 0.5$ and $T = 1.0$); the stellar and shadow bars take longer to dynamically mature and, consequently, have not evolved to be as massive over the same span of time. This effect is smaller in the cored rotating halo compared to the cusped rotating halo, suggesting that the cuspy or cored nature of the halo dominates the evolution when compared to rotation in these models. We will discuss these trends further in a future paper.

1.4.2 Disc Maximality

As discussed in section 1.2.1.1, our fiducial model is a submaximal disc (as are all F-series models), chosen to correspond to cosmological simulations. Simulations with maximal discs (such as the C-series models) are subject to a violent disc instability that results in a qualitatively different bar formation scenario than that of our fiducial F-series models[17]. The violent disc instability may create a noisy bar formation process that inhibits the formation of the dark disc required for the stellar bar to then trap into the shadow bar. The C-series models nearly reach their maximum trapping fraction within several dynamical times of formation where the F-series models trap continuously over many dynamical times (see Figure 1.12). This illustrates a the distinct differences between the fast and slow mode of bar growth in our models. The variations with time, including untrapping of some orbits, suggest that the trapping is more tenuous in a violent instability. The fast and slow modes of bar growth will be studied further in future work. If these differences can be detected in an out-of-plane luminous tracer population (e.g. spheroid or thick disc stars in

[17]The C-series models have a significantly reduced fraction of dark matter within a scalelength, initially $M_{\rm dm}/M_\star(R < 0.01) = 0.332$, reducing to $M_{\rm dm}/M_\star(R < 0.01) = 0.231$ at $T = 2.0$ (owing to an increase in disc mass at $R < 0.01$). Compare this to values for the fiducial model in Section 1.3.1.

the Milky Way), we may be able to discriminate between these two modes of formation in nature.

It is also likely that the relative contributions to the potential from the disc and halo will change the formation efficiency of the shadow bar, an effect we have already seen qualitatively in the contrast between the cusp and core simulations. In the simulations with cores, the halo material interior to R_d is approximately half that in the cusp simulation, so that even when the same fraction of material is trapped (e.g. the middle panel of the cored simulation in Figure 1.12), the contribution to the overall bar potential is low (e.g. the right panel of the cored simulation in Figure 1.12). Furthermore, a more violent formation of the bar may change the structure of the dark matter wake. In this bar formation scenario, the formation of the dark disc and subsequent shadow bar trapping, both of which are slow processes, could be disrupted. A study of the implications of stellar disc maximality for the shadow bar and dark matter wake will be investigated in future work.

1.5 Conclusion

Our main findings are as follows:

(1). The stellar bar traps dark matter into a *shadow bar*. This shadow bar has a mass that is $>$6 per cent of the stellar bar mass after the bar forms, and this ratio increases with time throughout the simulations to values $>$9 per cent by mass. The halo is deformed by the presence of the disc as well as the continued torque from the stellar and shadow bar, creating a population of disc-like orbits (with a preferred angular momentum axis). We suggest that this reservoir increases the trapping rate of dark matter orbits.

(2). Trapping in the dark matter halo and the stellar disc takes place both at bar formation and throughout the simulation.

(3). The existence and strength of the shadow bar does not change appreciably in the presence of a core or rotation in the halo. However, the trapping rate of both the dark matter halo and the stellar component strongly depends on halo profile and the initial angular momentum distribution in the halo.

(4). The dark matter halo exhibits a density and velocity signature indicative of a reaction to the presence of the stellar disc at radii much larger than that of the bar radius. The density and velocity structure change with the angle to the bar, even at several bar radii. This could have important implications for direct dark matter detection experiments.

(5). Approximately 12 per cent of the total halo inside of the bar radius ($R < 0.01$), and 45 per cent of the dark matter satisfying $\cos\beta > 0.9$ within $0.003 < R < 0.01$, is trapped after 4 Gyr. These trapped orbits are precisely the ones that dominate the secular angular momentum transfer to the halo in the absence of trapping. The trapping changes the secular angular momentum transfer rates that one would estimate without trapping. We demonstrate this point with a simulation that suppresses trapped orbits by artificially decorrelating the halo orbit apsides with the bar position. This increases the halo torque on the bar after formation by a factor of three! Stronger bars are likely proportionally larger fractions of their haloes. This suggests that halo torques may be much smaller than theoretically predicted, especially for strong bars, helping to resolve the tension between the ΛCDM scenario and the observational evidence for rapidly rotation bars.

In concept, the idea of trapped dark matter is striking in its simplicity: when disc orbits and halo orbits occupy similar places in phase space, they will respond similarly to a perturbation. We have only begun to explore the parameter space necessary to characterise dark matter trapping, as well as the implications for the evolution of isolated galaxies. Therefore, we expect that other simulations have shadow bars as well, but previous stud-

ies have not investigated or identified the halo trapping and have not undertaken a detailed study of trapped populations in the disc component. Our k-means orbit finding algorithm can be used as a technique to further understand the dynamics of strongly time-dependent evolution, such as the bar-disc-halo system. In future papers, we will present a detailed breakdown of the orbit populations in the disc and halo components using the k-means technique.

Many simulations have shown that galactic bars efficiently transport angular momentum from the disc to the halo, causing the bar to slow, lengthen, and increase in strength (Debattista & Sellwood 2000; Athanassoula & Misiriotis 2002; Debattista et al. 2006; Weinberg & Katz 2007b). Many of these same authors have argued that bars are long-lived, as no mechanism for their destruction has been observed in simulations of isolated systems (e.g. Athanassoula et al. 2013). The results of Hernquist & Weinberg (1992) then suggest that the bar either cannot be strongly coupled to the halo, or requires fine-tuning to eliminate lower-order resonances to reduce the strong torque. The suggestion that bars cannot be strongly coupled to the halo seems to be in direct conflict with the angular momentum transfer rates observed in simulations depicting a rapidly slowing bar. The production of a shadow bar, and the trapping of halo orbits by the bar more generally, offers a possible way out of this dynamical conundrum. Without a sink of halo particles that are distributed asymmetrically in phase space relative to the bar, there can be no torque. Our discussion in section 1.4.1 suggests that the existence of the shadow bar is robust, but that its magnitude will depend on the galaxy profile and the details of the subsequent bar formation. If a significant dark disc exists as the remnant of shredded satellites accreted by the galaxy, the magnitude of the shadow bar could be significantly enhanced.

Although the shadow bar is kinematically similar to the stellar bar, the findings presented here provide new insight into the kinematics of the galactic centre. Observationally, stellar surveys may detect rotation in the stellar halo toward the inner Galaxy that would be indicative of trapping in a spherical component. For stars and stellar systems that may

have formed prior to the formation of the MW bar (such as metal-poor halo stars, thick-disc stars, or globular clusters), the findings presented here indicate that these components could also be trapped into the bar potential. Suggestions in the literature dating as early as Blitz & Spergel (1991) of a triaxial rotating component at the centre of the galaxy could be the result of an originally spheroidal component trapped by the bar potential. Recent observations by Babusiaux et al. (2014) and Rossi et al. (2015) have pointed out kinematic signatures (e.g. an anomalous tangential and radial velocity dispersion) that could be consistent with this interpretation. New stellar survey data available in the coming years will provide further insights. The results of this paper suggest that stellar survey data may be able to discriminate between fast and slow-growth bar formation and evolution in the MW.

Finally, evidence for a shadow bar in our own Milky Way could be directly detected through future direct dark matter detection experiments, including directional direct detection experiments, which would provide significant dynamical insights into the unseen dark matter component.

CHAPTER 2

THE DYNAMICAL RESPONSE OF DARK MATTER TO GALAXY EVOLUTION AFFECTS DIRECT-DETECTION EXPERIMENTS

2.1 Introduction

In the currently favored form of weakly interacting massive particle (WIMP) theory (see e.g. Jungman et al. (1996); Bertone et al. (2005)), dark matter is composed of a single particle with a mass in the range of 10 $\mathrm{GeV/c^2}$, which a number of experiments are working to directly detect XENON100 Collaboration et al. (2012); Aalseth et al. (2013); Bernabei et al. (2014); SuperCDMS Collaboration et al. (2015); Angloher et al. (2016); LUX Collaboration et al. (2016); Agnes et al. (2016); Amole et al. (2016); Tan et al. (2016); Agnese et al. (2016); Undagoitia & Rauch (2016). Direct-detection (DD) experiments seek to measure the weak nuclear recoils during elastic scattering between dark-matter (DM) particles and the nuclei of a target detector. The unambiguous detection of particle dark matter would address fundamental questions about the nature of the Universe, but despite considerable effort being focused on the direct detection of dark matter, a verifiable signal remains elusive. Limits on WIMP properties derived from these nondetections depend on poorly constrained parameters from astrophysics McCabe (2010, 2011). The astrophysical uncertainties in the structure of the DM halo have been recently implicated as a possible resolution for the disagreement between experiments with tentative detections (DAMA/LIBRA and CDMS-Si) and the null results from experiments such as LUX and superCDMS Mao et al. (2013); Pillepich et al. (2014); Bozorgnia et al. (2016); Kelso et al. (2016); Sloane et al. (2016).

Several simulation-based studies of Milky Way-like galaxies (e.g. a multicomponent model featuring at a minimum a stellar disk and responsive DM halo) have determined

Table 2.1. Halo Models.

Model Name	Designation[a]	Radial Profile	Dynamic?	Core?	Rotation?
Standard Halo Model	SHM	isothermal	N	N	N
Pristine NFW	pNFW	NFW	N	N	N
Adiabatically Contracted NFW	acNFW	NFW	Y[b]	N	N
Fiducial Dynamical NFW	fdNFW	NFW	Y	N	N
Cored Dynamical NFW	cdNFW	NFW	Y	Y	N
Rotating Dynamical NFW	rdNFW	NFW	Y	N	Y
Cored Rotating Dynamical NFW	rcdNFW	NFW	Y	Y	Y

[a]Designations are used in Figures, Model Names are used in text.

[b]Idealized evolution; see text.

velocity distributions for the DM halo that differ from the so-called standard halo model (SHM), finding that the spherical density and isotropic velocity distribution assumptions underlying the interpretation of most DD experiments are unlikely to be accurate owing to the presence of substructure in the halo Kuhlen et al. (2010); Purcell et al. (2012); Lisanti & Spergel (2012). Another class of studies primarily focus on the difference between DM-only simulations and simulations that include a stellar component Pillepich et al. (2014); Bozorgnia et al. (2016); Kelso et al. (2016); Sloane et al. (2016), finding largely the same results. However, little disagreement exists between these studies regarding the expected response for DD experiments, and the underlying dynamical causes have not been thoroughly investigated.

For example, these studies have been unable to reach a consensus on the applicability of a Maxwell-Boltzmann (MB) distribution to describe the DM velocity distribution in the Milky Way (MW) near the Sun, and are roughly divided into groups that claim a MB distribution does describe the tail of the DM velocity distribution Kelso et al. (2016); Bozorgnia et al. (2016), and those that find that the tail is suppressed relative to a MB distribution Pillepich et al. (2014); Sloane et al. (2016).

In addition, the 'dark disk', an axisymmetric, flattened DM feature roughly on the size scale of the stellar disk observed in some simulations, comprises an additional component for detection Read et al. (2008, 2009); Bruch et al. (2009); Purcell et al. (2009); Ling et al. (2010); Pillepich et al. (2014), but its existence continues to be debated. However, as we show in (Chapter 1), a dark disk that mimics the appearance of the stellar disk is a natural consequence of the presence of a stellar disk in a DM halo, something that is obviously present in our own galaxy. The dark disk effect may be enhanced further by the disruption of satellites Pillepich et al. (2014), which other studies contend may not be a generic result of cosmological simulations Kelso et al. (2016). This scenario is qualitatively different from the dark disk described in Chapter 1. Other studies have claimed that the DM density at the Sun's location should differ by less than 15% from the average over a constant

density ellipsoidal shell using high resolution cosmological simulations Vogelsberger et al. (2009) and that the density distribution is only slightly positively skewed Kamionkowski & Koushiappas (2008). Yet other studies point out that many open questions remain regarding the presence of substructure near the Sun owing to either intact or destroyed subhalos Read et al. (2008, 2009); Kuhlen et al. (2012); Lisanti & Spergel (2012); O'Hare & Green (2014). In the face of these conflicting claims, seeking fundamental effects from known Milky Way (MW) causes is a prudent approach to illuminating the information that DM halo models can provide for DD experiments.

Galaxies evolve structurally through the interaction of the baryonic matter in their disks with the DM in their halos mediated by resonant gravitational torques. The strongest evolution of this type is likely to occur in barred galaxies (i.e. galaxies with prolate stellar distributions in their central regions with lengths on the order of the disk scale length). The barred nature of the MW was first suggested in the 1960s as an interpretation of observed gas kinematics de Vaucouleurs (1964), and subsequently confirmed through diverse observations in the ensuing half century (see Gerhard (2002) and Bland-Hawthorn & Gerhard (2016) for reviews). Recent observations have indicated that the bar hosted by our MW galaxy may be significantly longer than previously thought Wegg et al. (2015). Although the MW bar is known to have many consequences for observed astrophysical quantities, the bar's effect on the DM distribution has not been considered when characterizing the DM density and velocity distribution function that determines detection rates for DD experiments.

In this chapter, we present the implications of non-axisymmetric DM density and velocity distribution functions caused by the bar of the MW for DD experiments. We offer a qualitative analysis of recently published studies in an attempt to unify the seemingly disparate results. In Chapter 1, we demonstrated that particles in the DM halo will be trapped into a shadow bar that resembles the stellar bar—in addition to forming a DM wake visible in both the density and velocity structure of the dark matter halo at radii on the scale of

the stellar disk—the first such study that attempts to isolate the DM structure that results from interactions with the stellar bar. The effect of the shadow bar is cumulative with the expected response of an equilibrium galaxy DM halo to the presence of a stellar disk, resulting in a model for the DM halo that does not resemble the SHM. We will see that bar-driven galaxy evolution affects both the DM density and the kinematics at the Earth's location.

Using simulations designed to study the mutual dynamical evolution of the baryonic disk and DM halo for a Milky-Way-like galaxy, we characterize the secular evolution of an initially exponential stellar disk and spherically symmetric dark matter halo. We do not consider any satellite debris or stellar streams at the solar circle Freese et al. (2004); Savage et al. (2006), although these may be present. Rather, we detail significant differences from the SHM due to the stellar bar of the MW. Similar to previous studies Mao et al. (2013), we find that realistic DM distributions in galactic halos can dramatically increase the predicted detection rates for high v_{min} experiments. Moreover, the effects of long-term evolution in a barred galaxy further increases the tension between heavy and light nuclei experiments Frandsen et al. (2013). We demonstrate key regimes in which experiments can use the DM halo structure resulting from the MW bar to their advantage. Conversely, Pillepich et al. (2014) report an improvement in the tension between the heavy and light nuclei experiments if the detection signal were dominated by a DM debris disk from merger events, which has a sharply decreasing velocity tail. It is possible, of course, that the MW also has a DM debris disk from a merger event. This underscores the importance of the actual MW evolutionary history to DM detection predictions and motivates further detailed study.

This chapter is organized as follows. In section 2.2, we provide the relevant details about the simulations used for this analysis, including a comparison of the simulations to the MW in section 2.2.2. We then describe the results in section 3.3, beginning with the density and kinematic features of the simulated galaxy in section 2.3.1 before detailing the calculation of detection rates in section 2.3.2. We compare to previous findings in

Table 2.2. List of Milky Way Disk Scale Lengths in the literature.

Method	Scale Length (kpc)
Asymptotic Giant Branch Stars Nikolaev & Weinberg (1997)	4.00 ± 0.55
COBE/DIRBE Bissantz & Gerhard (2002)	2.1
G-dwarfs (α-old) Bovy et al. (2012)	2.01 ± 0.05
G-dwarfs (α-young) Bovy et al. (2012)	3.6 ± 0.22
G-dwarfs (mass-weighted) Bovy & Rix (2013)	2.15 ± 0.14

section 2.4.1 (including both the SHM and empirical models), then explore the effect of our results for detection rates in DD experiments (sections 2.4.2 and 2.4.3). Section 7.6 provides a broad overview of our results and prospects for future work.

2.2 Methods

2.2.1 Simulations

The n-body simulations analyzed here are presented in Chapter 1. We summarize the initial conditions for their relevance to the results and refer to Chapter 1 for details of the simulation methodology and dynamical interpretations. We list the simulations used in this chapter in Table 2.1.

We represent the axisymmetric disk density profile by an exponential radial distribution with an initially isothermal sech^2 vertical distribution, consistent with observations of the MW Bovy & Rix (2013). The DM halo is a fully self-consistent, cosmologically-motivated DM halo (Navarro et al., 1997, NFW) with $c = R_{\rm vir}/r_s \approx 15$ where r_s is the scale radius, and $R_{\rm vir}$ is the virial radius. The functional form of the NFW profile is given by

$$\rho(r) \propto \frac{r_s^3}{(r + r_{\rm core})(1 + r_s)^2} \tag{2.1}$$

Observations of the central density profile in the MW are consistent with either a pure NFW profile or a cored NFW profile Bovy & Rix (2013). The latter choice is motivated both by observational data and dynamical theory: a cored halo is more likely to be unstable to bar formation. We therefore test exampless of both models by selecting $r_{\rm core} = 0.0$ or 0.02. We

call the model with $r_{\rm core} = 0.0$ the *fiducial dynamical NFW* model, and use it as the primary model throughout our work. The $r_{\rm core} = 0.02$ model is called the *cored NFW* model. In practice, the cored halo model increases the relative disk density to halo density near the center of the simulation, while causing a variation of 20% at the approximate solar radius. We construct these initial halos without rotation, but acknowledge that true DM halos are expected to have some net rotation Bullock et al. (2001); we present two additional models with modest rotation to probe any possible effects. The $r_{\rm core} = 0.0$ and $r_{\rm core} = 0.02$ rotating models are called the *rotating NFW* and *cored rotating NFW* model, respectively.

Our simulations employ $N_{\rm disk} = 10^6$ and $N_{\rm halo} = 10^7$, disk and halo particles, respectively. These values ensure there is enough phase-space coverage to model resonant torques and to resolve collective features such as stellar bars and spiral arms. The disk particles have equal mass and the halo-particle masses are assigned to satisfy both the NFW density requirement with a steeper number density distribution, $n(r) \propto r^{-2.5}$. Relative to an equal-mass assignment, this improves the resolution of the mass and length scales in the gravitational potential of the DM halo by a factor of approximately 100 in the vicinity of the stellar disk, i.e. it is equivalent to the resolution of a $N_{\rm halo} = 10^9$ model.

A DM halo in dynamical equilibrium will respond to the growth of a baryonic disk through dissipation. This slow-growth process is often modeled in the adiabatic limit and is called 'adiabatic contraction'. It causes the halo density profile to become mildly oblate in response to the disk potential. To test the importance of this process, we additionally draw on the results of a simulation presented in Chapter 1 that artificially freezes the stellar disk profile while the DM halo self-consistently evolves. While not strictly an adiabatic process, we refer to this as the *adiabatically contracted NFW* model.

We also compare the dynamically evolved models listed above to the static *pristine NFW* model given by eq 7.3 with $r_{\rm core} = 0.0$, as well as the *standard halo* model (SHM).

2.2.2 Calibrating to the Milky Way

2.2.2.1 Dynamical Units

We scale the dynamical units of the simulations to the mass of the MW halo without attempting to tune the initial conditions to produce a model that more closely matches the details of the MW (e.g. its rotation curve, bar length, and bar amplitude). We plan to more closely mimic the MW in future simulations. We select a snapshot of the simulation after initial bar formation ($T = 1$ Gyr) and a subsequent 'secular evolution time' $\Delta T_{\rm se} = 3$ Gyr, defined as the time after the bar has formed, during which the bar strengthens and grows in length as a result of continued angular momentum transfer by secular processes (see Chapter 1). In general, the results are qualitatively similar for all outputs after bar formation. We discuss possible variations owing to the time selection where relevant.

To better compare the MW with the simulation, we may choose to scale the Galactic radius of the solar position to the disk scale length, to the bar length, or to something in between. The first scaling is fraught with astrophysical uncertainties, such as the variation of disk scale length with metallicity. This induces a dependence on the age of the stellar population used to estimate the disk scale length. In Table 2.2, we list some literature measurements of the disk scale length. Comparing to our simulation, we find that the Sun could be located anywhere between two and four disk scale lengths. The uncertain location of the Sun in the phase-space of the halo has been previously described as a large source of uncertainty (Mao et al., 2013). We, therefore, report a range of results that correspond to the uncertainty for the location of the Sun in this model. As noted in Chapter 1, further study of the MW bar history will reduce uncertainties related to scaling simulations to the MW.

Scaling to the length of the bar better represents our goal of studying the influence of the bar on the DM distribution at the solar position. Nevertheless, calibration to the bar is also uncertain owing to the diversity of parameter measurements for the MW bar in the literature. In Table 2.3, we list bar parameters measured for the MW. Using this scaling, the

Table 2.3. List of MW Bar parameters in literature.

Method	Bar Length (kpc)	Bar Angle
Asymptotic Giant Branch Stars Nikolaev & Weinberg (1997)	3.3 $\pm$0.1	24°$\pm$2°
OH/IR Stars Sevenster (1999)	$< 3.5^a$	–
near-infrared photometry Hammersley et al. (2000)	4.0	$43° \pm 7°$
Local stellar velocities Dehnen (2000)	$<5.3^a$	$20° - 45°$
COBE/DIRBE Bissantz & Gerhard (2002)	3.5	$20° - 25°$
near-infrared photometry Babusiaux & Gilmore (2005)	2.5	$22° \pm 5.5°$
Red Clump Giants (UKIDSS) Cabrera-Lavers et al. (2008)	4.5	$42.44° \pm$ 2.14°
Methanol Masers Green et al. (2011)	$< 3.3^a$	45°
Red Clump Giants (compilation) Wegg et al. (2015)	5.0 ± 0.2	$28° - 33°$

[a]Denotes a measurement of corotation, considered to be an upper limit for the bar length.

Table 2.4. Physical versus Simulation Parameters for the Milky Way.

Quantity	MW Value	Simulation Value
Scale Length, R_d	2.01-4.00 kpc (see Table 2.2)	3 kpc
$R_\odot$ Scale Height	0.37 $\pm$0.06 kpc Bovy & Rix (2013)	0.3 kpc
Disk Mass (Stellar)	$4.6 \pm 0.3(\mathrm{ran.}) \pm 1.5(\mathrm{syst.}) \times 10^{10}$ $M_\odot$ Bovy & Rix (2013)	3.25×10^{10} $M_\odot$
Halo Mass	1.6×10^{12} $M_\odot$ Boylan-Kolchin et al. (2013)	1.6×10^{12} $M_\odot$
Virial Radius	304 ± 45 kpc Garrison-Kimmel et al. (2014)	300 kpc
$R_\odot/R_d^a$	2.08-4.13 (see Table 2.2)	2.08-4.13 (see Section 2.2.2.1)
$R_\odot/R_{\mathrm{bar}}^a$	1.57-3.32 Reid et al. (2014); Chatzopoulos et al. (2015) (see Table 2.3)	1.57-3.32 (see Section 2.2.2.1)
$R_\odot$ Circular Velocity	218 ± 10 km s^{-1} Bovy et al. (2012)	218 km s^{-1}

[a]Using $R_\odot$=8.3 kpc Reid et al. (2014); Chatzopoulos et al. (2015)

Sun is located between 1.57 and 3.32 bar radii. We choose a nominal scaling of 2 bar radii for the Sun as a compromise between measurements of the disk scale length and bar radii. Additionally, Wegg et al. (2015) presents a bar mass in the range of $1.1 - 1.81 \times 10^{10}$ $M_\odot$, or $0.24 - 0.39 M_{\rm disk}$ (using the scaling from Bovy & Rix (2013)). This broadly agrees with the bar mass in the simulation at $\Delta T_{\rm se} = 3$, which we find to be $0.35 M_{\rm disk}$.

Since the Sun is measured to be only 25 pc above the disk midplane Jurić et al. (2008), and this is smaller than the resolution scale of our simulation, we will consider the Sun to be in-plane for the purposes of our calculations here. In practice, this introduces errors below the 1% level. Throughout the chapter, in-plane refers to $|z| < 1$ kpc. As in previous simulation-based studies Kuhlen et al. (2010); Purcell et al. (2012); Pillepich et al. (2014), we define a region of interest around the solar neighborhood from which to draw velocity samples. To achieve an accurate velocity distribution with the desired spatial sampling, we create wedges 1 kpc in radius, 2 kpc in height, and $\frac{\pi}{7}$ in azimuth. In addition, we sum 20 phase space outputs (total $\delta T = 0.08$ Gyr) near $\Delta T_{\rm se} = 3$ in a frame of reference rotating with the stellar bar, to decrease the noise further. Each bin has $> 10^5$ particles.

We caution that the scalings presented in this chapter are tied to the virial mass of the Milky Way DM halo, with a linear scaling in density, but a much more complex and poorly understood effect on the velocity structure. We choose a virial halo mass of 1.6×10^{12} $M_\odot$, as determined from the motion of the MW satellite Leo I Boylan-Kolchin et al. (2013). Local stellar kinematics imply a halo mass of 8×10^{11} $M_\odot$ Bovy et al. (2012) and suggests a factor of two uncertainty in this calibration. In addition, the rotation curve in our model deviates from the estimates of the MW rotation curve in Bovy & Rix (2013); the rotation curve in our simulation is slowly rising inside of three disk scale lengths rather than flat. We cannot comment quantitatively on the importance of the relative disk-to-halo potential contribution in the inner galaxy, a quantity that is poorly constrained in the MW as well Bovy & Rix (2013).

2.2.2.2 Velocity Definitions

The velocity of the Earth in the MW relative to the galaxy's inertial frame is the sum of three terms

$$\vec{v}_e(t) = \vec{v}_{\rm LSR} + \vec{v}_\odot + \vec{v}_\oplus(t). \tag{2.2}$$

where $\vec{v}_{\rm LSR}$ is the *local standard of rest* (LSR), $\vec{v}_\odot$ is the peculiar motion of the Sun, and $\vec{v}_\oplus(t)$ is the relative motion of the Earth. It is traditional to define the LSR as the mean motion of stars in the neighborhood of the Sun on a hypothetical orbit about the center of the Galaxy. This hypothetical orbit need may not circular, although circularity is often assumed. We define the three velocity directions $U,\ V,\ W$ in the LSR frame as follows: U points toward the Sun from the Galactic Center, V points in the direction of Galactic rotation, and W points perpendicular to the Galactic disk. The first velocity in equation (2.2) is the velocity of the LSR relative to the Galactic Center. We adopt $\vec{v}_{\rm LSR} = (0, 218 \pm 6, 0)$ km s^{-1}Bovy et al. (2012). The second term is the motion of the Sun relative to the LSR, the peculiar velocity, defined as $\vec{v}_\odot = (11.1^{+0.69}_{-0.75}, 12.24^{+0.47}_{-0.47}, 7.25^{+0.37}_{-0.30}) {\rm km\ s^{-1}}$ Schönrich et al. (2010), though somewhat larger values of $U_\odot = 14$ km s^{-1}Schönrich (2012) and $V_\odot = 23.9^{+5.1}_{-0.5}$ km s^{-1}Bovy et al. (2012) have been reported. The third term is the motion of the Earth in orbit around the Sun, for which we follow Lewin & Smith (1996). For the purposes of this study, we will consider only the velocity maxima and minima for the alignment and anti-alignment, respectively, of the Earth's velocity with the LSR motion. These epochs provide the largest kinetic energy difference and occur on approximately June 1, $V_\oplus = (0, 27.79, 0)$ km s^{-1}, and on December 1, $V_\oplus = (0, -27.79, 0)$ km s^{-1}, using the standard speed for the Earth of 27.79 km s^{-1}. This simple parameterization of the Earth's velocity relative to the Sun avoids the discrepancy in Lewin & Smith (1996) pointed out by Lee et al. (2013); McCabe (2014).

We scale the simulations to select $v_{\rm LSR}$ as the azimuthal velocity at the solar radius, as chosen in section 2.2.2.1. The scaling to the $v_{\rm LSR}$ (as well as the corresponding peculiar motions of the Sun relative to LSR) comprises the largest uncertainty in our comparison,

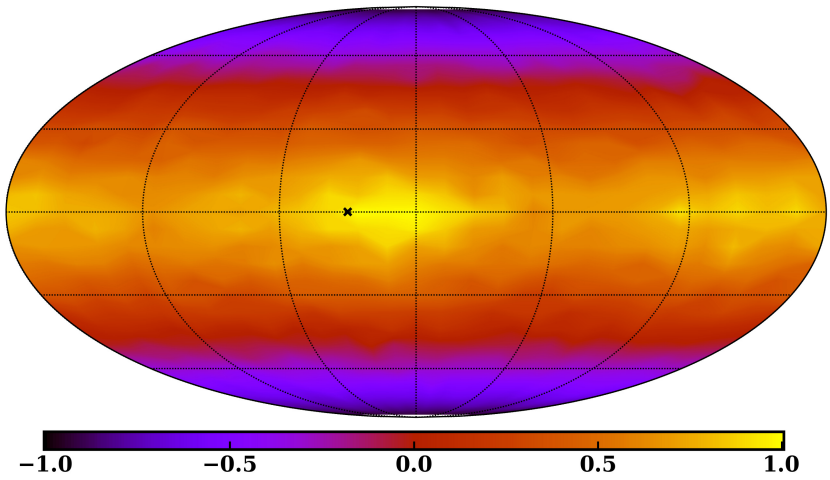

Figure 2.1. Mollweide projection of the relative DM density deviation at the solar radius to the mean DM density at the same radius for the fdNFW model. The coordinate system is oriented such that the bar angle is (0°,180°). The approximate position of the Sun is marked with an '**x**'. The flattening of the halo is clearly seen as a decrease in the density at the poles. The effect of the bar is seen as peaks at approximately (-15°,165°).

but we emphasize that the relative importance of the shadow bar for the direct detection of DM remains unchanged.

2.2.2.3 Summary of Key Differences

The fiducial dynamical NFW model results in a barred galaxy that has many properties similar to the MW. However, we identify two potentially important differences:

1. The fiducial model does not have a flat rotation curve at the solar circle in contrast to observations Bovy & Rix (2013), and thus the tuning of velocity in the simulation to that of the MW may have some systematic errors. The choice of $v_{\rm LSR}$ affects the width of the calculated speed distribution through the dispersion.

2. The ratio of the length of the bar to the disk scale length may suggest a different (i.e. triggered) origin for the MW bar, possibly from an orbiting satellite such as the

Sagittarius dwarf Purcell et al. (2011) or the Large Magellanic Cloud whereas our simulation forms a bar in isolation.

We comment on the possible effects of these differences at relevant points throughout the chapter, and again stress that the model has not been specifically tuned to the MW, but should rather be considered MW-like. Table 2.4 provides a concise comparison of measured MW parameters to the simulation parameters, valid for all NFW-derivative halo models.

2.3 Results

We begin this section by reporting the salient differences between static and dynamically evolving galaxy models that affect the DD rate. We describe the DM density and velocity variations in response to the bar in section 2.3.1. We compute the detection rates in section 2.3.2. In this section we restrict our analysis to the fiducial dynamical NFW model, comparing to other models in sections 2.3.2.2, 2.3.2.3, and 2.4.1.1.

2.3.1 Dark Matter Distribution Features

We begin with a discussion of the self-consistent response of the DM halo to a bar-unstable disk. There are two clear deviations from a spherical distribution: flattening (Section 2.3.1.1), and non-axisymmetric contributions due to the bar (Section 2.3.1.2). We then analyze the velocities and speed distribution in Section 2.3.1.3.

2.3.1.1 The Dark Disk

As a first characterization of the halo structure, we compute the ellipsoidal axes by diagonalizing the moment of inertia tensor as in Allgood et al. (2006). Similar to the findings of Kuhlen et al. (2007), we find that the halo becomes flattened owing to the presence of the disk with $(c/a = 0.5)_{\rm fdNFW}$ at the chosen solar radius, where c and a are the minor and major ellipsoidal axes, respectively. We find that $(c/a = 0.6)_{\rm acNFW}$ at the chosen

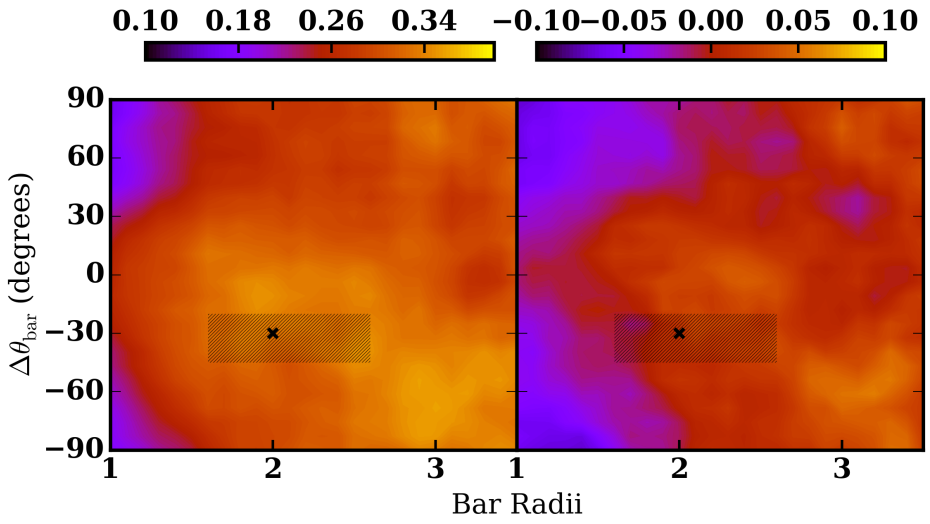

Figure 2.2. In-plane relative DM density as a function of bar radius and bar angle for the fdNFW model. Left panel: the simulation at $T = 4$ Gyr versus the pristine NFW model. Right panel: the simulation at $T = 4$ Gyr versus an adiabatically contracted model. The best choice solar position is marked with an 'x'. The possible solar locations consistent with astronomical uncertainties are denoted by the hatched region. Both panels show similar features, including a quadrupole disturbance owing to the bar that appears as a density enhancement trailing the bar. The patchiness in the relative density determinations owe to the self-consistent evolution (see Chapter 1 for further discussion).

solar radius for the adiabatically contracted NFW model. Fitting a disc and NFW halo model potential to the vertical structure of halo giant stars in the MW suggests $c/a = 0.8$ at the solar circle Bienaymé et al. (2014); Piffl et al. (2014), a smaller deviation from spherical than our findings. However, this ratio is poorly constrained by presently available data. The apparent disagreement may reflect the complexity of modeling the DM distribution from stellar data more than a problem with our models. For example, the halo stars at large distances from the disk are likely the result of hierarchical formation and satellite accretion and are unlikely to be affected by the environmental processes that affect DM near the disk in our simulation.

Figure 2.1 illustrates the deviation from a spherical distribution by showing a Mollweide projection of the relative density on a sphere at the solar radius: $(\rho - \langle\rho\rangle)/\langle\rho\rangle$. The approximate position of the Sun is marked, showing that the Sun resides in a strongly overdense region in our simulation relative to the spherical average. Two effects are clearly at play in causing the density of the DM halo to deviate from spherical. The first is the compression towards the disk plane, which is clearly seen as a gradient from low latitude to high latitude. The second, variations in longitude (non-axisymmetric structure), will be discussed in the following section.

The compression of the halo to an oblate figure is caused by two independent dynamical effects. The first, adiabatic contraction, is a response of the spherical halo to the potential of the embedded stellar disk. However, as noted above, $(c/a)_{\rm fdNFW} < (c/a)_{\rm acNFW}$, i.e., the fiducial dynamical NFW model is more oblate than the adiabatically contracted NFW model. This extra contraction is caused by the bar, which torques the halo through secular resonant interactions (see Chapter 1 for further dynamical details). $(c/a)_{\rm fdNFW}$ decreases as $\Delta T_{\rm se}$ increases, suggesting that the in-plane density may not have been as large in the past.

We refer to the enhanced (in-plane) contraction as the *dark disk* owing to its phase space resemblence to the stellar disk, while noting that previous works have used this term

to refer to shredded satellites that contribute DM in a kinematic disk-like structure Read et al. (2008); Bruch et al. (2009); Read et al. (2009); Purcell et al. (2009); Pillepich et al. (2014). The similarity of the DM distribution to the stellar distribution at corresponding radii is discussed in section 2.3.1.3 and extensively in Chapter 1. As discussed in Chapter 1, the primary driver of large-scale aspherical structure in the DM halo is the combination of the stellar disk and bar. We do not find any evidence for the claim that the presence of baryons in a simulation will make the halo more spherical Kelso et al. (2016).

2.3.1.2 The Shadow Bar and Density Wake

In addition to the dark disk creating an axisymmetric overdensity, the stellar and dark-matter shadow bar create non-axisymmetric density variations that correspond to a global quadrupole. This response of the DM halo to the stellar bar results in a collisionless wake; this wake appears as a diffuse $m = 2$ spiral see Figure 1.6 for details). The effect of this DM feature is readily seen in Figure 2.2, which plots the in-plane relative DM density as a function of bar radius and bar angle. When comparing the fiducial NFW model to the pristine NFW distribution (left panel), we see a clear density enhancement at a $>$15% level everywhere, peaking at $>$40% lagging just behind the bar at two bar radii. At the approximate solar location, we find a 35^{+5}_{-3}% enhancement relative to a spherical distribution.

When we compare to the adiabatically contracted NFW model to isolate the effects of the stellar and shadow bar (right panel), we find that the fiducial NFW model exhibits an over density along the bar major axis relative to the minor axis of approximately 15% at $T = 4$ Gyr at the solar circle, corresponding to $> 30\%$ of the total effect when compared to the difference between the fiducial NFW and pristine NFW models. The fiducial dynamical NFW model has an average of 10% (30%) greater density everywhere when compared to the adiabatically contracted NFW model (pristine NFW model). The fiducial model has a lower azimuthally-averaged density within two bar radii, caused by the transport of angular

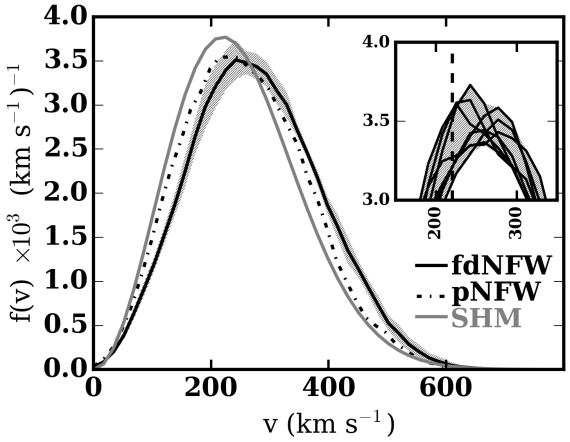

Figure 2.3. Speed distribution at the solar position in three different halo models. The hatched region around the fdNFW line indicates the extent of the possible solar locations in the simulation. The pNFW model is plotted as a dot-dashed line. The SHM is plotted as a dashed line. Inset: zoom-in on the peak of the speed distribution, with the extent of the solar position uncertainty indicated as a shaded band. Thin lines represent individual realizations of the region of interest used to calculate the solar position speed distribution. $|v| = 220\ \mathrm{km\ s^{-1}}$, the peak of the SHM, is marked as a vertical dashed line. Note that peaks for individual realizations range between 230 and 280 $\mathrm{km\ s^{-1}}$.

momentum from the stellar disk, making the DM orbits gain in net angular momentum and thus experience some radial expansion.

2.3.1.3 Dark Matter Kinematic Wake

In Figure 2.3, we plot the speed distribution at the solar circle. We choose the solar circle as nine regions of interest centered at each combination of $R = [1.6, 2.0, 2.4]$ bar radii and $\Delta\theta_{\mathrm{bar}} = [20^\circ,\ 30^\circ\ 40^\circ]$. We plot the speed distribution for the SHM, which is a MB distribution centered at 220 km s^{-1}, as a dashed line for comparison. The peak of the speed distribution shifts upward, and is now between 230 and 280 $\mathrm{km\ s^{-1}}$ with more populated tails than in the standard MB distribution. The shift in the peak relative to the SHM is caused by a non-isotropic velocity structure in the DM halo, which is evident in Figure 2.4.

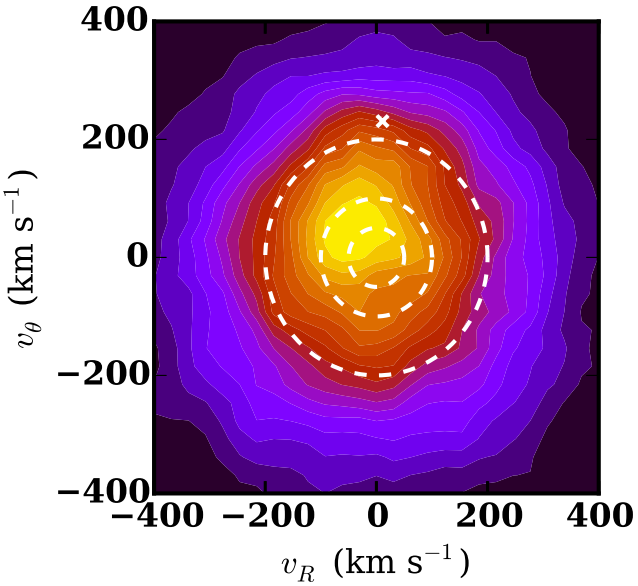

Figure 2.4. Radial (v_r) versus tangential (v_θ) velocities in galactocentric coordinates at the solar position for the fdNFW model. To illustrate the deviation from an isotropic distribution, we plot circles with $|v| = 50,\ 100,\ 200\mathrm{km\ s^{-1}}$. The velocity of the Sun in $v_r - v_\theta$ space is marked with a white 'x'.

The shape of the distribution depends on both the initial phase-space distribution and the galaxy's evolutionary history, so we can not provide a generic parametrization at this time. The magnitude of the wake increases with $\Delta T_{\rm se}$, meaning that an older bar with more time to transfer angular momentum to the halo will enhance the azimuthal velocity of orbits in the halo.

Similar to Pillepich et al. (2014), we opt not to fit a MB distribution to the peak of the speed distribution. As noted by Mao et al. (2013), the MB distribution does not provide a good fit to the speed distribution. We demonstrate in section 2.3.2 that the underlying reason a MB distribution is a poor descriptor for our DM velocity distribution owes to a combination of adiabatic contraction and the stellar+shadow bar. The underlying distribution may not be well described by a single fitting-function parametrization dependent upon escape velocity (e.g. Mao et al. (2013)).

In Figure 2.4, we plot the distribution of the radial (v_r) versus azimuthal (v_θ) velocity components in galactocentric coordinates. The shift in the peak of the azimuthal velocity distribution, $\delta v_\theta = +50\ \mathrm{km\ s^{-1}}$ shows that the dark disk has gained net rotation. In addition, the peak in radial velocity has been decreased owing to the DM wake induced by the bar ($\delta v_r = -30\ \mathrm{km\ s^{-1}}$). A similar analysis performed on the adiabatically contracted NFW model yields a nearly isotropic distribution. Thus, the bias of the velocity distribution to higher tangential velocities and lower radial velocities solely owes to the non-axisymmetric evolution of the disk, i.e. the bar, without a net gain in angular momentum.

Despite concerns that the dark disk could inhibit direct detection of DM Billard et al. (2013) by causing 10-50% of the DM at the solar radius to co-rotate (consistent with our findings), we find that the formation mechanism of the dark disk increases the tails of the velocity distribution and, thus, increases the fraction of particles with velocities greater than prospective values of v_{min}. The speed distribution is shifted to significantly higher velocities, with the tail falling more steeply than that of the SHM, similar to the findings of several studies Mao et al. (2013); Pillepich et al. (2014); Sloane et al. (2016). The implications of the tails for DD experiments are discussed in section 2.3.2.

In summary, we find that the stellar+shadow bar causes the halo in our simulation to deviate from the standard halo model in three important ways: (1) the presence of the stellar disk potential causes the halo to contract toward the plane, producing an oblate spheroid; (2) the stellar+shadow bar causes a density enhancement along the bar axis; and (3) the stellar+shadow bar causes a further contraction toward the plane and a non-isotropic velocity distribution by transferring angular momentum to the dark disk. Future simulations matched in detail to the MW will be able to provide a more nuanced understanding of the shape and structure of the speed distribution.

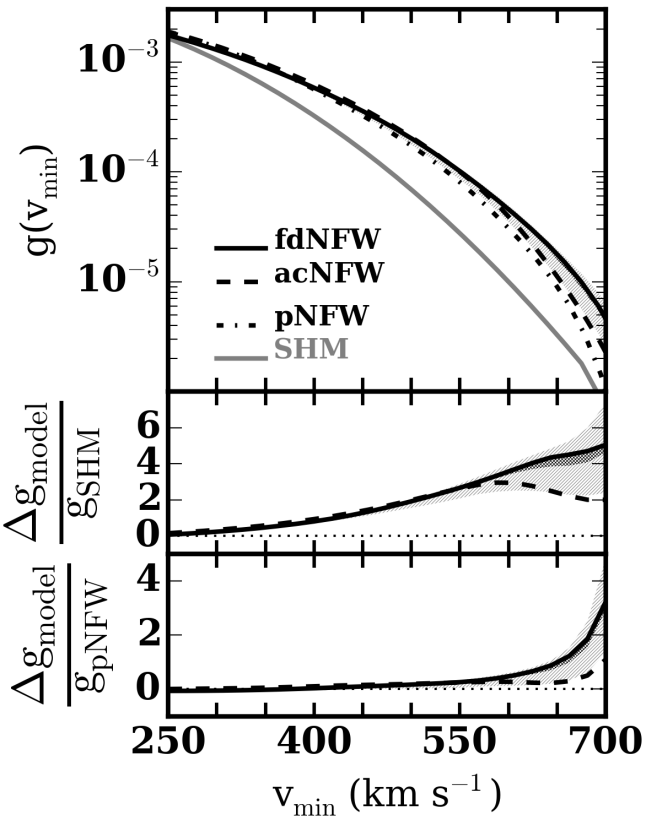

Figure 2.5. Upper panel: $g(v_{\rm min})$ as a function of $v_{\rm min}$ for the fiducial dynamical NFW model. The best fit solar location is shown as a solid black line. The uncertainties due to the solar position are shown; the combination of radial and azimuthal uncertainty is lightly shaded, while the azimuthal uncertainty alone is darkly shaded. The pristine NFW distribution and adiabatically contracted NFW distributions are shown as the dot-dashed and dashed black lines, respectively. The standard halo model is shown as a solid gray line. Middle panel: comparison of the empirical simulation results to the SHM. The solid black line shows the relative value of $g(v_{\rm min})$ $((g(v_{\rm min})_{\rm NFW} - g(v_{\rm min})_{\rm SHM})/g(v_{\rm min})_{\rm SHM})$ for the most likely solar position in the empirical NFW halo to $g(v_{\rm min})$ for the standard halo model. The lightly-shaded region shows the uncertainty only due to the radial and azimuthal uncertainty and the darkly-shaded region shows the uncertainty due to the azimuthal uncertainty. The dashed black line shows the same quantity for the adiabatically contracted NFW model. Bottom panel: comparison of the empirical simulation results to the pristine NFW distribution $((g(v_{\rm min})_{\rm NFW} - g(v_{\rm min})_{\rm pNFW})/g(v_{\rm min})_{\rm pNFW})$. The lines are the same as in the upper and middle panels.

2.3.2 Dark Matter Detection Rates

In this subsection, we present computations for the DD rates, as well as a physical justification for the observed phenomena. We first discuss the detection of DM in general, then move to the fiducial dynamical NFW model, the adiabatically contracted NFW model, and the pristine NFW model (sections 2.3.2.1 and 2.3.2.2, respectively). We also qualitatively discuss the results of other halo models presented in Chapter 1 (section 2.3.2.3). Taken together, these sections implicate the self-consistent dynamical evolution in the fiducial model as the driver of the observed variation in expected detection rates, the principal finding of this work.

Following other studies that compute the magnitude of these effects for DD experiments (e.g. Kuhlen et al. (2010); Purcell et al. (2012)), we calculate differential event rates, in counts per day per unit nucleus mass per unit exposure time per unit velocity (cpd/kg/(km s^{-1})), as a function of the minimum velocity ($v_{\rm min}$) using the new density and speed distributions obtained from the simulations:

$$\frac{dR}{dv_{\rm min}}\left(v_{\rm min}\right) = \frac{\sigma_\chi}{2\mu m_\chi}\rho_0 g(v_{\rm min}) \tag{2.3}$$

where σ_χ is the spin-independent WIMP cross-section for scattering on a proton, ρ_0 is the WIMP density in the solar neighborhood, m_χ is the WIMP mass, $\mu = (m_N m_\chi)/(m_N + m_\chi)$ is the WIMP-nucleus reduced mass, and the quantity $g(v_{\rm min})$ is the integral in velocity space of the speed distribution divided by the WIMP speed,

$$g(v_{\rm min}) = \int_{v_{\rm min}}^{\infty} \frac{f(v)}{v} dv. \tag{2.4}$$

The threshold speed, $v_{\rm min}$, can be translated to the nuclear recoil energy E_R via the relation $v_{\rm min} = \sqrt{\frac{E_R m_N}{2\mu^2}}$ for calculating specific experimental detection rates. In the interest of exploring the astrophysical variations, we ignore the nuclear form factor and dependence on recoil energy $F(E_R)$, as well as detector atomic mass number A, which would both

typically influence the detection rates. Instead, we restrict our analysis on the detectability of DM to the astrophysical quantities, ρ_0 and $g(v_{\rm min})$. We also restrict our analysis to the range of $m_\chi = 5 - 10$ GeV/c^2 and $\sigma_\chi = 10^{-40}$ cm^2 throughout the rest of this section. These benchmark rates can simply be scaled for different values of m_χ, σ_χ, A, and $F(E_R)$ as dictated by detections and individual experiments.

In the following subsections, we examine and describe the results from the individual models in detail, pointing out the physical mechanisms responsible for the observed rates.

2.3.2.1 Fiducial Dynamical NFW Model

Calculating the detection rates hinges on accurately determining the product of ρ_0 and $g(v_{\rm min})$. We have presented the magnitude of the density variations from spherical in sections 2.3.1.1 and 2.3.1.2. We find that the in-plane value can be increased by 50% relative to the spherical average, while the azimuthal variations can add up to an additional 40%. The deviation from an isotropic velocity distribution was discussed in Section 2.3.1.3; both the shift of the peak and the modification of the high-speed tail changes the DM detectability. At low $v_{\rm min}$, the increase in non-spherical density dominates the signal, while at high $v_{\rm min}$, the deviation from an isotropic velocity distribution significantly enhances the signal.

In the upper panel of Figure 2.5, we plot $g(v_{\rm min})$ as a function of $v_{\rm min}$. The distribution at the solar position as calculated from the simulation is shown as a solid black line. Uncertainties in the azimuthal position of the Sun are represented by the dark gray shaded region, while uncertainties as a result of the combination of both the radial and azimuthal uncertainty are represented as the light gray shaded region. The radial uncertainty of the solar position relative to the length of the bar causes significant deviations, with a trend to lower $g(v_{\rm min})$ as the radius increases. The azimuthal uncertainty is also significant, even for a single choice of the solar radius. The value of $g(v_{\rm min})$ increases as the angle to the bar decreases, peaking when just slightly lagging the bar (at a position angle of -10°). The uncertainty increases greatly at $v_{\rm min} > 550$km s^{-1}, the result of a strong velocity distribu-

tion component, as illustrated by the uncertainty in the speed distribution based on choice of location (see Figure 2.3).

In Figure 2.5, the dot-dashed and dashed black lines depict $g(v_{\rm min})$ for the pristine NFW profile and the adiabatically contracted NFW model, respectively. These will facilitate comparisons with all DM-detection experiments and can help to isolate the effect of the dark disk and the shadow bar. We analyze this further in section 2.3.2.2. The SHM model is shown as the solid gray line, which will be discussed further in section 2.4.1.1.

In Figure 2.6, we present the detectability of DM for the simulations presented in Chapter 1. We use equation 2.3 to calculate $dR/d(v_{\rm min})$ as a function of $v_{\rm min}$. The absolute detection rates are scalable for different nuclear and DM parameters, but the dominant shape of the curve is given by ρ_0 and $g(v_{\rm min})$. The curves are plotted using the same scheme as in Figure 2.5. For ease of interpretation, Figure 2.6 also has vertical lines indicating experimental detection limits at $m_\chi = 5$ GeV (as well as a horizontal line to indicate the $v_{\rm min}$ values as m_χ increases to 10 GeV, at the left edge of the line), discussed further in section 2.4.2.

While both $g(v_{\rm min})$ and ρ_0 increase with $\Delta T_{\rm se}$, the corresponding scaling change required to hold the bar radius fixed (as discussed in Section 2.2.2.1) leads to a decrease in ρ_0 with increasing $\Delta T_{\rm se}$. Thus, the overall results for $dR/v_{\rm min}$ are not strongly dependent on $\Delta T_{\rm se}$, despite the dependence of the individual factors on $\Delta T_{\rm se}$. An accurate age and formation history for the MW bar will lead to a more precise prediction.

In general, an enhancement relative to the SHM qualitatively means that exclusion in $m_\chi - \sigma_\chi$ space becomes more stringent. However, the subtleties of the shape of $g(v_{\rm min})$ (see Figure 2.5) make placing experiments on the $m_\chi - \sigma_\chi$ plane difficult. From equation 2.3, we see that the variation of $g_{\rm NFW}/g_{\rm SHM}$ with $v_{\rm min}$ implies that for a fixed number of detections $dR/dv_{\rm min}$, σ_χ/m_χ will have an inverse dependence on $v_{\rm min}$ for low m_χ.

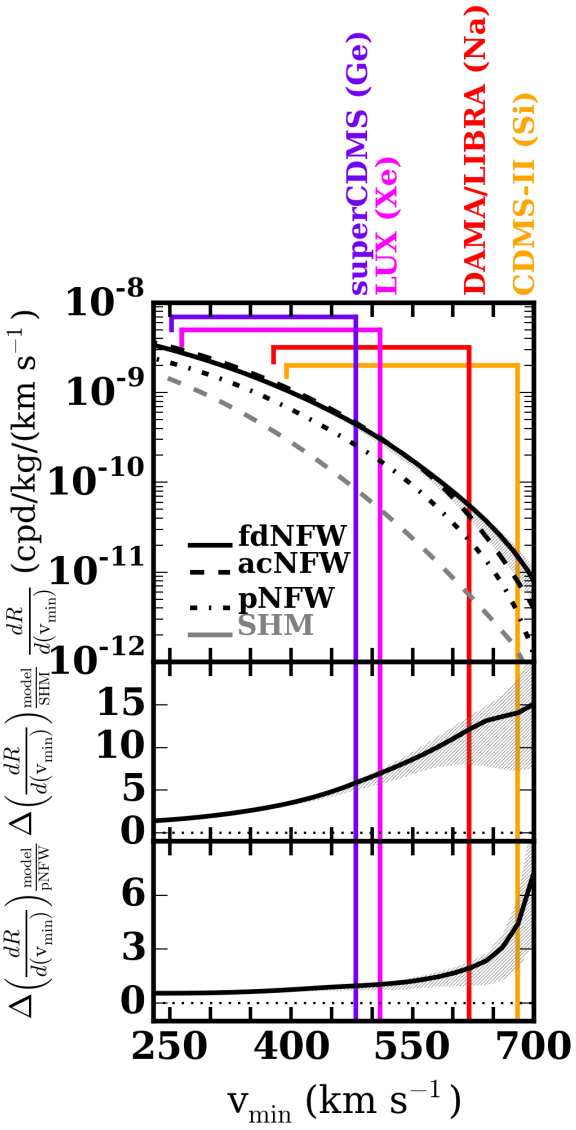

Figure 2.6. Upper panel: $dR/d(v_{\rm min})$ as a function of $v_{\rm min}$ for various halo models. Line styles are the same as in Figure 2.5. The shaded region around the fiducial NFW mode (black line) represents the total positional uncertainty effects on both density and the velocity distribution. Middle panel: detectability relative to the standard halo model, $(dR/d(v_{\rm min})_{\rm model} - dR/d(v_{\rm min})_{\rm SHM})/(dR/d(v_{\rm min})_{\rm SHM})$. The shaded region again reflects the total uncertainty from both density and velocity distributions. Bottom panel: detectability relative to the pristine NFW model, $(dR/d(v_{\rm min})_{\rm mode} - dR/d(v_{\rm min})_{\rm pNFW})/(dR/d(v_{\rm min})_{\rm pNFW})$. The shaded region is the same as in the middle and upper panels. The vertical lines indicate the reported sensitivity limits for several direct detection experiments at $m_\chi = 5$ GeV. The experiments are labeled above the figure, with the target nuclei listed in parentheses. Experiments are discussed further in Section 2.4.2. Each experiment also has a horizontal line spanning $m_\chi = 10$ GeV (left) to $m_\chi = 5$ GeV (right, connecting to the vertical line) to demonstrate how the $v_{\rm min}$ threshold would change as a function of WIMP mass.

2.3.2.2 Idealized NFW models

We compare the fiducial dynamical NFW model to idealized NFW models. First, we discuss the results as compared to the pristine NFW profile, then discuss the adiabatically contracted NFW model.

The pristine NFW profile (eq. 7.3) is already demonstrably different from the SHM, in both ρ_0 and $f(v)$ or $g(v_{\rm min})$ (this is discussed further in section 2.4.1.1). To understand the effect that the dark disk and shadow bar have on the detectability of DM, we compare to the pristine NFW profile rather than to the SHM. The relative enhancement factors for the fiducial dynamical and adiabatic contraction NFW models are depicted in the lower panels of Figures 2.5 and 2.6. We find that the pristine NFW profile largely describes $g(v_{\rm min})$ below $v_{\rm min} = 400$ km s^{-1} and to within 50% up to $v_{\rm min} = 550$ km s^{-1}, above which the fiducial model turns up sharply and the adiabatically contracted model turns up slightly. The sharp upturn of the fiducial model owes to the response of the DM particles to the bar. However, the bottom panel of Figure 2.6 shows that the density increase enhances the detectability relative to the pristine NFW profile. When the fiducial model is compared to the adiabatically contracted model (the solid gray line in Figure 2.5), we see that the effect is roughly the same below $v_{\rm min} = 550$km s^{-1}, implying that the variation owes primarily to the dark disk, an effect present in both simulations. In Figure 2.6, the fiducial and adiabatically contracted models are largely the same below $v_{\rm min} = 550$km s^{-1}. Above $v_{\rm min} = 550$km s^{-1}, the fiducial and adiabatically contracted models deviate, indicating that the effect results from the wake. The $v_{\rm min}$ value above which the adiabatically contracted model and the fiducial model diverge varies weakly with the secular evolution time, $\Delta T_{\rm se}$. As $\Delta T_{\rm se}$ increases, the point of deviation moves to lower $v_{\rm min}$. As the in-plane DM density is approximately 10% larger in the fiducial model, an offset exists $dR/dv_{\rm min}$ between the two models, but the $v_{\rm min}$ value where the two models begin to deviate is the same as in Figure 2.6.

In addition, the range in $g_{\rm NFW}/g_{\rm SHM}$ owing to solar position uncertainties increases with $v_{\rm min}$, indicating that predicting detection rates at high $v_{\rm min}$ may be particularly difficult until the MW bar parameters are more precisely constrained. As discussed in Section 2.3.2.1, the range in these ratios owe solely to the fact that the uncertainty in the angle and radius of the solar position relative to the bar are large. Constraining the radial and angular position of the Sun relative to the MW bar, as well as the fundamental parameters of the MW bar, is crucial to accurately predicting the DD rates.

2.3.2.3 Cored and rotating NFW models

In section 2.2.1, we discussed the selection of the fiducial NFW model in a cosmological context, noting that other halo models could also meet the cosmological criteria. In this section, we describe variations that result from changing this choice. Details of the supporting simulations are presented in Chapter 1.

For the cored NFW profile, the speed distribution peaks at even higher speeds than the fiducial NFW model presented in Figure 2.3, up to $+80$ km s^{-1}. The broadness of this distribution leads to an even larger detectability compared to the SHM, up to a factor of 25 at $v_{\rm min} > 650$ km s^{-1}. Interestingly, the radial velocity peak is not significantly shifted (in contrast to $\delta v_r = -30$ km s^{-1} for the fiducial NFW model). This suggests that the shift in the speed distribution owes to an increase in the azimuthal velocity as a result of rapid angular momentum transfer during bar formation in this simulation (see Chapter 1).

The rotating halos demonstrate similar radial velocity shifts to their nonrotating counterparts. Specifically, the fiducial and rotating NFW halos both peak at smaller radial velocity than their cored counterparts. However, the azimuthal velocity peaks for both rotating models are shifted to significantly higher values, >100km s^{-1} for some possible solar positions. This shift owes to additional angular momentum transfer that creates an even larger density in the galactic plane, which can begin to rotate like the stellar disk. The speed distributions for the rotating models demonstrate a clear shoulder where the dark disk con-

tribution provides an excess signal near $v = 450\ \mathrm{km\ s^{-1}}$, similar to the findings in Purcell et al. (2012) for a particularly strong dark disk. Thus, the rotating models are the easiest to detect, adding an additional 50% enhancement in $g(v_{\mathrm{min}})$ over their non-rotating counterparts (see Figure 2.5).

While each model is cosmologically consistent, rotating and non-rotating models may represent qualitatively different initial conditions in a cosmological setting. For instance, if the presently observed stellar bar is not the first bar to have formed in the MW, the DM halo may be imprinted with a relic response to a bar or other strong bisymmetric structure (e.g. spiral arms) from the past that have decayed or dissipated since those early times. Further study of the history of the MW bar and the stellar populations in the disk may help determine the formation time of the MW bar and the likelihood that either a previous bar existed or that the current bar had significantly different parameters in the past. A triggered bar may begin as a longer structure and subsequently shrink–in such a scenario, the non-isoptropies generated by such an ancient bar may remain in the halo, adding further substructure that is not present in our isotropic initial conditions.

2.4 Discussion

We begin this section with a discussion of our results in the context of the literature (section 2.4.1), then discuss the implications of our fiducial model for DD experiments, first as absolute sensitivities in section 2.4.2, then for experiments that are sensitive to annual modulations in section 2.4.3.

2.4.1 Literature halo models

The DD literature is largely dominated by use of the SHM. To connect with those results, we analyze our models and the results presented in 2.3.2 and compare to the SHM. In the absence of measurable density and velocity profiles for the MW DM halo, the SHM has been used as a benchmark. However, extensive reports exist in the literature (e.g. Kuhlen

et al. (2010); Purcell et al. (2012); Pillepich et al. (2014)) regarding the inaccuracy of this model compared with cosmological simulations, though recently, studies have claimed that the SHM may be a viable model Bozorgnia et al. (2016); Kelso et al. (2016). In these studies, empirical halo models have been used to constrain the parameter space for dark matter properties in the $m_\chi - \sigma_\chi$ plane. We qualitatively discuss the results of those works in section 2.4.1.2 and attempt to reconcile the results using the physical explanations presented in section 2.3.2.

2.4.1.1 The Standard Halo Model

The SHM has a density profile of $\rho \propto r^{-2}$ to satisfy the requirement of a flat rotation curve at the solar circle, normalized such that $\rho_0 = 0.3\ \mathrm{GeV/c^2}$ is the density at the solar circle, with an isotropic velocity distribution given by a MB distribution

$$f(v) = 4\pi v^2 \exp\left(-\frac{v^2}{2\sigma^2}\right) \tag{2.5}$$

with $\sigma = v_{\mathrm{LSR}}/\sqrt{2}$ and $v_{\mathrm{LSR}} = 218\ \mathrm{km\ s^{-1}}$. Because the MB distribution has infinite tails, the SHM typically includes a truncation for the galactic escape speed, either by using an error function or by subtracting a MB distribution with a velocity v_{esc}. Several studies have investigated the galactic escape speed using stellar kinematics, with findings ranging from $v_{\mathrm{esc}} = 533^{+54}_{-41}$ Piffl et al. (2014) to $v_{\mathrm{esc}} = 544^{+64}_{46}$ Smith et al. (2007) to $v_{\mathrm{esc}} = 613$ Piffl et al. (2014).

We will compare the SHM to the fiducial dynamical NFW model by choosing v_{esc} to be the highest velocity particle in the simulation, and note the effect of a lower galactic escape speed where relevant (see Lavalle & Magni (2015) for an investigation of the explicit effects of escape speed choice). Conversely, some simulation particles will have speeds higher than the nominal escape velocity. Although these may be transient particles that are not bound to the DM halo, these particles will still contribute to the signal. This is likely for the real MW as well and thus motivates our choice to depart from literature choices of v_{esc}

for the purpose of this comparison, and instead apply our own empirical $v_{\rm esc}$ to perform the analysis. This may be a large source of the disagreement between these findings and other works.

The middle panels of Figures 2.5 and 2.6 demonstrate the strong detection enhancement for the fiducial NFW profile relative to the SHM. Figure 2.5 presents the effect of the velocity structure alone. Figure 2.6 compares the computations of Equation 2.3 and describes the effects of both the velocity and the density; i.e., the total effects of the more realistic NFW halo model. Owing to the broadening in the model speed distribution when compared to the SHM, $g_{v_{\rm min}}$ is enhanced for all $v_{\rm min}$ and increases with increasing $v_{\rm min}$. Figure 2.5 shows that the velocity distribution function alone yields a factor of four increase at high $v_{\rm min}$, steadily increasing for all $v_{\rm min}$. Figure 2.6 shows that the estimates for DM detection rates may be 20 times larger than the SHM estimates for some experiments as a result of the strong enhancements of $g(v_{\rm min})$ and ρ_0.

Best-fit MB distributions will indeed overpredict the tail of the velocity distribution, consistent with findings in the literature Sloane et al. (2016). However, the SHM is not measured as a best-fit MB distribution, but rather a specific evolution-dependent distribution as described in section 2.3.2.1. While using a parameterization for the velocity distribution that includes $v_{\rm esc}$ may be tempting to ease the tensions between lighter and heavier nuclei experiments, our results indicate that there is little dynamical reason to expect a strong dependence of the shape of the velocity distribution on $v_{\rm esc}$. Additionally, the tensions between ligher and heavier nuclei experiments cannot be resolved with our models.

2.4.1.2 Simulation-based models

We first discuss the reported simulated DM density and velocity distributions in the literature before making a direct comparison to our work. We then discuss potential dynamical reasons for the differences.

In the absence of strong constraints on the DM density at the solar circle, simulations which attempt to match various other parameters to define a 'MW-like' galaxy have a variety of DM densities at the solar circle. In particular, while some studies explicitly discuss the presence of a dark disk Purcell et al. (2012); Pillepich et al. (2014), others find no evidence for a dark disk Kelso et al. (2016), and others still find a dark disk in some simulations but not others Bozorgnia et al. (2016); Sloane et al. (2016). No previously reported simulations attempt to characterize the dependence of DM density on azimuth.

In addition to the variations in DM density, the reported velocity distributions of the simulations vary considerably. Generally, studies seek to explain the speed distribution through a parameterization at least reminiscent of the MB distribution. Upon inspection of various velocity components in this work (see section 2.3.1.3), it is not clear why a MB-derived one-dimensional speed distribution should be expected. In examining literature examples, each dimension of the velocity distribution appears to depart from Gaussians.

An attempt to find an empirical form to describe a halo velocity distribution function led to the result of Mao et al. (2013), which parametrizes the speed distribution as a function of the escape velocity and a parameter p that controls the steepness of the tail of the distribution, such that the tail approaches an exponential distribution at low velocities instead of a Gaussian. Pillepich et al. (2014) find that the speed distribution parameterization of Mao et al. (2013) fits their empirical velocity distributions better than the SHM.

In addition to the fully self-consistent simulations in Mao et al. (2013) and Pillepich et al. (2014), Fornasa & Green (2014) constructed a model that allowed for an anisotropic velocity distribution in the DM of the MW, and used an extended Eddington inversion formalism to calculate the distribution function including the separate mass components of the MW (stellar disk, bar, bulge, interstellar medium, DM halo). Relaxing the assumption of isotropy by including different mass components increased the parameter space of $f(v)$, including a factor of 2 change in the high-velocity tail. These results are consistent with the phenomenological N-body simulation parametrization of Mao et al. (2013).

In light of our findings presented in this chapter (section 2.3.1), we discuss the compatibilities of our results with the simulations discussed above. The largest difference between previous empirical halos and our work is the inclusion of the bar dynamics and its resulting DM response. In particular, several papers with which we compare results analyze galaxies with no apparent bar Vogelsberger et al. (2009); Kuhlen et al. (2012); Pillepich et al. (2014); Bozorgnia et al. (2016); Kelso et al. (2016); Sloane et al. (2016). Previous studies have also focused on contributions from a dark disk Read et al. (2008, 2009), tidal streams Vogelsberger et al. (2009); Kuhlen et al. (2012); O'Hare & Green (2014), and debris flows Kuhlen et al. (2012); Lisanti & Spergel (2012).

Regardless of the included prescriptions for various astrophysical processes or included components, simulations must adequately describe gravity and address the findings presented here (the dark disk and kinematic structure resulting from both the disk and stellar bar). Thus, it is difficult to reconcile simulations that do not observe an in-plane overdensity Bozorgnia et al. (2016); Kelso et al. (2016), or those with little in-plane overdensity Pillepich et al. (2014) with this work (section 2.3.1.1 and 2.3.1.2) and the associated dynamical results in Chapter 1.

The dearth of dark disk material may be due to merger history (as has been claimed), though the simulations of Sloane et al. (2016) appear to show that models of the MW that have undergone recent quiescent periods still support our findings regarding the influence of bar-driven dynamics. We conjecture that Kelso et al. (2016) and other simulations are inhibiting the formation of a dark disk as a natural response to the stellar disk regardless of the merger history (both simulations discussed in Kelso et al. (2016) have a relatively quiescent history). Possible causes include the initial temperature of the halo (as measured in velocity dispersion), over-heating of the stellar (and therefore dark) disk, and insufficient potential and phase space resolution. Bozorgnia et al. (2016) does not provide enough information on merger history for us to make even a qualitative assessment of their dark disks (or lack thereof).

We have demonstrated in Chapter 1 that in sufficiently accurate simulations secular processes change both the ratio of the radial to azimuthal action, which manifests as a change in orbital eccentricity, and induces a net rotation. Thus, DM particles secularly evolve into dark disk orbits. As described in section 2.3.1.3, these effects are both at play in the velocity structure presented here. Both Bozorgnia et al. (2016) and Kelso et al. (2016) report bulk rotation ($\delta v_\theta \approx 20$ km s^{-1}) in their DM halo models, albeit at a smaller δv_θ than reported in our simulations. As shown in Figure 2.4, the $v_r - v_\theta$ relationship is altered by the presence of the quadrupole wake, which results from the stellar+shadow bar. The deviations may be below the sensitivity threshold of other simulations, in particular those that cannot probe the $v_r - v_\theta$ plane a function $\Delta\theta_{\rm bar}$. If the numerical sensitivity does not allow for a characterization of these deviations, then we would expect them to recover a MB distribution, consistent with the findings of Bozorgnia et al. (2016); Kelso et al. (2016); Sloane et al. (2016).

In previous works, the limits and detection regions imposed by DD experiments are primarily affected by the density distribution at the high-mass end ($m_\chi > 10$ GeV), while both the velocity distribution and density of the self-consistent models affect the low-mass end ($m_\chi < 10$ GeV). As $v_{\rm min}$ increases, the $\sigma_\chi - m_\chi$ parameter space covered is particularly sensitive to DM halo model choice. Above $m_\chi = 20$ GeV, the velocity differences are less pronounced, but the ρ_0 determination is still crucial for placing accurate limits. The parametrization presented in Mao et al. (2013) allows for a steeper fall-off in the speed distribution, which may alleviate some of the tension between DD experiments (see Section 2.4.2), though this has not been functionally demonstrated Pillepich et al. (2014); Bozorgnia et al. (2016); Sloane et al. (2016). The next section discusses the effect of our models on the interpretation of DD experiments.

The results from Pillepich et al. (2014) and Fornasa & Green (2014) are generically consistent with results for the adiabatically contracted NFW model, but fail to match the secular evolution caused by the bar, an effect we have shown is significant to the prediction

of the DD rates. In both our work and Purcell et al. (2012), the inclusion of the stellar disk potential increases $g(v_{\rm min})$ by broadening the speed distribution in the plane. The overall DM detection rates presented here are qualitatively similar to those in Purcell et al. (2012), but for different physical reasons. In our model, the uncertainty in the solar position, which may contribute a factor of two to the detection rates, is significantly larger than the variation between the models in Purcell et al. (2012) (approximately 40% at the largest). As Purcell et al. (2012) seeks to model the effect of the Sagittarius dwarf (a satellite of the Milky Way presently having strong interactions with the disk), their $<$40% result, when compared to our $>$100% result, suggests that the stellar+shadow bar is a significantly larger effect than the Sagittarius dwarf for all realistic assumptions about the stellar bar and the Sagittarius dwarf.

We note that these cosmologically-based studies (Kuhlen et al. (2010); Purcell et al. (2012); Pillepich et al. (2014); Bozorgnia et al. (2016); Kelso et al. (2016); Sloane et al. (2016)) do have advantages when compared to the models presented here, namely added realism from the growth of the stellar disk over time, as well as the presence of substructure in a DM halo that evolves self-consistently. We intend to address the generic dynamical effects of these phenomena in future work. Regardless, the dynamical findings that manifest as detectable signals in this work are bolstered by theoretical predictions (e.g. Weinberg (1985)). Further, it is difficult to see how other dissipational-component specific processes (e.g. star formation, feedback) would preferentially affect the halo; we therefore expect the results presented in this chapter to be generic.

2.4.2 Implications for Direct Detection Experiments

Clearly, no simulations can yet make robust predictions for absolute DD rates in the MW. Qualitatively, the increased detection rates observed in simulations relative to the SHM is a boon to DD experiments. Perhaps more importantly, to accurately interpret DD experiment results, and when comparing different DD experiments, the speed distribution is

the largest uncertainty (see the discussion in Section 2.3.2). Because the speed distribution is composed of the three components of the velocity, changes to the Gaussian nature of any of these distributions will result in a non-MB velocity distribution.

In Figure 2.6, the approximate sensitivities to $m_\chi = 5\,\mathrm{GeV/c^2}$ DM are plotted as vertical lines to illustrate the potential cumulative effect the dark disk, density wake, and kinematic wake can have for various experiments (see Aalseth et al. (2013); Bernabei et al. (2010); Agnese et al. (2013); Angloher et al. (2016); XENON100 Collaboration et al. (2010) for sensitivity determinations, where E_R has been translated to $v_{\min}$ as in Section 2.3.2). Each experiment has been able to place limits on σ_χ and m_χ, with the earlier generation CDMS-Si experiment Agnese et al. (2013) finding three possible events that make the most likely model for a DM particle $m_\chi = 8.6\,\mathrm{GeV/c^2}$ and $\sigma_\chi = 1.9\times10^{-41}\,\mathrm{cm^2}$, consistent with the CoGeNT results Aalseth et al. (2013), as well as the DAMA (Na) results Bernabei et al. (2014). We also plot horizontal lines connecting the vertical line at $m_\chi = 5$ GeV (right extent) to a limit at $m_\chi = 10$ GeV (left extent) as a function of $v_{\min}$ to demonstrate the different values of $dR/dv_{\min}$ each experiment would reasonably expect to observe.

Recently, tensions between different experiments, notably the LUX, XENON100, superCDMS and CDMS-Si experiments have been reported. Frandsen et al. (2013) appears to find that varying astrophysical parameters cannot explain the observed CDMS-Si and XENON100 tension, which our findings support. As discussed in section 2.4.1.1, the dependence of $g_{\mathrm{NFW}}/g_{\mathrm{SHM}}$ on $v_{\min}$ suggests that experiments with significantly different $v_{\min}$ thresholds will be up to 10 times discrepant in their detection rates for realistic galaxy models when compared to the SHM at $m_\chi = 5$ GeV. Of course, the experiments sensitive to the lowest energy thresholds still have the largest absolute values of $g(v_{\min})$, but the relative ability to detect $m_\chi = 5\ \mathrm{GeV/c^2}$ DM for experiments with higher energy thresholds is significantly enhanced (middle panel of Figure 2.5). Specifically, the detection rates for the CDMS-Si experiment increase by a factor of >15 (4) at $m_\chi = 5$ GeV ($m_\chi = 10$ GeV)

while for the LUX the detection rates increase by a factor of 7 (2) at $m_\chi = 5$ GeV ($m_\chi = 10$ GeV). Thus if CDMS-Si had set the same limit as LUX using the SHM as the halo model, the limit of CDMS-Si would actually be twice as sensitive if one used a more realistic halo model. However, the low energy threshold of LUX (1.1 keV, LUX Collaboration et al. (2016)) still allows LUX to set the more stringent limit.

2.4.3 Implications for Annual Modulation Signals

For an isotropic DM distribution velocity distribution in the LSR frame, an annual modulation of the DM signal will arise from the oscillation of the Earth's azimuthal velocity ($V_\oplus$) between its minimum and maximum values relative to the DM halo. This modulation has been fit by a sinusoid that peaks at the day of highest azimuthal velocity (e.g., Pillepich et al. (2014)). In our dynamical model, two effects are at play: the modulation will be affected by asymmetries in the velocity centroid and the shape of the velocity distribution with respect to the LSR (as described in section 2.3.1.3 and illustrated in Figures 2.3 and 2.4).

In the upper panel of Figure 2.7, we plot the amplitude of the annual modulation as the difference between the minimum and maximum detection rates during a year, $(R_{\rm max} - R_{\rm min})/(R_{\rm max} + R_{\rm min})$ as a function of $v_{\rm min}$. The annual modulation amplitude increases in all models with increasing $v_{\rm min}$ but, owing to adiabatic contraction, the modulation in both the adiabatically contracted model and the fiducial model are highly enhanced, particularly at high $v_{\rm min}$. The differences between the adiabatically contracted model and the fiducial dynamical simulation are caused by the stellar and shadow bar.

In the middle panel of Figure 2.7, we compare the fiducial and adiabatically contracted models to the SHM. Compared to the SHM, both the adiabatically contracted model and the fiducial model are enhanced for $v_{\rm min} > 300$ km s^{-1}, of interest to most detection experiments (also pointed out in Purcell et al. (2012); Pillepich et al. (2014)). In the bottom panel of Figure 2.7, we compare the fiducial and adiabatically contracted NFW models to

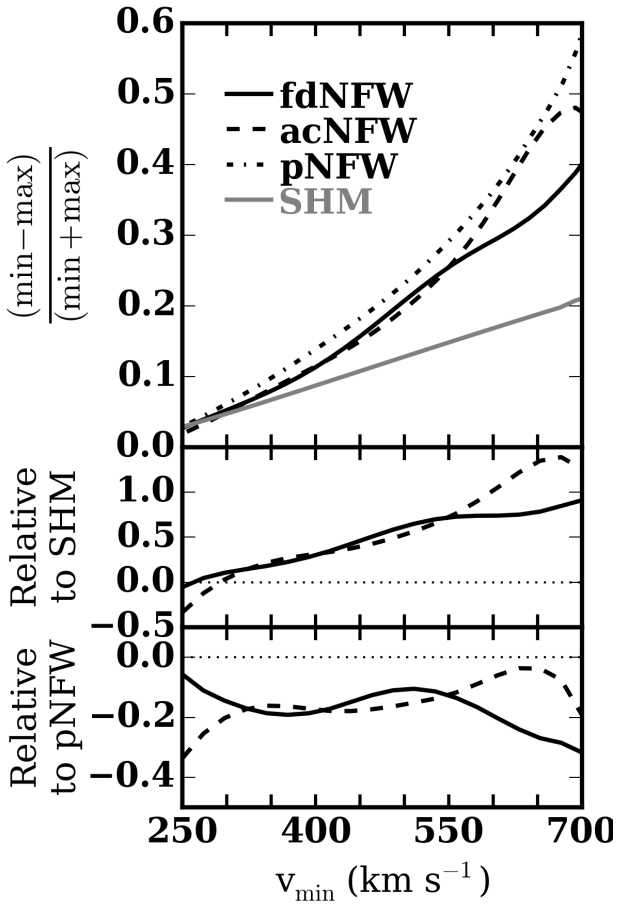

Figure 2.7. Upper panel: Annual modulation fraction, $(R_{\rm max} - R_{\rm min})/(R_{\rm max} + R_{\rm min})$, as a function of $v_{\rm min}$. The models are shown following the same convention as in Figures 2.5 and 2.6. Middle panel: relative enhancement factor for the fiducial dynamical NFW model and the adiabatically contracted NFW model, compared to the SHM. Bottom panel: relative enhancement factor for the fiducial model and the adiabatically contracted model, compared to the pristine NFW profile.

the pristine NFW profile. Here, we see an opposite effect to the comparisons to the SHM: the annual modulation signal is decreased.

Clearly, dynamical evolution affects the annual modulation predictions. We now focus on the comparison between the fiducial and adiabatically contracted model to isolate the effect of the stellar+shadow bar. The velocity ellipsoid of the fiducial model is isotropic and skewed to lower radial and higher tangential velocities, in contrast to the adiabatically contracted model (and the SHM), as shown in section 2.3.1.3 and Figure 2.4.

A comparison of the fiducial and adiabatically contracted models illustrate the effect of the anisotropic velocity ellipsoid on the annual modulation. For $v_{\rm min} < 300$ km s^{-1}, the amplitude of the fiducial model is enhanced relative to the adiabatically contracted model, while for $v_{\rm min} > 550$ km s^{-1}, the adiabatically contracted model is enhanced relative to the fiducial model. In Purcell et al. (2012), the Sagittarius stream DM material is out of phase with the annual modulation signal (the stream originates from galactic north). We find that the annual modulation signal in their simulations will closely match the result of our adiabatically contracted model, due to the contribution of the dark disk.

However, in the presence of the bar feature, differences arise. We find that the tail of the speed distribution is dominated by orbits tangential to the LSR motion, but owing to the difference between the expected annual modulation velocity vector from an isotropic distribution and the solar velocity vector (see Figure 2.4), the effect is lessened as some of the DM co-rotates. However, at low velocities, the radial velocity peak being centered at $v_r < 0$ contributes some signal relative to the adiabatically contracted model.

Freese et al. (2013) provides an overview of the prospect for annual modulation given the status of DD experiments; we point out here that while the overall amplitude of the annual modulation detection signal in our NFW model increases relative to the SHM, the effect of the stellar+shadow bar reduces the effect at high velocities, increasing it at low velocities. As the absolute scaling of the amplitude depends on the location of the peak of the speed distribution relative to the annual modulation velocity variation, we cannot defini-

tively say that the annual modulation signal will be increased. Nonetheless, the trends in the current experimental data are broadly consistent with the isolated effects of the shadow bar provided by the fiducial dynamical NFW and adiabatic contraction NFW models: experiments with low energy thresholds have reported possible annual modulation signals, and high energy threshold experiments have not.

2.5 Conclusions

The major results of the chapter are as follows:

1. The density of the DM halo at the solar position varies depending on the Earth's location relative to the stellar bar. Smaller angles relative to the bar as well as a smaller ratio of $R_{\odot}/R_{\rm bar}$ can increase the density relative to a spherical distribution by a factor of 2.

2. The DM velocity profile is reshaped by the stellar+shadow bar. The characteristic quadrupole wake in the DM that forms as a response to the stellar bar lags the bar in velocity and, therefore, enhances the detectability of DM when compared to the SHM (adiabatically contracted NFWmodel) by a factor of 3.5 (2) at $v_{\rm min} = 300$ km s^{-1}. At $v_{\rm min} = 650$ km s^{-1}, detectability relative to the SHM is increased by a factor of 10, and up to a factor of 40 for a cored NFW halo model. Enhancements for initially rotating models are approximately equal to the respective non-rotating model (fiducial dynamical NFW and cored NFW).

3. A number of recent astrophysical models suggest the importance of the MW evolutionary history to modeling DM detection rates. As detectability depends on $v_{\rm min}$ (which is sensitive to the velocity distribution), and we have demonstrated effects on the velocity distribution from known features in the MW, experiments need to move beyond the SHM to compare with other experiments that have different energy thresholds.

4. Similarly, annual modulation in the DM signal will have different detectabilities compared to the SHM as a function of $v_{\rm min}$. The stellar+shadow bar, when compared to the adiabatically contracted model, *reduces* the annual modulation signal for experiments sensitive to high energy thresholds by approximately 20%, and *boosts* the annual modulation signal for experiments sensitive to low energy thresholds by approximately 20%.

5. When compared to the SHM, we expect an enhancement in detectability and annual modulation. We use an adiabatically contracted model that fixes the gravitational potential of the disk to calibrate the importance of dynamical evolution to the DM detection predictions. For example, when we compare our fiducial dynamical NFW model to the adiabatically contracted NFW model at $v_{\rm min} = 475$ km s^{-1} (the nominal value for superCDMS at $m_\chi = 5$ GeV), we expect an enhancement in detectability of 100%, but an unchanged annual modulation signal. This illustrates the influence of dynamical evolution.

The results presented in this chapter can be succinctly summarized as indicative that the expected rates of observation for DD experiments is strongly sensitive to realistic DM halos. Models that incorporate known physical processes can be used at a minimum to determine astrophysics-related constraints on DM m_χ and σ_χ. While the literature now has no shortage of simulations touting different halo velocity distributions, the field is still not able to accurately create a MW analogue that accounts for evolutionary history. Acknowledging this fact, in this chapter we study the effects of simple dynamical models, implemented through n-body simulations, on DD experiments. We stress that the effects presented in this chapter are generic results of the gravitational interaction between the stellar disk and the DM halo. The power in these inferences is a motivation for marrying DD experiments with realistic astronomy. Astronomically realistic models will provide realistic constraints with more power to discriminate between WIMP hypotheses.

The change relative to the SHM affect primarily lower m_χ values. This owes to the low $v_{\rm min}$ values implied by $m_\chi > 20$ GeV, allowing experiments to probe nearly the entire $g(v_{\rm min})$ space. In contrast, if $m_\chi < 10$ GeV, the discrepancy between our fiducial model and the SHM will be large: $v_{\rm min}$ is in the tail of the $g(v_{\rm min})$ distribution, where we have demonstrated $\left(\Delta g(v_{\rm min})\right)/g(v_{\rm min})$ changes rapidly.

The results presented here are by no means an exhaustive parameter search, nor a best-fit MW model. However, the MW is a disk galaxy with a moderate bar. The features induced in the DM distribution by dynamical evolution in our simulations realistically represent those expected in the MW and will obtain generally for any disk galaxy. The density enhancements and velocity asymmetries will have clear impacts on the sensitivities of the various direct-detection experiments and are likely to make the tensions between upper limits and tentative detections stronger and more interesting. Future iterations of direct detection experiments, such as superCDMS (at SNOLAB) SuperCDMS Collaboration et al. (2015), LUX-ZEPLIN LZ Collaboration et al. (2015), and XENON1T XENON100 Collaboration et al. (2014), will build upon the constraints from previous studies. Halo models that accurately account for known dynamical effects in the MW are necessary for meaningful hypothesis testing.

Finally, directional detectors will enable a detailed study of the kinematic signature at the solar position. Early efforts may be able to detect a bias in the tangential and radial velocity peaks, as in Figure 2.4, which may even prove a discriminating factor for determining the halo profile. This hints at the possibility of DM astronomy in the future.

CHAPTER 3

USING COMMENSURABILITIES AND ORBIT STRUCTURE TO UNDERSTAND BARRED GALAXY EVOLUTION

3.1 Introduction

The disc of a galaxy, as described by an axisymmetric exponential radial profile, is dominated by orbits that appear in the $x - y$ plane to be rosettes of varying eccentricities, the morphology of which are dictated by the radial energy. Such regular orbits have constant phase-space coordinates and are considered integrable, and can be represented by a combination of three fundamental frequencies. As stated by the Jeans theorem (Jeans, 1915), for an axisymmetric system the distribution function is a function of the classical integrals of motion, the energy E and the angular momentum L_z. This principle has been used in a number of analytic studies over the past century (see Binney & Tremaine 2008), including recent advancements (Binney & McMillan, 2016). Additionally, the Jeans equations (Jeans, 1922) have been used to perform simplistic assessments of the orbital structure of real galaxies under the assumption that galaxies are semi-isotropic, i.e. they can be described by the classical integrals of motion (Cappellari, 2008).

Unfortunately, the assumption that galaxies are semi-isotropic rapidly breaks down whenever degrees of realism are added to dynamical studies. While typical rosette orbits in an axisymmetric system fill an area of the disc after many orbital periods, commensurate (or resonant) orbits arise when a perturbation is applied. Commensurate orbits are governed by the equation

$$m\Omega_p = l_1\Omega_r + l_2\Omega_\phi + l_3\Omega_z \tag{3.1}$$

where $\Omega_{r,\phi,z}$ are the polar coordinate frequencies of a given orbit and Ω_p is some pattern frequency, e.g. the frequency of a bar or spiral arms. Commensurate orbits are closed curves and have formally zero volume, and are the sites where classical integrals of motion can change, leading to secular evolution.

Even in the case of relatively simple potentials, such as an exponential stellar disc embedded in a spherical dark matter halo, finding the distribution function, fundamental frequencies, and/or commensurate orbital structure analytically can rapidly become intractable. Few axisymmetric potentials that resemble real galaxies can be described via separable potentials (de Zeeuw & Lynden-Bell, 1985). Further, the inclusion of non-axisymmetric features, such as a bar, can render the potential calculation virtually impossible[1]. Simply changing the halo model from a central cusp to a central core is known to alter the families of bar orbits present near the center of the galaxy (Merritt & Valluri, 1999). Thus, the orbital structure of realistic, evolving galaxies is difficult to constrain. The lack of works in the literature with potentials applicable to realistic galaxies (e.g. non-axisymmetries) motivates finding new methodologies with which to determine the orbital content of a disc galaxy, such as the one presented in this work.

Analytic and idealized numeric studies of potentials that are similar to barred galaxies show a basic resonant structure that underpins the bar, the commensurate x_1 orbit (Contopoulos & Papayannopoulos, 1980; Contopoulos & Grosbol, 1989; Skokos et al., 2002). However, small adjustments to the mass of the model bar can admit new commensurate subfamilies of x_1 orbits, necessitating a model-by-model (or galaxy-by-galaxy) orbit census. For simulated galaxies, taking a census of the orbital families present means being able to (nearly) instantaneously identify the family of a given orbit, as the orbit may be changing over a handful of dynamical times. Worse, the orbits may only be near a closed orbit in phase-space, blurring the morphological features of commensurate orbits. Bifurca-

[1]Though for simple analytic bar potential expressions, extensions of analytic studies are able to make some progress (e.g. Binney, 2018).

tions of prominent orbit families can also be caused by alterations to the potential shape, resulting in families such as the 1/1 orbit, a family that results from the bifurcation of the x_1 family (Papayannopoulos & Petrou, 1983; Martinet, 1984; Petrou & Papayannopoulos, 1986). For consistency, we refer to this orbit throughout this work as an x_{1b} orbit, denoting that the family is a bifurcation of the standard x_1 orbit.

Finding resonant features has proven to be particularly difficult in an analytic framework (Binney & Tremaine, 2008). Even more difficult is identifying the act of 'trapping', or capture into resonant orbits, which by definition truly fixed potential models cannot inform. Recently, techniques to describe orbits observed in self-consistent simulations such as those drawn from N-body simulations, i.e., those that are allowed to evolve with gravitational responses, have been used to find the rate at which orbits change families and join different features (Chapter 1).

Despite of all the effort placed into studying both analytic potentials and self-consistent simulations, a vast gulf of understanding exists between analytic potentials, idealized (fixed) potentials, and self-consistent potentials. The wisdom of linear or weakly non-linear galaxy dynamics can only be extended so far. At some point, the distortions become so strong that it is insufficient to consider perturbations to the system, and one must treat the entire system in a self-consistent manner. However, fully self-consistent simulations are encumbered by the many parameters necessary to describe a galaxy, all of which can be difficult to control when designing self-consistent model galaxies, making matching the observations of real galaxies challenging. Cosmological simulations circumvent this problem by simulating many galaxies, some of which resemble the Milky Way (Garrison-Kimmel et al., 2018; Nelson et al., 2018), but they cannot reach the resolution required to track an ensemble of individual orbits. Hence, the need for a bridge between analytic and self-consistent work: fixed potential orbital analysis.

Within this framework, many previous studies have used frequency analysis to discern the properties of orbits, describing orbits by their frequencies in various indepedent dimen-

Potential Number	Simulation Name, Time	Potential Name	Scalelength $R_{\rm d}$ [$R_{\rm vir}$]	Disc Mass [$M_{\rm vir}$]	$M_{\rm halo}(< R_{\rm d})$ [$M_{\rm vir}$]	R($M_h = M_d$) [$R_{\rm vir}$]	Pattern Speed Ω_p [rad/$T_{\rm vir}$]
I	Cusp Simulation $T = 0$	Exponential Cusp	0.01	0.025	0.0050	0.0167	90
II	Cusp Simulation $T = 2$	Barred Cusp	0.01	0.025	0.0050	0.0172	37.5
III	Core Simulation $T = 0$	Exponential Core	0.01	0.025	0.0022	0.0317	70
IV	Core Simulation $T = 2$	Barred Core	0.01	0.025	0.0024	0.0282	55.6

Table 3.1. Potential models used in the detailed fixed potential study.

sions. The result is a partitioning of orbits into families that reside on integer relations between frequencies. It is a natural extension to attempt frequency analysis on an ensemble of real orbits, via either spectral methods (Binney & Spergel, 1982; Binney & Spergel, 1984) or frequency mapping (Laskar, 1993; Valluri et al., 2012, 2016). In some cases, real frequencies can be discerned and orbit families can be identified on the fly. However, this condition is only satisfied when the evolution of the system is slow, or the evolution is artificially frozen. Therefore, we develop a new methodology based on a simple and robust geometric algorithm that balances the unambiguous determination of orbital features from frequency analysis, while operating on short orbital time series so as to be physically relevant for the real universe.

In this chapter, we present a simple methodology with which to understand orbital structure in the fixed potential limit, with a particular emphasis on commensurate orbits. This work presents significant upgrades to one method previously published (Chapter 1), as well as an entirely new algorithm. The true power of each method relies on the mutual interpretation of the simulations with both methods. The goal of this project is to compare orbits between fixed potential simulations and fully self-consistent simulations to discern the evolution of different structures in the self-consistent simulation. Along the way, we demonstrate that (1) we can efficiently dissect bar orbits into dynamically relevant populations, (2) orbit integration can be dissected by modes in self-gravitating components, (3) commensurate orbit families can be efficiently found, (4) commensurate orbits of the same family can be tracked through time across different fixed-potential realizations. (5) commensurate orbits provide a useful method to analyze self-consistent simulations, and (6) the dynamical status of barred galaxies may be possible to infer from this methodology.

We emphasize that the utility of this method extends beyond the proof-of-concept presented here. We are presently testing the analysis of orbits as models evolve, using the libraries computed from the fixed potential. An advantage to this orbital atlas analysis is its ability to move beyond the standard methods of locating resonances. In this methodology,

we are able to empirically determine the location of the closed orbits in both physical and conserved-quantity space.

The organization of the chapter is as follows. We describe the models we studied in the course of this work and present new techniques in Section 6.2. Results from different fixed potential models are presented in Section 3.3. We then discuss the implications of the findings for interpreting other models in Sections 3.3.3. We discuss the implications of the results for observational studies in Section 5.5. We then use the lessons from the fixed potential analysis to interpret evolution in the self-consistent simulations in Section 3.5. We conclude and propose future steps in Section 7.6.

3.2 Methods

We first present the initialization and execution of self-consistent disc and halo simulations in Section 3.2.1. An overview of the improved k-means orbit classifier presented in Chapter 1 are discussed in Section 3.2.2. The extracted potentials we use for detailed study of fixed-potential integration are described Section 3.2.3 and the determination of the bar position and pattern speed in Sections 3.2.3.2 and 3.2.3.3, respectively. In Section 3.2.4, we describe the creation of an orbital atlas for each model, including the initial condition population (Section 3.2.4.1), and integration method (Section 3.2.4.2).

3.2.1 Simulations

We employ two galaxy simulations in this work. The simulations used here are updated slightly from the simulations presented in Chapter 1, including a modestly more concentrated halo and significantly longer integration. We justify both changes at the end of this section.

3.2.1.1 Initial Conditions

Both simulations feature an intially spherically-symmetric Navarro-Frank-White (NFW) dark matter halo radial profile (Navarro et al., 1997), which may be generalized to include

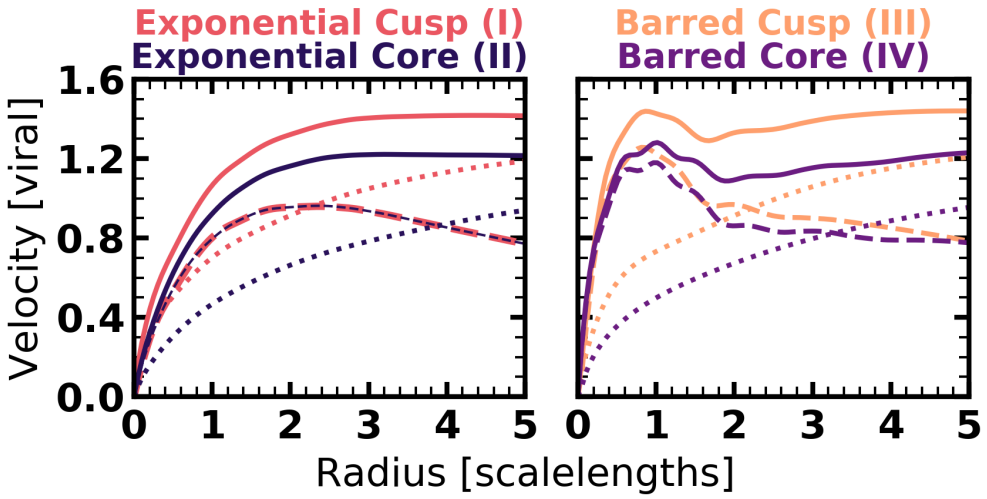

Figure 3.1. Circular velocity curves as a function of radius, computed for the cusp and core simulations at $T = 0$ and $T = 2$. The left panel shows the two exponential disc models ($T = 0$, the initial conditions of each simulation), while the right panel shows the two barred models ($T = 2$, after moderate evolution in each simulation). Both panels are color coded as shown above the panels. The solid lines are circular velocity at each radius computed from the monopole for the total system. The dashed (dotted) lines are the monopole-calculated circular velocity for the disc (halo) component only.

a hamonic core where the density $\rho(R)$ becomes constant with radius:

$$\rho(R) = \frac{\rho_0 r_s^3}{(R + r_c)\,(R + r_s)^2} \tag{3.2}$$

where ρ_0 is a normalization set by the chosen mass, r_s is the scale radius, here set to be $r_s = 0.04 R_{\rm vir}$, $R_{\rm vir}$ is the virial radius, and r_c is a radius that sets the size of the core. r_s is related to the concentration, c, of a halo by $r_s = R_{\rm vir}/c$. We design the halo to have $c = 25$ ($r_s = 0.04$), within a 'normal' distribution of halo concentration from recent cosmological simulations (Fitts et al., 2018; Lovell et al., 2018). In Chapter 1, we used $c = 15$. The normalization of halo units is set by the choice of virial units for the simulation, such that $R_{\rm vir} = M_{\rm vir} = v_{\rm vir} = T_{\rm vir} = 1$. Scalings for the Milky Way suggest that $R_{\rm vir} = 1 = 300$ kpc, $M_{\rm vir} = 1 = 1.4 \times 10^{12}$ $\mathrm{M}_\odot$, $v_{\rm vir} = 1 = 140$ km s^{-1}, and $T_{\rm vir} = 1 = 2$ Gyr. The motivation behind generalizing the NFW profile to include a core lies in the ambiguity of the central density of dark matter halos in observed galaxies, including our own (McMillan, 2017). The pure NFW profile extracted from a dark matter-only simulations does not feature a core ($r_c = 0$), but rather a cusp, where the density continues to linearly increase as the radius approaches zero. The first two models have $r_c = 0$ and, therefore, we refer to these as 'cusp' potentials, exctracted from the 'cusp simulation'.

We embed in this coreless halo an exponential disc, where the three-dimensional structure of the disc is given as an exponential in radius and an isothermal sech^2 distribution in the vertical dimension:

$$\rho_d(R, z) = \frac{M_{\rm d}}{8\pi z_0 a^2} e^{-R/a} \mathrm{sech}^2(z/z_0) \tag{3.3}$$

where $M_d = 0.025 M_{\rm vir}$ is the disc mass (in line with estimates for the present-day MW; Bland-Hawthorn & Gerhard 2016), $a = 0.01 R_{\rm vir}$ is the disc scale length, and $z_0 = 0.001 R_{\rm vir}$ is the disc scale height, which is constant across the disc.

The second simulation is different from the first in that we set $r_c = 0.02R_{\rm vir}$, and thus we refer to the simulation as the 'core simulation'. We tailor ρ_0 for the cored simulation initial condition such that the virial masses are equal to that of the cusp simulation, i.e. $M_{\rm vir,cusp} = M_{\rm vir,core} = 1$. We again embed a $0.025M_{\rm vir}$ intially exponential disc in this halo.

Both simulations presented here have $N_{\rm disc} = 10^6$ and $N_{\rm halo} = 10^7$, the number of particles in the disc and halo component, respectively. The disc particles have equal mass. Rather than having equal mass particles in the halo, we employ a 'multimass' scheme, where the halo particles have a number density $n_{\rm halo} \propto r^{-\alpha}$ with $\alpha = 2.5$. The resolution of the inner halo, $R < 0.05R_{\rm vir}$, is improved by roughly a factor of 100, making the mass of the average halo particle in the vicinity of the disc equal to that of the disc particles.

As in Chapter 1, the halo velocities are realised from the distribution function produced by an Eddington inversion of the density profile (see Binney & Tremaine 2008). Eddington inversion provides an isotropic distribution, roughly consistent with the observed distributions in dark-matter only ΛCDM simulations. The disc velocities are chosen by solving the Jeans' equations in cylindrical coordinates in the combined disc–halo potential, also as in Chapter 1. We describe the methodology in detail in that work, and it employs standard techniques such as those found in Binney & Tremaine (2008).

The evolution is the same, qualitatively, between the 'cusp simulation' presented here and 'Model F' from Chapter 1. The same is true for the 'core simulation' presented here and 'Model C' from Chapter 1. A discussion of the dependence on halo concentration is beyond the scope of this chapter and will be studied in future work. Given the lack of qualitative differences in the initial conditions anthe evolution between the simulations presented here and those from Chapter 1, one may naturally wonder why new simulations were executed. As discussed in Chapter 1, the 'maximality', $f_D \equiv V_{c,\star}/V_{c,\rm tot}$, the contribution to the total circular velocity by the peak disc mass distribution, of typical disc galaxies was found to be $f_D = 0.4 - 0.7$, with $\langle f_D \rangle = 0.57$ by Martinsson et al. (2013). Increasing

the concentration, even modestly, provided better agreement with values for typical disc galaxies. Our cusp simulation has $f_D = 0.65$ and our core simulation has $f_D = 0.75$. With the new simulations, we evolve until $T_{\rm vir} = 4.5$. For a MW-like galaxy, this is equivalent to 9 Gyr. We acknowledge that it is unrealistic to expect that a galaxy will evolve in a purely secular fashion for half the age of the universe, without interactions or mass accretion. However, integrating the simulations for a substantial time allows for a full range of evolutionary states to develop (as discussed below), which help to probe the dynamical mechanisms behind bar evolution in the real universe.

3.2.1.2 N-body Simulation

To integrate orbits, both in the self-consistent simulations and in the fixed potential integrations described below, we require a description of the potential at all points in physical space. We accomplish this using a bi-orthogonal basis set of density-potential pairs. Density-potential pairs are generated using the basis function expansion (BFE) algorithm implementation EXP (Weinberg, 1999). In the BFE method (Clutton-Brock, 1972, 1973; Hernquist & Ostriker, 1992), a system of bi-orthogonal potential-density pairs that are solutions to the Sturm-Louiville (SL) equation are calculated and used to approximate the potential and force fields in the system. The functions are calculated by numerically solving the SL equation for eigenfunctions of the Laplacian, of which Poisson's equation is a special case. The description and study of the eigenfunctions that describe the potential and density is the focus of Chapter 5.

For the halo, a nearly spherical system, we use spherical harmonics given by Y_l^m where $m \leq l$, with the radial functions determined from the corresponding model NFW potential such that the radial function corresponding to the lowest order Y_0^0 spherical harmonic matches the potential and density of the input radial NFW profile exactly. To capture evolution, the halo is described by $(l_{\rm halo}\,(l_{\rm halo}+2)+1) \times n_{\rm halo}$ terms, where $l_{\rm halo}$ is the maxmi-

mum order of spherical harmonics retained and $n_{\rm halo}$ is the maximum order of radial terms kept (per l order).

A cylindrical basis represents the disc, as described in Weinberg (1999). The cylindrical basis is expanded into $m_{\rm disc}$ azimuthal harmonics with $n_{\rm disc}$ radial subspaces. Each subspace has a potential function with corresponding force and density functions. In the implementation of EXP, the lowest-order disc pair matches the initial equilibrium profile of the analytic functional form of the component in question (in this case, the exponential stellar disc with a constant scale height, see details in Chapter 1). We select higher-order pairs to follow structure formation over a physically interesting range of scales, which has the added benefit of reducing small-scale noise (in particular, two body scattering). The functions may be thought of as the allowed evolutionary modes of the system; in this manner, we may select different features by excluding modes that are not of interest.

The potential at any point in the simulation may be represented by $(m_{\rm disc}+1)\times n_{\rm disc}$ coefficients for the corresponding orthogonal functions. The disc basis functions are identical between the cusp and core models. The halo basis functions are necessarily different to capture the initial density profile in the lowest-order term. We retain azimuthal and radial terms ($m_{\rm disc}$=$l_{\rm halo}=m_{\rm halo}\leq 6$, $n_{\rm disc}\leq 12$, $n_{\rm halo}\leq 20$) chosen for both the disc and halo depending upon the scope of the problem. We discuss the effect on our results owing to the inclusion or exclusion of higher-order harmonic subspaces ($m=3,4,5,6$) in detail in Section 3.3.1.3. The halo has a larger number of radial (n) terms owing to the larger range in radius that the halo basis must span. The disc basis is truncated at $R=0.2R_{\rm vir}$, outside of which we calculate its contribution using the monopole only.

As will become important below, EXP allows potential models to be easily calculated. Owing to the functional representation of the basis, we can create an extremely high-accuracy force field from nearly any distribution of particles. The key limitation of the BFE method lies in the non-adaptive nature of the constructed basis. The system must resemble the constructed basis. However, this limitation can also be a great asset in gaining

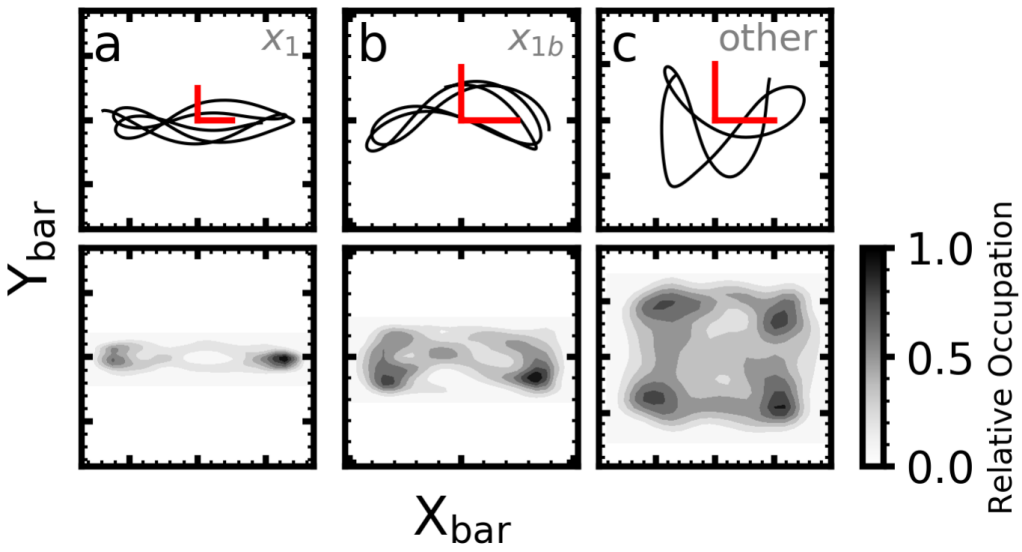

Figure 3.2. Three primary self-consistent bar orbit families classified from the cusp simulation near $T = 2$. The upper panels are the trajectories, while the lower panels are the time-integrated densities, or relative occupation (i.e. showing where the trajectory moves faster or slower such than an orbit resides at a position for longer). The orbits are organized from largest radial extent to smallest, with the red bars indicating $0.5a$ in each panel. From left to right: (a) A standard x_1 orbit. (b) A bifurcated x_{1b} orbit. (b) An 'other' bar orbit, in this case, a nearly 4:2 orbit. (c)

physical insight; if the evolutionary allowed modes can be restricted to physically enlightening functions, valuable comparisons with other methods (e.g. matrix methods or standard perturbation theory) can be made.

3.2.2 Computing Trapping

Though discussed at length in Chapter 1, we have developed several improvements to the method that enables one to determine the growth of different subpopulations beyond the bar-supporting orbits during the simulations. No conclusions from Chapter 1 change as a result of this upgrade; the classification is simply more detailed with the new scheme described here. The more sophisticated algorithm builds upon the same k-means technique, but selects more refined quantites to calculate the resulting metrics and determine trapping.

The details of the classification procedure are described in Section 3.2.6. In this section we give a qualitative overview and discuss the theoretical motivation behind our cluster-based orbit classification.

The orbits that make up a galaxy model are both a reflection of, and support, the potential of the galaxy. The pioneering work of Contopoulos & Papayannopoulos (1980) presented a census of bar-supporting orbits, culminating in a principal x_1 family. x_1 orbits exist at various energies, set by the shape of the potential. However, determining family membership in self-consistent models has remained elusive. The concept of trapping (a term coined by Barbanis 1976) of orbits into reinforcing structures in the potential is a dynamically complex, but straightforward, process under idealized conditions. In the case of perturbation theory, one may compute a capture criterion or trapping rate (e.g. Contopoulos, 1978; Binney & Tremaine, 2008; Daniel & Wyse, 2015), i.e., the probability that an object (in this case, a star) joins a particular resonance parented by some closed commensurate orbit for which the potential may be specified. Unfortunately, in a self-consistent, evolving galaxy, such as the models presented here, the process and probability of being captured into a resonance, and even the resonance itself, can be difficult to ascertain. Several techniques have focused on the use of so-called 'frozen' potentials, where a model is evolved in a self-consistent manner until some time, and then the potential is prevented from evolving further. Orbits are then integrated in the fixed potential to determine the orbital structure. We use a hybrid approach, where we simultaneously analyze frozen potentials and self-consistent simulations. With input from analytic orbit family descriptions, we hope to dissect our models at every timestep to determine the constituent orbits in an 'in vivo' manner. In practice, this means selecting some finite window of the orbit's evolution with which to determine membership in an orbital family. We are largely insensitive to variations in family membership on time scales smaller than half the rotation period of the bar.

The mass that supports the bar feature is a fundamental quantity in a barred galaxy model. However, determining the trapped mass is not an easy task. Parameters for determining trapped orbits in vivo must be empirically found, and both systematic and random errors contribute to the uncertainty. Despite this, a k-means technique efficiently locates and identifies orbits that are members of the bar, sacrificing only minimal time resolution (time resolution is on the scale of a handful of turning points per orbit). Other classifiers rely on instantaneous spatial or kinematic determination of the disc galaxy structure. The strength of our k-means method is that it depends only on the positions of the turning points relative to the bar angle. This makes the methodology (a) fast and (b) independent of detailed simulation processing. The closest analog to our procedure found in the literature is that of Molloy et al. (2015), who used rotating frames to more accurately calculate the epicyclic frequency. However, this procedure is only robust for orbits that are not changing their family over multiple dynamical times. Our method is robust to orbits that are only trapped for one or two dynamical times.

We classify three primary types of bar orbit, with prototypical orbits for each shown in Figure 3.2:

1. x_1 orbits, the standard bar-supporting orbit (panel 'a' of Figure 3.2).

2. 1/1 orbits, a subfamily (resulting from a bifurcation) of the x_1 family, which we will hereafter refer to as x_{1b} orbits (panel 'b' of Figure 3.2).

3. Other bar-supporting orbits, which are coherently aligned with the bar potential but are not part of the x_1 family, generally demonstrating higher-order behavior (panel 'c' of Figure 3.2).

The orbits are drawn from the cusp simulation as having been trapped into their respective (sub)families at $T = 2$. Each orbit has the time series from the cusp simulation $T = 1.8 - 2.2$ plotted in the upper row, with the time-averaged orbit density shown in the bottom row. In the presented examples, as in most cases drawn from self-consistent simulations,

the true nature of the orbit is difficult to determine from the trajectory, but becomes apparent from the time-integrated location, motivating our inclusion of the time-integrated location, or 'relative occupation' in space, throughout this work.

3.2.3 Fixed Potentials

An in-depth study where one investigates the potential at every timestep is computationally intractable. Therefore, we select four illuminating potentials with the purpose of fully decomposing and describing the orbit structure in the given potentials, and apply the general results to the evolution of barred systems in later sections.

3.2.3.1 Potential Selection

From each of the cusp and core simulations, we compute the fixed potential at two times, $T_{\rm vir} = 0$ and $T_{\rm vir} = 2$. As discussed in Section 3.2.1.2, to extract the potential structure at any given time in the simulation, we compute the coefficients for the basis functions used for integration by EXP. Each particle's contribution may be calculated by projecting the particle onto the tabulated basis functions. We calculate the potential for the entire ensemble by accumulating the contribution from all particles in the system, resulting in coefficients that serve as the weights for the different functions. The coefficients for the exponential models are calculated from the initial distribution, and are dominated by the lowest order term, by design. The coefficients for the barred models are calculated from the self-consistent evolution of the systems. The first model is the initial exponential disc embedded in the spherical NFW cusp halo, Potential I (Exponential Cusp). We also self-consistently evolve the exponential disc to a state where a bar has formed, Potential II (Barred Cusp). We select the evolution after two virial time units in the self-consistent cusp simulation, $T_{\rm vir} = 2$, well after the bar has formed, but while the bar is still slowing and evolving. The evolution of the cusp simulation is discussed in Section 3.5.1. The cored halo simulation underpins the two 'core' potentials, Potential III (Exponential Core), and the self-consistently evolved state featuring a prominent bar, Potential IV (Barred Core).

The bar in this self-consistent model is also still slowing and evolving, including active lengthening at the time we selected. The evolution of the core simulation is discussed in Section 3.5.2.

To physically characterize the models, in Figure 3.1 we show the circular velocity calculated from the monopole contribution (i.e. the enclosed mass) as a function of radius (solid lines). The four potentials are color coded as indicated in the figure. In both panels, we decompose the total circular velocity into contributions from the halo (dotted lines) and disc (dashed lines). As the initial discs are the same between the cusp and core simulations, the difference in total circular velocity is set purely by the halo. The halo models remain largely unchanged between the Exponential and Barred version of the models, with modest ($<$10 per cent) changes to the enclosed mass between the initial and barred states within a scalelength, where both models have become more concentrated. Further, the monopole of the disc models, which are identical in the Exponential Cusp and Exponential Core models, are remarkably similar in the Barred states. In the Barred Cusp model, the disc contribution is nearly identical outside of two scalelengths (but appreciably different inside of two scalelengths), while the Barred Core model deviates significantly from the initial distribution out to four scalelengths, the product of a more violent bar formation epoch that rearranges the entire disc distribution.

3.2.3.2 Bar Parameters

A crucial ingredient in the algorithm to compute trapping is the phase angle of the bar. Owing to the nature of the simulation, we have $m = 2$ power at a variety of scales as set by the nodes of the basis. Previously we had employed ellipse fitting (Chapter 1), the most traditional bar determination metric, or stellar surface density Fourier analysis; both of these methods are subject to large-scale contributions that may not be related to the actual bar feature. The modal method for determining the gross rotational properties of the bar

is more robust than an ellipse fitting method, which may be biased by the selection of bar metrics, such as the chosen ellipticity where the bar ends.

We use the *second*-lowest radial order from the disc basis. This choice is partly theoretical in nature and partly empirical; the largest-scale radial orders will seek to capture the outer disc variations, where the majority of the mass resides. However, the bar is also a comparatively large-scale structure, suggesting that the best choice of radial order for the bar determination will be a relatively large scale. The choice of the second-largest radial order ($n = 2$) is a balance between the undesired power of the $m = 2$ of spiral arms and the largest scale desired power of the bar feature. The $m = n = 2$ function has been verified to produce the best characterization of bar pattern speed for all models studied in this work. A comparison of the $m = 2,\ n = 1$ mode shows that the position angle varies only modestly from the $m = n = 2$ mode; however, periodicity from the resolution of spiral arm structure is apparent, hence our choice to use $m = 2,\ n = 2$.

Unfortunately, our approach is limited in application to our methodology; the expansion requires radial orders to discriminate between bar-relevant $m = 2$ power and spiral arm or otherwise induced $m = 2$ power. For the applications in this work, requiring precision bar location and pattern speed determination in order to find commensurate structure in the system, such an otherwise-unapplicable but accurate methodology is preferred.

3.2.3.3 Figure Rotation

While the position angle is important, the dynamics and orbital structure are set by the pattern speed of the bar, Ω_p. The rotation of the model introduces the so-called 'inertial forces', the Coriolis and centrifugal forces, which depend on Ω_p. The centrifugal force, $F_{\rm centrifugal} = \Omega_p^2 r$, in particular plays a role in setting the location of locale minima and maxima in the potential by shifting the location of the local minima, which result from the ellipsoidal bar distortion alone, outward.

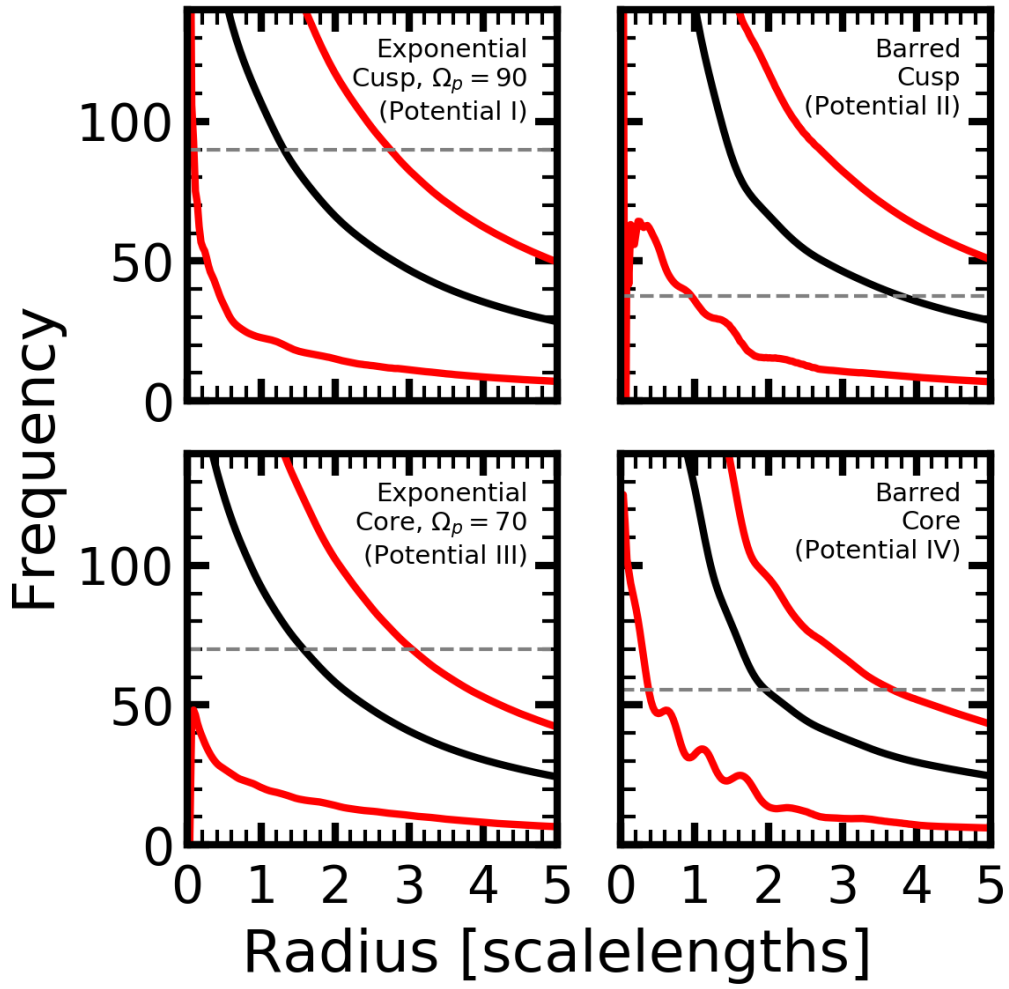

Figure 3.3. Frequency versus radius (in disc scalelengths) for the four galaxy fixed potentials. In the barred potentials, the frequency is computed along the major axis of the bar. The black lines are Ω_ϕ, which marks corotation (CR); the lower red lines are $\Omega_\phi - \frac{1}{2}\Omega_r$, the inner Lindblad resonance (ILR); the upper red lines are $\Omega_\phi + \frac{1}{2}\Omega_r$, the outer Lindblad resonance (OLR). The dashed gray line is the measured (assumed) pattern speed for the barred (exponential) potentials.

For the barred potential models, we determine Ω_p by calculating finite differences in the rate of change of the coefficient phase in a finite window of the time series of coefficients from the self-consistent simulation, as we just discussed. We find that variations of 5 per cent to the pattern speed (the approximate instantaneous uncertainty) make little difference to the resultant orbital structure. For the exponential potentials, Potentials I and III, we test two pattern speeds: $\Omega_p = 0$, which reveals the inherent potential structure of the disc+halo system, and an estimated Ω_p from the self-consistent simulation. The value of Ω_p at $T = 0$ is difficult to directly determine owing to the lack of significant $m > 0$ features. Therefore, we calculate Ω_p using the coefficient phases as above for the earliest possible times ($T \sim 0.2$) and assume that to be the pattern speed at $T = 0$ as well. For the exponential cusp we use $\Omega_p = 90$ and for the exponential core, we use $\Omega_p = 70$. As one will see in the orbital atlases below, the introduction of figure rotation, and thus Coriolis and centrifugal forces, reveals that orbital structure varies with Ω_p in surprising ways.

In Figure 3.3, we show the classical analysis of resonance radii computed from the potential and extracted pattern speed. From the left panels, the exponential potentials (Potentials I and III), we see that lowering the assumed pattern speed would move the calculated corotation radius outward. We also observe that the inner Lindblad resonance (ILR) does not exist in the exponential core model for all realistic values of Ω_p. The outer Lindblad resonance (OLR) exists for all values of Ω_p. However, in the barred cusp, the radius of the OLR is at such large radii (and thus low stellar density) so as to have little influence on the structure of the disc. In the right panels, the barred potentials (Potentials II and IV), we compute the frequency along the axis of the bar; selecting other azimuths will result in the computed locations of resonances moving outward in radius. In all panels, we plot the calculated pattern speed to estimate the location of key resonances. The presence of the bar, despite the increased concentration of mass (obvious in the changed circular velocity curve at $R < 2a$, cf. Figure 3.1), results in the location of the key resonances being at larger radii than in their exponential counterpart. The bar is also strong enough to create an

ILR in the barred core potential (Potential IV) where none existed in the exponential core (Potential III), as well as creating a second ILR in the barred cusp potential (Potential II).

3.2.4 Orbit Atlas Construction

In this section, we detail the construction of an atlas of orbits for the studied fixed galaxy potentials. The atlas consists of a time-series of orbits for each model with a range of initial conditions. In section 3.2.4.1, we describe the initial conditions for the orbits that we integrate. In section 3.2.4.2 we describe both the principles of orbit integration and the details of our implentation.

3.2.4.1 Initial Condition Selection

In Chapter 1 we describe phase space by the orthogonal dimensions of energy and angular momentum. Angular momentum was expressed as a fraction of the angular momentum of a circular orbit at the same radius, i.e. $\kappa \equiv L_{z,\mathrm{orbit}}/L_{z,\mathrm{circular}}$ to create a roughly rectangular grid that extended from radial to circular obits. For this work, we choose a more observationally-motivated set of dimensions: apocenter radius (R_{apo}) and apocenter tangential velocity (V_{apo}). R_{apo}-V_{apo} space can be imagined as 'de-squaring' the $E-\kappa$ coordinates, such that $\kappa = V_{\mathrm{apo}} = 0$ is a radial orbit, while $\kappa = 1$ corresponds to $V_{\mathrm{apo}} = V_c(R_{\mathrm{apo}})$. The orbital apocenters are defined along the major axis of the bar potential. We have investigated other release angles, but find that (1) the bar axis is the most illustrative of the dynamics, and (2) reserve the off-axis angles for future work. While the dimensions do not fully sample phase space, this 'pseudo phase space' gives a intuitive understanding of the system, and can be directly applied to observations.

For this study, we start with orbits that are restricted to the plane. The inclusion of non-planar motion is straightforward, although the phase-space is complex to explore, and we reserve the study for a future work. We choose to uniformly sample this plane, despite large regions of this space being irrelevant for physical systems (i.e. highly radial orbits at large radii in the disc). The space that is physically inaccessible for a regular galaxy

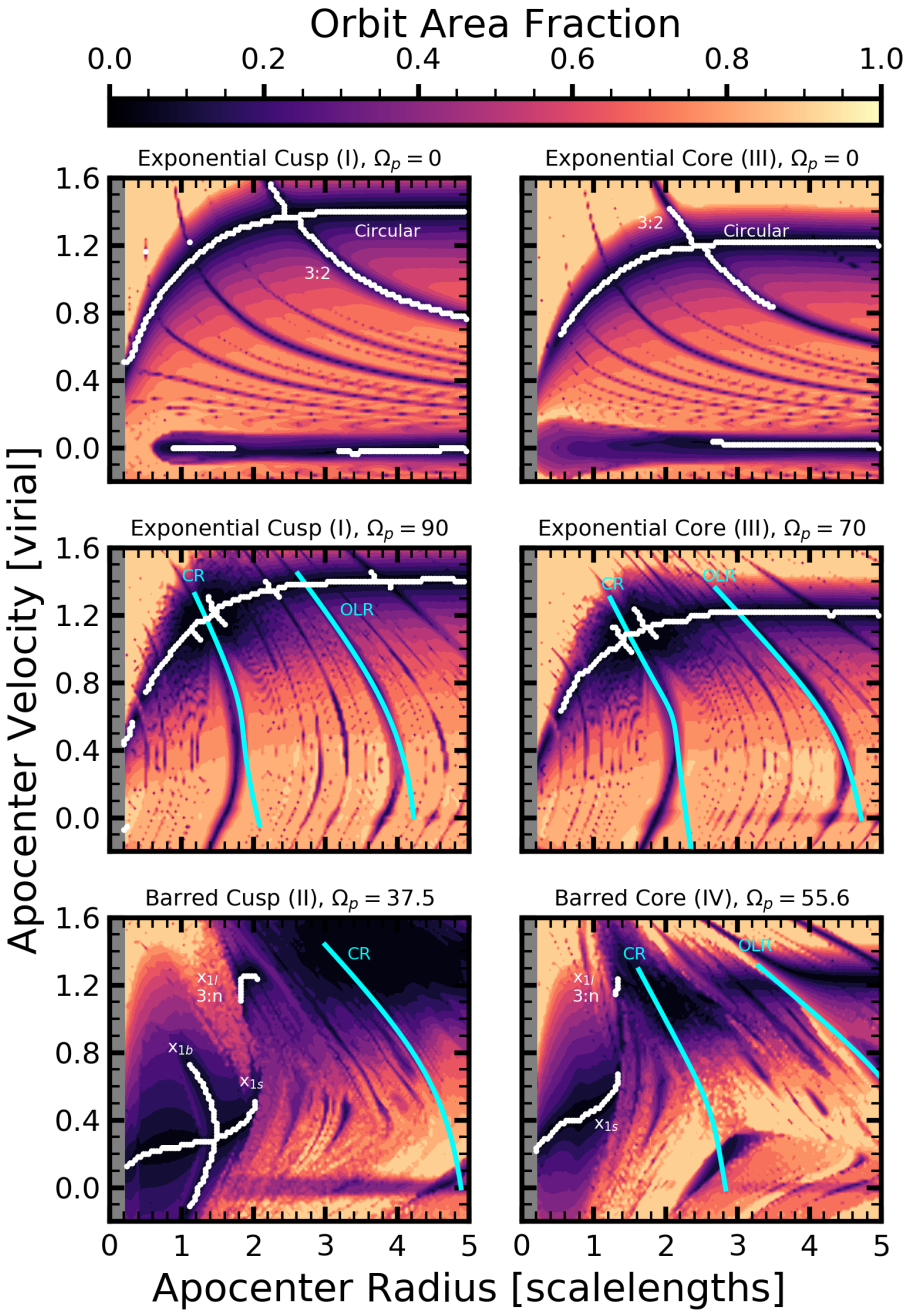

Figure 3.4. Relative orbit area plots for the four models, including two values of Ω_p for each of the exponential models. In each panel, we highlight and label key commensurabilities identified with the geometric algorithm in white. We plot and label the locations of corotation and the outer Lindblad resonance, as computed numerically from the monopole where possible, in cyan. The commensurabilities are discussed in detail in Section 3.3.1 for the cusp model and Section 3.3.2 for the core model. The gray region at $0.0 < a < 0.2$ was not integrated, owing to the limits of numerical resolution of this study.

is of intrinsic interest to a holistic study of galaxy evolution and will be discussed further in future works. We choose $R_{\rm apo} \in (0.2a, 5a)$ and $V_{\rm apo} \in (-0.2, 1.6)$. The lower limit on $R_{\rm apo}$ is one of practicality; the technique for understanding orbit structure discussed below is not applicable to very small radius orbits owing to the requirement that orbits have regularity, an assumption that is not guaranteed at $R < 0.2a$. We will return to the question of central orbits in future work. The choice of maximum $R_{\rm apo}$ is driven by a desire to study the structure of the stellar disc; outside of this radius, where the stellar density has significantly diminished, we do not observe any strong commensurabilities worth noting.

For $V_{\rm apo}$, we wish to explore the entirety of the relevant phase space. From an initial study of the simulations, we see that retrograde orbits play some role in the dynamics of the disc at small radii. Thus, we do not truncate $V_{\rm apo}$ at zero, but choose to study the relevant retrograde phase space. Similarly, at the maximum end of $V_{\rm apo}$, we want to include the circular velocity as well as the possibility that some orbits may occasionally be temporarily scattered or driven to larger velocities than the circular velocity at a given radius. Thus, our choice of a maximum boundary of $V_{\rm apo} = 1.6$.

3.2.4.2 Integration

In principle, the integration of the time-series of orbits to assemble the atlas could be accomplished using a variety of integrators, so long the integrator has high accuracy over tens of dynamical times. In the rest of this section, we describe various specifics to our integration scheme, which is based on the leapfrog integrator used in EXP. The integrator we use here also implements the following speedups relative to a general-purpose leapfrog integrator: (1) an implentation of adaptive timesteps from EXP, described in Chapter 1, with minimum timestep thresholds set; (2) completion criteria set by either total integrated time or the number of apsides reached. For the purposes of the experiment here, we match the timestep to the minimum timestep in the self-consistent simulations, $dt_{\rm vir} = 3.2 \times 10^{-5}$.

We truncate the evolution after 50 radial periods have been completed or a maximum of $\Delta T_{\rm vir} = 0.64$.

As noted in Section 3.2.1.2, each component is defined by a unique set of basis functions. Therefore, in addition to filtering the spatial scales to those of interest, the integration can either include the whole potential as extracted from the self-consistent simulation, or can pick and choose elements that make the computational problem more tractable in some way. By excluding higher-order terms that do not influence the integration of individual orbits, we can achieve $\frac{n-n'}{n}$ or $1 - \frac{l'^2}{l^2}$ per cent speedups, where n (l) is the total number of radial (azimuthal) halo functions and n' (l') is the number of retained radial (azimuthal) halo functions. After inspection of the signal-to-noise in the coefficients, we do not retain higher order halo azimuthal terms $l > 2$, resulting in an 88 per cent speedup of the halo calculation, without suffering any important dynamical consequences.

Our integration is left flexible in the following ways: (1) an on-the-fly selection of disc azimuthal harmonics to be included, which allows for the primary test cases of restricting to the monopole potential and eliminating of odd harmonics; (2) a selection of the radial subspaces to be included, which allows for noise-based experiments; and (3) adjustable figure rotation velocities for testing the pattern speed of the bar. For all the fixed potential integrations presented, we do not apply odd multiplicity azimuthal harmonics, as the pattern speed is independent of the even multiplicity pattern speed, such that the integration becomes unstable. In principle, different values of Ω_p could be employed for individual harmonic orders, e.g. $\Omega_{p,\, m=1}$ and $\Omega_{p,\, m=2}$, allowing for an investigation of the dipole's influence separately from the quadruople. We aim to study this phenomena in future work.

3.2.5 The Geometric Algorithm

From a time series of discrete (x, y, z) points, we use Delaunay triangulation (DT) to compute the physical volume that an individual orbit occupies, transforming a discrete time-series of points to a volume. As we are restricting our analysis to the disc plane in this

Model	$x_{1s,l}$	x_{1b}	CR	3:n	Boxlets
Exponential Cusp (I), $\Omega_p = 0$	✗	✗	✗	✗	✗
Exponential Cusp (I), $\Omega_p = 90$	✗	✗	✓	✓	✗
Barred Cusp (II)	✓	✓	✓	✓	✗
Exponential Core (III), $\Omega_p = 0$	✗	✗	✗	✗	✗
Exponential Core (III), $\Omega_p = 70$	✗	✗	✓	✓	✗
Barred Core (IV)	✓	✗	✓	✓	✓

Table 3.2. Comparison of different orbital families present in the potential models.

study, the problem is simplified to two-dimensional DT and we can calculate an area. We have tested three-dimensional DT, and will make vertical commensurabilities, which are revealed in three dimensions, the focus of future work. We perform this computation for all the orbits we integrate in the $R_{\rm apo}-V_{\rm apo}$ plane. We refer to this as the orbit atlas. The orbital atlas provides a 'skeleton' of the orbits in a given potential, tracing the commensurate orbits which support the structure of the galaxy model. We, therefore, refer to the figures that show the orbit area at each point in the $R_{\rm apo} - V_{\rm apo}$ plane as 'orbital skeletons'.

Finding the orbits in each atlas that have sufficiently small fractional areas will reveal the commensurate orbits. Identification of commensurate orbits provides an important theoretical link to find and describe trapped orbits between a perturbation theory interpretation and fully self-consistent simulations (Contopoulos & Papayannopoulos, 1980; Tremaine & Weinberg, 1984b; Weinberg & Katz, 2007a,b, Chapter 1). In the following sections, we present the findings from the commensurability searches on the various models.

3.2.5.1 Area Measurement

Given a series of samples at discrete times for an orbit, we wish to approximate the area that an orbit would sample in the limit where $dt \to 0$ and $T \to \infty$. To measure the area of an annulus or volume of a sphere that a discrete set of orbit time samples would eventually fill as $T \to \infty$, we require a tesselation technique that transforms discrete time series of points into an integrable area ($dt \to 0$). One such computational technique is Delaunay triangulation. We construct a procedure that uses Delaunay triangulation (DT), taking an

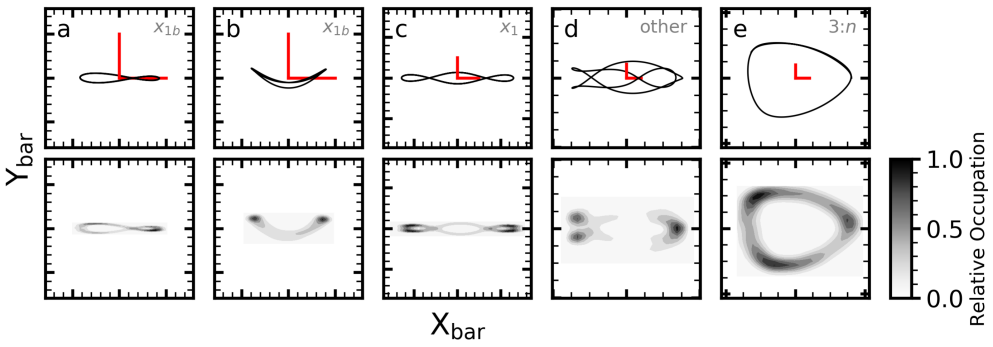

Figure 3.5. Five example integrations from the Barred Cusp (II) model. In each column, we show the trajectory (upper panel) and time-integrated density (lower panel). Panels a and b show 1/1 orbits, the x_{1b} family, where panel a is a 'symmetric' 1/1 orbit, and panel b is 'asymmetric'. Panel c shows a strong x_1 orbit. As it is a shorter period x_1 than another x_1 subfamily at this value of $R_{\rm apo}$, we call this an x_{1s} orbit. Panel d shows a derivative of an x_1-like orbit with higher-order structure and a long period, which would be an 'other' orbit in our classification. Panel e shows a 3:2 orbit. In each of the upper panels, the red scalebar is half a scalelength.

input that is a set of two-dimensional points in the $x - y$ plane and returning a single value that is the (normalized) computed orbit area from the sum of individual tesselated triangles[2].

The steps to calculate the area of a given orbit from the time series of discrete points are as follows:

1. Integrate the orbit in a given potential using discrete timestep dt, including a rotating bar potential with specified pattern speed Ω_p, as in Section 3.2.4.2 to obtain a set of two-dimensional points.

2. Transform the orbit points to a frame co-rotating with the imposed bar pattern.

3. Compute the triangulation of the transformed points by applying DT to the (x, y) orbit points.

[2]An equivalent procedure may be followed to generalize the orbit measurement to a volume, i.e. by using all three dimensions for the orbit. In such a procedure, triangles become tetrahedrons from which a volume can be computed.

4. Prune the triangulation by eliminating triangles with axis ratios above some threshold.

5. Compute the area of each remaining triangle and sum to obtain A, the area of the orbit.

6. (optional) Normalize the area of the orbit by the area of a circle with radius $r_{\rm max}$, the maximum distance from the inertial center in the time series.

We use the computational geometry library CGAL (CGAL Project, 2018) to perform the DT. From the input of a time-series comes a list of triangles with length-ordered sides a, b, c, where a is the length of the longest side. The low density (and therefore least important for computing the area) regions are removed by ignoring triangles with extreme axis ratios, in this case chosen to be $\frac{a}{c} > 10$. Adjusting this threshold to 5 or 15 does not produce qualitatively different results.

Examples of the technique are shown in Figure 3.6. The upper panel shows the integration of two orbits over the entire time window, $T = 0.64$, which is 2000 steps at $dt = 3.2 \times 10^{-5}$. Both orbits are shown in the frame co-rotating with the bar. While the black orbit has sampled the entire phase-space trajectory, the purple orbit has not. It is clear that the purple orbit will fill an entire torus in physical space given enough time. In the lower panel, we show the triangulation for each orbit. The black orbit, nearly closed, features vanishingly small triangles, while the purple orbit, which previously only sampled a fraction of the torus, is now filled with triangles. We can now evaluate the area in physical space that each orbit occupies.

As described in the optional final step above, to compare the area of orbits with hugely different energies, we normalize by the area of a circle with a radius equal to the maximum radius of the orbit over the course of integration: $A_{\rm norm} = \sum^k T_k/(\pi R^2_{\rm apo})$. This yields values $A_{\rm norm} \in (0, 1]$. As we always opt to normalize the area, we eliminate the subscript and simply refer to the normalized area as A throughout this work. In the bottom panel of

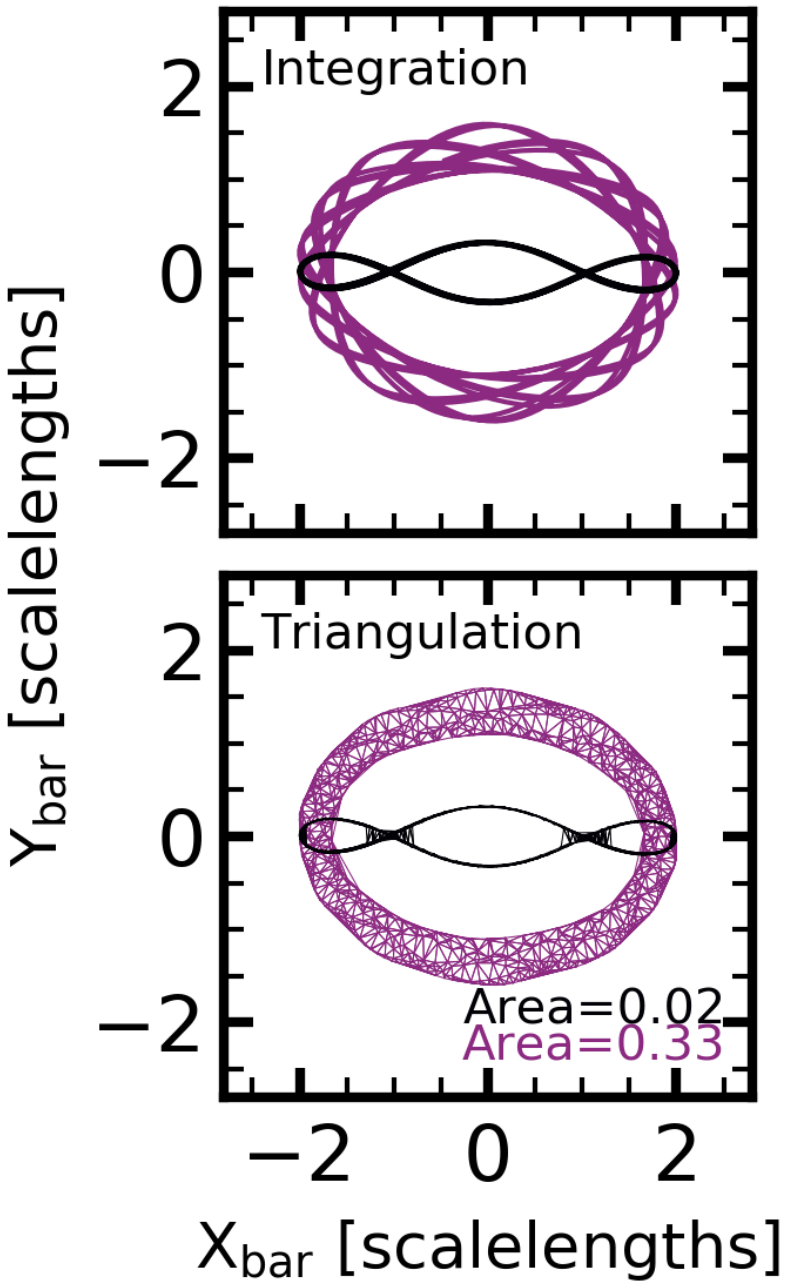

Figure 3.6. Two orbits in the barred cusp potential, Potential II. The black orbit starts from $(R_{\rm apo},\ v_{\rm apo}) = (0.02, 0.45)$, and the purple orbit starts from $(R_{\rm apo},\ v_{\rm apo}) = (0.02, 1.05)$. The upper panel shows the integration of the orbits in the potential for $\Delta T = 0.64$, with the orbits presented in a frame co-rotating with the bar. The lower panel shows the same orbits, with the fraction of a circle that the orbit fills in (area) computed using the geometric algorithm. Some residual triangles not successfully trimmed by the simplex rules are seen in the black orbit, limiting the absolute precision of the technique.

Figure 3.6, we list the area for both orbits; the closed black orbit has an area $A = 0.01$, demonstrating the uncertainty owing to the traingulation (as a closed orbit should have zero area, $A = 0$). The purple orbit has an area $A = 0.33$.

3.2.5.2 Skeleton Tracing

As shown in Figure 3.6, a commensurate orbit will occupy a smaller area in physical space than a non-commensurate orbit. We exploit this to find commensurabilites in the potential. We further know that true commensurabilities occupy zero (or a vanishingly small) volume in phase space, suggesting that tracing valleys in orbit area will follow commensurate orbit tracks. The procedure we use to trace commensurabilities in the $R_{\rm apo} - V_{\rm apo}$ plane is as follows:

1. Identify all orbits below a certain threshold in normalized area. We use $A < 0.02$, which balances the finite measurement accuracy from the triangulation while still excluding non-commensurate orbits.

2. Connect contiguous areas using a standard marching-squares algorithm, as in contour finding, which checks adjacent orbits in the $R_{\rm apo} - V_{\rm apo}$ grid to detemine which adjacent orbits meet the threshold criteria and subsequently connect the points, which we call the threshold map.

3. Perform valley-finding on the threshold map using the algorithm of Steger (1998). The algorithm calculates the Hessian matrix of the threshold map by convolving the threshold map with derivatives of a Gaussian smoothing kernel and then determining the vanishing point of the gradient, i.e. a valley.

4. Inspect individual orbits in the atlas near the commensurability for connection to known families of orbits and frequency ratios.

3.2.5.3 Monopole-calculated Commensurabilities

One may numerically compute the location of resonances in an axisymmetric potential by determining the table of frequencies for each E and κ in a grid and solving Equation 7.2 for a given combination of (m, l_1, l_2, l_3). For our expansion of the potentials in harmonic orders, simply selecting the monopole component of the potential is sufficient to reduce the potential to an axisymmetric case. For orbits outside of the bar radius, at evolutionary stages after the bar has formed, the monopole is a reasonable approximation for the potential in the plane. As we are restricting our analysis to the (x, y) plane in this work, $l_3 = 0$.

We calculate the (E, κ) locations of CR $(m, l_1, l_2) = (2, 0, 2)$ and OLR $(m, l_1, l_2) = (2, 1, 2)$ using the monopole approximation. In general, the resonances have little dependence on E, existing at a single value of E for all κ. To place the (E, κ)-calcuated locations of resonances on the $(R_{\rm apo}, V_{\rm apo})$-based figures in this work, we compute the transformation between $(R_{\rm apo}, V_{\rm apo})$ and (E, κ). In the axisymmetric case, the mapping is monotonic, albeit warped. The location of ILR, $(m, l_1, l_2) = (2, -1, 2)$, is not possible to approximate using this method owing to the strongly non-axisymmetric potential at those radii. In this case, the geometric algorithm and skeleton tracing are preferred.

3.2.6 Orbit Classification

For an orbit conserving L_z and E, the location of the apsides will follow a pattern set by the orbital frequencies, a principle underpinning the classification of orbits in this work. As we are most interested in the classification of orbits related to the bar, we evaluate the coherence of the apsis locations relative to the maximum of the bar potential, e.g. the bar position angle. This coherence may be used to classify orbits into different families, motivating the use of a clustering algorithm. We select k-means (Lloyd, 1982) as a simple methodology with which to partition apsides for a given orbit into families that show similar morphologies, which we then connect to known classical orbit families. Briefly, the k-

means algorithm iteratively separates a collection of points into k clusters by minimizing the sum of the distance between each point and the center of a determined cluster, where the distance metric used in this work is standard Cartesian space.

The steps to prepare an orbit for k-means analysis are as follows:

1. Extract x, y, and z time series for a given orbit.

2. Determine the radial turning points (apsides).

3. Transform the x, y positions of the apsides into a frame where the bar position angle is aligned with the x axis.

4. For each apsis: determine the 19 other nearest apsides in time and run the k-means algorithm on the $x_{\rm bar} - y_{\rm bar}$ positions of the apsides. The time of each apsis sets the points in time at which the coherence is precisely determined.

The output of the k-means algorithm is two-fold: (1) the partitioned k clusters of apsides, and (2) the location of the spatial center (equivalently listed in $(R_{\rm cluster}, \theta_{\rm cluster})$ or $(x_{\rm cluster}, y_{\rm cluster})$ for each cluster. Therefore, to determine membership in the bar, a set of metrics relating to the radial turning points, or apsides, is calculated for each orbit:

1. $\langle \delta\theta_{\parallel} \rangle \equiv \max\left(\langle \theta_{\rm bar} \rangle_N\right)_k$, the standard trapping metric from Chapter 1 that assesses the average angular separation in radians from the bar axis, $\theta_{\rm bar}$, for N apsides in k clusters. The returned value is the maximum angular separation from the bar for the k clusters. N is a parameter that should be set based on the dynamical time of the bar, which we set to be $N = 20$ for all analyses in this work.

2. $\langle R_{\rm cluster} \rangle_k$, the radius of each cluster center, averaged over k clusters.

3. $\langle \sigma_{R_{\rm cluster}} \rangle_k$, the variance in radius for all apsides in a cluster, averaged over k clusters. Variation in this quantity is aphysical for a trapped orbit, allowing for a strict limit to remove contaminent orbits.

4. $\langle \sigma_{\theta_{\rm cluster}} \rangle_k$, the variance in position angle for all apsides in a cluster, averaged over k clusters. Variation in this quantity is the product of both uncertainty in the bar angle as well as being possibly indicative of a family that would be better fit by an increase in the number of clusters k.

5. Ω_r, the instantaneous radial frequency, computed as the finite difference in time between the central apsis and the next nearest apsis in time. Used to calculate orbits that fall below the Nyquist frequency for time sampling as well as orbits whose radial frequency makes it impossible for the orbit to be a bar member.

Some combination of these five quantities will describe different orbit families to within an acceptable contamination tolerance. We estimate our contamination rate at 1 per cent from visual inspection of classified orbits. Additionally, choosing the correct metrics for family classification is largely model-indpendent. However, the dynamical time of a given model can affect the time resolution, meaning that determinations can be noiser in models with rapidly changing pattern speeds (and therefore rapid secular evolution).

To calibrate the trapped orbit metrics for a given model, the quantities listed above can be tabulated for all orbits at some late time, when secular evolution is relatively slow. Once the quantities have been tabulated, one may inspect given features in the parameter space determined by the metrics above to find trapped orbits. Significant progress may be made using theoretical considerations: orbits that are part of the bar will show small values of $\langle \delta\theta_{\parallel} \rangle$, and orbits which are consistent members of a single family will show small values of $\langle \sigma_{R_{\rm cluster}} \rangle_k$. The best descriminator between different orbit families is empirically found to be $\langle \sigma_{\theta_{\rm cluster}} \rangle_k$. We assume that orbits with $\Omega_r > \Omega_p$ are not a part of the bar.

Once the process verifying the chosen criteria is complete, we proceed with a full analysis of the simulation from the beginning. For full simulation analysis, the closest apsis in time is chosen as representative of the orbit's current status (we attempt no interpolation to increase the effective time resolution and use single apsides). Therefore, the time resolution for studying coherence is dependent on the radial period of individual orbits, though

we find the varying resolution is a small part of the (already small) overall uncertainty. We analyze both the cusp and core simulations in their entirety using this methodology in Section 3.5.

In addition to general implemenation improvements in the software, we identify four concrete improvements over Chapter 1:

1. Implementation of the 'k-means++' technique of Arthur & Vassilvitskii (2007) when the standard (Lloyd's) k-means technique (Lloyd, 1982) fails (approximately 0.6 per cent of orbits in the cusp model, the primary calibrator for the methodology).

2. Use the closest N apsides in time to the indexed time, rather than enforcing $\frac{N}{2}$ apsides on either side of the target time.

3. Set a threshold, $T_{\rm thresh}$, that is some multiple of the bar period $T_{\rm bar}$ in which the N apsides must reside. This guards against choosing unrelated apsides (the threshold is exceeded for approximately 15 per cent of the fiducial model orbits, at which point the orbit is not analyzed at that timestep).

4. The inclusion of $\left\langle \sigma_{\theta_{\rm aps}} \right\rangle_k$ allows subdivision into 2:1 and 4:1 (and higher) families even while using $k = 2$.

Table 3.2.6 lists the empirically-determined classification criteria for two families of orbits. Table 3.2.6 also lists an 'Undetermined' classifier for orbits with Ω_r above the Nyquist frequency of the time-series sampling (orbits which are close to the center). Future work to study the potential on the smallest scales closest to the center of the model is possible. Additionally, while $x_{2,3,4}$ orbits exist in small quantities in our models, these orbits play little if any role in the dynamics described in this work, and so we do not focus on their classification here.

As we also have interest in empirically locating the bifurcated members of the x_1 family (the x_{1b} orbits, which we refer to as a subfamily), we employ a secondary classification

Family	$\langle\theta_{\rm bar}\rangle_{20}$	Ω_R	$\left\langle\sigma_{R_{\rm aps}}\right\rangle_k$	$\left\langle\sigma_{\theta_{\rm aps}}\right\rangle_k$
x_1	$\left[0, \frac{\pi}{6}\right]$	$< \frac{1}{2\delta t}$	$[0, 0.1a]$	$\left[0, \frac{\pi}{16}\right]$
Other Bar	$\left[0, \frac{\pi}{6}\right]$	$< \frac{1}{2\delta t}$	$[0, 0.1a]$	$\left[\frac{\pi}{16}, \frac{\pi}{8}\right]$
Undetermined	-	$> \frac{1}{2\delta t}$	-	-

Table 3.3. Membership definitions for being classified into families. '-' indicates that no constraint was placed on the parameter.

scheme on orbits that we determine to be part of the larger x_1 family. Unfortunately, the coherence of the apsides for x_{1b} and $x_{1s,l}$ orbits are indistinguishable, such that the quantities discussed above do not allow for separation of the morphologically-distinct $x_{1s,l}$ and x_{1b} orbits. However, a clear morphological difference in the bifurcated x_{1b} orbits and the short- or long-period x_1 orbits is the presence of varying numbers of $x_{\rm bar}$ and $y_{\rm bar}$ local maxima (or equivalently, points where the velocity in one dimension relative to the bar goes to zero). Therefore, a classification scheme that takes local maxima in the time-series of $x_{\rm bar}$ and $y_{\rm bar}$ may allow for a distinction between the subfamilies. Such a classification scheme is computationally expensive, requiring tracking the entire time-series for a given orbit after it has been identified as an x_1 orbit (which, as shown in this work, may be 30 per cent of all disc orbits in the simulation). Additionally, the classification may be fraught with uncertainty, as it requires a precision transformation to an occasionally ill-defined bar frame, and the transition between the parent orbits of x_1 subfamilies may be rapid.

Despite this uncertainty, we make estimates of membership in the x_{1b} family from the $x_{\rm bar}$ and $y_{\rm bar}$ frequencies, $\Omega_{x_{\rm bar}}$ and $\Omega_{y_{\rm bar}}$ as determined by the local maxima of the $x_{\rm bar}$ and $y_{\rm bar}$ time series. From pedagogical orbits, the x_{1b} orbits trace two morphologies: infinity symbol-like orbits, and smile- or frown-like orbits. Infinity symbol orbits have $\Omega_{x_{\rm bar}}/\Omega_{y_{\rm bar}} = 1.5$, while smile and frown orbits have $\Omega_{x_{\rm bar}}/\Omega_{y_{\rm bar}} = 2$ (this is because the strongest smiles and frowns actually counter-rotate in the bar frame). The subclassification into x_{1b} orbits benefits from the distinction with standard x_1 orbits, which have $\Omega_{x_{\rm bar}}/\Omega_{y_{\rm bar}} = 1$ or $\Omega_{x_{\rm bar}}/\Omega_{y_{\rm bar}} = 3$ (in the case of x_1 orbits with so-called 'ears', see Figure 3.6). At some point, the classification becomes subjective, where individual orbits

are judged to be 'more similar' to x_{1b} or x_1 orbits. Therefore, we offer only a coarse estimate of the membership, assuming that orbits with $1.5 \geq \Omega_{x_{\rm bar}}/\Omega_{y_{\rm bar}} \leq 2$ are x_{1b} orbits, which we can then classify into infinity or smile/frown orbits via the presence or absence of counter-rotation. The broad classification by frequency is a necessity as orbits do not spend large fractions of time as 'pure' members of the subfamilies, with small integer combinations of $\Omega_{x_{\rm bar}}$ and $\Omega_{y_{\rm bar}}$, but rather exhibit modest resemblence to the parent orbit as secular evolution proceeds.

Our estimate of membership in the bifurcated families in this work, but owing to the uncertainty for any given orbit at a particular time, we consider orbits only over large windows of time during our analysis, reducing uncertainty, but limiting the time resolution of our estimates for the fraction of x_1 orbits in a bifurcated subfamily to $dT = 0.1$.

Lastly, the sign of the maxima can also help determine the preferred orientation of bifurcated orbits, which naturally include some symmetry-breaking. That is, we may determine whether the crossing point in the infinity orbits is preferentially located toward one end of the bar, or whether the counter-rotating portion of the smile/frown orbits such as the example in panel 'b' of Figure 3.5 is toward one direction along the bar minor axis. Such collecting of crossing points or counter-rotating directions is responsible for the $m = 1$ amplitude, which we discuss in Chapter 5.

3.3 Fixed Potential Study Results

We apply the tools to the bar models described in Section 3.2.3 with the goal of locating and identifying the commensurate orbit families in each. Commensurability maps for the six orbital atlases calculated from the four potential models are shown in Figure 3.4. The maps are in $R_{\rm apo} - V_{\rm apo}$ space. The color map shows the values of the area A, as sampled by the initial conditions listed above. The color scheme is uniform throughout the chapter, such that colors in Figure 3.4 may be compared to the two orbits in Figure 3.6 for intuition on the colormap. The white lines in Figure 3.4 are the identified ridgelines. We do not plot

all the ridgelines identified, but rather restrict ourselves to those with dynamical import to avoid confusion. Further, where possible, we use the monopole-calculated frequency to calculate the location of CR and OLR.

With the ridgelines mapped, we can see that commensurabilities follow tracks through physically adjoining regions of the galaxy model by inspecting the morphology of orbits. In many cases, the commensurabilities cross over other commensurabilites. At these points, we expect to find chaotic behavior in a self-consistent simulation. Where commensurabilites can be identified, important regions of the galaxy model can be queried for other physically important quantities, such as angular momentum transfer, which we discuss below. Overall, we find similar orbit families to classic analytic studies (e.g. Contopoulos & Grosbol 1989; Athanassoula 1992; Sellwood & Wilkinson 1993). Figure 3.4 bears some resemblance to the so-called 'characteristic diagram' found in the analytic literature, although the advantage of the commensurability map is to additionally demonstrate the area over which orbits may resemble the parent orbit. Table 3.2.5 summarizes the observed orbit families for each of the galaxy models.

We first discuss the cusp models before turning to the cored models. For both sets of models, we first discuss the non-rotating axisymmetric models to understand the zeroth-order commensurabilies (Sections 3.3.1.1 and 3.3.2.1). We then impose a pattern speed upon the axisymmetric models (Sections 3.3.1.2 and 3.3.2.2), followed by the bar-like non-axisymmetric models in Sections 3.3.1.3 and 3.3.2.3. In Section 3.3.3, we present the results of applying the geometric algorithm to orbits extracted from the self-consistent simulation. We compare the differences between the fixed potential models and the self-consistent simulations in Section 3.3.4.

3.3.1 Cusp Models

3.3.1.1 Exponential Cusp (I), $\Omega_p = 0$

The zero pattern frequency exponential cusp potential (Potential I) reveals the inherent zeroth-order commensurabilites that arise when a disc is embedded in a dark matter halo. We present the commensurability structure, calculated from the orbital atlas in the upper left panel of Figure 3.4. The orbital skeleton overlaid, determined via the geometric algorithm.

The natural circular orbit curve (labeled) appears as the strongest ridge. Crossing the circular orbit ridge are several m:n commensurabilities, where n is the radial order and m is the azimuthal order, satisfying the standard commensurability equation. The 3:2 commensurability (labelled) is the strongest. As we shall see below, the 3:n families exist in barred potentials as well, including the 3:1 family, which has been studied in the literature (Athanassoula, 1992), where it is listed as a bifurcation of the x_1 family. Here, we treat the 3:n families as a separate resonance that often overlaps in phase-space with the x_1 family. The orders increase toward smaller radius, such that the next strongest commensurability curve is 5:2, then 7:2, and so on. Even radial orders are disallowed by the axisymmetry of the potential. The weaker lines correspond to m:4 commensurabilities, where m is odd. These resonances are not expected to be important for the evolution of the system. We will show that this expectation is accurate in section 3.5. A physically uninteresting radial orbits ridge appears at $V_{\rm apo} = 0$.

Additionally, while we show the theoretical space above the circular velocity curve, we do not expect to see many orbits populating the region of phase space that is super-circular in a real galaxy[3]. For a barred model, this is not explicitly true: orbits that are perpendicular to the bar at some radius may appear faster than circular when parallel to the bar axis. In the barred models, launching at velocities faster than circular will lead to orbits that may be

[3]In fact, this must be true for an axisymmetric model.

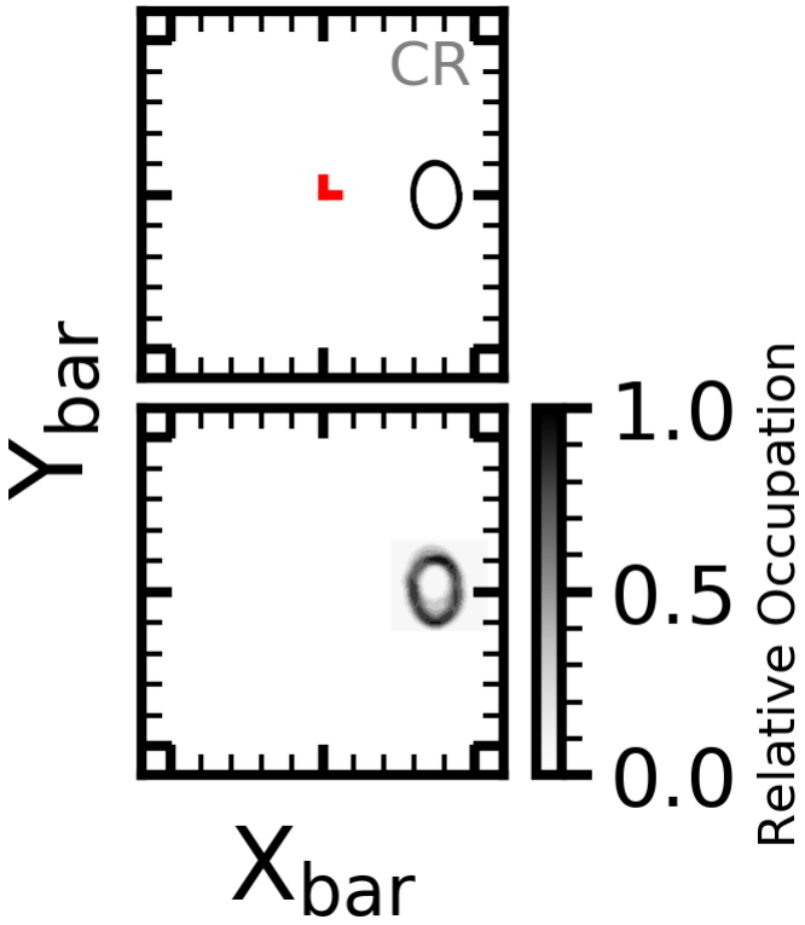

Figure 3.7. An example corotation orbit integrated in the barred cusp potential (II). The red scalebar is half a scalelength.

commensurate perpendicular to the bar, to which we are not sensitive. Thus, for the most part, we will restrict our discussion of features to those related to regions of phase space that have a lower energy than that of a circular orbit at the same radius.

3.3.1.2 Exponential Cusp (Potential I), $\Omega_p = 90$

The rotating exponential cusp, also with the underlying Potential I, reveals new structure not present in the non-rotating version of the potential model when we impose a pattern speed of $\Omega_p = 90$. We present its commensurability structure in the middle left panel of Figure 3.4. Owing to the axisymmetric nature of the potential, the circular orbit ridge is

unchanged from the same potential model with $\Omega_p = 0$. However, the radial orbit commensurability is no longer stable and has disappeared.

A rotating model admits strong low-order resonances, including the inner Lindblad resonance (ILR), corotation (CR), and the outer lindblad resonance (OLR). In this axisymmetric model, we can use the lines shown in the upper left panel of Figure 3.3 to guide our interpretation. We expect to see ILR at $R = 0.2a$, CR at $R = 1.3a$, and OLR at $R = 2.8a$ along the circular orbit track. We can compute the location of CR and OLR using the monopole component of the potential, following the description in Section 3.2.5. With the monopole-derived commensurabilities placed on Figure 3.4 in cyan, we see an extended patch of low relative orbit area intersecting the circular orbit track at $R = 1.3a$ coincident with the cyan CR line. At lower tangential velocities than circular orbits, and thus higher eccentricities, corotation appears as a thin track that descends in velocity with a mild dependence on radius ($1.4a < R_{\rm apo} < 1.8a$), deviating from the cyan track for high eccentricities, where the assumptions underpinning the monopole calculation begin to break down. Additionally, one can see OLR crossing the circular rotation track at $R = 2.8a$, and continuing to lower $V_{\rm apo}$. However, we do not see an obvious ILR in the diagram, as one expects given the minimum radius of the orbit map and the estimate from Figure 3.3.

Many higher-order resonances are also observable as dark regions. These features correspond to the higher order resonances discussed above for the nonrotating model, and are again unlikely to be important, as the nature of the changing potential is such that the higher-order resonances are less persistent and have less time to induce changes to conserved quantities.

3.3.1.3 Barred Cusp (Potential II)

The barred cusp model (Potential II) admits wholly different classes of orbital families from the exponential cusp in either the non-rotating or rotating cases (Potential I), owing

to the strong non-axisymmetric disturbance. We classify three types or subfamilies of x_1 orbits:

1. x_{1b} orbits (symmetric and asymmetric 1/1 orbits; a symmetric 1/1 orbit is shown in panel 'a' of Figure 3.5, and an asymmetric 1/1 orbit is shown in panel 'b')[4].

2. x_{1s} orbits, short-period bifurcated standard x_1 orbits (with 'ears', panel 'c' of Figure 3.5).

3. x_{1l} orbits, long-period elongated x_1 orbits (which may be simple 2:1 orbits, or may exhibit higher-order commensurate structure as in panel 'd' of Figure 3.5).

We identified the orbit families through visual inspection of the orbit atlas. While many m:n orbits with $m > 1$ are clearly observed in Figure 3.4, we choose to mark only the strongest (lowest-order) m family, namely, where $m = 3$. As several low-order even n orders comprise the $m = 3$ feature, and are co-located, this is labeled as 3:n in Figure 3.4.

With a fine enough grid, arbitrarily high order commensurabilites can be found (see, e.g. the unidentified structure in Figure 3.4 from the 3:n position to CR and beyond). In this work, we restrict our analysis to the low-order strong commensurabilities that form the persistent backbone of the barred galaxy. In panel 'e' of Figure 3.5, we plot an example 3:2 orbit. All orbits that are asymmetric across the x-axis in Figure 3.5 have corresponding mirror image orbits, where an orbit with one symmetry leads the bar pattern and an orbit with the other symmetry trails it.

In Figure 3.7, we show an example CR orbit in the barred cusp potential (Potential II), which has a strong CR feature. CR is the lowest-order resonance present in the model, with wide-ranging dynamical effects for secular evolution discussed extensively in the literature (see Sellwood 2014 for a review). CR orbits are particularly easy to recover using

[4]While non-intuitive, 'symmetric' in the case of 1/1 orbits refers to symmetry across the y axis in the literature. Thus panel 'a' of Figure 3.5 is a 'symmetric' 1/1 orbit, owing to the y-axis symmetry, and panel 'b' is asymmetric. Without any figure rotation, the symmetric x_{1b} orbit looks exactly like an infinity sign, that is, the crossing point is centered rather than off-center.

the geometric algorithm owing to the minimal area spanned by their trajectory, evident in Figure 3.7. For Figure 3.4, we use the monopole component of the potential to compute the location of CR, as in the above section, following the procedure in Section 3.2.5. The monopole-calculated commensurability is largely consistent with an apparent commensurability track in Figure 3.4. Owing to the long radial periods near CR in this model the skeleton–tracing algorithm described in Section 3.2.5 can return ambiguous results, so we opt to include only the monopole-derived commensurabilities at radii outside of the bar radius.

The inclusion of higher-order harmonic subspaces, $m > 2$, plays a large role in the orbital structure, allowing new families to appear, while the potential may appear to vary insignificantly. The exclusion of the $m > 2$ azimuthal subspace from the barred cusp results in an appreciably different orbital structure, including the disappearance of the x_{1b} family. This is particularly relevant for studies of orbital structure that rely on only a quadrupole term to represent the bar. Further, recent models for the Milky Way have suggested the importance of the $m = 4$ component of the bar for reproducing the observed velocities near the Sun (Hunt & Bovy, 2018). In Figure 3.8, we integrate the same orbits as in panels 'a' and 'b' of Figure 3.5, except we limit the harmonic subspaces included in the potential to $m \leq 2$. The orbits are no longer x_{1b} orbits. The infinity morphology x_{1b} orbit is now a part of the less dynamically complex x_1 family. The smile morphology x_{1b} orbit has become a 'boxlet' orbit, a morphology which we discuss below.

Indeed, inspection of all orbits that are part of the x_{1b} family when all m orders are included reveals that the x_{1b} track no longer exists when we restrict the potential to $m \leq 2$. However, this should not be interpreted as evidence that $m > 2$ causes new resonant structure into which the x_{1b} orbits are trapped, but rather that $m > 2$ distorts the potential shape allowed by the quadrupole only into a structure that admits x_{1b} orbits. In Section 3.5, we will see that x_{1b} orbits are important for growing the bar in length and mass. This also

suggests that $m = 2$ parameterizations of the MW bar[5], such as those derived from the potential of Dehnen (2000), (e.g. Antoja et al., 2014; Monari et al., 2016, 2017; Hunt et al., 2018) may entirely miss important families of orbits, *even if the orbits do not appear to exhibit four-fold symmetry*.

In the barred cusp potential (Potential II), corotation intersects the circular orbit track at $R_{\rm apo} = 3.1a$. In practice, any observational signature of corotation will occur at larger radii, owing to the energy dependence of the orbital structure and the mild eccentricity of disc orbits, even at a few scalelengths. Curiously, corotation is at a fairly large radius in this potential model; if we assume that the radial terminus of the x_{1s} family is the length of the bar, then the ratio of corotation to the bar length in this model is $\mathcal{R} = \frac{3.1a}{2.1a} = 1.47$, well within the 'slow' regime for bars. That the pattern speed has slowed so greatly since formation has implications for the observed fast bar-slow bar tension (see e.g. Chapter 1), suggesting that an observational test that can assist in the determination of the x_{1s} radial terminus would prove a powerful diagnostic for determining the pattern speed of bars (see Section 5.5). Slowing (raising) the pattern speed artificially causes the location of the x_{1s} upturn to move outward (inward) in radius; decreasing (increasing) the amplitude of the non-axisymmetric components of the potential, causing the $V_{\rm apo}$ locus to drift to lower (higher) velocities, before the x_{1s} upturn ultimately settles at $V_{\rm apo} = 0$ in the case of an axisymmetric disc.

At all values of $R_{\rm apo}$ with $V_{\rm apo} < v_c(R)$ resolvable using this technique, we observe a 'backbone' of regular orbits. In particular, the barred cusp model has regular cylindrical orbits at small radii ($R \sim 0.2a$), in contrast to the barred core, discussed below. We see that the axisymmetric assumption that underlies the calculation of frequencies in Figure 3.3 results in a significant error in the calculation of the expected corotation radius: $R_{\rm CR} = 3.8a$

[5]However, ellipsoid-derived bar models such as the Ferrers bar (Binney & Tremaine, 2008) will naturally admit $m = 4$ power, depending on the axis ratio, such that an increase in axis ratio will increase the $m = 4$ power relative to $m = 2$. Additionally, the density profile of the bar will contribute to the $(m = 4)/(m = 2)$ ratio, with an increase in central density leading to a lower $(m = 4)/(m = 2)$ ratio.

from the frequencies, $R_{\rm CR} = 3.1a$ from the commensurability mapping. The discrepancy is larger for OLR, which is observable in the commensurability map at $R_{\rm OLR} = 4.4a$, but is located at $R_{\rm OLR} \approx 6a$ in the Lindblad diagram (Figure 3.3).

Lastly, a comment about the ultra-harmonic resonance (UHR), which occurs when $\Omega_p = \Omega - \kappa/4$. While simulations reportedly are able to detect the UHR (Ceverino & Klypin, 2007), we do not find any evidence for UHR orbits in our simulations. However, in the fixed potential analysis of the barred cusp model, a curious gap in the x_1 track appears with nonzero orbit area computed for the trajectories. Analytic work (Contopoulos, 1988) suggests that the UHR can grow smoothly from the x_{1s} orbits we observe, and inspection of the orbit trajectories, despite their nonclosure, supports this conclusion. Thus, we appear to see evidence for UHR effects in the fixed barred cusp potential, although not in the form of a detectable closed orbit.

3.3.2 Core Model

3.3.2.1 Exponential Core (Potential III), $\Omega_p = 0$

The nonrotating exponential cored model shares many similarities with the nonrotating cusp model (Potential I). The comparison of the cusp (I) and cored (III) nonrotating models, the upper panels of Figure 3.4, show the effect of the halo model on the zeroth order commensurabilities from a disc embedded in the halo. Figure 3.1 may also be an instructive comparison, demonstrating that despite the nearly identical nature of the disc monopole, as shown by the similarity in the disc component of the circular velocity curve, the contrast in halo model monopole acts to create a significantly different total circular velocity within a few scalelengths. In particular, the peak of the circular velocity curve drops from $V_{\rm apo} = 1.4$ in the cusp model to $V_{\rm apo} = 1.2$ in the cored model. The location of the m:n commensurabilities shift to smaller radii for all values of $V_{\rm apo}$. We mark the strong 3:2 commensurability and note that the other obvious tracks are equivalent to the tracks in the nonrotating cusp model.

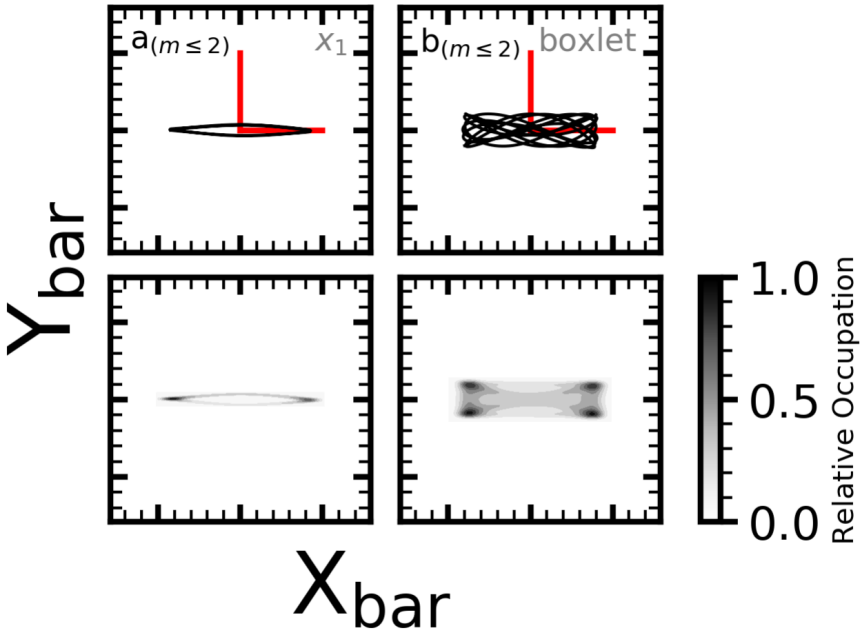

Figure 3.8. Left column: the same orbit as in panel 'a' of Figure 3.5, integrated applying only up to the quadrupole potential disturbance ($m \leq 2$). The orbit is now a standard x_1 orbit. Right column: the same orbit as in panel 'b' of Figure 3.5, also integrated applying only up to the quadrupole potential. The orbit is now a boxlet. In both upper panels, the red scalebar is half a scalelength.

3.3.2.2 Exponential Core (Potential III), $\Omega_p = 70$

The orbit area diagram for the rotating exponential core model is shown in the middle right panel of Figure 3.4. While we applied a lower imposed pattern speed than the exponential cusp model, as dictated by an estimate from the self-consistent core simulation, we see similar structure in the rotating exponential core model (III) to that of the rotating exponential cusp (I). For $v < v_c(R)$, corotation reaches larger values of $R_{\rm apo}$ than those reached in the rotating exponential cusp, reaching a maximum at $R_{\rm apo} = 2.1a,\ V_{\rm apo} = 0.4$. We observe a stronger 3:2 commensurability at larger values of $R_{\rm apo}$ compared to the rotating exponential cusp model (I). This is to be expected owing to the combination of lower pattern speed as well as a shallower potential (and thus shallower energy gradient) for the cored model.

We overlay the monopole-calculated CR and OLR on the orbit area diagram, finding similar results to the rotating exponential cusp model. CR and OLR intersect the circular velocity curve at positions more or less in agreement with the estimate from Figure 3.3.

3.3.2.3 Barred Core (Potential IV)

The barred core model (IV), in contrast to the non-rotating and rotating exponential core models (III), demonstrates clear differences from that of the barred cusp (II). While many of the major commensurabilities remain intact, albeit at significantly different locations in $R_{\rm apo} - V_{\rm apo}$ space, we crucially do not observe the x_{1b} family. As in the barred cusp model, we see both x_{1s} and x_{1l} orbits, where the x_{1l} again are spatially co-existent with the $m = 3$ series of commensurabilities[6].

Corotation is at a significantly smaller radius than in the barred cusp model (II), intersecting the circular orbit curve at $R_{\rm apo} = 1.8a$ compared to $R_{\rm apo} = 3.1a$ for the barred cusp. This occurs despite the models having approximately identical disc monopoles (cf.

[6]While not a formal phase-space, as discussed elsewhere in this work, residing near the same location in the orbital atlas $(R_{\rm apo}, V_{\rm apo})$ implies that orbits and families must be adjacent in phase-space as well, as the mapping to (E, κ) is unique.

Figure 3.1). However, coupled with the maximum radial extent of the x_{1s} orbits being at $R_{\rm apo} = 1.4a$, the ratio of corotation to bar length ends up being approximately equal to that of the barred cusp: $\mathcal{R} = 1.28$, versus $\mathcal{R} = 1.47$ for the barred cusp (II), within the fast bar regime. Similarly, OLR appears at a smaller radius when compared to the barred cusp model (II). The prominent commensurability that appears to cause a gap in the circular orbit track between corotation and OLR is the 5:2 m:n commensurability, flanked by higher n order commensurabilities. As in other models, near the circular orbit curve, the commensurabilities follow isoenergy lines in $R_{\rm apo} - V_{\rm apo}$ space.

While below the radial resolution of the orbit atlas constructed for Figure 3.4, we find from inspection of the self-consistent simulation that so-called 'boxlets' (such as in the right panel of Figure 3.8) exist at small radii in the simulation (Miralda-Escude & Schwarzschild, 1989; Lees & Schwarzschild, 1992; Schwarzschild, 1993). Orbits that do not show structure in the inertial frame will appear to be rectangular 'boxes' in the rotating frame, filling in an entire box-like region, as they effectively feel a simple triaxial potential. The extension of these apparent box orbits informs the structure of the potential, but is again reserved for future work studying the innermost regions of the potential models. In a rotating frame, some box orbits will show commensurate structure, and have been called boxlets. Boxlet orbits show higher-order m and n structure, but no preference for orientation. These orbits do not appear in the barred cusp potential (II) owing to the lack of a harmonic core in the potential.

3.3.3 Fixed-Potential vis-a-vis Self-Consistent Simulations

As discussed in Section 3.2.3, both of the barred potentials are drawn from larger self-consistent simulations. In this section, we place the single snapshots back into the self-consistent context, using outputs drawn from the self-consistent simulations. To retain similarity with the chosen fixed potential models (extracted at $T = 2.0$), we use phase-space outputs satisfying $T \in [1.8, 2.2]$, with $dT = 0.002$, for a total of 200 outputs.

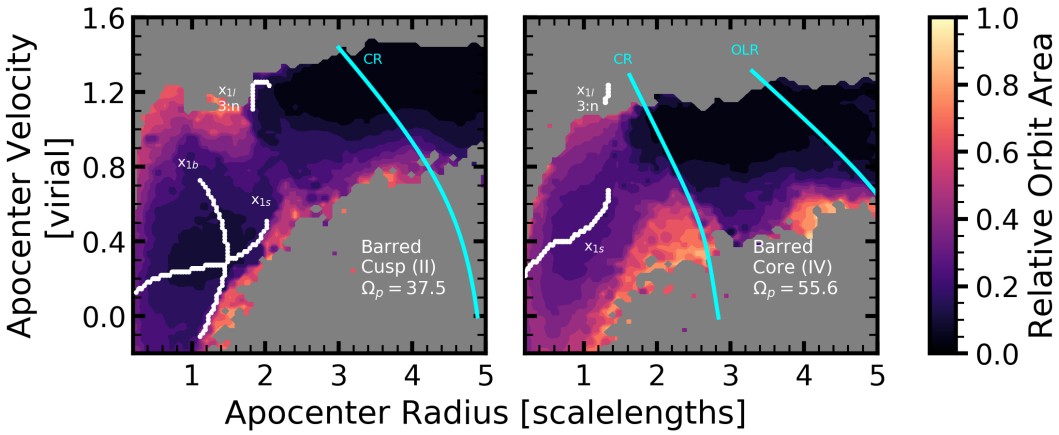

Figure 3.9. Relative orbit area as a function of $R_{\rm apo}$ and $V_{\rm apo}$ for live simulation orbits, computed from the lowest decile for each bin in $R_{\rm apo}$ and $V_{\rm apo}$. Regions without sufficient orbit sampling (i.e. fewer than ten orbits in a bin) are grayed out. The left panel shows orbits from the barred cusp model (II) and the right panel shows orbits from the barred core model (IV). The commensurability tracks for the corresponding model from Figure 3.4 are overplotted in white, and monopole-determined commensurabilities are plotted in cyan.

In Figure 3.9, we use the phase-space outputs to generate self-consistent orbit area maps. We do this by first transforming the 200 outputs to a frame co-rotating with the bar, then feed the sequences for each orbit to the geometric algorithm, returning the relative orbit area for each of the orbits. The uncertainty of the orbit area is smallest for orbits within three scalelengths, which have completed several rotation periods within $\Delta T = 0.4$, and thus have interpretable results from the geometric algorithm, but orbits at larger radii are significantly more uncertain. For each orbit, we then calculate its apocenter in the $\Delta T = 0.4$ window and the corresponding tangential velocity at apocenter. The orbits are put into rectangular bins with $dR = 0.1a$ and $dV = 0.05$. Once orbits have been assigned to a bin, for each bin we calculate the lowest decile ($10^{\rm th}$ percentile) relative area from the distribution of relative areas found by the geometric algorithm. We tested alternate particle selection critera per bin, including mean, median, and minimum, and find that the lowest decile value provided an appropriate balance between feature extraction and overemphasis of outliers that appear in given bins owing to the errors in determining $R_{\rm apo}$ and $V_{\rm apo}$.

The left panel of Figure 3.9 shows the results for self-consistent orbits drawn from the barred cusp model (II). Immediately, it is clear that many regions in the $R_{\rm apo} - V_{\rm apo}$ plane are not populated in the self-consistent simulation. The phase space in $R_{\rm apo} - V_{\rm apo}$ for discs is limited both by the effective circular velocity (set by the local potential) and the stability of radial orbits, in practice limited to $\kappa > 0.6$. Regions of low relative orbit area correspond to the commensurability tracks from Figure 3.4 superposed in white. The maximum $V_{\rm apo}$ for a given $R_{\rm apo}$ is set by the circular velocity curve, as expected. The region within $2a$ is dominated by nearly commensurate bar orbits near the commensurability track. However, the distribution is not symmetric in $V_{\rm apo}$ around the x_{1s} track, but is biased to larger $V_{\rm apo}$. This bias is supported by close inspection of the self-consistent simulation, which exhibits orbits that resemble x_{1b} orbits primarily leading the bar, expected for larger $V_{\rm apo}$ orbits.

At $R_{\rm apo} = 2a$ and $V_{\rm apo} = 1.2$, a ridge appears that is not prominently seen in the tracks from Figure 3.4. An artifically drawn extension of the 3:n series commensurabilities following an isoenergy line would approximately account for this ridge, which suggests that the fixed potential integrations may be missing some key ingredient that affects the self-consistent evolution. We discuss some possible reasons in Section 3.5.3. Corotation has only a modest presence in the model. OLR appears to have driven some orbits to higher eccentricities, a region of low relative orbit areas is seen at lower $V_{\rm apo}$ than expected in the vicinity of OLR, but a detailed analysis is not possible owing to the small time window of the analysis. To be sensitive to OLR with the geometric algorithm, one would need to integrate longer orbit time series, to the point where the underlying potential evolution would likely render the determination of OLR irrelevant.

The right panel of Figure 3.9 shows the results for orbits drawn from the self-consistent barred core model. We again see that the phase space is limited by the circular velocity curve. Once again, orbits with low relative orbit area gather near the x_{1s} track. A second low relative orbit area feature, at similar $V_{\rm apo}$ to the x_{1s} track but at $R_{\rm apo} \sim 3a$, is also apparent. Comparison with fixed potential orbits reveals that this feature is probably an

extension of the 3:n orbits to lower energies. CR creates a clear ridge in the self-consistent barred core model, which extends along an isoenergy track to significantly lower values of $V_{\rm apo}$, more than the commensurability tracks from Figure 3.4 would suggest. A similar behavior is also observed for OLR. The relative prominence of the low $V_{\rm apo}$ features in the self-consistent orbits when compared to the fixed potential orbits suggests that a missing dynamical degree of freedom in the fixed potential integration influences the stability of the orbits in the self-consistent simulation, as in the barred cusp model.

3.3.4 Summary

The primary goal of identifying orbit families and their resulting structure is to use the unique features of the orbital families in each model to inform the underlying potential and discriminate between halo models. We find a number of important features that both inform dynamical principles and help discern the potential structure:

1. We empirically locate CR and OLR, finding that the barred cusp potential (II) CR location is at a substantially larger radius than the barred core potential (IV).

2. We find the presence of the x_{1b} orbit family in the barred cusp potential, but not in the barred cored potential (or either of the axisymmetric models).

3. The x_{1l} and 3:n commensurabilities are co-located at the end of the bar.

4. Orbit families observed in the self-consistent simulation cannot be recovered without the $m = 4$ harmonic included in the potential.

The most obvious difference between the barred cusp (II) and core (IV) potentials is the presence of the x_{1b} track, which clearly affects the structure of the orbits in the barred cusp model. Additionally, the 3:n tracks lie in populated regions of phase-space in the barred cusp model. Inspection of the self-consistent orbit shows that a channel to grow the bar exists when orbits transition from 3:n, where ($n = 2, 4$) to x_{1s} orbits over short timescales, fueling the continued growth of the bar. Regions with commensurability overlap may lead

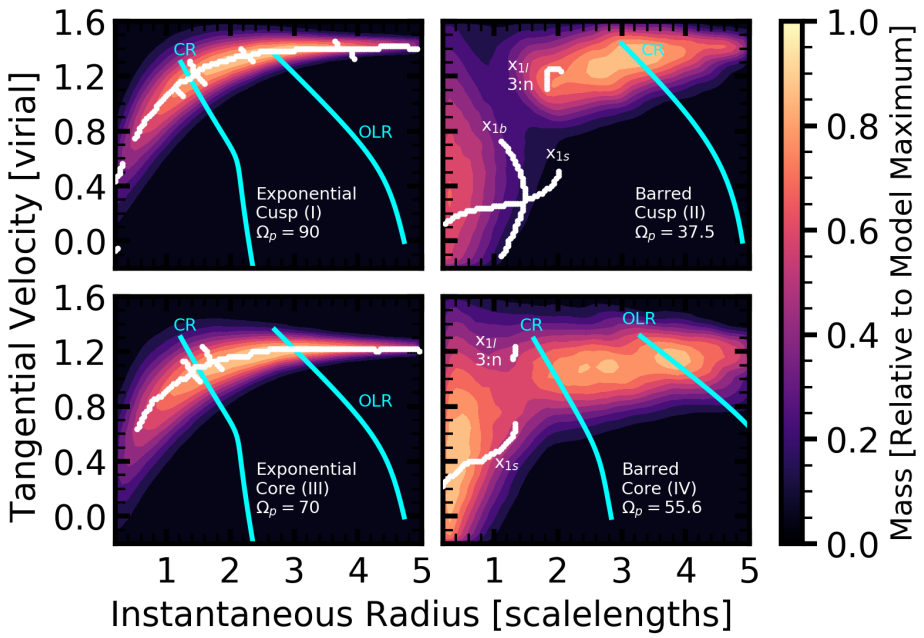

Figure 3.10. Instantaneous tangential velocity, calculated as $v_T = (x\dot{y} - y\dot{x})/R$ versus instantaneous radius, drawn from the corresponding self-consistent cusp simulation. The color map is the mass relative to the maximum mass at the same radius R in the (v_T, R) plane, for the four potential models. Overlaid on each are the traced commensurabilities from Figure 3.4, including assumed values of Ω_p for the exponential models.

to orbit family switching, so-called chaos (Chirikov 1979; for an example of a similar mechanism at work in radial migration see Sellwood & Binney 2002). In this case the 3:n commensurability serves as a conduit by which orbits can join the x_{1l} family, which in turn can transfer orbits to the x_{1s} family. No such channel exists in the barred core case as the phase-space region where the 3:n and x_{1l} orbits overlap is not populated (cf. Figure 3.9). We will see in Section 3.5 that the lack of such a channel is illustrative of the dynamical state of a barred galaxy.

3.4 Application to Observations

In this section, we describe the tools presented in the context of observations and observational interpretation. The fixed potential analysis is useful for making direct inferences

about the presence of different commensurabilities in observed galaxies, while comparison with the self-consistent simulations provides a diagnostic with which to understand the dynamical status of a barred galaxy.

The fixed potential integrations presented here form a bridge between analytic potential study and fully self-consistent simulations. Canonical works on the dynamics of a disc and halo system have relied on the use of potentials with separability, such that the actions can be directly calculated (see, for example, Binney & Tremaine (2008)). Thus, by and large, dynamical models that one fits to galaxies assume axisymmetry, which will automatically disagree with the findings presented here. Both classic and modern Milky Way potentials are largely assumed to be axisymmetric, in stark contrast to a multitude of observations indicating that the Milky Way is strongly barred (e.g. Bland-Hawthorn & Gerhard, 2016). Unfortunately, this means that we, as dynamicists, are reduced to studying careful simulations, having to convince ourselves of their validity and the validity of the inferences that we make. Therefore, a connection between self-consistent simulations and analytic understanding will reduce this tension. The fixed potential clearly has an incredible utility for determining orbital structure and provides a complete picture of the orbital structure in the system. In a future application, we can train orbit finding algorithms to detect complex, sparsely sampled members of the orbit library.

One may naturally wonder about the application of the theoretical technique presented here, in which orbits are averaged over a significant time window, to real galaxies. We select $R_{\rm apo} - V_{\rm apo}$ as our coordinates to aid future comparisons with future integral field unit (IFU) observations. In Figure 3.10, we show the stellar mass as a function of instantaneous tangential velocity and instantaneous radius computed from the phase space distribution of the particles in the self-consistent simulation. To normalize the density map, we find the maximum mass in $R_{\rm apo} - V_{\rm apo}$ space, set the value to be equal to 1 and scale all the other masses at the same radius accordingly. In contrast to the discussion in Section 3.3.3, here we use only the instantaneous information from the phase space distribution. We expect

that as we are selecting orbits at a random phase in their orbit, ascribing meaning to the observed mass density in $R_{\rm apo} - V_{\rm apo}$ space will be noisy. However, as orbits spend a larger fraction of their time near apocenter, the signal may not be as diluted as one feared, and direct comparison of instantaneous quantities and apocenter quantities may be undertaken.

The upper panels show the cusp potentials, with the exponential cusp potential (I) on the left and the barred cusp potential (II) on the right. Overlaid on each of the panels in white are the corresponding commensurability traces from Figure 3.4. The location of CR is particularly interesting as it relates to the mass distribution. The rotating exponential cusp model (I) places corotation at a smaller radius, $R_{\rm CR} = 1.3a$, than the peak of the mass distribution[7]. Both the rotating and non-rotating exponential cusp potentials admit a zero-order 3:2 frequency at $R_{\rm CR} = 2.6a$. We also note the 3:2 commensurability for its possible importance in shepherding orbits into the bar, as informed by the barred cusp model.

The barred cusp potential (II, the upper right panel of Figure 3.10) shows a number of features in the mass distribution that may be correlated with the commensurability traces. In particular, the bar resides within the maximum radius of the x_{1b} track, with the material at the end of the bar ($R = 1.8a$) bounded at the low radius end by the x_{1l} and 3:n orbits. The location of corotation is exterior to the peak of the mass distribution. Crucially, gaps in the mass density along the circular orbit track appear to be correlated with higher-order commensurabilities, suggesting that the regions of commensurability act as moderately repellant structures where orbits do not live for long periods of time.

For the exponential core (III, the lower left panel of Figure 3.10), like the exponential cusp, the bulk of the mass distribution lies along the empirically-determined circular orbit track (shown in white). The spread in the measured tangential velocity values (at a fixed radius), reflects non-circular motions in the self-consistent determination. As with the ex-

[7]The peak of the mass distribution, by definition, is $R = 2.2a$ for an exponential disc.

ponential cusp, corotation is interior to the peak of the mass distribution, at roughly the same radius, $R = 1.5a$.

More interesting is the mass density plot for the barred core model (IV), in the lower right panel of Figure 3.10. Here, the contrast with the barred cusp model is striking. The mass distribution is more continuous between the eccentric bar orbits ($R < 1.4a$) and the nearly circular orbits ($R > 1.4a$). Without the presence of an x_{1b} commensurability track, the bar is limited by the x_{1s} track. Additionally, the x_{1l} and 3:n commensurabilities, despite residing in nearly the same physical region of phase space, do not appear to control the structure of the mass density. Rather, that role is ceded to corotation, which meets the circular orbit track at $R = 2.0$, where a pile-up of orbits resides. We again see that higher-order resonances (in this case part of the 5:n series) cause a disruption in the circular orbit track at $R = 3a$. Orbits are largely too eccentric to take part in the OLR commensurability track.

Taken together, the barred cusp (II) and barred core (IV) models provide an opportunity to better understand which commensurabilities are be responsible for structure in barred galaxies. In both models, the x_1 family dominates the structure of the bar itself, with the location and extent of the mass distribution controlled by commensurabilities. The differences between the cusp and core models are significant enough to be discernible by an IFU with $\delta v \sim 10$ km s^{-1} velocity resolution targeting galaxies close enough to achieve $\delta R \sim 0.5$ kpc resolution. Even though we do not have sufficiently flexible models in this study to fully inform the orbital composition of real galaxies, IFU observations will provide important data for dynamical models by constructing the $R_{\rm apo} - V_{\rm apo}$ diagram. Such a diagram would be straightforward to construct using IFU data for a range of inclinations using a simple process: (i) transform the line-of-sight velocity distribution to x and y velocities, with the x axis aligned with the bar major axis, (ii) bin the position and velocity data by radius and velocity, (iii) plot the binned data in an $R_{\rm apo} - V_{\rm apo}$ plane. As shown in Figure 3.10, the features resulting from commensurabilities are discernable even without

knowing the true apocenter values. This is because the orbits spend proportionally more time at apocenter than at any other point in the orbit, leading to an effective weighted average. It is an open question whether this procedure will be more illuminating for stars or for gas. While the models presented here are stellar models only, the gas may more prominently reflect the closed orbits at resonances.

The features we discern in the IFU-like $R_{\rm apo} - V_{\rm apo}$ diagram suggest that the role of corotation is appreciably different between the barred cusp and core models, with corotation playing a large structure-controlling role in the barred core model, but having little effect in the barred cusp. Indeed, the large radius of corotation in the barred cusp model suggests that it plays a minimal role in the evolution at this time. The clearest diagnostic is the near-discontinuity in the mass distribution at the end of bar in the barred cusp model, while the barred core model maintains a track connecting bar and non-bar orbits.

That many of the orbits in the self-consisent simulation reside at considerable phase-space distance from true commensurabilities suggests that even in an apparently (slowly evolving) stable system, orbits can be distant from the true parent orbit. This in turn means that Schwarzshild orbit superposition (Schwarzschild, 1979; van der Marel et al., 1998) and made-to-measure (Syer & Tremaine, 1996; Dehnen, 2009; Morganti & Gerhard, 2012; Portail et al., 2015) models may not reveal the true structure in many observed galaxies, including the MW, owing to some combination of transients and the limitations discussed in the Section 3.5.3.

3.5 Self-Consistent Simulation Interpretation

In this section, we interpret the simulations through the lens of the fixed potential orbital structure in Sections 3.5.1 and 3.5.2, and also discuss the limitations of the methodology (Section 3.5.3). Owing to the caveats discussed elsewhere in this work, we do not expect this to be a final accounting of the processes at work in the simulation, but rather it provides a unique view that illuminates the effect of potential on orbital structure and

the relationship with the resultant evolution. The lessons learned from the fixed potential may be applied through time to disentagle some elements of bar formation and evolution in the self-consistent simulations. In particular, we are able to identify the appearance and disappearance of orbit families and correlate the appearance/disappearence events with milestones in the bar life cycle. The cusp and core simulations evolve in starkly different manners, yet adhere to similar phases given a similar orbit structure. We first walk through the evolution of the cusp simulation, Section 3.5.1, then the core simulation, Section 3.5.2, before we draw comparisons and contrasts between the two in Section 3.5.4. In each of the first two sections, we describe the overall evolution of the simulation before looking at the underlying orbital structure.

In each simulation, we identify three phases for the bar: (i) assembly, (ii) growth, and (iii) steady-state. While the assembly phase begins at roughly the same time for both models, the evolution rapidly diverges, as the assembly continues at a slower pace for the cusp model, before transitioning smoothly into the growth phase, then finally reaching a steady state at late times. The core simulation rapidly assembles, then hits a steady-state plateau. At late times, after subtle rearrangement of the mass distribution, the bar begins to grow again.

3.5.1 Cusp Simulation Evolution

In Figure 3.11, we illustrate the power of geometric commensurability finding to reveal different mechanisms at work in the cusp simulation. The upper panel shows the trapped fraction, computed at each simulation timestep as $N_{\rm family}/N_{\rm disc}$, in the two populations described in Section 3.2.2 versus time for the cusp simulation, in system units, using our k-means orbit classifier. We also include the subfamily of x_{1b} orbits as a dotted black line. The first population to appear are the blue other bar-supporting orbits, who exhibit clear $k = 2$ power but modest coherence in apsis locations, consistent with a standard picture of orbit apsis precession building the bar. With enough other bar-supporting orbits in place,

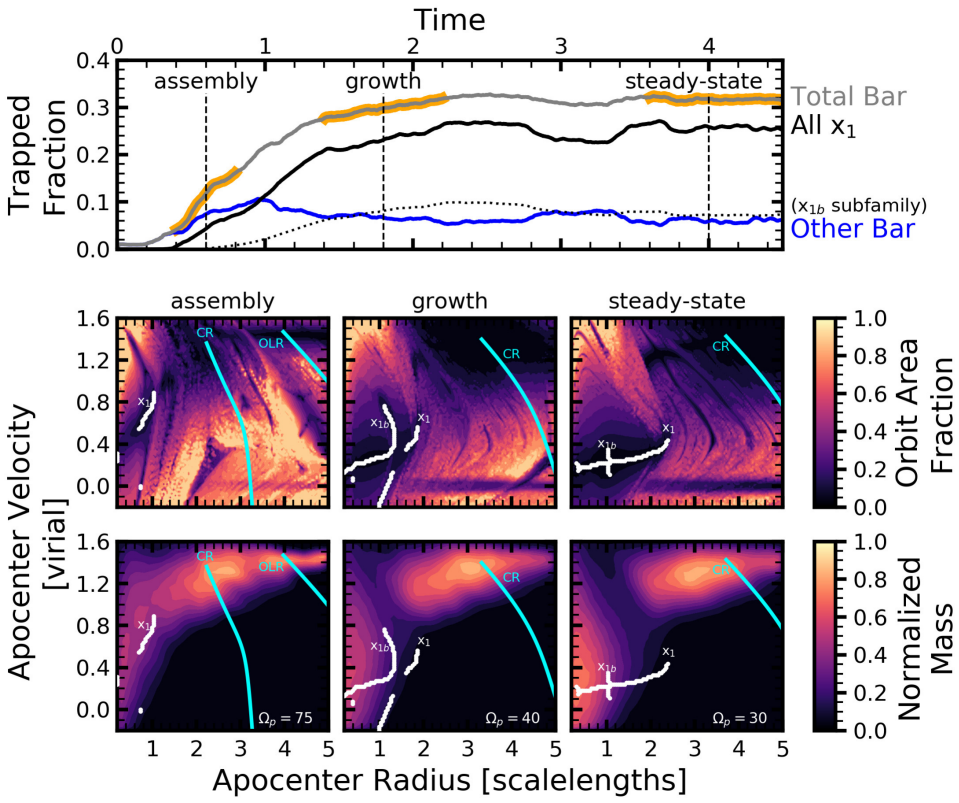

Figure 3.11. Upper panel: Disc trapped fraction versus time for the cusp simulation, in system units. The black line is the bar-parenting x_1 family, the blue line is a collection of other bar-supporting orbits that are not formally members of the x_1 family, and the thin dotted black line is are the orbits in the x_{1b} subfamily (a subset of the black line). The gray line in the upper panel is the sum of the black and blue lines, which is the total mass trapped in and supporting the bar. Three distinct epochs are highlighted: bar assembly (a), bar growth (b), and steady-state (c). A dashed line indicates the central time for each epoch, when we extract the corresponding potential from the self-consistent cusp simulation and construct an orbit atlas. Middle panels: Computation from the geometric algorithm at each of the times indicated in the upper panel as a function of $R_{\rm apo}$ and $V_{\rm apo}$. The color indicates A, the fraction of the area an orbit fills relative to a circle with the same radius as $R_{\rm apo}$. Strong commensurablities are marked and the evolutionary implications are described in the text. White lines correspond to geometric algorithm-calculated commensurabilities, and cyan lines correspond to monopole-calculated commensurabilities. Calculation details are in the text. Lower panels: Instantaneous tangential velocity, calculated as $v_T = (x\dot{y} - y\dot{x})/R$ versus instantaneous radius, drawn from the corresponding a, b, or c time during the simulation. The colormap is normalized relative to the peak mass of the disc. Overlaid on each are the traced commensurabilities as in the middle panels.

the x_1 family appears (the black line in Figure 3.11), first at $T = 0.4$. The two populations grow in tandem until $T = 1$, when the x_1 family begins to dominate. Eventually, the rapid assembly of the bar draws to a close at $T = 1.4$, and the x_1 orbits grow at a slower rate until $T = 2.4$, during which time some other bar-supporting orbits are converted into x_1 orbits. The feature near $T = 3$ where the x_1 orbits experience a rapid decline before an eventual recovery owed to the settling of the bar into a final state as the bar stops slowing. The mechanism by which this occurs is addressed in Chapter 5.

The gray line in the upper panel of Figure 3.11 measures the total bar mass, here the sum of the x_1 and other bar supporting orbits. On this line, the three phases of bar evolution that we highlight are most apparent: bar assembly (a), bar growth (b), and steady-state (c). After the assembly and growth phases, the bar is 30 per cent of the entire disc population, in line with observational results.

The assembly phase of the bar is marked by nearly equal contributions from the x_1 family and other bar orbits. With the additional information provided by the commensurability map (panel a, the lower left of Figure 3.11), we see that the relative weakness of the x_1 family is expected, as the family is both truncated at approximately $1a$ and features a prominent break in the x_1 track, particularly as compared to the later panels b and c. Corotation, while present at $T = 0.6$, has begun to migrate outward substantially from its initial position ($R_{\mathrm{CR,\ T=0.0}} = 1.4a$, $R_{\mathrm{CR,\ T=0.6}} = 2.0a$), and has not yet reached the peak of the disc mass distribution. The outer disc, $R > 3a$, appears to be nearly untouched at this time.

The middle panels of Figure 3.11 are the results of extracting the potential at the times labelled in the upper panel of Figure 3.11 and integrating the standard initial grid described in Section 3.2.4.1, constructing an orbit atlas. As in Figure 3.4, the color in the middle panels indicates A, the fraction of the area an orbit fills relative to a circle with the same radius as R_{apo}, as calculated in Section 3.2.5. Thebottom panels are similar to those in Figure 3.10 but at the labelled times. When present, we mark in the lower panels of Figure 3.11 the bar-parenting family x_1, the bifurcation of the bar-parenting family x_{1b}, and

the location of corotation orbits, CR, following the procedure in Section 3.2.5. Many other weak higher-order m:n resonances are present, in particular in panel (b), indicative of a rich resonant structure. The differences in the lower panels reveal the mechanisms behind the three distinct phases. During bar assembly, panel (a), the location of the families in $R_{\rm apo} - V_{\rm apo}$ space changes rapidly, resulting in discontinuities and weak resonances. While the bar grows, panel (b), prominent x_1 and x_{1b} families are present, and a large density of resonances at the end of the bar ($R_{\rm apo} \geq 2a$ and $V_{\rm apo} \geq 1$) and near corotation continue to feed the growth. During the growth period, the fraction of x_{1b}/x_1 orbits consistently increases, to a maximum fraction of 40 per cent. When the bar has reached a steady state, panel (c), the resonant tracks have become more well defined but sparse, and the bar orbits have settled into a lower-energy x_1 track as the x_{1b} track has disappeared. Fewer resonances at the end of the bar and beyond causes the bar to no longer grow. As the structure in the barred cusp potential (II), shown in Figure 3.4 is for $T = 2$, we see similarities with the bar growth phase in Figure 3.11.

The correlation between bar growth and the presence of the x_{1b} orbits suggests that the bifurcated x_{1b} family may be an easier channel by which orbits join the bar. Indeed, inspection of the left panel of Figure 3.9 suggests that the x_{1b} family may simply cut through a more populated region of phase space, enabling the commensurability to more efficiently act as a resonant channel. Study of this mechanism via a torque-based analysis is addressed in Chapter 4.

The result from Section 3.3.1.3 where the $m \leq 2$ fixed potential experiment removing the x_{1b} family prompts us to develop another line of inquiry to investigate the role of $m > 2$ modes in the disc, their effect on the x_{1b} population, and the subsequent evolution of the model. In addition to allowing potential models to be easily calculated, EXP allows for easy manipulation of different basis functions so as to investigate the role of individual modes on the overall evolution. To this end, we perform a numerical experiment where we restrict the azimuthal orders in the disc to be $m \leq 2$, but at a point after the bar has already

formed. Using the cusp simulation, we duplicate the simulation at $T = 0.9$. Allowing the simulation to proceed, we suppress the $m > 2$ terms in the disc by applying an error function prefactor. The error function is centered at $T_{\rm off} = 1.2$ with a width $\delta T_{\rm off} = 0.12$, which corresponds to roughly two bar periods. The $m > 2$ coefficients are fully suppressed by $T = 1.5$. Construction of an orbit atlases at $T = 1.2$ and $T = 1.4$, when the prefactor on the $m > 2$ terms is 0.5 and 0.0 respectively, conclusively demonstrates that the x_{1b} family is not present when the model is restricted to the dipole and quadrupole terms. Further, the bar rapidly evolves to a new, shorter configuration rather than continuing to grow as in the unmodified cusp simulation. The probable interpretation of this experiment is that the $m = 4$ component of the potential is necessary for x_{1b} orbits to exist, and that these orbits are the main 'backbone' of the long bar, even though the x_{1l} orbits provide the principal observed length.

Identifying orbit families in self-consistent simulations takes on importance in the context of a MW study. Binney et al. (1991) interpreted observations of gas dynamics toward the center of the Milky Way to be the result of x_1 orbits and the x_2 family, eccentric orbits elongated perpendicular to the bar. While the non-bifurcated x_1 family becomes more eccentric as one moves inward, as noted by Binney et al. (1991), the x_{1b} family remains highly elongated even to the end of the bar, a point which may have observational implications for the MW. Additionally, although we have not discussed the x_2 orbits in this chapter, our method to compute trapping and the geometric algorithm are both perfectly suitable for the identification and classification of x_2 orbits.

3.5.2 Core Simulation Evolution

Some elements of the core simulation are similar to that of the cusp simulation, including the observations of multiple distinct phases of bar evolution. However, clear differences are observed within the distinct phases. In particular, the presence of an unstable steady-state phase for the bar evolution is obvious in the core simulation. As in Figure 3.11, the

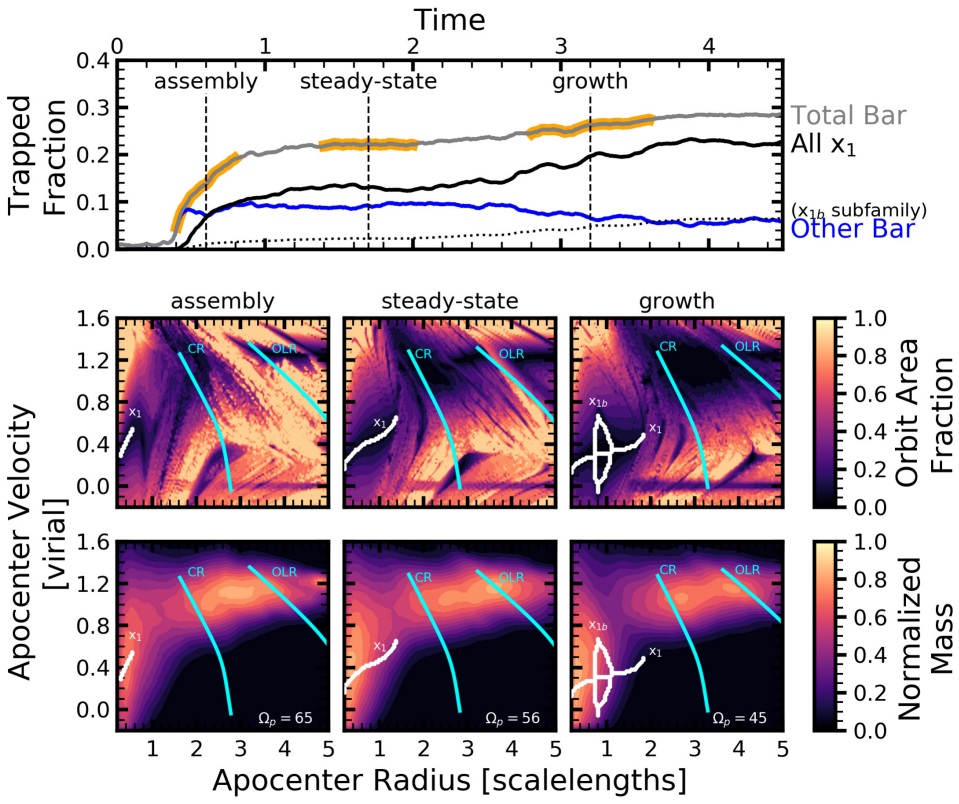

Figure 3.12. Upper panel: Disc trapped fraction versus time for the core simulation, in system units. The colors are as in Figure 3.11. Three distinct epochs are highlighted: bar assembly (a), steady-state (b), and bar growth (c). In this simulation, the bar reaches an unstable steady state before growing further. A dashed line indicates the central time for each epoch, when we extract the corresponding potential from the self-consistent cusp simulation and construct an orbit atlas. Middle panels: Computation from the geometric algorithm at each of the times indicated in the upper panel as a function of $R_{\rm apo}$ and $V_{\rm apo}$ in white, with monopole-calculated commensurabilities marked in cyan. Colors and indicators are again as in Figure 3.11. Lower panels: Instantaneous velocity versus instantaneous radius for the corresponding times a, b, and c. The commensurability tracks from the middle panels are overlaid.

gray line in the upper panel of Figure 3.12 measures the total bar mass. However, in this simulation as labelled, while bar assembly is (a), a steady-state is seen in (b) and bar growth in phase (c). After the assembly and growth phases, the bar is 28 per cent of the entire disc population, still in line with observational results. However, for a substantial fraction of time during the simulation, the bar is <25 per cent of the total disc population.

The bar assembly phase, marked as 'a' in the upper panel of Figure 3.12, begins at roughly the same time as in the cusp simulation, $T = 0.4$. However, the x_1 family, shown in black, has already begun to dominate the bar mass fraction by $T = 0.6$, when we make the first orbit atlas (panel 'a' in the bottom of Figure 3.12). Despite the relative mass equality between x_1 orbits and other bar orbits, the orbit atlas does not show a prominent, contiguous x_1 track, instead it is broken by the presence of an additional higher-order bar-related commensurability at $R = 0.8a$.

After $T = 0.6$, instead of the other bar orbits (blue line) being converted to x_1 orbits, the two populations remain distinct until $T = 2.4$. Having reached a definitive steady state at $T = 1.4$, one would be excused for believing the evolution in the system was complete, but one entire time unit later at $T = 2.4$, the x_1 family begins growing, and converts some of the other bar orbits into x_1 members (labelled as 'b' in the upper panel of Figure 3.12; the orbit atlas processed with the geometric algorithm is shown in the bottom middle panel). From $2.4 < T < 3.8$ the bar grows, in much the same manner as the bar growth phase in the cusp simulation. We label this phase 'c', and calculate the commensurability map from the orbit atlas in the bottom right panel of Figure 3.12. During this time period, the fraction of x_{1b}/x_1 orbits begins increasing, from 15 per cent of the x_1 family to a maximum fraction of 30 per cent.

The commensurability map for the unstable steady-state phase, panel 'b' in the lower center of Figure 3.12, bears resemblence to the steady-state evolution of the cusp simulation (panel c in Figure 3.11), particularly in the resonant density. The strong resonances parenting the x_1 family and corotation are clearly observable, as well as several other higher-order

resonances. By comparison to the right panel of Figure 3.9, which is near to panel b in simulation time, we see that the phase space near the resonances is not populated. However, in panel c, the lower right of Figure 3.12, we see a rich resonant structure, akin to that during the bar growth phase in the cusp simulation. The higher-order resonances have swept into the bulk of the phase-space density in the simulation, which is not particularly different in footprint from Figure 3.9. Additionally, the x_{1b} family has appeared within the bar radius.

3.5.3 Limitations of Fixed Potential Analysis

While we have presented snapshots in this study of evolving barred galaxies, the orbits themselves evolve with time. Thus, our results are restricted at present to a description of the times we have chosen to study in depth and the dynamics they illustrate; future work will attempt to create a cohesive look through time at the changing orbital structure, using the same technique.

The commensurability tracks risk overinterpretation of both self-consistent models and observations. A comparison between Figures 3.4, 3.9, and 3.10 suggests that many of the higher order features in Figure 3.4 may not truly exist in the self-consistent simulation owing to system evolution. Further, we noted subtle but important differences between the fixed potential and self-consistent orbits in Section 3.3.3, indicating that the fixed potential orbits are missing some dynamical degree of freedom that will limit the applicability to both self-consistent simulations and observations. The culprit is likely a time-dependent feature that was excluded in order to make the fixed potential integration stable: (1) odd azimuthal modes, (2) modal interplay and/or multiple pattern speeds, and (3) a frozen noise spectra.

Inspection of orbits drawn from the self-consistent time series suggest that x_1 orbits are robust against inclusion of odd modes in the self-consistent simulation, so it is likely not simply the inclusion of the odd azimuthal modes that will create the observed behavior. Based on a reconstruction of the perturbing $m = 1$ disturbance, the peak of the response

is at $R < a$, and thus, not likely to be changing the orbital structure in the outer disc more than the inner disc. To test the role of modal interplay, we have integrated potential models where the azimuthal series only included the monopole $m = 0$ and the quadrupole $m = 2$ as a representation of the bar. These models immediately disagree with the structure observed in the simulation. While this can be resolved by using analytic fits to an ellipsoidal bar model, we caution that these potential models are insufficient to recover the orbital structure of the self-consistent simulation. Additionally, all azimuthal harmonics $m > 0$ have the same pattern speed imposed, artificially curtailing any dynamical interaction between the modes. A future investigation will allow for variable pattern speed by azimuthal order. Lastly, it is possible that the choice of any single snapshot may freeze unwanted small-scale noise into the potential. While we believe that the self-consistent field technique will largely smooth out such aphysical fluctuations in the potential, particularly relative to other implementations of realistic frozen potentials, it is not guaranteed that our implementation of the potential is free of aphysical noise on small scales.

For all three concerns, the agreement in identified orbits between the k-means classifier of self-consistent orbits (Figure 3.2) and orbits integrated in the corresponding fixed potential (Figure 3.5) suggests that the possible negative effects are subdominant.

3.5.4 Summary

The differences in evolution between the two models are easy to describe and difficult to explain. Despite this, one can draw several simple conclusions from the comparison of the evolutionary status in the self-consistent simulation and the features in the commensurability maps:

1. Bar assembly is a multi-feature event. Attempts to construct the orbital atlas reveal complex structure in the inner disc ($R < a$) that cannot be simply explained by the barred potential models examined in Section 3.3.

2. The bar growth phase in both the cusp and core simulations includes the presence of the x_{1b} family. The family is not present with prominence in either the bar assembly phase or a steady-state phase. While the two simulations do not comprise an even remotely exhaustive study of parameter space, the similarities in dynamical mechanisms, despite the apparent differences in evolution of the bar, presents an interesting explanation for an avenue of bar growth.

3. The steady state phase, whether stable (in the case of the cusp simulation), or unstable (in the case of the core simulation) is marked by less resonant density in the commensurability map.

4. Despite all that can be gleaned from the commensurability map, it is still limited in its utility as a population diagnostic, and must instead be used in tandem with other diagnostics to fully interpret simulations.

3.6 Conclusion

In this chapter, we present a new geometric algorithm with which to identify commensurabilities in arbitrary potentials to help elucidate their orbit family structure. The geometric algorithm generalizes fixed potential studies to evolving potentials. We apply the algorithm to two self-consistent simulations (the cusp and the core simulation), from which we select four potentials (at $T = 0$, $T = 2$ for each simulation), corresponding to six total models (including testing $T = 0$ at two different values of Ω_p), to learn about the commensurability structure in Milky Way-like models. We fully characterize the orbit structure of the models and completely identify the commensurability structure.

Our main finding from the fixed potential analysis is that the study of realistic fixed potentials can provide a discriminating look at the orbit families admitted by different potential models, primarily delineated by the shape of the halo profile, allowing for differentiation between the underlying potential models by observing orbits in self-consistent

simulations. We also 'rediscover' the x_{1b} family of orbits, referred to as 1/1 orbits in the early literature, but largely excluded from recent potential studies. We demonstrate that the x_{1b} orbits are harbingers of bar growth. With the geometric algorithm, we are able to draw connections with self-consistent simulations and analytic works. In particular, we interpret previously identified epochs of bar evolution (assembly, growth, and steady state) using commensurability maps. The distinctions between different commensurability maps, such as the presence or absence of known key orbit families, have an apparent effect on the evolution of the barred galaxy, and may be used to assess its dynamical state.

We propose a simple new method to interpret IFU data by using a pseudo phase space, the $R_{\rm apo} - V_{\rm apo}$ (or $r - v$) plane. For external galaxies, different commensurability map models may be compared to the $R_{\rm apo} - V_{\rm apo}$ plane to ascertain whether the galaxy is near a dynamical equilibrium, based on the location of breaks and features in the $R_{\rm apo} - V_{\rm apo}$ plane (cf. Figure 3.10).

This methodology can be connected to observations of real orbits in the Milky Way. Work done in the near future will reveal more about the orbit structure of the inner Milky Way. We predict that if the Milky Way has either a cusped dark matter profile or an old bar, that x_{1b} orbits will be present. If observed, these orbits would be an indicator of long-term stability in the bar, as they comprise an extremely stable family in the self-consistent simulations. This work drastically improves upon previous studies of possible orbit structure in a Milky Way-like barred galaxy. In particular, popularly used potentials for the Milky Way, such as `MWPotential14` from `galpy` (Bovy, 2015), are known simplifications that meet only the most rudimentary requirements for matching the potential of the Milky Way. Here, we make little attempt to match the data for the Milky Way beyond scaling the system to match the virial units of the Milky Way, but rather seek to describe phenomena that may be prominent in observed barred galaxies, but have not been discussed in the literature.

Additional applications for this methodology include an extension to other non-separable realistic potentials, and studying the rate at which orbits transition between families (when coupled to self-consistent simulations). These rates could be connected to simple chemical models to attempt to explain chemically-distinct components of galaxies. In the future, we plan to extend the method to three dimensions and develop fit potentials for a range of realistic galaxies.

CHAPTER 4

USING ANGULAR MOMENTUM AND TORQUE TO UNDERSTAND BARRED GALAXY MODELS

4.1 Introduction

The transfer of angular momentum in galaxies gives rise to one of the most spectacular large-scale features of spiral galaxies: bars. The bar feature owes to a redistribution of angular momentum in the galaxy as it reorganizes stars from the exponential disc into an energetically preferable bar. Thus, a bar is both a manifestation of past evolution as well as a harbinger of possible evolution to come. Fundamentally, theorists have built their understanding of the disc-bar-halo system evolution through the transport of angular momentum, beginning with the seminal work of Lynden-Bell & Kalnajs (1972). It is, therefore, imperative to build our best understanding of the channels through which angular momentum transfer occurs through the multi-component disc-bar-halo system to determine the manner in which bars evolve.

Galaxy bars comprise a long-term (many Gyr) semi-stable (not completely stable owing to continued secular evolution) perturbation that serves to drain angular momentum from the disc. Because the bar is a negative angular momentum perturbation in the sense that it may transport angular momentum outward as a structure that trails the circular frequency (Kalnajs, 1971; Lynden-Bell & Kalnajs, 1972), the bar becomes stronger when it loses angular momentum, giving rise to the picture that bars grow, lengthen, and slow over the course of their evolution. The strength of the bar, therefore, depends on how efficiently the bar can shed angular momentum to willing sinks, such as the outer disc or dark matter halo. Canonical wisdom (Tremaine & Weinberg, 1984b; Weinberg, 1985; Hernquist & Weinberg,

1992; Athanassoula, 1996; Debattista & Sellwood, 1998, 2000; Athanassoula & Misiriotis, 2002; Athanassoula, 2003; Holley-Bockelmann et al., 2005; Sellwood, 2006) states that bars will slow their pattern speed Ω_p by depositing angular momentum into a spherical component such as the dark matter halo (a spherical bulge has also been demonstrated to be a viable sink for angular momentum, Saha et al. 2012). Thus, the key properties of bars are their length and pattern speed, both of which may be determined observationally (see examples of determining the length and strength of bars by stellar mass in Muñoz-Mateos et al. 2013 and see Tremaine & Weinberg 1984a for a method to determine bar pattern speeds). However, simulations indicate that the length and pattern speed of bars do not follow a simple trend that one can associate with age or evolutionary status, but are instead a complex combination of myriad parameters, primarily pertaining to the position-velocity phase-space distribution of mass in the total system. To make progress in understanding the secular evolution resulting from bars, we require a deeper understanding of the physical mechanisms that ultimately result in the observed features of barred galaxies.

Unique locations in the phase-space of a galaxy where an individual orbit may change its conserved quantities (energy, E, and angular momentum, $L_{\rm z}$) control the transfer of angular momentum. Those locations are resonances, where an orbit may gain or lose significant $L_{\rm z}$ over a handful of rotation periods owing to low-integer commensurabilities between orbital frequencies Ω, which we understand in the three cylindrical coordinates (r, ϕ, z), and Ω_p, the pattern speed of the global mode. The most well-known resonance is corotation (CR), where the orbital frequency Ω_ϕ equals that of the pattern Ω_p. More generally, resonant (or commensurate) orbits satisfy the equation

$$l_1\Omega_r + l_2\Omega_\phi + l_3\Omega_z = m\Omega_p, \tag{4.1}$$

where (l_1, l_2, l_3) is a triple of small integers (usually $l_{1,2,3} \leq 3$) and m is the multiplicity of the pattern, such that the quadrupole $m = 2$ corresponds to a bar or two-arm spiral. The phenomena is referred to as resonant coupling, where the disc transfers angular momentum

to the halo at resonances, and has been studied extensively in the literature (see e.g. Lynden-Bell & Kalnajs 1972; Tremaine & Weinberg 1984b; Hernquist & Weinberg 1992; Weinberg & Katz 2002; Ceverino & Klypin 2007; Weinberg & Katz 2007a,b). To an observer sitting on the bar, resonant (or commensurate) orbits trace closed, non-axisymmetric paths (we will refer to these as trapped orbits). Because the orbits are non-axisymmetric, they can be torqued by the bar. Once an orbit is trapped, its angular momentum L_z marches in lockstep with the slowing of the bar as the bar transfers angular momentum to the dark matter halo and/or outer disc. In this case, the changing bar pattern speed allows the pattern speed to sweep through frequency space such that new orbits satisfy the resonant equation and become trapped. Generally, to trap into a self-gravitating pattern, one of the quantities in the pattern must be changing, such as the angular momentum (which is directly related to the pattern speed), or the geometry of the bar. The collective pattern continues to slow as more orbits trap, at a rate that is not rapid enough to release stars from their stable commensurate orbits (though we explore this assumed mechanism in this work, which may not be absolutely correct or complete).

The ability to understand the transfer of angular momentum that drives the observed features has previously been confined to the realm of analytic calculations, which suffer from necessary idealizations (e.g. fixed bar pattern speeds, small amplitude perturbations), and n-body simulations, which are fraught with their own uncertainties (numerical precision, prescriptive evolution for processes below resolution limits), and oftentimes have little ability to definitively implicate the mechanisms observed in analytic calculations as the cause of the n-body features. Owing to the time-static nature of observations in the real universe, understanding the transfer of angular momentum via observations, no matter how sophisticated, is all but intractable. We choose to use n-body simulations to study this angular momentum transfer because analytic theory can only inform in the linear regime (owing to its lack of time dependence, see Weinberg 2004 for some progress), yet galaxy evolution contains many non-linear processes, even for isolated disc galaxies, as the trapping into pat-

terns is inherently non-linear. Hence, a modern picture of bar dynamics must move beyond analytic theory limitations to explore and explain the rich non-linear processes that occur in real barred galaxy evolution. The earliest live halo work (Sellwood, 1980) indicated that processes beyond simple linear theory were involved in angular momentum transfer, as evidenced by the observed slowdown of bars (Sellwood, 1981), subsequently bolstered by the calculations of (Tremaine & Weinberg, 1984b; Weinberg, 1985). The ensuing decades have both confirmed the applicability of linear theory in many cases, but simulations have consistently demonstrated a panoply of mechanisms that are not clearly interpreted via linear theory (examples include bar buckling instabilities and bar destruction). The primary culprit in the breakdown of the analytic linear theory is likely the assumed validity of the averaging theorem, i.e. time averaging over many orbital times, as compared to the real universe, where orbits (stars) may complete only tens of rotation periods during a Hubble time, and the potential may secularly change at a rate comparable to the orbital period of individual stars, to make no mention of other changing quantities in the galaxy (e.g. mass accretion, satellite harrassment).

In Chapter 1, we presented a new manifestation of the standard dynamical mechanism that forms stellar bars, the trapping of the dark matter halo component, which we call the shadow bar, and detailed its impact on secular evolution. We extend the rudimentary angular momentum transfer analysis presented in Chapter 1 in this chapter to provide the theoretical underpinning for the evolution of an n-body simulation. It is imperative to develop a mechanistic understanding of this important fundamental physics to build confidence in the physical validity of numerical models as large simulations continue to be the primary means to inform observations. We analyze how the simulations presented in this chapter may be connected with the analytic frameworks, and where the comparison of analytic and numerical interpretations falls short. Chapter 3 describes the underlying orbital structure and the importance of different potential features, primarily $m = 4$, for barred galaxy evolution. Chapter 5 describes a harmonic analysis interpretation of barred galaxy models.

Additionally in Chapter 3, we demonstrated a method to decompose sets of orbit trajectories into trapped and non-trapped orbits. In this work, we build on this orbit-based analysis to study the angular momentum transfer properties of different orbit families. Using an n-body simulation, Athanassoula & Misiriotis (2002) integrated orbits in a fixed potential using a procedure similar to that of Chapter 3, demonstrating in specialized cases that the slowdown of the bar was the result of a loss of angular momentum from orbits near resonances in the inner disc. The angular momentum was absorbed by orbits near the same resonances in the halo, with possible observable effects for breaking halo axisymmetry (Chapter 2). In this chapter, we are now in a position to extend the fixed potential approach to a fully self-consistent simulation and analyze the transfer of angular momentum that is a consequence of temporal evolution, an underexplored aspect of barred galaxy model evolution, allowing an opportunity to study nonlinear effects. We explicitly show how angular momentum moves through two example simulated barred galaxies. We elucidate the torque mechanisms through careful accounting of the angular momentum budget and a systematic study of the applied forces for each individual orbit. We connect the mechanisms to observables through studying the gross properties of the trapped orbits, their phase-space distribution, the change in angular momentum of individual orbits, and the torques applied by different dynamically-relevant ensembles of material.

This chapter is organised as follows. In the next section, Section 6.2, we present our methodology, describing the initial conditions and n-body integration technique in Section 6.2.1, and relevant analysis tools in Section 4.2.2. The gross properties of the bar and its evolution are described in Section 4.3, including an observationally-motivated look at the simulations in Section 4.3.1. We track the angular momentum transfer for orbits in Section 4.4, first by looking at the change in angular momentum for individual particles, then by looking at the applied torque. Section 7.5 contextualizes the results and its implications for galaxy evolution and discusses a potential application to integral field unit (IFU) observations. We conclude in Section 7.6.

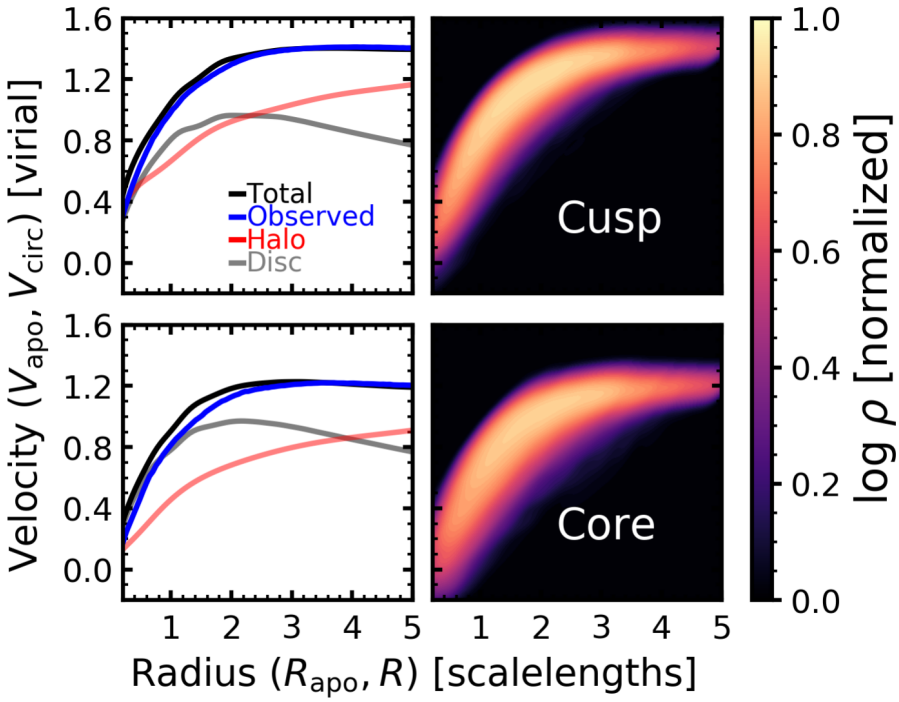

Figure 4.1. Initial conditions for the two simulations. The upper two panels are for the cusp simulation, while the lower two panels are for the core simulation. In the upper panels (the cusp simulation), we plot the decomposition of the circular velocity curve in the left panel, with the disc in gray, the contribution from the halo in red, the total in black, and the 'observed' circular velocity in blue (quantified as the azimuthally-averaged tangential velocity computed directly). In the right panel, we plot the log density computed directly from the particles using their apocenter radius, $R_{\rm apo}$, and corresponding tangential velocity at apocenter, $V_{\rm apo}$. We normalize the density such that the peak of the density distribution has a value of 1. The lower panels show the same quantities for the core simulation.

4.2 Methods

4.2.1 n-body Simulations

The simulations explored here were described in detail in Chapter 3. For completeness, we describe the realization of the initial conditions and integration only briefly here. We study two model galaxies, called the 'cusp' and the 'core' simulations for the shape of the halo profile, described below. Both model galaxies are made up of a stellar disc ($N_{\rm disc} = 10^6$) and dark matter halo ($N_{\rm halo} = 10^7$).

For the dark matter halo, we use a ΛCDM-motivated Navarro-Frenk-White Navarro et al. (1997) motivated halo model in our simulation with $\rho_{\rm halo}(r) \propto (r + r_c)^{-1}(r + r_s)^{-2}$, where r_s is the scale radius, defined by the concentration parameter $c = R_{\rm vir}/r_s = 20$ and $R_{\rm vir}$ is the virial radius of the halo. The difference between the simulations lies in the value of r_c, the halo core radius. The galaxy model with $r_c = 0$ has a $\rho \propto r^{-1}$ cusp that persists to the center of the model and is, therefore, called the 'cusp' simulation. The galaxy model with $r_c = 0.02$ has a halo density profile that flattens to $\rho \propto {\rm constant}$ towards the center of the model, resulting in a harmonic core. We call this model the 'core' simulation. While a cuspy halo has been shown in other studies to retard or limit bar formation–with limited theoretical support–we find, similar to Polyachenko et al. (2016), that bar formation occurs in a cuspy halo potential[1].

We model the stellar disc as a three-dimensional exponential of the form

$$\rho_{\rm disc}(r, z) = \frac{M_{\rm disc}}{2\pi a^2} \exp\left(\frac{-r}{a}\right) {\rm sech}^2\left(\frac{z}{z_0}\right) \tag{4.2}$$

where $M_{\rm disc} = 0.025 M_{\rm vir}$ is the total mass of the disc, $a = 0.01 R_{\rm vir}$ is the scale length, and $z_0 = 0.001 R_{\rm vir} = 0.1a$ is the scale height for the isothermal vertical distribution described by the ${\rm sech}^2$ distribution. We set the velocities in the halo by an Eddington inversion of

[1]There are regions of disc-to-halo mass parameter space where a bar cannot form in a cuspy halo potential, but will form in an equivalent mass cored halo potential, but this is a specialized regime that is unlikely to be probed.

the distribution function, and by solving the Jeans equations for the disc. The Toomre Q parameter sets the radial velocity dispersion in the disc, $\sigma_r^2(r) = 3.36\Sigma(r)Q\Omega_r(r)^{-1}$, where $\Sigma(r)$ is the surface density and Ω_r is the radial frequency. We set the velocity ellipsoid to be axisymmetric, e.g. $\sigma_r = \sigma_\phi$.

We do not include a bulge in the present models. A cursory exploration of bulge parameter space suggests that below a threshold in bulge-to-total mass, the bulge does not play an appreciable role in the evolution described here, i.e. for bulges less than 10 per cent of the stellar disc mass. We scale all units to so-called virial units with $G = 1$, i.e. $R_{\rm vir} = 1$ and $M_{\rm vir} = 1$, which describe the mass and radius of the halo in a ΛCDM cosmology. In physical units, if we take the halo mass to be that of the Milky Way, $M_{\rm vir} = 1.6 \times 10^{12} {\rm M}_\odot$ (Boylan-Kolchin et al., 2013), then the unit of time is 2.0 Gyr, the unit of length is 300 kpc, and the unit of velocity is 150 km s^{-1}. While the disc particles all have equal mass ($m_{\rm disc} = 2.5 \times 10^{-8}$), we assign the halo particles masses based on their initial radii, following a number density $n_{\rm halo} \propto r^\alpha$, where $\alpha = 2.5$. Using this 'multimass' scheme, the halo particle mass at radii $r < 5a$ are equal to or smaller than the mass of disc particles, such that our multimass halo is equivalent to a halo with $N_{\rm halo,eff} = 10^9$.

The upper left panel of Figure 4.1 shows the total initial circular velocity curve for the cusp simulation calculated from the basis expansion potential field (black curve) using $v_c^2 = R\left(d\Phi_{\rm disc}/dR + d\Phi_{\rm halo}/dR\right)$ where Φ is the potential. We compute the contributions to the potential from the disc and halo separately, and show these results in gray and red, respectively. We plot the tangential velocity curve measured directly from the particle distribution in blue. Owing to noncircular motions, the measured tangential velocity curve and the calculated circular velocity curve do not match; the two curves only grow more discrepant as the simulation evolves, suggesting that the central portions of galaxy rotation curves with apparent non-axisymmetric structures should be regarded with caution. The upper right panel of Figure 4.1 shows the log density distribution of the particles, where particles have been placed on the radius-velocity plane by calculating their apocenter, $R_{\rm apo}$,

and the corresponding tangential velocity at apocenter, $V_{\rm apo}$. This plane will be discussed in more detail in Section 4.3.1. Briefly, it captures the non-circular motions of orbits at each radius. The lower panels of Figure 4.1 show the same circular velocity curve, decompositions, and log density as in the upper panel, except for the core simulation. Owing to the reduced mass from the dark matter halo, the rotation curve peaks at a lower maximum rotation speed. The initial discs are identical in density and profile between the two simulations. We introduce the $R_{\rm apo} - V_{\rm apo}$ plane as an observationally-relevant pseudo phase-space. In principle, the $R_{\rm apo} - V_{\rm apo}$ plane may be constructed from integral field unit (IFU) observations of galaxies, and comprises a more dynamically illuminating space with which to view galaxies.

We integrate orbits using the self-consistent field code EXP (Weinberg, 1999), which creates an orthonormal potential-density basis set whose lowest order profile matches that of the disc and halo exactly (we use a separate basis for the disc and halo). Particles are advanced using a leapfrog integrator. A more detailed description of the parameters of the simulation can be found in Chapter 3, and we describe the basis selection in Chapter 5. For relevance to the study presented here, we save each orbit position at every $\delta T = 0.002$, the master timestep. However, we integrate the disc orbits based on a timestep criteria defined in Chapter 1, allowing the disc timesteps to decrease in factors of two such that the smallest timestep may be up to 2^4 times smaller than the master timestep. In practice, over 90 per cent of the orbits are always in the smallest time step. At each intermediate timestep below the master timestep, the coefficients are partially accumulated for orbits that participate in the timestep to update the basis. We fully recompute all the basis coefficients at each master timestep. We recover the angular momentum flow analyses presented here at each individual timestep, which we use to eliminate artifacts that may otherwise be present in individual outputs. We find that owing to the evolution of the system, we require such a fine resolution of saved phase spaces to properly analyze the evolutionary phases, and in

particular the transition between evolutionary phases. We evolve the simulation for 5.2 time units. When scaled to the Milky Way, this is 9 Gyr of evolution.

4.2.2 Bar Identification

In the literature, identifying the bar has been partly a matter of taste. Motivated by observations, one could choose to call the entirety of the observed stellar elongated feature 'the bar'. However, this definition makes the strong assumption that all the orbits in the enclosed region are part of the bar, which we demonstrate to be false. Much analytic theory has shown that the backbone of the bar feature is a particular resonant orbit family (x_1 in the parlance of Contopoulos & Papayannopoulos 1980, see Binney & Tremaine 2008), parented by the inner Lindblad resonance (ILR). We call the orbits that are commensurate in a transformed (corotating) bar frame *trapped orbits* and refer to the ensemble of trapped orbits as *the bar*. We refer to orbits that linger near the potential minima created by the trapped orbits but are not commensurate as *dressing orbits*, as they 'dress' the trapped orbits by residing in the same location in physical space. Despite this lingering near the potential minima, these orbits do not gain or lose energy or angular momentum.

With a wealth of metrics to choose from, it might seem conceited to propose yet another method for identifying the bar. However, our technique is theoretically motivated by analytic commensurate orbit analysis (e.g. Sellwood & Wilkinson, 1993) and resonant evolution (e.g. Binney & Tremaine, 2008), allowing us to more accurately capture the relevant dynamical quantities for secular evolution. For this work, we identify the bar-supporting orbits to extract the potential of the bar, and also to identify the net angular momentum of the feature and its role in the transfer of angular momentum throughout the system. We examine orbits in the rotating frame of the bar, which reveals orbits commensurate with the pattern speed of the bar, Ω_p, i.e. orbits whose radial turning points (apsides) do not precess. We automate identification of the commensurate orbits using a k-means technique (Lloyd, 1982). We describe the full procedure in Chapter 3.

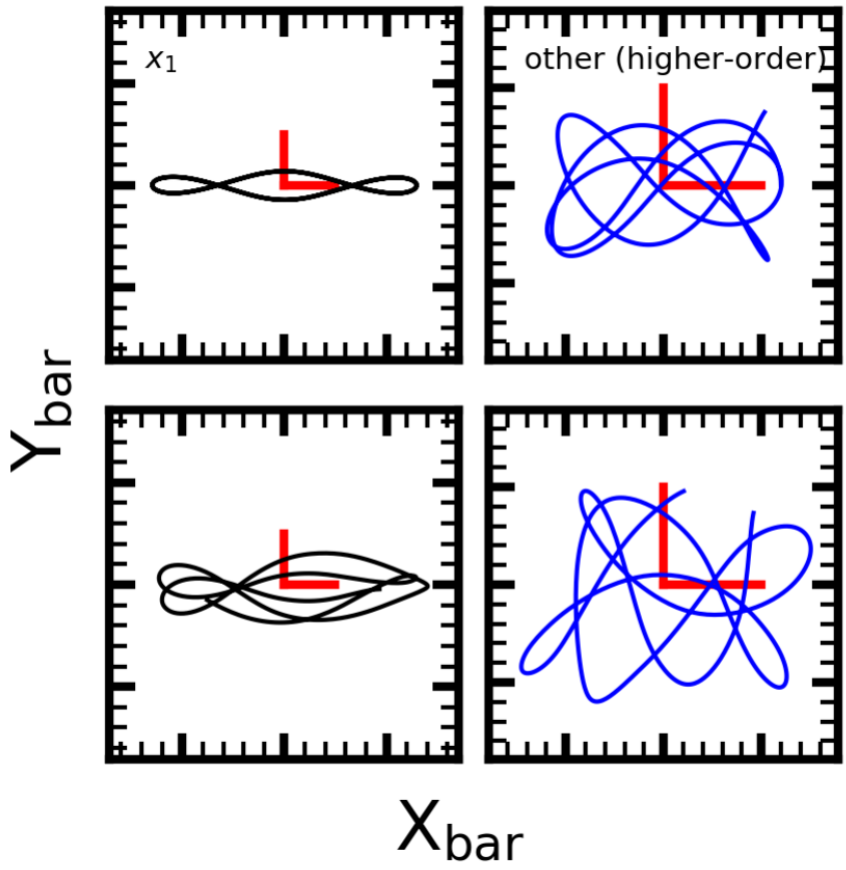

Figure 4.2. Example classified orbits. The upper panels show theoretical orbit family members drawn from a fixed potential extracted from the cusp simulation at $T = 2$, and integrated as in Chapter 3. The lower panels show orbits extracted from the self-consistent cusp simulation, highlighting the difficulty of obtaining family membership over small windows of time. The left column shows an x_1 orbit, while the right column shows an 'other' higher-order bar-supporting orbit, following the classification scheme used in this chapter.

Briefly, the k-means technique divides a collection of points into k clusters. In our implementation, for each orbit, we determine the position of all its apsides. We then transform the (x, y) coordinates for each apsis into the rotating bar frame, (x_b, y_b). At each apsis in the set, we make a series of the 20 nearest apsides in time, using the (x_b, y_b) positions to minimize the separation from k iteratively determined centroids. Once the centroids have been computed, we calculate the phase angle $\theta_k = \arctan\left(y_{\mathrm{centroid},k}/x_{\mathrm{centroid},k}\right)$. We define the maximum of the k values of θ_k to be $\langle \delta\theta_{\parallel} \rangle_{20}$, the deviation from the bar position angle for a set of 20 apsides. For determining bar membership, we restrict our analysis to $k = 2$. For each orbit in the simulation, at each apsis in time, we compute $\langle \delta\theta_{\parallel} \rangle_{20}$, $\delta\sigma_{R_{\mathrm{aps}}}$, and $\delta\sigma_{\theta,\parallel}$. Clear groupings emerge at late times when the bar is fully established, from which we empirically calibrate a matched filter to identify known orbit families. We describe the matched filter in detail in Chapter 3.

We define two key families for bar evolution: x_1 (and its associated subfamilies) and 'other' bar-supporting orbits. The x_1 orbits use the nomenclature consistent with classic orbit studies, e.g. Contopoulos & Grosbol (1989), while the other bar-supporting orbits reinforce the potential of the bar, but are distant enough from commensurate orbits such that their exact structure cannot be identified. The limits for membership in each family and the details of the classification process are given in Chapter 3. Once we have associated individual particles with the bar, a wide range of physically motivated quantites are made available. In later sections, we will make heavy use of this fact to help characterize the processes at play in the simulation. In Figure 4.2, we show example orbits drawn from the simulation and classified (lower panels) matched to a classified family nearby in phase space (upper panels). The left column shows an x_1 orbit and the right column shows a other bar supporting orbit. The x_1 orbit is the only classified family that clearly resembles its parent orbit; the other two have trajectories that are only reminiscient of the classifying family. However, when using the k-means apsis classifier, the other bar orbits are easily identified as having little precession in their apsides over extended time windows. The pri-

mary subfamily of the x_1 orbit identified in our work is the bifurcated x_{1b} family, which has dynamical importance as discussed in Chapter 3. We detail the methodology to determine membership in the x_{1b} subfamily in Chapter 3.

In this work, we draw upon the results of Chapter 3, where we mapped commensurabilities for the cusp and core simulations using two different techniques: a geometric algorithm to find strongly non-circular commensurate orbits, and a frequency map derived from the monopole potential to find corotation (CR) and the outer Lindblad resonance (OLR). Throughout this chapter, we will show commensurabilities determined via the geometric algorithm as white overlays, and commensurabilities determined via the frequency map as cyan overlays, and simply apply the results from Chapter 3 where applicable in this chapter. Where possible, we identify bar orbits in the x_1 family (parented by the ILR, including long period x_{1l} orbits and short-period x_{1s} orbits as well as bifurcated x_{1b} orbits), orbits that exhibit 3:n symmetry (where 3 corresponds to the number of radial oscillations per n rotation periods, in a frame co-rotating with the bar), orbits associated with CR, and orbits associated with OLR.

4.3 Simulation Gross Properties

In this section, we first describe the phase space distributions of the simulation in the observationally-motivated $R_{\rm apo} - V_{\rm apo}$ plane in Section 4.3.1. We then characterize the bar using a variety of dynamically-informative metrics in Section 4.3.2. In Section 4.3.3, we discuss and quantify the observed phenomena of previously trapped orbits leaving the bar.

However, we first present an overview of bar evolution in the simulations. As in Chapter 3, we identify three phases of evolution for the simulations, denoted by different epochs in the bar lifetime:

1. The bar *assembles* owing to a local dynamical instability.

2. The dynamical instability gives way to a secular instability where bar *growth* continues.

3. The bar evolution, and therefore the galaxy evolution, reaches a standstill, or *steady-state*. The steady-state may be stable or quasi-stable.

We use these three phases throughout the chapter to discover the mechanisms that control the evolution. In general, although all bars start with the assembly phase, the other two phases can proceed in any order and can occur more than once. The most well-understood of the three phases is the growth phase. The growth phase is the standard secular evolution phase, well-studied by perturbation theory. We largely find that known secular processes can explain evolution in the growth phase. The other two phases have been probed by simulations, but a satisfactory dynamical explanation has been lacking, in particular because self-consistent tracking of dynamical quantities has not been undertaken in a systemic manner. The inability to track dynamical quantities and their changes owing to nonlinear processes has limited the understanding of mechanisms in simulations. We, therefore, attempt to make progess by providing further information about the phase space and gross properties of the bar during these phases.

4.3.1 Phase-Space Distributions

We seek a simple, observational, description of the simulations that can be used to discriminate between the different evolutionary phases, yet still be connected to the underlying dynamics. To this end, we use the position-velocity plane defined by radius and circular velocity. This plane is well known as the standard rotation curve of galaxies. In our characterization, however, we move beyond the simple determination of azimuthally-averaged circular velocities to account for the dynamics contained in non-circular motions. More powerful is the radius-velocity plane where the quantities are tabulated at apocenter for individual orbits, $R_{\rm apo}$ and $V_{\rm apo}$, where $R_{\rm apo}$ is the apocenter radius of a given orbit, and $V_{\rm apo}$ is the tangential velocity at apocenter (where the radial velocity is, by definition,

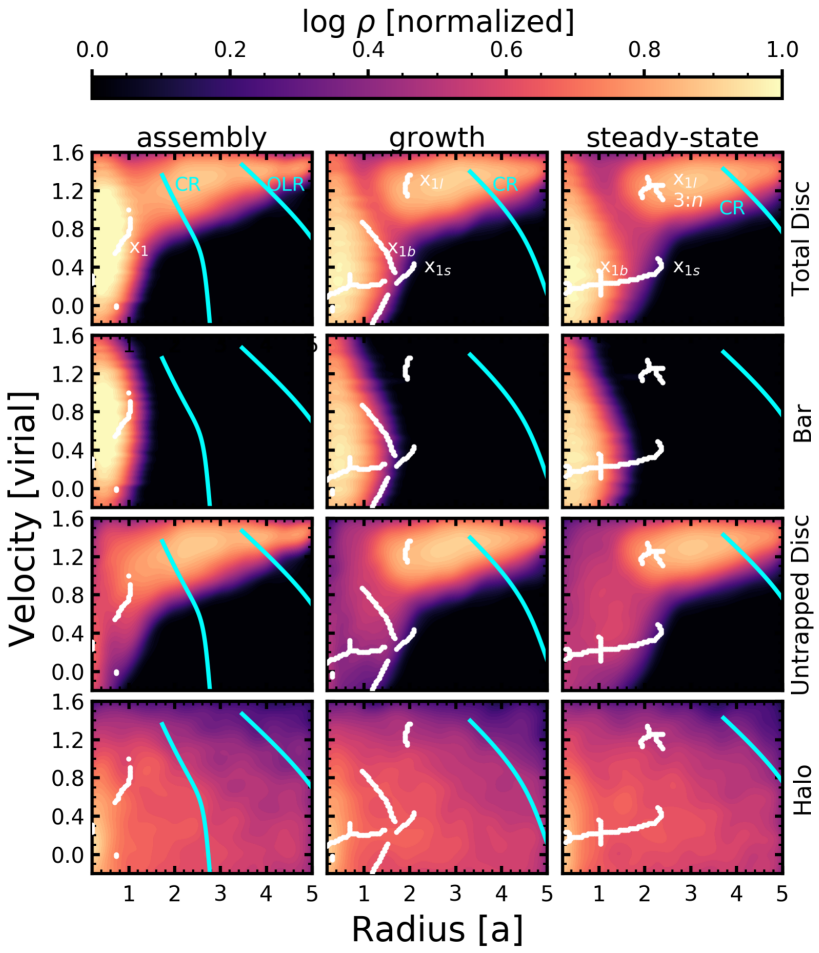

Figure 4.3. Log density for the cusp simulation in the $R_{\rm apo} - V_{\rm apo}$ plane, normalized to the peak in each panel, for four different ensembles of particles (total disc, bar, untrapped disc, and halo, top to bottom). The columns correspond to the observed epochs of evoluion, assembly (left column), growth (middle column), and steady-state (right column). For each column, we overlay the commensurabilities calculated and colored using the methodology described in Section 4.2.2 and Chapter 3. The main commensurate families are labelled in the upper row, and apply to every row in the corresponding column.

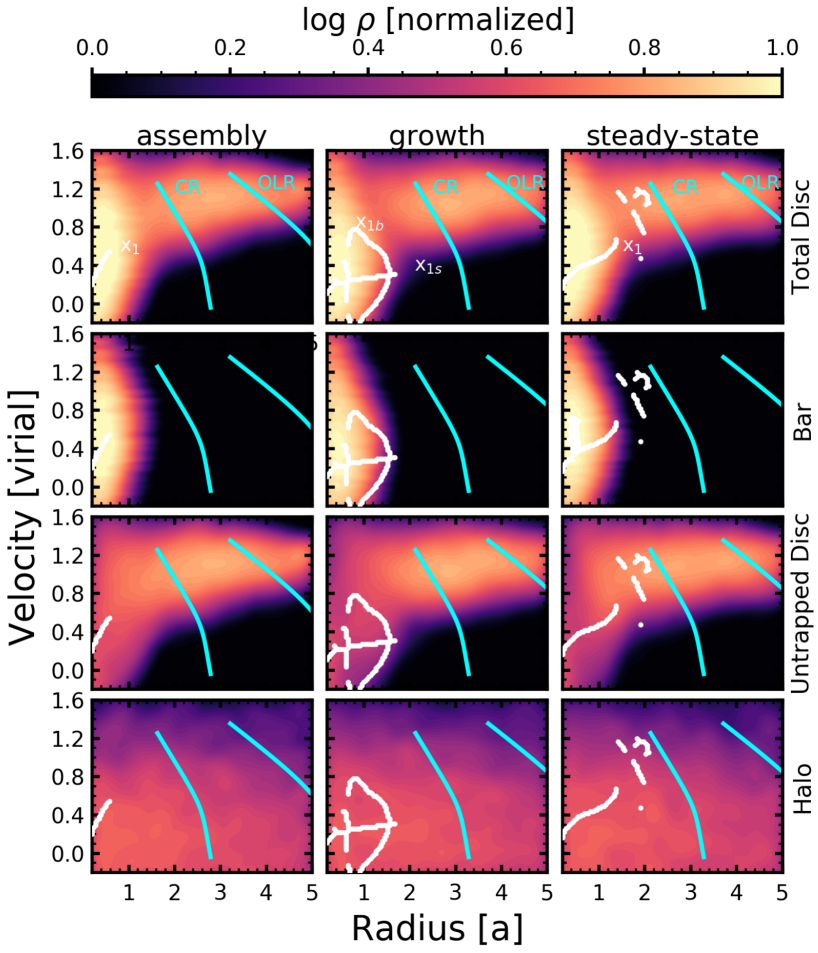

Figure 4.4. Same as Figure 4.3, but for the core simulation.

zero). Though not strictly a phase-space, $R_{\rm apo} - V_{\rm apo}$ gives a functional description of the distribution of particles in the simulation.

In Figure 4.3, we show the normalized log density from the cusp simulation in the $R_{\rm apo} - V_{\rm apo}$ plane for three components (bar, untrapped disc, and halo), as well as for the total disc (a combination of the bar and untrapped disc) during the three identified evolutionary phases (assembly, a; growth, b; steady-state, c). The normalization is the same across all panels in the figure, so that relative densities may be compared. We compute the density distributions using instantaneous values drawn from the simulation at the center of each epoch. Therefore, this is not the true $R_{\rm apo} - V_{\rm apo}$ space distribution. However, since linger near $R_{\rm apo}$ for a larger fraction of their trajectories, this distribution of radius and velocity is not too different from the true $R_{\rm apo} - V_{\rm apo}$ distribution. We, therefore, use the instantaneous radius and instantaneous planar tangential velocity $v_t = (x\dot{y} - y\dot{x})/(x^2 + y^2)$ to place orbits on the radius-velocity plane. For the rest of the work, when we refer to the radius-velocity plane, the velocity is the planar tangential velocity.

The upper row of Figure 4.3 shows the density distribution for the total disc at the three identified epochs. Additionally, we overlay the commensurability structure for the three epochs as mapped in Chapter 3. The changes between the assembly phase (a) and the growth phase (b) are stark, representing the rapid reorganization of the disc in response to the transfer of angular momentum. The observed changes, in particular the appearance of a valley in phase-space density between the bar and the bulk of the untrapped disc material, may provide observational hints of when a bar is dynamically young and still assembling.

We can break down the disc into the trapped bar (upper middle row of Figure 4.3) and untrapped disc (lower middle row of Figure 4.3) to see that the bar assembly process, which is ongoing in the left column, has not yet drawn a significant fraction of orbits out to a scalelength. The presence of untrapped material at radii smaller than a bar length lends support to our identification of dressed orbits (cf. Section 4.2.2), and the observationally confusing role they play in determining bar properties.

The velocity of the bar orbits decreases from an average velocity of $v_{\rm bar,assembly} = 0.75$ to $v_{\rm bar,growth} = 0.35$. In all three of the bar panels (upper middle panels), the average velocity of the bar is consistent with the velocity of the x_1 family. During the growth phase, the bar has consumed the majority of the material interior to $1.5a$, though some material remains to be trapped. The length of the bar is limited by the x_{1b} track identified in Chapter 3, rather than the extent of the x_1 track, suggesting that the x_{1b} family plays an important role in the dynamics of barred galaxies. We label the bifurcation of the x_1 family, the x_{1b} family, in the center upper middle panel of Figure 4.3. Curiously, untrapped material persists even during the steady-state phase (c) at similar radii and velocities to that of the bar.

The decomposition of the disc into the bar and untrapped components, when compared to the total disc radius-velocity distribution, reveals a clear divide in the location of particles in the steady-state phase. This gap might be used as an indicator of an evolved barred galaxy, where the orbits have been kinematically sorted by the bar. The halo, as an isotropic distribution, is less informative when mapped onto the radius–tangential velocity plane (lower panels of Figure 4.3). However, we can see a clear enhancement within a scalelength at non-zero velocity. Further, it is relevant to the dynamics that few halo orbits exist near what would be circular orbits for the disc, as those orbits are the halo orbits that preferntially take part in the angular momentum exchange. Clearly, the halo does not accumulate near the disc circular velocity curve, much less near the commensurabilities, making any deviation from the expected velocity distribution compelling to examine. Below, we will use different metrics to explain the distribution of the halo density.

In Figure 4.4 we plot the same quantities for the core simulation. As we shall see below, a steady-state evolution epoch precedes the growth epoch in this model, but to facilitate the comparison of mechanisms which drive both epochs, we show the phases in the same order as in Figure 4.3. We note many similarities between the two simulations. During the assembly phase, the average velocity of bar particles is higher ($v_{\rm bar,assembly} = 0.45$) than

during the growth phase ($v_{\rm bar,growth} = 0.25$), but the change is much less significant than in the cusp simulation. Additionally, during the steady-state phase between the assembly and growth phases, the average velocity of bar particles is the same as during the assembly phase. As in the cusp simulation, during the growth phase, when the x_{1b} orbit family is present, the length of the bar coincides with the location of the bifurcation. We mark the location of the x_{1b} family in the right upper middle panel of Figure 4.4 (the x_{1b} family does not exist in the other identified epochs). As in Figure 4.3, we mark the approximate location of CR on the untrapped disc panels. The assembly and growth of the bar again occurs when CR is located in a region of high orbit density. However, unlike in the cusp simulation, CR is located in a region of high orbit density during the steady-state epoch as well. Also unlike in the cusp simulation, the total disc does not ever reach a clearly kinematically sorted state, consistent with our knowledge that the steady-state phase in the core simulation is an unstable equilibrium.

A clear difference between the cusp and core simulations is evident in the halo distribution. As the cored halo has appreciatly less mass in its interior, the dynamical effects that are observed in the cusped halo are less pronounced, if at all present. The velocity distribution appears to be skewed modestly positive at less than two scalelengths during all three phases, suggesting that the assembly of the bar dynamically alters the inner halo (Weinberg & Katz, 2002).

4.3.2 Bar Properties

In the following sections, we compute and describe the gross properties of the bar: the bar mass $M_{\rm bar}$, the bar angular momentum $L_{\rm z,bar}$, the radius that encloses 99 per cent of the bar mass, which we will refer to as the length of the bar $R_{\rm bar} \equiv R_{99}$, the moment of inertia of the bar $I_{\rm bar}$, and the pattern speed of the bar, Ω_p, computed from the ratio of bar angular momentum and bar moment of inertia $I_{\rm bar}$. Figures 4.5 and 4.6 shows the evolution of these gross properties for the important bar orbital families in the simulations. Each of

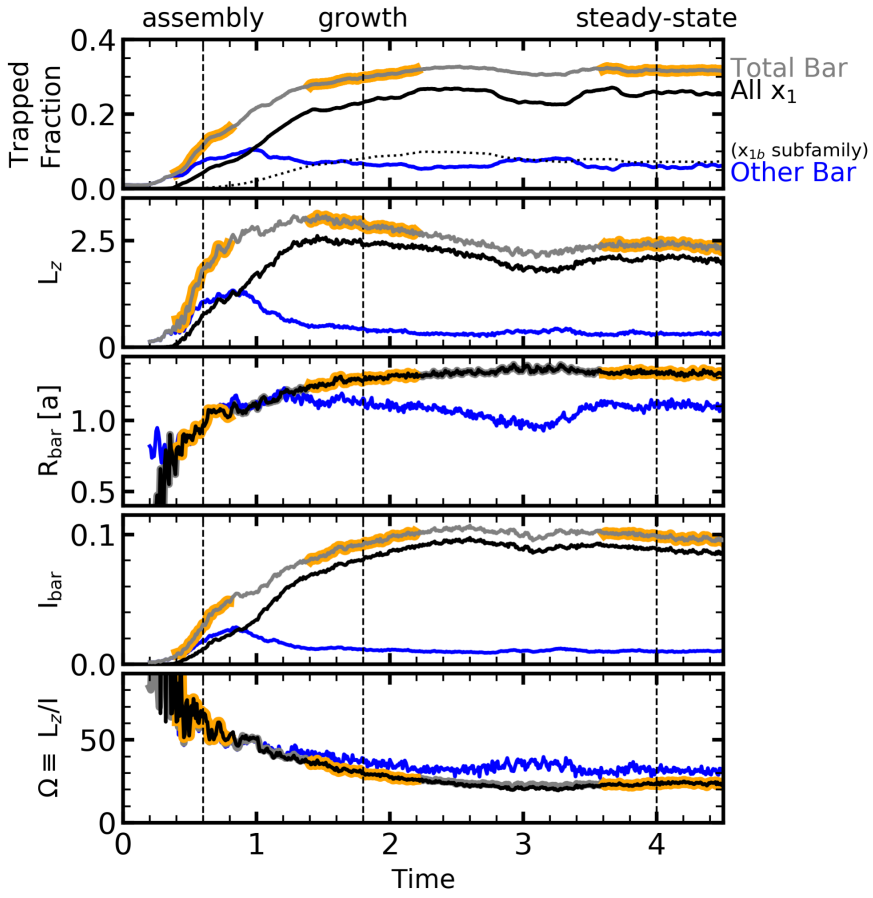

Figure 4.5. Bar property evolution in the cusp simulation. Top panel: Trapped fraction of disc orbits for two classifications: x_1 (black) and other bar orbits (blue). We additionally show the x_{1b} subfamily as a dotted line. The sum of the trapped fractions, comprising the total bar fraction, shown as a gray line. Three periods of bar evolution are defined: assembly, growth, and steady-state, labeled above the top panel. Upper middle panel: Total angular momentum in each component listed in the upper panel. Lower middle panel: $99^{\rm th}$ percentile radius for all members of each family. Bottom panel: Pattern speed, calculated as $\Omega \equiv L_z/I$, for each family. In each panel, we highlight the evolution of each quantity during the three epochs, drawing attention to the differences, primarily in the sign of the slope.

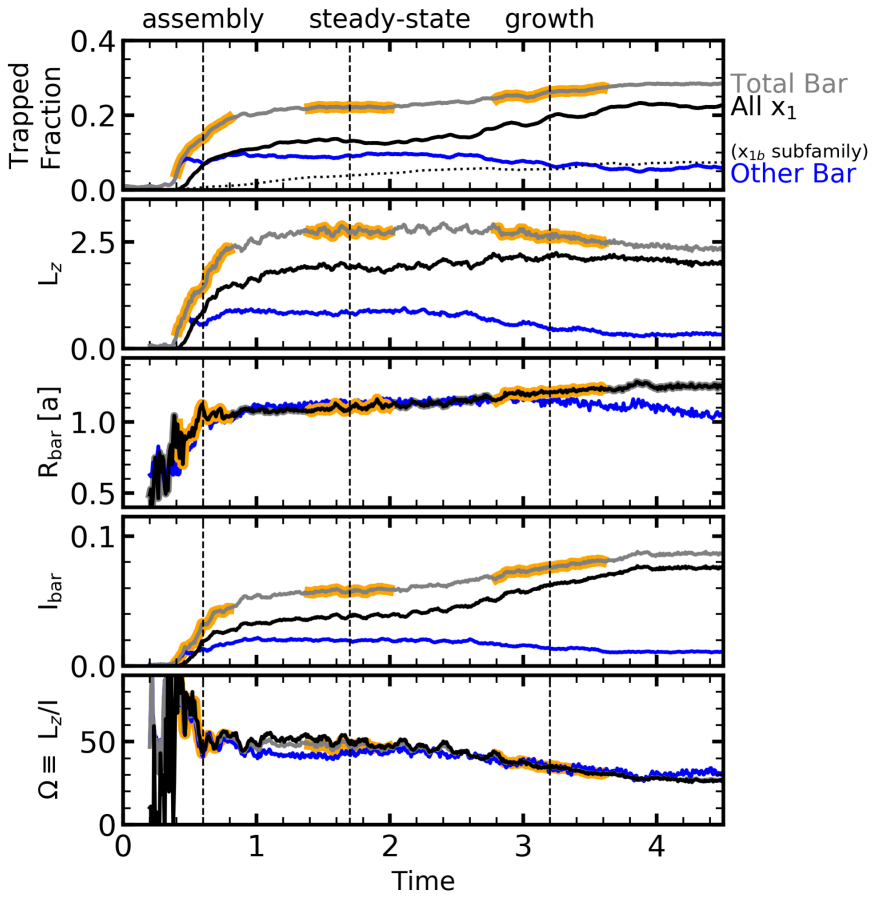

Figure 4.6. Angular momentum accounting for the bar in the core simulation. Panels and colors are the same as in Figure 4.5. The phases of bar evolution are in a different order in this simulation: assembly, then steady-state, and finally growth, as labeled above the top panel.

the quantities is dynamically revealing. Here we highlight relevant points in evolution for further dynamical investigation in Section 4.4. Generally speaking, changes to the sign of the slope in each quantity tend to represent a new era in evolution, though all are symptoms rather than underlying causes of the dynamical status–the causes will be discussed in Section 4.4.

4.3.2.1 Bar Mass

The trapped fraction of disc orbits, which is equivalent to the mass of the bar, defines the fraction of particles which satisfy the criteria to be members of the bar pattern. We measure three classes of orbits: orbits that either join together to make the bar, the x_1 family, are a subfamily of x_1 with dynamical importance (the x_{1b} subfamily), or otherwise support the bar directly as higher-order families (other bar supporting orbits). The combination of the x_1 family and other bar supporting orbits makes up what we call the total trapped bar orbits. We use the trapped fraction of the bar as the main descriptor for the evolutionary phases that occur in the simulation. As we shall see below when looking at phase-space distributions, and by the inspection of surface density plots, many untrapped orbits reside in the same physical regions of a galaxy, and would be considered part of the bar in a standard analysis, while they in fact do not participate in the dynamics in the same manner as trapped orbits, remaining distinct from the angular momentum transfer of the trapped bar orbits.

In the upper panels of Figure 4.5 and 4.6, we show the trapped fraction as a function of time for the x_1 family (solid black), including the x_{1b} subfamily (dotted black) and the other bar supporting orbits (solid blue). We sum the x_1 and other bar supporting orbits to make the solid gray line, the total trapped fraction of the bar. These panels clearly demonstrate the three evolutionary epochs of the bar.

In the cusp simulation, following the upper panel of Figure 4.5, the evolution proceeds in the order listed above: assembly, then growth, then steady-state. The core simulation (following the upper panel of Figure 4.6) exhibits all three modes, but upon conclusion

of the assembly phase, the galaxy is in an apparent steady-state phase of evolution, where evolution appears to be complete (but in reality progresses slowly), until finally the galaxy has been slowly reorganized to allow new families of stable orbits, principally the x_{1b} subfamily (cf. Chapter 3), to exist and the bar begins to grow again. Thus, in the upper panel of Figure 4.6, we see an assembly phase followed by an unstable steady-state phase, followed by a growth phase[2]. The simulation reaches a second stable steady-state phase at the end of the simulation, which we do not study in this work. Suffice it to say that the mechanisms are the same as in the steady-state epoch of the cusp simulation, as discussed below. In both simulations, an increase in x_{1b} orbits corresponds to a decrease in other bar orbits.

As we observe that the evolution of the two simulations proceed differently, we seek other explanations for why each model behaves as observed. This leads us to look at other metrics to understand the physics that governs the different evolutionary phases, and why the models behave differently after a bar has assembled.

4.3.2.2 Bar Angular Momentum

The upper middle panels of Figures 4.5 and 4.6 show the angular momentum that resides in each of the three tracked families from the upper panel. In the cusp simulation (the upper middle panel of Figure 4.5), the three evolutionary phases of the bar have clear trends in their total angular momentum. During the assembly phase, the bar rapidly accumulates angular momentum, as the mass of the bar increases (the specific angular momentum, or average angular momentum per bar particle, decreases). After the assembly phase concludes, the bar *loses* total angular momentum, even as it grows in mass, during the growth phase. This inflection point in the total $L_{\rm z}$ is reflected in the structure and evolution of the torque that is applied, as we will discuss below. During the steady-state phase, the bar

[2]Elsewhere in this chapter we display the core simulation phases in the same configuration as the cusp simulation phases (e.g. assembly, growth, steady-state) to ease comparison between dynamically similar phases, despite the fact that the primary steady-state phase in the core simulation precedes the growth phase.

does not add or subtract angular momentum, owing to a lack of favorable orbits available to be torqued and the lack of available phase-space in the halo or outer disc to accept angular momentum. Chapter 3 describes orbit families that may be more readily torqued, and Chapter 1 described the implications of reducing the available phase-space for angular momentum acceptance via secular evolution. The core simulation (the upper middle panel of Figure 4.6) reveals the same behavior as the cusp simulation, when one considers the evolutionary phase. The angular momentum grows during the assembly phase, decreases during the growth phase, and increases only slightly during the steady-state phase.

The total angular momentum of the bar is the most sensitive indicator of the evolutionary status in both models, as the sign of the slope changes between the assembly and growth phases, and does not change during the steady state.

4.3.2.3 Bar Length and Moment of Inertia

We understand the bar length and moment of inertia in tandem, as the observed trends are qualitatively similar, as plotted in the middle panels of Figures 4.5 and 4.6. We define the length of the bar to be the radius that encloses 99 per cent of the trapped orbit's apocenters. We eliminate the largest 1 per cent that may be spuriously determined to be trapped (consistent with our estimate for contamination in the trapping metric, cf. Chapter 3). This quantity tells us the radius that orbits primarily reside within, and is less confusing than using surface density plots, which may be biased by a relatively small number of orbits that linger near the end of the bar; so-called 'dressing' orbits that we will discuss below and in detail in Chapter 5. Unsurprisingly, the x_1 family has a longer length than the other bar orbits, with the 99th percentile reaching roughly 1.5 scalelengths during the steady-state phase of bar evolution.

R_{99} is an observable quantity given some velocity information (we present a method in Chapter 5), and is more robust than isophote fitting to low-amplitude noncircular variations. In the cusp simulation (the middle panel of Figure 4.5), the length of the x_1 family

increases rapidly during the assembly phase, continues increasing during the growth phase, and does not change during the steady-state phase. In the core simulation (the middle panel of Figure 4.6), we see the same behavior in the assembly and growth phases, but during the steady-state phase, the x_1 orbits increase modestly in length. This length change is reflected in the moment of inertia. The moment of inertia for an ensemble of particles is given by $I_{\rm family} = \sum_{i=1}^{N} m_i r_i^2$. We compute this quantity for the ensemble of orbits in each of the three families. The moment of inertia informs the geometry of the bar in a more nuanced way than the simple R_{99} length, but is more difficult to observe.

In the traditional view of bar-induced secular evolution, orbits trapped in the bar transfer $L_{\rm z}$ to the outer disc and elongate. As the moment of inertia grows steadily throughout the simulation, we conclude that the assembly of the bar proceeds as orbits preferentially join the end of the bar. Additionally, the ratio of the moment of inertia to the mass of the bar tells us how self-similarly the bar grows over time. An inspection of the mass and moment of inertia shows that the ratio M/I, which we refer to as the self-similarity index, changes throughout the simulation. A changing self-similarity index implies that the bar does not grow in a self-similar manner. Because of the non-self-similarity in the formation of the bar, we suspect that the transfer of $L_{\rm z}$ is more complex. By inspecting individual orbits, we see that the bar lengthens by trapping near orbits at larger radii. We are careful to point out that the lengthening of bars does not mean that individual orbits change their radial extent; rather that new orbits with larger apocenters join the bar, causing the bar to appear longer. The addition of orbits at the end of the bar was shown in Chapter 3, where the commensurability skeleton tracing ILR and identified maximal x_1 orbits continue to move to larger $R_{\rm apo}$ throughout the simulation.

The lower middle panels of Figures 4.5 and 4.6 show the quantity $I_{\rm family}$ for each of the families defined in the upper panel. For relevancy to the bar, we highlight the black curve, which corresponds to the x_1 orbits. The decrease of moment of inertia during the

steady-state phase results from the changing geometry of the bar, primarily related to the growth of a bulge.

In the core simulation (Figure 4.6) the moment of inertia for the x_1 family (black line) increases slightly during the steady-state phase, in contrast to the cusp simulation. This different behavior during the steady-state phase owes to the sustained evolution of the bar, which continues to grow as orbits change their geometry. Thus, during the steady-state phase, the self-similarity index M/I increases, rather than decreasing as in the cusp simulation. The difference in M/I behavior for the cusp and core simulations during the steady-state phases means that the apparent equilibria in bar growth are not as similar as they appear on the surface. Metrics discussed in later sections will shed more light on this difference. For the assembly and growth phases in both models, which behave roughly the same in M/I ratio for the x_1 family, we expect the increase during assembly, while the flat evolution of the M/I ratio during growth is a result of self-similar growth, as described above.

In both simulations, the moment of inertia drops as the fraction of x_{1b} orbits increases. By inspecting individual orbits we see that x_{1b} orbits are created by the conversion of other bar orbits into x_{1b} orbits, which has the additional effect of reducing the moment of inertia. The conversion happens preferentially for the other bar orbits with the largest radial extent, so the angular momentum in the other bar family drops rapidly.

4.3.2.4 Bar Pattern Speed

The collective rotation frequency of different orbit families can be computed from the angular momentum of that family and the moment of inertia of the orbits in the family, such that $\Omega_{\rm family} = L_{z,\rm family}/I_{\rm family}$. The bottom panels of Figures 4.5 and 4.6 show the tangential frequency for the three different orbital families.

For the x_1 orbits, $\Omega_{\rm x_1}$ provides an independent measure of the pattern speed of the bar Ω_p that does not depend on the global $m = 2$ response. However, we do find that $\Omega_{\rm x_1} \approx$

Ω_p, again suggesting that our robust quantification of the bar. For the other bar orbits, $\Omega_{\rm other}$ gives a measure of the higher-order structure of the bar not along the major axis. When compared with the total angular momentum of the bar (the upper middle panels of Figures 4.5 and 4.6), we can qualitatively understand how much of the angular momentum change owes to the changing geometry of the bar, and how much is lost to the outer disc or halo. We present a detailed study of these channels in Section 4.4.

In the cusp simulation (bottom panel of Figure 4.5), the rotation frequency of the x_1 orbits (and therefore of the primary bar component) decreases during both the assembly and growth phases before becoming constant during the steady-state phase. The other bar supporting orbits behave in a qualitatively similar manner, albeit at modestly different frequencies. The x_1 family of the core simulation (bottom panel of Figure 4.6) is qualitatively similar to the cusp simulation during the assembly and growth phases. However, the rotation frequency decreases slightly during the steady-state phase, again owing to the changing geometry of the bar. The other bar supporting orbits are consistent with a constant rotation frequency during the steady-state epoch, as in the cusp simulation during this same evolutionary epoch.

In summary, the gross properties of the bar are one way to compare the simulations with one another, and readily reveal the different phases of bar evolution. However, they are also difficult to obtain through observations as they are a product of several underlying quantities for individual orbits, which cannot be observationally resolved. We report and discuss them here in the hopes that the metrics could be used to compare different simulations, to understand the variety of physical mechanisms across simulation methodologies and their explored parameter spaces.

4.3.3 Untrapping

Formally, the secular capture of orbits is a two-way process, where the release of orbits from resonance is also possible (Binney & Tremaine, 2008; Daniel & Wyse, 2015). In our

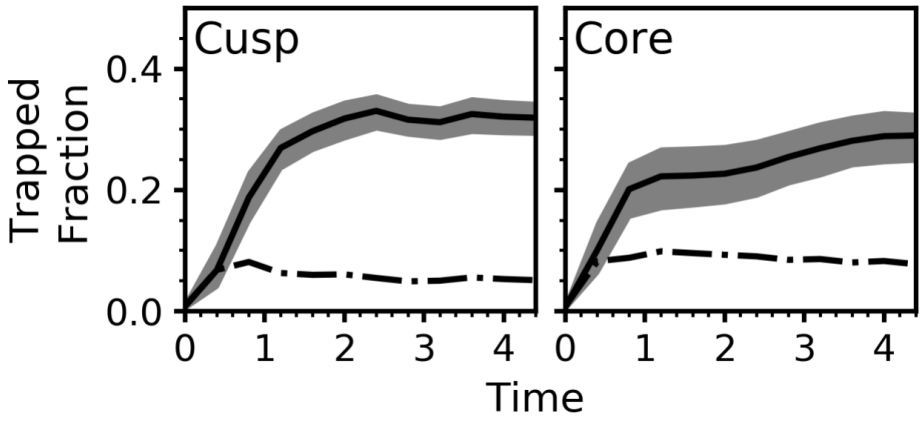

Figure 4.7. Bar trapped fraction versus time for the cusp simulation (left panel) and core simulation (right panel). The gray band shows the range of orbits that are trapped for at least 75 per cent of each bar rotation (lower bound) to the orbit fraction that is trapped for at least 25 per cent of each bar rotation (upper bound). The dot-dash black line is the difference between the upper and lower bound, a measure of the fraction of orbits that may be untrapped at any given time.

analysis of the simulations, we assumed that the fraction of orbits released from trapping has been negligible, such that once an orbit becomes trapped into the bar, it does not leave the bar. Our precise determination of membership in the bar at any given time enables us to make quantitative statements about the rate at which orbits may 'untrap'. Quantifying the frequency of untrapping has implications for observations of stars that are in the vicinity of the bar in the Milky Way, and whether stars born in the bar may be found outside of the bar at later times.

In the upper panels of Figures 4.5 and 4.6, we presented a simple total of the trapped orbits instantaneously at a given time in the simulation. However, this panel does not provide any information about whether the particles that become trapped remain trapped. To address this question, we define the fraction of time an orbit remains trapped in a chosen time window, ζ. We choose to define the quality of orbit trapping using the terms *fully trapped* and *loosely trapped*. Quantitatively, fully trapped orbits are those which, over a given time window, here chosen to be roughly a bar period ($\Delta T = 0.2$), are associated with a trapped family for $>$75 per cent of the window. Loosely trapped orbits are those

which over a given time window are associated with a trapped family for >25 per cent of the time, but less than 75 per cent. Qualitatively, we do not consider family switching to be untrapping, so an orbit that goes from x_1 to an 'other' bar supporting orbit or vice versa would not be considered untrapped.

Figure 4.7 shows the number of orbits that trap and untrap during both simulations, as defined by our fully and loosely trapped definitions. The left panel shows the bar trapped fraction for the cusp simulation in black. The gray region is the boundary of the orbits that are fully trapped (lower bound) to loosely trapped (upper bound). The dot-dashed line shows the difference between the fully and loosely bound orbits. The right panel is the same except for the core simulation. The figures demonstrate that approximately 6 per cent of the total disc (≈20 per cent of the bar) is loosely trapped in the cusp simulation, and 8 per cent (≈30 per cent of the bar) in the core simulation. At any given time, these percentages of orbits join and leave the bar. However, the instantaneous trapped line, shown in black, suggests that the population of orbits that are loosely trapped remains roughly constant with time. However, it is not as simple as a one-way channel, e.g. the orbits are not guaranteed to be loosely trapped before becoming fully trapped. In fact, in general, orbits rapidly become fully trapped when they join the bar, and a separate population of orbits that were previously fully trapped into the bar become a loosely trapped population. In terms of physical location, the loosely trapped orbits are located near the end of the bar, where the commensurability density is high. Note also that the core simulation always has a higher fraction of loosely trapped orbits relative to the instantaneously trapped orbits.

4.4 The Angular Momentum Economy

In this section, we partition orbits into different ensembles (stellar bar, untrapped disc, and dark matter halo) to examine the effect that each has on angular momentum transfer. We construct a phenomenological picture of the transfer of angular momentum between the stellar bar, untrapped disc, and dark matter halo. Each is connected to the other; determin-

ing the magnitude of the exchanges connecting the components sheds light on the process of angular momentum transfer in galaxies. Throughout both the dynamical and secular instability phases, angular momentum is rearranged, primarily between the outer disc and dark matter halo, catalyzed by the bar. The dark matter has a resultant wake, indicative of the transfer of angular momentum (Weinberg, 1985). The cusp and core simulations are more similar than different as regards angular momentum transfer mechanisms. Therefore, we describe the other transfer between the components and detail the differences in the simulations where applicable. The evolution of the disc observed in physical space results from of the redistribution of energy and angular momentum; in this section we explain the features observed in the $R_{\rm apo} - V_{\rm apo}$ plane as this will facilitate comparison to observational metrics.

4.4.1 $\mathbf{L}_z$ Accounting From Particles

The most straightforward method to track angular momentum through the simulation is to directly compute the change in angular momentum for individual particles. However, this approach is dominated by first-order secular changes in the angular momentum of individual particles as they complete orbits. However, we must perform averaging to allow first-order cancellation to see the underlying trends that represent the true change in conserved quantities. We look to cancel first order variations by (1) using a value for angular momentum derived over a radial period, (2) using a large number of particles, and (3) by placing the particles on the $R_{\rm apo} - V_{\rm apo}$ plane where features can be associated with resonances. However, we acknowledge that even so we might not remove all first-order effects as the first order effects can still act on timescales significantly longer than the orbital time near resonant degrees of freedom.

For the three windows corresponding to the evolutionary epochs defined in Section 4.3 (assembly, growth, steady-state), we compute the angular momentum $L_{\rm z} = (x\dot{y} - y\dot{x})/(x^2 + y^2)^{1/2}$ averaged over a radial period, which we write as $\langle L_{\rm z} \rangle_R$. We define the change in an-

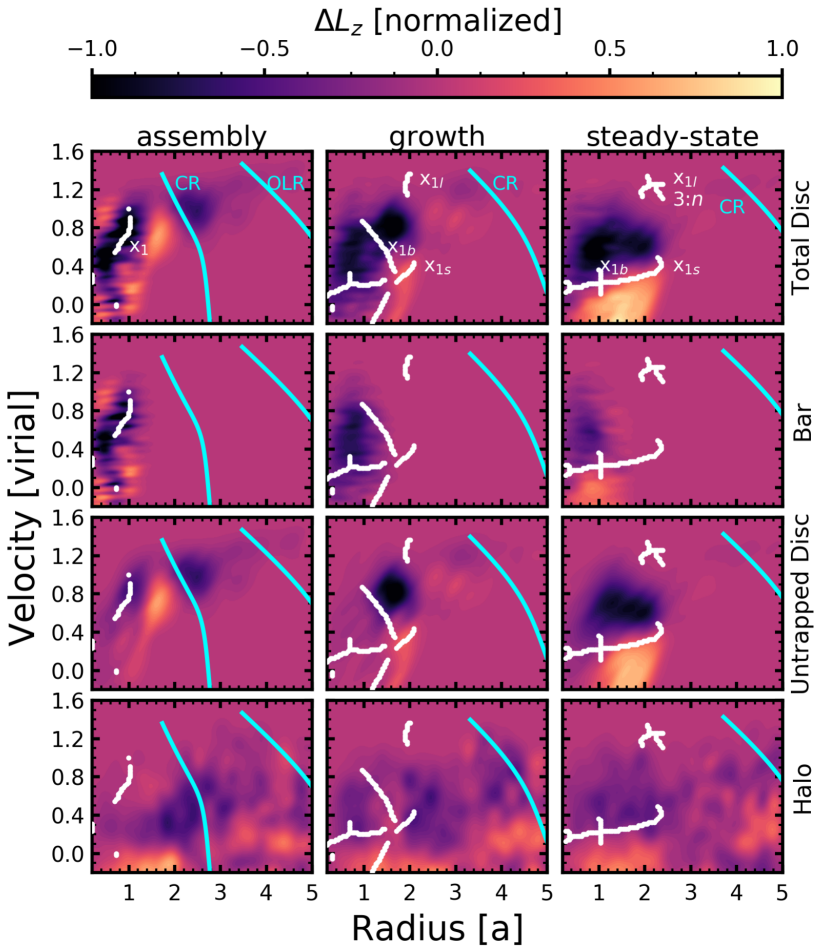

Figure 4.8. Transfer of angular momentum in the cusp simulation in $R_{\rm apo} - V_{\rm apo}$ space, as computed from finite differencing of ensembles of particles for the cusp simulation. All panels are normalized to the same angular momentum scale, where darker colors mean that the region of $R_{\rm apo} - V_{\rm apo}$ space lost angular momentum, and lighter colors mean the region gained angular momentum. Upper row: angular momentum change $\Delta L_{\rm z}$ for particles in the bar during assembly (left column), growth (middle column), and steady-state (right column). Middle row: same as upper row, except for the untrapped disc particles. Bottom row: same as upper row, except for the dark matter halo. As in Figure 4.3, the overlays in white and cyan show the commensurabilities identified at each timestep.

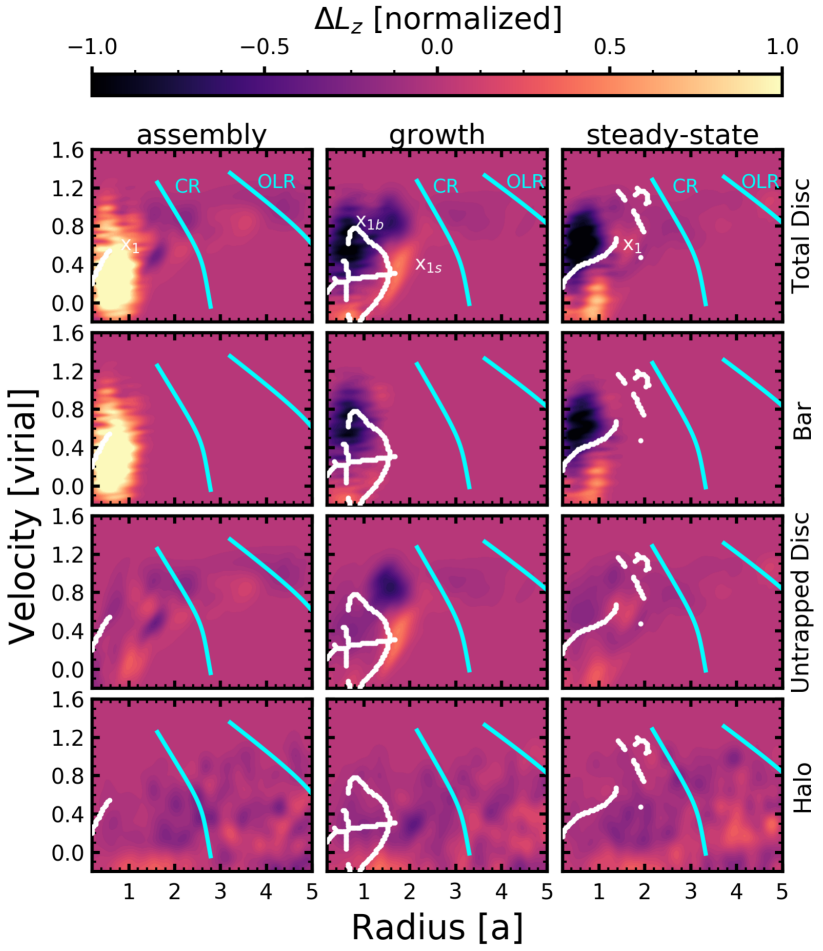

Figure 4.9. Similar to Figure 4.8, except transfer of angular momentum in the core simulation.

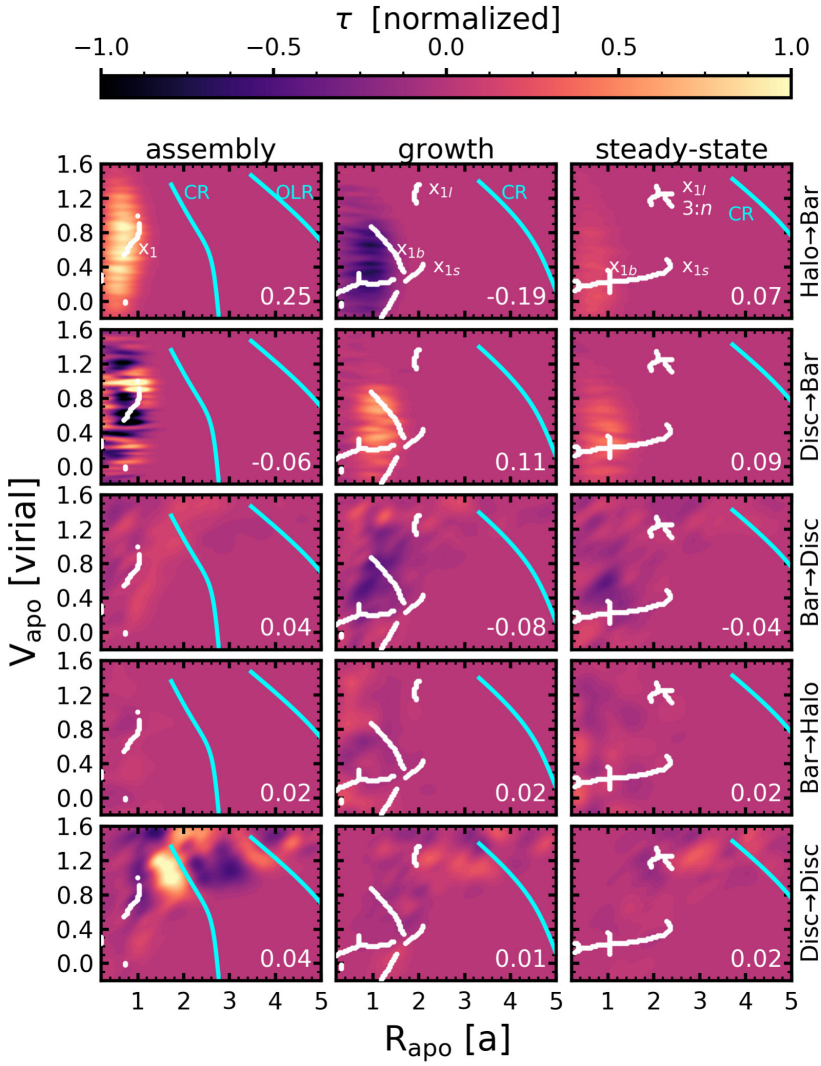

Figure 4.10. Instantaneous applied torque in $R_{\rm apo} - V_{\rm apo}$ space, as computed from the forces for the cusp simulation. Uppermost row: the torque applied by the halo to bar particles in the assembly phase (left column), growth phase (middle column), and steady-state (right column). Upper middle row: same as the uppermost row, except the torque applied to the bar by the disc particles. Middle row: same as the uppermost row, except the torque applied to the untrapped disc by the bar. Lower middle row: same as the uppermost row, except the torque applied to the halo by the bar. Bottom row: same as the uppermost row, except the torque applied to the disc by other untrapped disc particles. The corresponding commensurability structure has been overlaid on each panel, and relevant commensurabilities have been labeled where relevant. In the lower right corner of each panel, we report the mean torque per particle. The rows are organized from top to bottom by the relative importance of the channel for evolution.

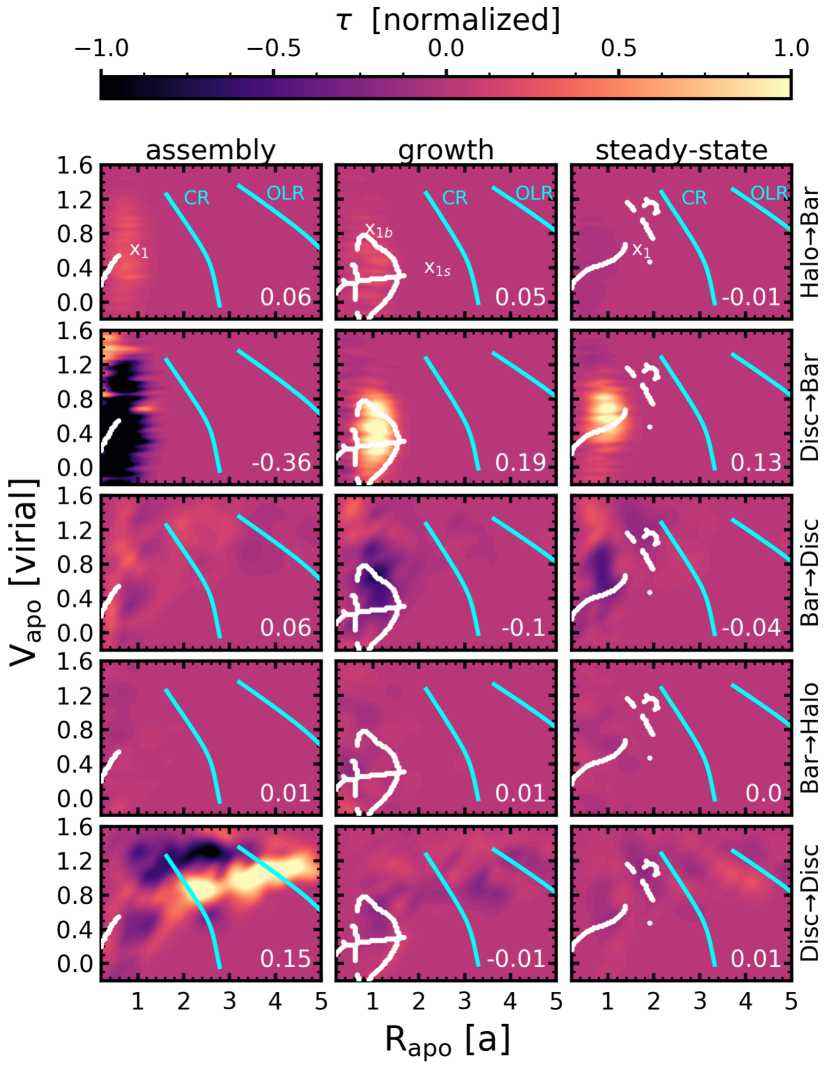

Figure 4.11. Similar to Figure 4.10, except for the core simulation. The row organization is the same, despite the diminished role of the halo, and the increased role of the disc in controlling evolution.

gular momentum for a given orbit as $\Delta L_{\rm z} \equiv \langle L_{\rm z} \rangle_{R,{\rm late}} - \langle L_{\rm z} \rangle_{R,{\rm early}}$, where the subscripts 'early' and 'late' indicate the *complete* radial periods closest to the beginning and end of the time windows, respectively. To maximize the interpretive power of the angular momentum transfer, we partition the orbits into bar, disc, and halo ensembles (we also show the total disc for its utility in observational comparisons). We describe the decomposition in Section 4.2.2. The density of the different components in the $R_{\rm apo} - V_{\rm apo}$ plane can be found in Figures 4.3 and 4.4, where we immediately observe that without the benefit of being able to decompose the disc into trapped and untrapped particles (which is not as straightforward as simply applying a radial cut, particularly owing to the existence of dressing orbits), the interpretation of our angular momentum tracking would be ambiguous at best.

In Figure 4.8, we show the transfer of angular momentum computed from the particles for the cusp simulation. As in Figure 4.3, we examine the angular momentum transfer during the three evolutionary epochs (assembly, growth, and steady-state), and for four ensembles of particles (total disc, bar/trapped disc, untrapped disc, halo). Unlike in Figure 4.3, we compute $R_{\rm apo}$ and $V_{\rm apo}$ for the orbits, making the placement of individual orbits in the plane less dispersed, and thus the signals stronger. We again normalize the total angular momentum change, but the scaling is the same between all the panels, so the colors may be directly compared. This is the total angular momentum, i.e. the sum of all the angular momentum lost by particles at that position in $R_{\rm apo} - V_{\rm apo}$ space. A comparison to the specific angular momentum change, e.g. $\Delta L_{\rm z}/M_{\rm R_{apo},V_{apo}}$ reveals the total change to be more informative for galaxy evolution.

The upper row of Figure 4.8 shows the change in angular momentum for all particles in the disc. The steady-state phase (c) is the most straightforward epoch to interpret. During this phase, the change in angular momentum is confined to particles within the maximum x_1 radius, $R_{\rm max\ x_1} \leq 2.5a$. The x_1 track splits the orbits that gain and the orbits that lose angular momentum, with the orbits that lose (gain) angular momentum being at higher (lower) velocities than the x_1 track. The magnitude of the gain and loss is nearly equal,

such that there is no net transfer of angular momentum in the disc. Orbits that lose angular momentum dominate the growth epoch, again located in $R_{\rm apo} - V_{\rm apo}$ space at higher velocities than the x_1 track. Of note, however, is the presence of the x_{1b} track, which passes directly through the angular momentum loss region. In this epoch, the loss of angular momentum in the disc outpaces the gain, so the disc loses angular momentum in net to the dark matter halo. During the assembly phase, the loss of angular momentum again outpaces the gain, meaning that angular momentum is still being lost to the halo. However, we also see a larger radii region of angular momentum loss, centered at $R = 2.4a$, which we attribute to CR, as determined via monopole resonance estimates. Clearly, during the assembly phase, CR is an important channel for angular momentum transfer, but its contribution to the bar evolution at later times becomes less important, including, surprisingly, during the growth phase.

The middle two rows of Figure 4.8 provide further insight into the transfer of angular momentum by breaking up the total disc into its bar trapped and untrapped components. In the upper middle panels, the trapped component is confined to smaller radii at all velocities, but also does not dominate the angular momentum transfer. Qualitatively, the trapped disc behaves the same was as the total disc, losing angular momentum during the assembly and growth phases, with its angular momentum remaining roughly constant during the steady-state phase. It is apparent that the commensurability structure controls the locations of angular momentum transfer, such that the x_1 and x_{1b} tracks act to provide barriers beyond which the angular momentum transfer either switches signs (in the case of x_1), or does not exist (in the case of x_{1b}). Comparing with the angular momentum versus time in Figure 4.5, where the angular momentum of the bar grows during the assembly phase, we can see that it is clearly dominated by the addition of new material, while for the material that is already trapped transfer to the dark matter halo has already begun. During the growth phase, the trapped orbits almost uniformly lose angular momentum, which is reflected in the overall angular momentum of the bar, even as mass is still being added. During the steady-state

phase, the low-velocity particles gain angular momentum to offset the angular momentum loss from high velocity particles, which is consistent with the net zero change seen during the steady-state phase in Figure 4.5 where no particles are being added to the bar and the angular momentum remains constant.

The untrapped disc panels of Figure 4.8 show how orbits may join the bar. In the assembly phase, orbits lose angular momentum both at the end of the fledgling x_1 track, and also at the location of CR. During the growth phase, orbits just outside of the x_{1b} rapidly lose angular momentum, fueling continued bar growth. In Chapter 3, we demonstrated that the primary channel for orbits to join the bar is by converting orbits spatially located near the end of the bar by passing through a 3:n family co-located with the long-period x_{1l} family at higher rotational velocities than the bulk of the bar. This channel makes up the bulk of the negative angular momentum seen near the end of the bar ($\sim 2a$) for the untrapped disc in Figures 4.8 and 4.9.

In the steady-state phase, both the bar and untrapped disc are angular momentum-neutral, gaining or losing angular momentum depending upon which side of the resonance the orbits exist. The x_1 track still acts as a transition point for which orbits gain and lose angular momentum, indicative of a 'leading-trailing' morphology where orbits at higher $V_{\rm apo}$ than the x_1 track exhibit a different morphology. Indeed, an inspection of x_{1b} orbits reveals that the y axis crossing point is located on one side of the x axis for leading orbits, and the other for trailing orbits[3].

In Figure 4.9, we show the transfer of angular momentum computed from the particles for the core simulation. The phases have been shuffled in time such that the growth and steady-state phases are shown as in Figure 4.8. The assembly phase in the core simulation is characterized by huge amounts of angular momentum *gain* in the total disc, which we can see by examination of the other rows comes from the trapped component. This is in

[3]Though not formally an x_{1b} orbit, the lower left panel of Figure 4.2 shows a y axis crossing point that is indicative of a leading or trailing orbit.

stark contrast to the cusp simulation. Thus, even though the assembly appears to be visually similar between the two models, the underlying process appears to be quite different. Looking closely for other differences in the assembly phase between the cusp and core models in Figures 4.5 and 4.6, we see that the ratio of x_1 to other bar orbits, as well as the geometry implied by the self-similarity index M/I ratio between the two families, appears in contrast between the two models. In particular, other bar supporting orbits dominate the cusp model until the end of the assembly phase, while the core transitions to being dominated by x_1 orbits at an earlier time. The increase in angular momentum for bar orbits in the core model during the assembly phase is likely related to the conversion of other bar supporting orbits into the longer x_1 family. The untrapped disc exhibits weak angular momentum transfer, likely related to the low phase-space density at the position-velocity locus of CR ($R_{\rm apo} = 2a$, $V_{\rm apo} = 1.2$, cf. phase-space density in Figure 4.4).

During the steady-state phase in the core model (right column of Figure 4.9), trapped particles dominate the change in angular momentum for disc particles, though there is no net transfer (cf. Figure 4.6 during the steady-state phase). As expected from our analysis of the cusp simulation, the x_1 track divides the orbits into those gaining and losing angular momentum based on their velocity relative to the x_1 track. The untrapped disc again transfers little angular momentum during the steady-state phase, as in the assembly phase (and unlike the steady-state phase of the cusp simulation, cf. Figure 4.5). However, some untrapped orbits that reside in the same region of $R_{\rm apo} - V_{\rm apo}$ space participate in the same angular momentum transfer as the bar particles, while not being clearly trapped. The growth phase of the core model (right column in Figure 4.9) exhibits essentially the same dynamical signatures as the growth phase of the cusp simulation (middle column in Figure 4.8): particles in both the trapped and untrapped bar participate in an exchange of angular momentum, with particles gaining (losing) angular momentum above (below) the x_1 track. The appearance of the x_{1b} bifurcation again divides the bar and untrapped disc particles. As in the cusp simulation, the angular momentum transfer exhibited by the halo

in $R_{\rm apo} - V_{\rm apo}$ space is ambiguous at best. Little-to-no angular momentum transfer occurs at the disc circular velocity at any given radius. In general, the angular momentum change for the cored halo is less everywhere compared to the cusp halo, reflective of the lower density in the halo at all radii relevant to the disc.

4.4.2 Torque Applied by the Field

The field quantities (e.g. density, forces, potential) at any given output time and for any given component are easily recovered with EXP[4]. Above, we discussed the utility of examining the emsemble quantities and examining the quantities for individual particles. Likewise, we can perform an analysis on the field quantities, and try to identify channels through which angular momentum travels. For angular momentum transfer (torque, τ), we can calculate the torque on any particle given the accumulated field as

$$\tau = \frac{dL_{\rm z}}{dt} = r \times \mathbf{F} = rF_{\theta}. \tag{4.3}$$

A self-consistent field code such as EXP allows us to easily track the forces throughout the simulation for any subset of particles[5]. We use this fact to determine the component of the force attributable to an ensemble of orbits. In turn, this allows us to trace the ensemble responsible for a given angular momentum transfer feature.

The instantaneous torque τ is a powerful indicator of dynamical evolution to come. However, during periods of transition, such as bar assembly, the value of τ at any point in $R_{\rm apo} - V_{\rm apo}$ space can change rapidly. Therefore, one must make predictions and find evolutionary implications in tandem with the density plots, which will in turn inform the

[4]The basis construction is a simple summation of the contribution of individual particles. Therefore, it can be partitioned into separate populations to calculate the self-gravity of particular features (e.g. the bar).

[5]While not formally explicit, the basis can be partitioned into subsets for which the coefficients of the basis functions can be partially accumulated. Owing to the conditioning of the basis on the underlying initial distribution, this partial accumulation results in very little noise in the reconstructed basis, within reasonable boundaries. We confine our subsets to be larger than 10 per cent of the total particles in a particular component.

expectations for the actual angular momentum transfer plots. Said another way, significant torque may be applied to one region of phase-space, and yet that region may not be populated. Similarly, we found in Chapter 3 that orbits known to be important for growing the bar, e.g. the 3:n family, were outside the bulk of phase space during periods of bar formation (cf. Figure 4.4).

Figures 4.10 and 4.11 show the torque, τ, evaluated instantaneously for each orbit in the simulation at their respective radius and tangential velocity, computed as above. In select places where relevant, we have noted the identified commensurabilities. The commensurability structure is the same through each column. We are interested in the torque induced on the untrapped disc by the bar, the bar by the untrapped disc, the untrapped disc by the halo, the bar by the halo, and the untrapped disc by the rest of the untrapped disc. We also inspected the remaining combinations (untrapped disc on the halo, halo on the disc, halo on the halo, and bar on the bar) and deemed them to be unimportant to and uninformative for the dynamics, classifying them as subdominant channels. This highlights the necessity of the bar as a mechanism to transfer angular momentum from the disc to the halo, as the disc is unable to efficiently torque or be torqued by the halo.

We plot each of the relevant channels in rows, at each of the evolutionary phases as columns in Figures 4.10 and 4.11. At the right edge of each column, we denote the component that is being acted upon by another component, e.g. the top row of Figure 4.10 is the torque applied to the bar by the halo. The channels are organized by importance from top to bottom, such that the halo torquing the bar is the most important channel for the bar evolution, followed by the disc torquing the bar. We quantify the importance of the channel by reporting the mean torque applied to particles in the lower right of each panel. The color bar is the normalized torque τ, and is the same in each panel. Negative torque means that the component applying the torque receives angular momentum from the component. Additionally, Figures 4.10 and 4.11 do not contain any information about the density in phase-space, and hence do not speak to the total torque applied or angular

momentum transfer observed in the simulation, but rather provides a tool with which to understand the detailed dynamics.

In the second row, where we plot the torque on the bar by the untrapped disc, we see that while assembly is a complex process, orbits at larger velocity than the x_1 track receive angular momentum which moves them toward the x_1 track. In an analogous plot exploring the torque applied to the bar by bar particles (not shown), we see an equally complex process, which we interpret as evidence for family switching within the bar, particularly for particles not near the x_1 track. During the growth and assembly phases, the disc applies a positive torque on the bar, transferring the bar angular momentum. This contrasts with what we observe for the gross properties of the bar in Figure 4.5, where the angular momentum of the bar decreases during the growth phase, and remains constant during the steady-state phase. Clearly, the torque applied on the bar by the disc is being offset by a different channel. In the case of the growth phase, the negative torque from the halo to outweighs the positive torque from the disc. However, during the steady-state phase the positive torque from the disc must be balanced by some other factor, such as orbital family switching.

The middle row of Figure 4.10 shows the torque applied on the untrapped disc by the halo. This is a channel where one might expect to see the effects of the induced halo wake. However, the radius–velocity plane is a complex way to examine the structure of the torque, and we see many features that only loosely correlate with the location of the identified commensurabilities. The clearest correlation occurs during the steady-state phase, where the halo applies a torque to the untrapped disc directly near CR[6], at $R_{\rm CR} = 3.5a$. Additionally, though subtle, the halo applies clear a torque along the x_{1b} track to the untrapped disc during the growth phase. This again shows the importance of the x_{1b} track for bar evolution, as described in Chapter 3. Furthermore, this may provide a mechanism for orbits to be

[6]The disagreement of the monopole-derived resonance locations and the regions where the dominant angular momentum transfer occurs demonstrates that one must move beyond classic secular evolution interpretations (e.g. passing through resonances) to recognize its complexity of the orbital and commensurability structure, and the implications for L_z in barred galaxies.

trapped from the disc by torques applied by the halo rather than needing to be torqued by the already-trapped bar particles.

One might expect that the torque on the halo by the bar would be illustrative. However, the torque applied by the bar is relatively small, and does not appear to correlate with any of the known commensurability features in $R_{\rm apo} - V_{\rm apo}$ space. The bar is unable to exact any significant rearrangement of angular momentum outside of the length of the bar, consistent with dynamical principles. This suggests that the bar does not directly change the dark matter halo significantly by applying torque, but rather the angular momentum that the halo accepts is a consequence of the torque it induces on the bar and untrapped disc. Additionally, one may naturally wonder whether the torque diagrams could be dominated by spurious first-order effects that exist on short enough timescales so as to be washed out during the evolution (some first-order effects do not actually cancel). To mitigate this concern, we inspect the torque diagrams across a range of times and choose a representative case that is not being affected by transient features in the potential (transient refers to features necessary to resolve the potential accurately at a single timestep, but which are not self-gravitating features).

The true utility of Figure 4.10 is realised by comparing it with Figure 4.8. The applied torque informs the channel that is responsible for the observed angular momentum transfer. Some features that we noted in the angular momentum transfer figure for the cusp simulation, Figure 4.8, can be interpreted in a new light. Likewise, if we do not see the features reflected in the torque diagram, this is a likely indication that the angular momentum exchange in Figure 4.8 is just the result of first-order effects that have not fully canceled. One can see an example during the steady-state phase, where despite the magnitude of the angular momentum transfer being observed in Figure 4.8, no responsible channel for a sustained torque can be seen in Figure 4.10 at those positions in $R_{\rm apo} - V_{\rm apo}$ space. We interpret this as an exhange of orbits; some disc orbits become more eccentric, and vice versa, in a manner that cancels any net angular momentum change. The halo torque during

the growth phase is the dominant channel causing the bar particles to lose angular momentum, as expected from dynamical friction (Tremaine & Weinberg, 1984b). The torque occurs across a range of velocities, but the magnitude is largest at velocities higher than the x_1 track, consistent with the observations in Figure 4.8. However, during the steady-state phase, the halo torque becomes positive, centered on the x_1 track, which we see reflected in the angular momentum change in the trapped component during the steady-state phase. A particular mystery when taken at face value appears to be the torque the halo exerts on the bar, which is positive during the steady-state phase. In truth, this change to positive signals the end of evolution, when the halo is no longer able to exert a negative torque on the bar. The torque that the untrapped disc attempts to add to the bar has also been reduced, and is confined to smaller radii. As the main source of angular momentum is the outer disc, when the torque and angular momentum transfer in and on the disc, both by the halo and bar, goes to zero at late times, we may reasonably conclude that the outer disc can no longer efficiently contribute angular momentum to the bar.

The assembly phase is unique: the halo torques the nascent bar (positive torque in halo→bar), while the disc receives angular momentum from orbits joining the bar (negative torque in disc→bar). Shortly after the assembly phase, the sense is reversed: the bar grows secularly by being torqued down by the halo (negative torque in halo→bar). On a granular level, one can observe the transformation happen differentially along the bar. The disc begins to place orbits at the end of the bar as the apsides align, while still robbing the inner bar of angular momentum. Conversely, the halo continues to to torque up the outer parts of the bar, but begins accepting angular momentum from the inner parts of the bar as the inner bar begins to rapidly rearrange.

Figure 4.11 shows the same analysis as in Figure 4.10 for the cored halo model. As in the L_z transfer analysis of Section 4.4.1, we see dynamical consistencies between the two simulations as well as some key differences. The formation mode for the bar differ markedly between the cusp and core simulations. We noted in Figure 4.9 that the bar

appeared to undergo a much more violent formation phase, as evidenced by a large gain in angular momentum by the bar particles. In Figure 4.11, we find that the largest source of torque on the bar comes from the untrapped disc rather than from the dark matter halo, as in the cusp simulation. **This indicates that the formation scenario for the bars in the cusp and core simulations is in fact different. In the cusp simulation the halo mediates bar assembly and growth, while in the core simulation bar assembly is mediated by the disc**. We can see this contrast in the torque diagrams for the two simulations during the growth phases. In the cusp simulation, the halo torque always occurs more interior than the outer disc torque, implying that the cusp efficiently couples with the disc and accepts angular momentum from ILR. Without the cusp, the cored halo is unable to accept angular momentum as efficiently, and must turn to the outer disc.

The importance of the torque applied by the disc persists in the other phases as well. The magnitude of the torque applied to the bar by the untrapped disc particles (upper middle row of Figure 4.11) during the steady-state and growth phases far outstrips any other the other ensembles during any phase save the torque by the untrapped disc on the untrapped disc during the assembly phase, which we have already discussed above as being a more violent process than in the cusp simulation. As in the cusp simulation, the growth phase is again marked by an increased torque by the bar on the untrapped disc particles, again centered on the x_{1b} family (indicated in the uppermost center panel of Figure 4.11). We identify the location of CR on the bottom panels of Figure 4.11, the torque on the untrapped disc by the untrapped disc, for its importance to the dynamics. In all three epochs, the torque from the untrapped disc on the untrapped disc dominates the torque from the halo on the untrapped disc, though they are closer in magnitude during the growth phase, meaning that the halo does play a role in the growth. This is consistent with our conjecture that they halo must be reconfigured to accept angular momentum before the growth phase can begin in the cored simulation. The sign of the torque on the bar by the halo is reversed for the steady-state and growth phases of the core simulation relative to the cusp simulation (the

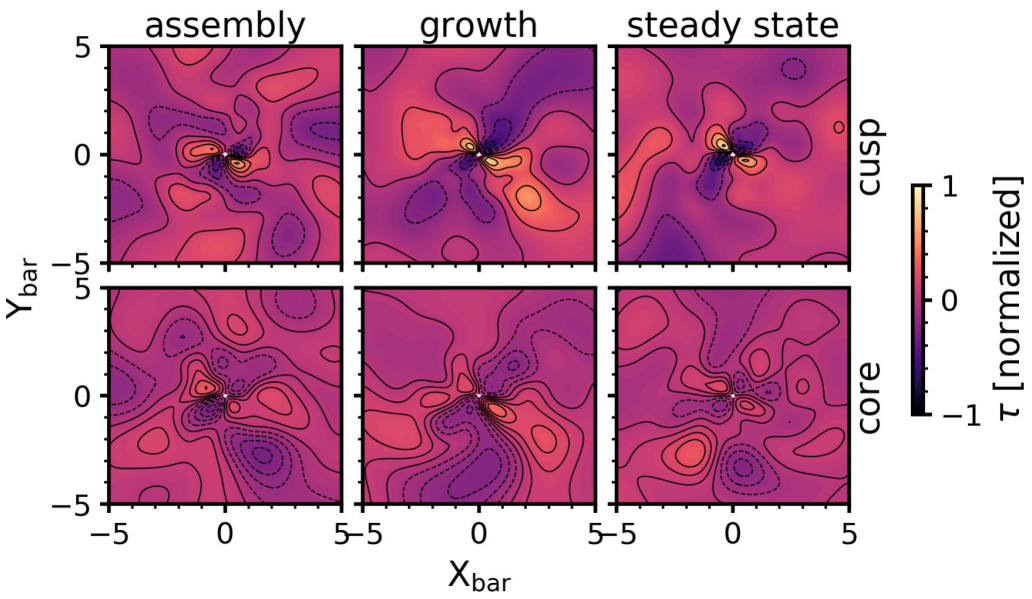

Figure 4.12. The torque field from the halo, computed from the halo basis as rF_θ. The torque has been normalized such that all panels are on the same scale. The disc bar is always oriented with the x axis. The columns correspond to the assembly, growth, and steady-state phases from left to right. The upper row is for the cusp simulation, and the lower row is for the core simulation.

cored halo induces negative torque on the bar during the steady-state epoch and positive torque during the growth phase, while the cusped halo induces negative torque during the growth phase and positive torque during the steady-state phase). However, the magnitude of the torque in the core simulation is a factor of ten less than that in the cusp simulation, so the reversed signs may indicate just how little role the halo plays in the direct dynamics of the core simulation relative to the cusp simulation.

4.4.3 Summary

While the previous sections offered a detailed look at two simulations, we may readily summarize the angular momentum economy using our conjecture that a halo with higher central density (the cusp model) will control the evolution, while a halo with a lower central density (the core model) will seek other channels, using the torque field in the halo.

Contrasting torque fields in the halo tidily summarizes the differences in evolution between the two models. Figure 4.12 shows the torque field during the three evolutionary phases (columns) for both models (rows). In contrast to the instantaneous torque figures (Figures 4.10 and 4.11), the torque fields contain no phase-space density evolution. Their interpretive utility lies in the characteristics of the torque field. A halo which is fully torqued will resemble a perfect quadrupole with no lag (position angle variation of the quadrupole with radius, or position angle different from that of the bar).

We identify the magnitude and the lag as the quantities of interest. We immediately see that the steady-state cusp simulation is both the strongest and most consistent with a pure $m = 2$ disturbance, suggesting that the halo has been fully torqued, in line with our interpretation that the cusp halo both accepted significant $L_{\rm z}$, and is not able to accept further $L_{\rm z}$. In contrast, the growth phase in the cusp has both smaller magnitude and a lag at larger radii, consistent with ongoing angular momentum transfer; and the steady-state phase in the core has significantly smaller magnitude. The assembly phase shows a forming $m = 2$ disturbance in both the cusp and core, where the cusp is clearly stronger even at these early times. Taken together, the torque fields support our conclusion that bar formation may be mediated by either the halo or the outer disc, depending upon the central density of the halo.

4.5 Discussion

In this section, we consider the results from the two simulations for their utility in informing both qualitative understandings of galaxy evolution (Section 4.5.1), and also direct information for comparing with observations (Section 6.5.2).

4.5.1 Implications for galaxy evolution

Identifying and elucidating the phases of bar growth in our simulations provides valuable insight into the evolution of real bars in the universe, and the physics that may govern

their evolution. The clear differences in angular momentum transfer during the different evolutionary phases means that we find different mechanisms during the evolution of the model, and thus it is insufficient to use a catchall term like 'bar-induced secular evolution'. In both simulations, the phase most analogous to what the term bar-induced secular evolution usually implies is the growth phase. Between the two simulations, the growth phase is the most dynamically consistent, with a similar behavior observed in the gross properties (compare the growth phase in the cusp simulation, Figure 4.5, to that of the core simulation in Figure 4.6), the angular momentum transfer (Figures 4.8 and 4.9), and torque (Figures 4.10 and 4.11). The exception is the torque of the dark matter halo on the bar, but this difference reflects the magnitude with which the inner halo is able to play a direct role on bar evolution between the cusp and cored halos. This in and of itself is an interesting point, where by and large the evolution will proceed with the same dynamical mechanisms between the cusp and core simulations, but will find different channels with which to enact the mechanisms. In the cusp simulation, the higher halo density means that it will play a larger role, while in the core simulation, the lower halo density means that the untrapped disc plays a larger part in the dynamics. This difference between the cusp and core simulations is a useful piece of information for trying to understand bar evolution in the real universe. Further work is needed to understand the phase-space distributions that will result in the halo controlling the angular momentum transfer versus the disc.

Further, the presence of a steady-state phase in both simulations suggests that bars may be able to reach a stable configuration more easily than previously thought. Thus, if red barred galaxies are observed, it is possible that these galaxies are actually in a steady-state, rather than continuously evolving. However, the difference in the steady-state phases between the cusp and core simulation means that even if a steady-state phase appears likely for observered bars, it may either be a final configuration (as in the cusp simulation), or an unstable equilibrium that will evolve slowly until new channels can open for its growth (as

in the core simulation). Currently, we cannot propose any metrics with which to separate the stable and unstable equilibria.

The duration of the assembly phase means that it may be possible to catch bars in the act of secular formation, if the disc has reached an unstable configuration. Inspection of the face-on surface density of the disc during assembly shows that a visually classifiable bar feature (e.g. apparent moderate ellipticity) is apparent from the outset of the assembly phase. As the assembly phase lasts for nearly 1 Gyr for a MW-like galaxy in our simulation, as observations reach to higher redshifts many observed barred galaxies may still be in the assembly phase. From our simulations, depending upon the interior density of the dark matter halo, the assembly phase may be a violent process where high fractions (> 50 per cent) of the stellar disk can be rearranged either by rapidly joining the bar, taking part in transient spiral arms (to be discussed in a future work), or being forced outward to larger radii by the formation of the bar. If the bar assembly proceeds from an unstable disc, the level of violence in the bar formation process may be able to efficiently erase any metallicity gradients, thus explaining the observations of a range of metallicity gradients in barred galaxies.

4.5.2 Utility for Observations

We have emphasized where relevant that the distribution of the disc in $R_{\rm apo} - V_{\rm apo}$ position-velocity space can be a useful tool for learning about the evolutionary state of observed barred galaxies. In this section, we summarize our findings and describe how they may be applied to real galaxies. Despite the information contained in all the figures in this work and the dynamical information they can provide, the only set that one can hope to use for real galaxies are the density plots, Figures 4.3 and 4.4. However, these are arguably the least informative for galaxy evolution, and are best interpreted with a wealth of other information. In spite of this, we can make progress and propose that the density plots in radius and velocity space can be used to rule out different scenarios.

In both the cusp and core models, we observe three distinct epochs: assembly, growth, and a steady-state (which is stable in the cusp simulation and unstable in the core simulation). The relevant question then is *during what phase of evolution do we observe real bars?* All three phases have extended durations during our simulation, at approximately 1 Gyr for a MW-like galaxy. Additionally, transitions between the phases, where a blended version of the trends seen during the clear epochs can lead to ambiguous signatures. In particular, the density plots are difficult to interpret except in the case of the steady-state plot. Thus, if a 'gap' is observed between the high velocity and low velocity peaks of the density, the bar is likely to be dynamically evolved.

Despite the complexity and potential ambiguity, with IFUs one can construct the density $R_{\rm apo} - V_{\rm apo}$ plane to look for the influence of angular momentum transfer in real observed galaxies. Unfortunately, the effects are subtle and rely on both high spatial resolution ($\sim$ 1kpc) and high velocity resolution ($\sim 10 \mathrm{km\ s^{-1}}$). However, instruments such as MUSE on the VLT may have the ability to create a useful $R_{\rm apo} - V_{\rm apo}$ diagram for some nearby barred galaxies and compare with the density plots presented in this chapter to look for (1) morpho-kinematic separation of the bar and untrapped disk, and (2) the pattern speed of the bar, which is the point where the bar feature reaches its largest radial extent, and (3) any suggestion of gaps owing to commensurabilities in the outer disc, which may determine the location of CR or other strong resonances.

4.6 Conclusion

We have presented a framework with which to analyze secular evolution in barred galaxy simulations based on the gross properties of unique subsets of orbits, defining the bar, disc, and halo. In both the simulations (which are roughly consistent with the Milky Way) we present, the disc transfers angular momentum, and torques up the bar, the bar transfers the angular momentum to the halo, and then the model arrives at an equilibrium. In many ways, this work is a return to classic bar dynamics: sources of angular momen-

tum seek to find a sink in which to donate their angular momentum, and a bar is both an efficient sink (at early times during assembly) and source (during secular growth), but may reach a limit to its catalyzing ability (the steady-state phase in the cusp simulation), or be temporarily in an unfavorable configuration to facilitate angular momentum transfer (as in the unstable steady-state phase of the core simulation). However, we have used methods designed to analyze nonlinear processes, isolating which part dominates the instantaneous torque through time, and associating the changes in evolutionary status with changes in the observed distribution of torques. The outer disc plays little role in the long-term evolution of the system. In particular, we find little role beyond CR for the disc during phases after assembly, which we argue are the most applicable phases to galaxy evolution in the real universe. It seems likely that bars and galactic discs spend a larger fraction of their lifetimes in the growth or steady-state phases.

In Chapter 3, we described the classes of orbits available in both models, finding that certain subfamilies of x_1 orbits, the bifurcated family x_{1b}, are particularly important for bar evolution. Using the information provided in Chapter 3, we associate different features in the τ and $\Delta L_{\rm z}$ figures with different commensurate orbits that will not be readily identified through frequency analysis. In this work, the identification of orbits associated with the bar allows for tracking $M_{\rm bar}$, $L_{z,{\rm bar}}$, $I_{\rm bar}$, and $R_{99,{\rm bar}}$. Additionally, the ability to compute $\Delta L_{\rm z}$ and τ for subsets of particles removes much of the anecdotal and circumstantial evidence for the angular momentum flow in barred disc galaxies. We place clear constraints on angular momentum signatures during different phases of secular evolution.

The main results of this chapter are as follows:

(1). Careful accounting of the angular momentum budget reveals that the angular momentum economy of the bar-disc-halo system is composed of several exchanges, including the assembly of the bar, the friction imposed by the halo on the bar, and the coupling of the disc to the halo. The coupling of the bar to the disc and halo is different in the cusp and core simulation, with the cusp simulation using the halo as

the primary driver of evolution, and the core simulation using the disc as its primary driver.

(2). The assembly of the bar is marked by individual orbits losing angular momentum then joining the bar pattern after being torqued by the halo (which gains angular mometum for the majority of the simulation). Resonances control the transfer of angular momentum from the bar pattern to the halo, as well as from the disc to the halo directly.

(3). The geometry of the bar changes appreciably with time and does not grow self-similarly, as evidenced by the trends in $M_{\rm bar}$ and $I_{\rm bar}$.

(4). We demonstrate that a long-lived bar will balance angular momentum transfer through opposing resonances that exert equal but opposite torques, reaching a steady-state in the cusp simulation where the bar pattern no longer slows. As far as we know, this is the first time such behavior has been shown in the literature.

(5). The instantaneous torque applied by different subsets of particles is a powerful dynamical tool that can explain the observed $L_{\rm z}$ changes of individual orbits (e.g. compare Figures 4.8 and 4.10 as well as Figures 4.9 and 4.11).

This work interfaces well with other techniques proposed to analyze the evolution of barred systems, namely orbital decomposition (Chapter 3) and harmonic analysis (Chapter 5). The techniques presented in this work to track both cumulative angular momentum flow and instantaneous torque, which we then associate with gross observables, are a quantitative avenue that numerical progress has enabled (e.g. high spatial and temporal resolution simulations). It may seem as though we have developed an independent technique from that presented in Chapter 3, but in actuality the two work in tandem to explain the microphysics of the system (the behavior of individual orbits) and the macrophysics (the gross properties of the observable collective features). To get a coupling between the disc and

halo you need a channel, which specific orbit families are able to provide. Resonances, and therefore commensurate orbits, provide the cleanest channel to funnel angular momentum from sources to sinks. Once a disc orbit converts into into a commensurate orbit, it will efficiently couple with the halo (along with the other orbits in the collective response) and slow, moving angular momentum to the halo. The angular momentum change by the orbit being captured is recovered by the untrapped disc across a variety of higher-order resonances. Thus, both the techniques presented in Chapter 3 and the technique presented here provide different but complementary for understanding evolution in simulations of barred galaxies, as well as its observational applications.

CHAPTER 5

USING HARMONIC DECOMPOSITION TO UNDERSTAND BARRED GALAXY EVOLUTION

5.1 Introduction

The clear presence of responses to disturbances in galaxies, which take the form of bars, spiral arms, warps, rings, and displacements, amongst other features, necessitate a higher-order harmonic description of stellar discs beyond an exponentially-decreasing monopole. Early studies characterized disc structure using Fourier amplitudes as a function of radius R, $A_m(R) = \frac{1}{2\pi}\int_{-\pi}^{\pi} f(R,\phi)e^{-im\phi}d\phi$ where m is the harmonic order and $f(R,\phi)$ is the weighting function corresponding to the luminosity (or ideally mass) as a function of angle ϕ around the galaxy (Considere & Athanassoula, 1988; Elmegreen et al., 1989). Barred galaxies, which make up more than half of the observed disc galaxies in the infrared (Sheth et al., 2008), are the strongest example of galaxies with large values of $A_2(\equiv \int A_m(R)dr)$ in the inner galaxy, and A_2 has long been used as a proxy for the 'strength' of a bar, a nebulously defined term that does not fully or necessarily accurately quantify the effect the bar will have on galactic evolution.

A more general approach than Fourier decomposition, performing a harmonic function expansion that correlates spatial to azimuthal structure more accurately represents the gravitational field that causes the non-axisymmetric structures. Such a harmonic analysis is an inexpensive way to parameterize both the evolution of large simulations and observational data by understanding the evolutionary mechanism or scenario for evolution. Connecting dynamical principles to galaxy evolutionary mechanisms allows one to fully benefit from the harmonic function expansion analysis of galaxies.

The harmonic decomposition technique has been used to both study and compare simulations, owing to its natural relationship with analytic perturbation theory (Weinberg & Katz, 2007a,b). Some n-body simulations use a technique explicitly built on bi-orthogonal functions, where one solves the Poisson equation using separable azimuthal harmonics. Generally, these techniques may be called basis function expansions (BFE; Clutton-Brock 1972, 1973; Kalnajs 1976; Hernquist & Weinberg 1992; Earn 1996; Weinberg 1999), which has many notable features that make them ideal for studying disturbances to equilibrium stellar discs. For simulations using BFE methods, harmonic function expansion analysis centers decomposing a distribution into linearly-summable functions that resemble expected evolutionary scenarios in disc galaxy evolution. The primary diagnostics available are the amplitude and phase of each function. When tracked through time, one unlocks another dimension for understanding evolution that may not clearly manifest itself in analytic studies (Weinberg, 2004). Using harmonic function expansion analysis in BFE simulations enables a quick and straightforward reconstruction of the potential at any time in the simulation, for any arbitrary combination of particles. This has already allowed us to locate resonances using perturbation theory and commensurability mapping (Chapter 3) and to determine which components are responsible for the primary transfer of angular momentum (Chapter 4).

The goal of this chapter is to enable an analysis of the evolutionary mechanisms in a stellar disc to determine the evolutionary phases of a barred galaxy model using a BFE method. To build a dynamical picture from evolutionary scenarios, we seek answers to the following questions: (1) Which mechanisms dominate the evolution? (2) What observables do the mechanisms have? (3) How do mechanisms interact with one another? By defining functions that describe evolutionary scenarios and mechanisms, the BFE method enables us to readily identify features correlated by self-gravity, which we then use to study the dynamical mechanisms responsible for the evolution. In this chapter, we show that a wealth of responses can result from secular evolution alone, provided that the phase-space admits

channels for secular evolution. Some of our results match previous findings, such as the slowdown of the bar, but many describe new dynamics, including harmonic–locking as a mechanism to slow or stop bar evolution.

The chapter is organized as follows. In Section 6.2, we motivate the choice of our BFE methodology and describe its details, as well as present the simulations, and our analysis performed in previous work (Chapter 3; Chapter 4) that we will employ here. In Section 5.3, we look at the global measurements of the simulation using the harmonics from the basis, including a direct comparison of ellipse fitting and dynamical measurements from harmonic function expansion analysis. In Section 7.5, we discuss harmonics relating directly to the bar and their amplitudes versus time to help identify mechanisms and evolutionary phases. Some harmonics and their related mechanisms are either not present in our simulation as expected, or present and appear to have less influence than expected. Section 5.5 presents a kinematic technique with which we determine the true length of orbits that form the backbone of the bar. We conclude in Section 7.6.

5.2 Methods

This chapter studies the paradigm of bar formation with n-body simulations where gravity is parameterized as the sum of two orthonormal basis sets describing the equilibrium of a galaxy disc (the first basis) and the dark matter halo (the second basis). Our primary tool is the BFE method as implemented in EXP (Weinberg, 1999). The BFE method has three primary advantages over tree and grid method gravity solvers: (1) the calculation of forces scales linearly with particle number, (2) the dynamic range of multi-scale systems such as the disc-halo system can be better resolved by tailoring the geometry and scale of components individually, (3) a sensitivity to weak global distortions is possible because small-scale noise can be suppressed or controlled, and (4) intercomponent interactions can be explicitly controlled to allow the study of different mechanisms individually (e.g. a mixture of live and fixed components, controlling the inclusion or exclusion of different

evolutionary mechanisms). We discuss the details of our implementation of the BFE algorithm in Section 5.2.1, the initial conditions of our simulations in Section 5.2.2, and our methods for measuring the bar in Section 5.2.3.

5.2.1 Empirical Orthogonal Functions

In collisionless BFE method n-body simulations, one numerically integrates the equations of motion for individual particles by calculating the entire potential field given by the Poisson equation, projecting particles on to a set of basis functions and subsequently evaluating of the force field at the position of each particle. The Poisson equation reduces to the fundamental Sturm-Louiville equation (SLE) and solutions to the SLE are orthogonal and complete with respect to some weighting function: the Fourier and Bessel expansions are two well-known examples. This form describes many physical systems, and may be written as:

$$\frac{d}{dx}\left[p(x)\frac{d\Phi(x)}{dx}\right] - q(x)\Phi(x) = \lambda\omega(x)\Phi(x) \tag{5.1}$$

where λ is a constant, and $\omega(x)$ is a weighting function. The eigenfunctions ϕ_j of the SLE form a complete basis set with eigenfunctions λ_j, where j may be truncated from the theoretically infinite series. The BFE potential solver is built using properties of eigenfunctions and eigenvalues of the SLE.

The halo can be expanded into a relatively small number of spherical harmonics Y_{lm} and appropriate radial functions, such that the total halo potential is given by $\Phi^j_{lm} = \phi^j_{lm} Y_{lm}(\theta, \phi)$. The disc is more complicated, and requires a specially constructed basis. As the Poisson equation may be written as an eigenfunction of the Laplacian, which has solutions that are a product of spherical harmonics in the angular variables and Bessel functions in radius (Weinberg, 1999), solutions to the SLE may be reduced to a separable form in polar coordinates with radial, azimuthal, and vertical functions[1] which satisfy a po-

[1]The Poisson equation can be separated in any conic system; the choice of cylindrical coordinates is motivated by the geometry of the disc.

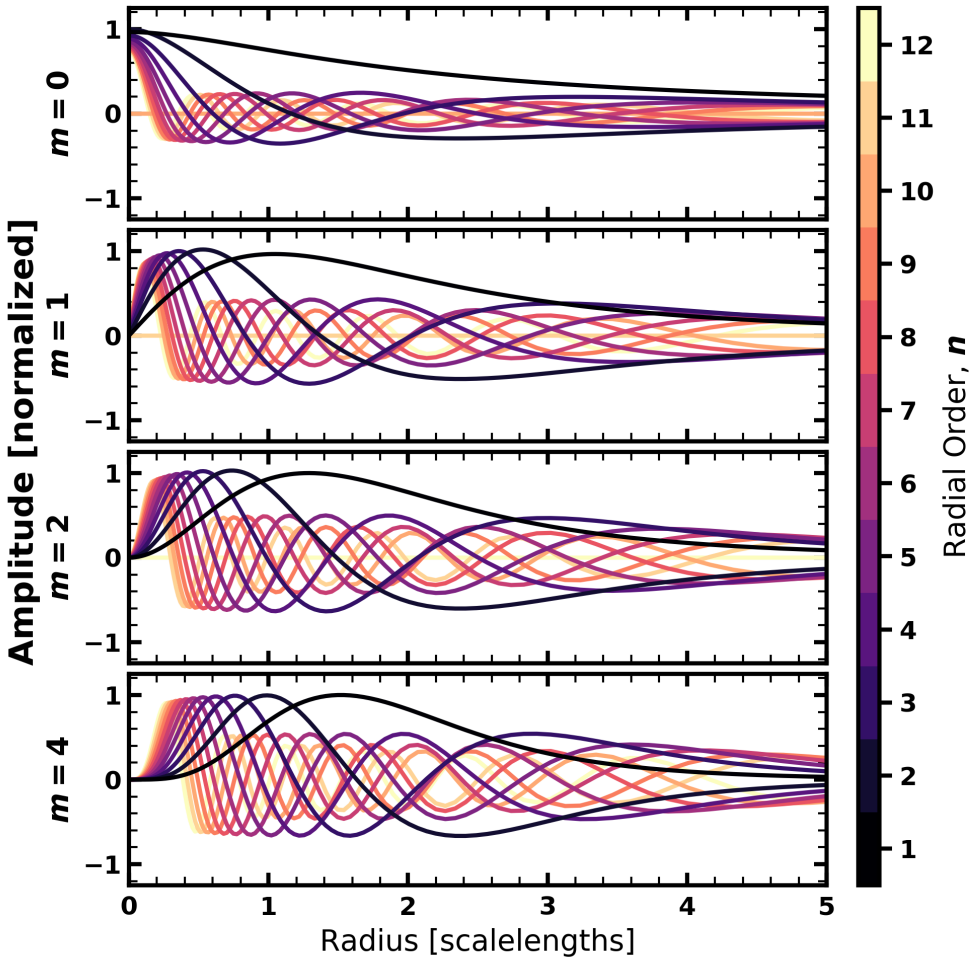

Figure 5.1. In-plane amplitude variations as a function of disc scalelength for all radial functions per harmonic order in the cylindrical disc basis. We show the $m = 0, 1, 2, 4$ harmonic subspaces as panels from top to bottom. The amplitude in each panel has been normalized to the maximum in the corresponding subspace. Functions that are zero everywhere are vertically asymmetric (see Figure 5.2).

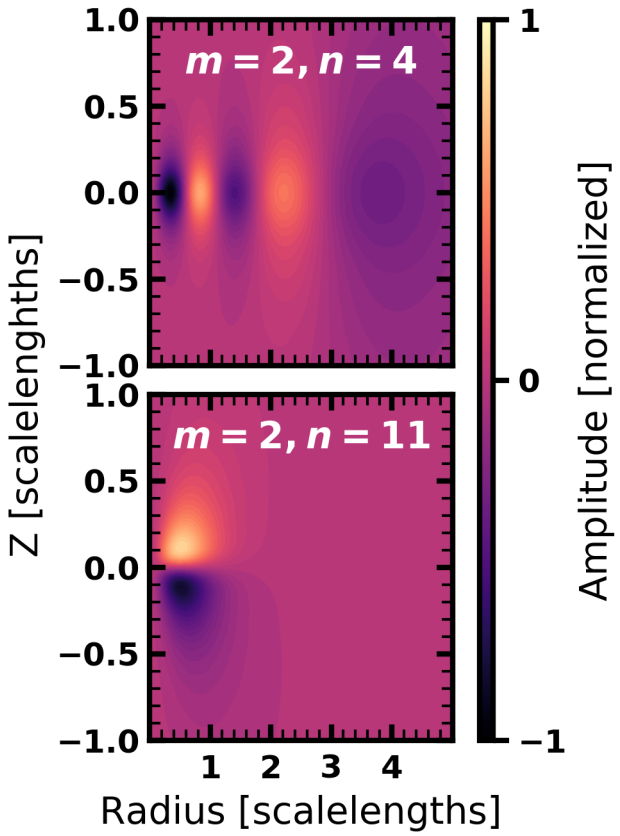

Figure 5.2. Examples of vertically symmetric ($m = 2, n = 4$, upper panel), and vertically asymmetric ($m = 2, n = 11$, lower panel) functions for the disc basis. The x and y axis correspond to the radial and vertical axes in the simulation, and the amplitude of the variations between panels has been normalized to the maximum $m = 2$ amplitude.

tential of the form $\Phi(r) = R(r)Z(z)\Theta(\theta)$. One may then look for potentials of the form $\Phi(r, z, \theta) = \Phi_0(r)\phi(r)Z(z)\Theta(\theta)$ where $\phi(r)$ is an eigenfunction that may be found by solving Equation 5.1 such that the orthogonality condition pertaining to the Poisson equation between the potential (Φ) and density (ρ) pairs is met:

$$-4\pi G \int_0^\infty dr r \Phi_0(r)\rho_0(r)\phi(r)^2 = -4\pi G \int_0^\infty dr r \Phi\rho = 1 \tag{5.2}$$

Each of the potential-density pairs solves the Poisson equation. The construction of the disc basis proceeds in spherical harmonics, where we admit functions up to $l = m = 36$. From this suite of functions, the n functions which maximize the variance are selected in each harmonic m order. Although one can construct a disc basis from the eigenfunctions of the Laplacian, the boundary conditions make the basis hard to implement. To get around this, our solution method starts with a spherical basis and uses a singular value decomposition to define a 'rotation' in function space to best represent a target disc density. That is, the new basis functions optimally approximate the true distribution in a linear least squares sense. Also, since the new eigenfunctions are also orthonormal and representable as a linear combination of solutions to the Poisson equation, the new functions are also solutions to the Poisson equation. Because we are free to break up the spherical basis into meriodinal subspaces, by azimuthal order the resulting two-dimensional eigenfunctions in r and θ are equivalent to a decomposition in cylindrical coordinates $R,\ z,\ \phi$. These techniques have been packaged into the n-body code EXP, which we use for our simulations.

We condition the initial disc basis functions on the analytic disc density such that the lowest-order potential-density pair matches the initial analytic mass distribution (parameterized in our simulation as in Equation 7.4). This acts to reduce small-scale discreteness noise as compared to conditioning the basis function on the realized positions of the particles (Weinberg, 1998).

Further, both simulations presented here have the same basis, allowing for a detailed comparison between differences in the disc profile, and a direct comparison of their shapes.

Throughout this work, we refer to disc azimuthal harmonics as m–orders, and radial subspaces as n–orders, such that an eigenfunction is given by $(\cdot, \cdot) \equiv (m, n)$ notation. In the halo, the azimuthal harmonics are l orders, with $m \in (-l, l)$, as in spherical harmonics. Radial subspaces in the halo are still referred to as n–orders. In this work, we largely ignore the halo harmonics, instead focusing on the disc harmonics to motivate our discussion of observational harmonic decomposition of barred disc galaxies. Using basis methods, we can understand the potential and density of a galaxy as a superposition of several basis functions. This allows us to decompose the galaxy into harmonic orders based on the multiplicity of the symmetry, where $m = 0$ is the monopole, $m = 1$ is the dipole, $m = 2$ is the quadrupole, and so on. The sine and cosine terms of each azimuthal order give the phase (angle) of the harmonic, which can be used to calculate the pattern speed. We also decompose the azimuthal harmonics into radial subspaces that also set the vertical structure. After trial-and-error, we determined that a scalefactor of approximately $\sqrt{2}$ was appropriate for setting the scale of the disc when deprojected onto spherical harmonics for computation of the basis. As we shall see later, this choice of radial scale does no appear to bias the radial subspaces that exhibit significant amplitude, and further, the choice of a scaling factor that is larger than the intrinsic scalelength of the selected disc (see below) provides dynamic range in the evolutionary phases that can be resolved (the maximal node spacing is larger).

Figure 5.1 shows the in-plane amplitude variations for radial functions (n orders) as a function of radius, separated by harmonic subspace (m orders). We show the four harmonic subspaces that are most relevant for the evolution of the simulation, $m = 0, 1, 2, 4$, from top to bottom in the panels. In each harmonic subspace, the lowest-order radial order, $n = 1$, has no nodes. The number of nodes increases with order n. The nodes are interleaved by radial order, but the increasing number of nodes means that the smallest radius node always decreases in radius as the number of nodes increases. Therefore, an increase in amplitude for higher–n–order harmonics corresponds to the movement of mass to smaller radii. Additionally, the spacing of nodes gives an approximate value

for the force resolution of the simulation. For example, the highest order $m=0$ radial function ($n=12$) has a zero at $R=0.2a$, or 600 pc in a MW-like galaxy. Additionally, the radial orders are interleaved between harmonic orders, such that $R_{\mathrm{firstnode,m=2,n=1}} \approx \frac{1}{2}\left(R_{\mathrm{firstnode,m=1,n=1}} + R_{\mathrm{firstnode,m=1,n=2}}\right)$. In Figure 5.2, we show examples of the vertical structure in the disc basis functions. The upper panel shows the $m=2, n=4$ basis function in radius–z space. This function is symmetric about the $z=0$ axis. The combination of vertically symmetric and asymmetric harmonics represent all possible variations in the gravitational field above and below the plane consistent with the spatial scales in the basis. In both panels, the color has been normalized to the maximum amplitude of the $m=2$ harmonic subspace.

As the simulation proceeds, we sum the contribution to the coefficients for each eigenfunction over the particle distribution as follows. We define our potential estimator in one dimension as

$$a_j = \int dx \bar{\phi}_j(x) f(x) \tag{5.3}$$

where $\int dx \bar{\phi}_j(x)\phi_k(x) = \delta_{jk}$ satisfies the orthogonality relation and $f(x)$ is some well-defined function, in this case the true potential (Weinberg, 1996). In the case of tabulated eigenfunctions and a discrete distribution of particles, such as in an n-body simulation, the coefficients that approximate the potential are

$$\hat{a}_j = \frac{1}{N}\sum_{k=1}^{N} \phi_j(x_k) \tag{5.4}$$

where ϕ_j is the potential eigenfunction that satisfies the bi-orthogonality relation, as above.Then, if we take $\hat{a}_j$ to be an estimate for a_j, we can estimate the function $f(x)$, here representative of the potential, as

$$\hat{f}(x) = \sum_{j=1}^{M} \hat{a}_j \phi_j(x). \tag{5.5}$$

Throughout this work, we will evaluate and report $\hat{a}_j$, which we will refer to as a 'coefficient' or 'amplitude' of a particular eigenfunction. Tracking the amplitudes for the bases

through time is the primary investigative tool used in this chapter. The coefficients for each n order have cosine and sine components that correspond to the analogous Fourier terms A_m and B_m. Thus we may compute the phase for any basis function. When we combine the sine and cosine terms to make a single amplitude for the particular (m, n) eigenfunction, we will use the notation $A_{m,n}$. The total amplitude in an azimuthal harmonic order will simply be noted as A_m. While the halo and disc evolve simultaneously (Chapter 4), we focus on disc evolution in this chapter.

Naturally, the BFE approach also has tradeoffs. The selection of the basis is fraught with uncertainties about whether the basis can capture all possible mechanisms of disc evolution. The truncated series of basis functions limits the possible degrees of freedom in the gravitational field. However, a basis function representation provides an information–rich summary of the gravitational field that provides insight into the overall evolution. Further, as we will see in Section 5.4.1, the methodology we employ in this work allows for the decomposition of different components into dynamically-relevant subcomponents, for which the gravitational field can be calculated separately. For brevity and instructive comparison to previous work, we will refer to the harmonic decomposition employed here as analogous to Fourier decomposition techniques, but we emphasize that the decomposition of galaxy models using orthogonal functions goes beyond traditional Fourier techniques, accounting for both radial harmonics and vertical structure of the disc galaxy, with few assumptions.

5.2.2 Initial Conditions

This chapter focuses on the detailed results from two simulations with different initial conditions. We briefly describe the initial conditions in this section and refer the reader to previous chapters that introduced the simulations in more depth (Chapter 3; Chapter 4). The initial condition realization technique has also been discussed in Holley-Bockelmann et al. (2005) and Chapter 1. As in other work, we adopt $G = 1$ and virial units where $R_{\rm vir} = 1$,

$V_{\rm vir} = 1$, $T_{\rm vir} = 1$. The simulations may then be scaled to obtain physical quantities for different galaxies.

The simulations begin with an exponential disc with density

$$\rho_{\rm disc}(R, z) = \frac{M_{\rm d}}{8\pi h a^2} e^{-R/a} {\rm sech}^2(z/h) \tag{5.6}$$

where $M_d = 0.025 M_{\rm vir}$ is the disc mass, $a = 0.01 R_{\rm vir}$ is the disc scale length, and $h = 0.001 R_{\rm vir}$ is the disc scale height. We embed the disc in a modified NFW (Navarro et al., 1997) dark matter halo with $c = 25$, whose density is given by

$$\rho_{\rm halo}(R) = \frac{\rho_0 r_s^3}{(R + r_c)\,(R + r_s)^2} \tag{5.7}$$

where ρ_0 is a normalization set by the chosen mass, $r_s = R_{\rm vir}/c$ is the scale radius for the turnover of the exponents, and r_c is a radius that sets the size of a core. The core radius r_c distinguishes between the two models: $r_c = 0$ in the cusp simulation, and $r_c = 0.02$ in the core simulation. The adjustable core radius allows us to explore the role of halo profile on secular dynamics.

We realize the initial positions and velocities in the halo via Eddington inversion of the halo model that includes the monopole contribution from the disc. We select the initial positions in the disc (Equation 7.4) via an acceptance–rejection algorithm. We select the velocities by solving the Jeans equations with an axisymmetric velocity ellipsoid in the disc plane ($\sigma_r = \sigma_\phi$). We characterize the velocity dispersion using the Toomre Q parameter,

$$\sigma_r^2(r) = \frac{3.36 \Sigma(r) Q}{\Omega_r(r)} \tag{5.8}$$

where $\Sigma(r)$ is the surface density and Ω_r, the radial frequency, is given by

$$\Omega_r^2(r) = r \frac{d\Omega_\phi^2}{dR} + 4\Omega_\phi^2. \tag{5.9}$$

where Ω_ϕ is the azimuthal frequency. We choose $Q = 0.9$, a 'cold' disc, in both cases to promote the rapid growth of disc structure. The vertical velocity dispersion is obtained directly from the Jeans' equations for a disc,

$$\sigma_z^2(r) = \frac{1}{\rho_d(R,z)} \int_z^\infty \rho_d(R,z) \frac{\partial \Phi_{\rm tot}}{\partial z} dz \tag{5.10}$$

where $\Phi_{\rm tot}$ is the sum of the disc and halo potential (Binney & Tremaine, 2008).

As both simulations use the same basis for the disc, we can compare the excited basis amplitudes directly between the two simulations. Although BFE reproduces any potential field in principle, truncation of the series limits its full adaptability. To check for any dependence on the basis center, we perform one additional simulation to study the effects of excluding $m = 1$ harmonics from barred galaxy evolution. In this simulation, which uses the same initial conditions as the cusp simulation, we do not allow forces for any odd harmonics to be applied to the particles. We refer to this simulation as the 'even–harmonic–only' cusp simulation.

5.2.3 Bar Measurement

We use two methods to parameterize the size and mass of the bar, (1) the traditional ellipse fitting to the isophotes of surface density, and (2) using the trapped orbits that support the bar potential.

5.2.3.1 Ellipse Fits

Many studies have made use of visually-determined bar lengths, including Galaxy Zoo (Hoyle et al., 2011) and S^{4}G (Sheth et al., 2008). Hoyle et al. (2011) found that individual observers report approximately a 6 per cent deviation relative to the mean of all observers who classify a bar length. While visually measuring a bar length is a quick process doesn't necessarily trace an isodensity surface and often offers no errors on individual measurements.

Other studies fit ellipses to bar isophotes (Muñoz-Mateos et al., 2013; Laurikainen et al., 2014; Kim et al., 2015; Erwin & Debattista, 2016; Kruk et al., 2018). The various ellipse measurements have known discrepancies. Athanassoula & Misiriotis (2002) demonstrate that different ellipse methods applied to the same galaxy can lead to variations of up to 35 per cent in measured bar length. However, as this method is commonly used, we also adopt it here. We fit isophotes using least-squares regression to a standard ellipse equation. Some studies use a generalized ellipse (Athanassoula et al., 1990), where the ellipse equation is given by

$$1 = \left(\frac{|x|}{a}\right)^c + \left(\frac{|y|}{b}\right)^c . \tag{5.11}$$

The standard conic ellipse assumes $c = 2$, while the generalized ellipse allows for a variable c. Values $c > 2$ yield 'boxy' isophotes. As pointed out by Athanassoula et al. (2013), the bar length can be overestimated relative to visual classification when c is not allowed to vary. In this work, we do not allow c to vary, and acknowledge that some fits may result in longer bars than the values reported here. However, we find that our results do not qualitatively change if we use a generalized ellipse instead. In our tests, the variance in the length of the fit ellipse was approximately 25 per cent if c is a fit parameter[2].

Muñoz-Mateos et al. (2013) measured bar lengths in the S^{4}G sample (Sheth et al., 2008) using four different ellipse metrics derived from either the ellipticity profile or position angle (PA) of the best-fit ellipse at a given radius. Connecting these methods, Herrera-Endoqui et al. (2015) demonstrated that visual fits to bar lengths are roughly comparable to lengths determined from the radius of maximum ellipticity. We compute the best fit ellipses over a range of isophotal values in the vicintity of the bar, and we assign the bar length as the maximum semi-major axis that has $\frac{b}{a} < 0.5$. We find that selecting different criteria such as the maximum ellipticity or a threshold in PA variation does not qualitatively change the results presented here, finding that all commonly-used ellipse measures return values

[2]Clearly, allowing c to vary changes the amount of $m = 4$ amplitude in the bar feature, which has discernable dynamical consequences (Chapter 3).

within approximately 30 per cent, in agreement with Athanassoula & Misiriotis (2002). For a more thorough introduction to measuring bar lengths, we refer the reader to Erwin (2005) for an observationally motivated viewpoint, and Athanassoula & Misiriotis (2002) for a theoretically motivated viewpoint.

5.2.3.2 Trapping Analysis

We draw upon the results of Chapter 3 to analyze the particles that are gravitationally bound to the bar. In Chapter 3, we analyzed bar membership through the clustering of the radial turning points, or apsides, for a given orbit. Orbits 'trapped' by the bar's gravity will show only libration about the position angle of the bar major axis. In this work, we consider only orbits that contribute to the structure of the bar: the x_1 family associated with the inner Lindblad resonance (ILR; $2\Omega_\phi - \Omega_r = 2\Omega_p$, where Ω_p is the pattern frequency of the bar). These orbits compose the 'backbone' of the bar and are highly eccentric orbits elongated along the bar axis. We also consider 'other' bar supporting orbits, which are composed of higher-order families that reinforce the bar potential but are not directly associated with ILR.

Briefly described, our method isolates the turning points in an orbit by looking for local maxima in radius. Using a rolling average of 20 apsides[3] in Cartesian coordinates that we transform to the frame, we compute the position angle for the center of two k–means–derived clusters relative to the bar, taking the maximum of the two values. The choice of two clusters is motivated to align with the two ends of the bar, as a trapped orbit will librate around the minimum of the potential caused by the bar, analogous to a swinging pendulum librating around its mimumum. In addition to the cluster position angles, we compute the variance in the position angle relative to the cluster center over the 20 apsides, $\sigma_{\theta_{\mathrm{bar},20}}$. These two quantities alone allow for a successful classification of orbits into the

[3]We determinte the rolling average of 20 empirically to be a sweet spot in a tradeoff between time resolution and signal-to-noise.

x_1 and 'other' bar supporting families as follows. We limit the average apse position to be $\langle\theta_{\rm bar}\rangle \leq \pi/8$ then subdivide based on the variance in x_1 with $\sigma_{\theta_{\rm bar,20}} \leq \pi/16$ and 'other' with $\pi/16 < \sigma_{\theta_{\rm bar,20}} \leq 3\pi/16$. From an empirical examination of the orbits, we estimate a contamination rate in both families of approximately 1 per cent. This uncertainty does not change any of the results we present in this work.

5.3 A BFE-based View of Bar Phases

The BFE potential–solving methodology of EXP naturally lends itself to harmonic function expansion analysis. In this section, we present the harmonic decomposition of the simulations, using both the amplitude and phase of basis function coefficients to characterize the global evolution of the simulations. Once we describe the basis functions that describe the forces in the simulation, we may isolate evolutionary phases, as described by the basis coefficients and functions, to apply complementary analyses such as perturbation theory, orbit analysis, and torque theory. In Chapter 3, we first identified three phases of bar evolution (assembly, growth, and steady-state) from the trapped fraction of orbits. In this section, we will correlate the phases of bar evolution identified from the trapped fraction with the harmonic decomposition of the simulation phase space. We first describe the evolution of azimuthal harmonics and introduce the three phases of bar evolution observed in our simulations in Section 5.3.1 before considering the radial subspaces in Section 5.3.2. We summarize the utility of harmonic decomposition for a detailed study of the evolution in Section 5.3.3.

In the BFE used in EXP, the coefficients are independent of any posterior tuning. Thus, if we can understand the evolution of the bar using the harmonic analysis only, in particular identifying key trends, the model physical properties can be efficiently summarized and represented for later theoretical and observational comparison.

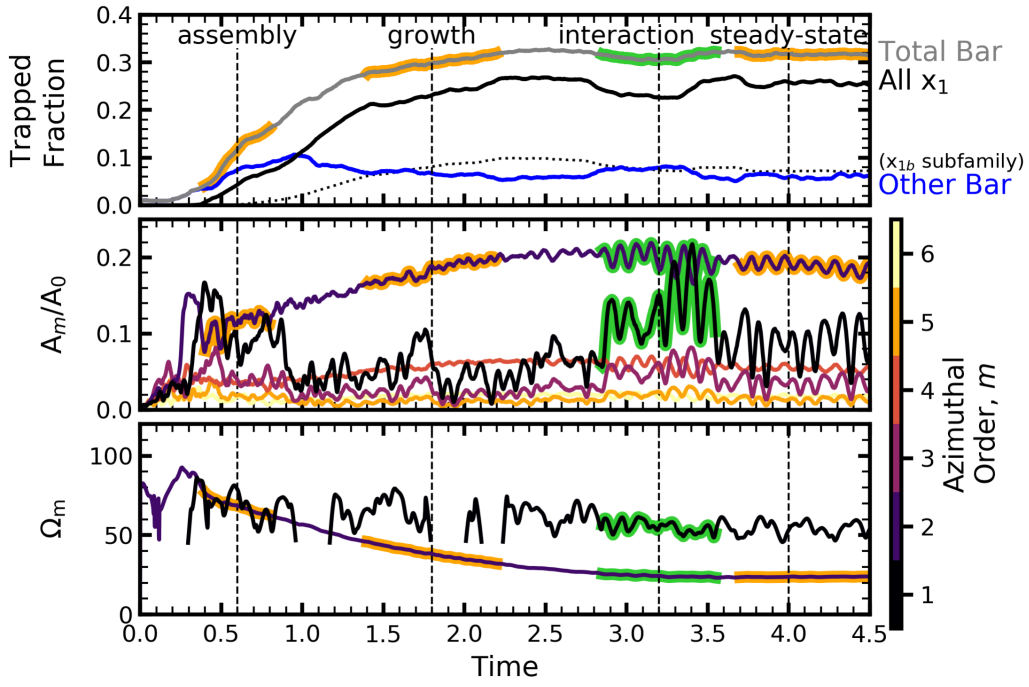

Figure 5.3. Upper panel: Bar membership in the primary x_1 (black) and 'other' bar-supporting (blue) families, and total (gray), versus time, from the cusp simulation. Middle panel: A_m, the amplitude per harmonic orders $m \in (1, 6)$. Lower panel: azimuthal harmonic pattern speed, Ω_m, where $m \in (1, 2)$. Windows of low phase signal are not plotted. The evolution of higher harmonic orders of m in pattern speed are the same as the other odd or even harmonics, respectively. In all panels, three prominent epochs in the bar lifetime are identified and highlighted in orange: *assembly*, *growth*, and *steady-state*. A prominent *interaction* between the $m = 1$ and $m = 2$ harmonics is highlighted in green.

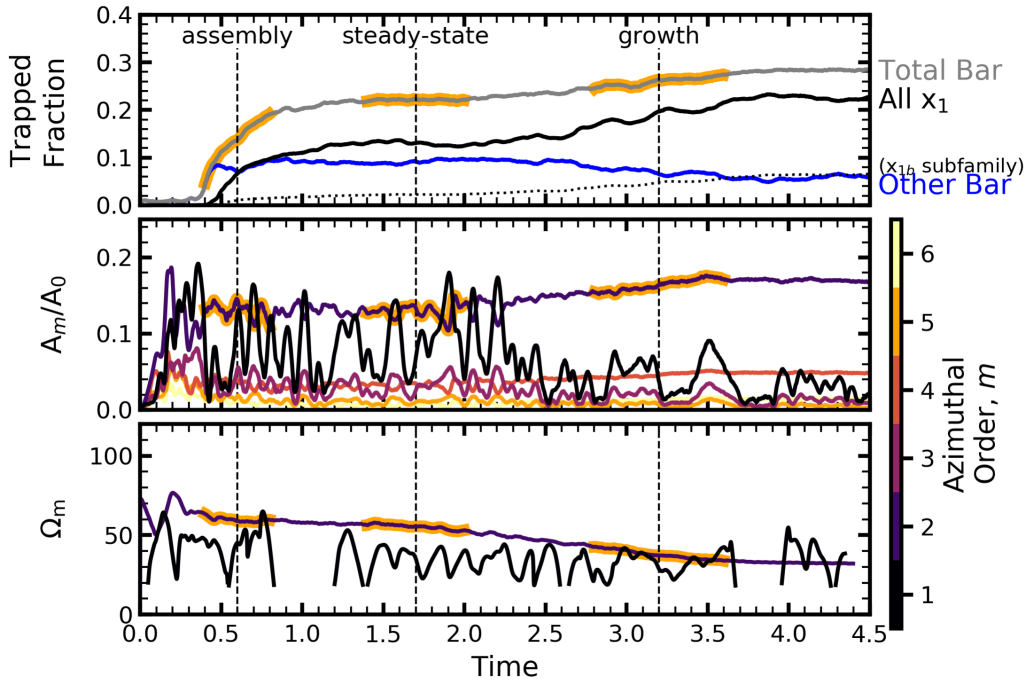

Figure 5.4. Same as Figure 5.3, but for the core simulation. In all panels, three prominent epochs in the bar lifetime are identified and highlighted, in order: *assembly*, *steady-state*, and *growth*.

5.3.1 Azimuthal Harmonics

With the trapped fraction analysis of Chapter 3 in hand, we can use our a priori knowledge about the basis and the qualitative features of the evolution to derive a diagnostic classification in terms of the basis. Figures 5.3 and 5.4 show the three epochs of bar evolution (described in Chapter 3), the corresponding coefficient power, and the pattern speed derived from the coefficients for the cusp and core simulations. In particular, we wish to draw contrasts between the cusp and core simulation, showing that a mild change to the halo profile can produce evolution that is qualitatively different.

The upper panel of Figure 5.3 plots the trapped orbit fraction versus time for the total bar (gray), and the two orbit families that make up the bar, the x_1 and higher-order ('other') bar supporting families (black and blue, respectively). We identify and label three qualitative epochs of bar evolution, the assembly phase (a), the secular growth phase (g), and the steady-state equilibrium state (s). We characterize the phases as follows: (1) the rapid formation of the bar during the assembly phase, where the trapped fraction grows quickly (assembly); (2) a secular growth phase where the bar continues to growth linearly (growth); and (3) a steady-state phase where the trapped fraction does not increase, but other global quantities may change (see the discussion in Chapter 4). The evolution of the trapped fraction distinguishes between the phases while a visual, i.e. isophotal, inspection of the bars does not (Chapter 4). The middle panel of Figure 5.3 shows the total contribution to each azimuthal harmonic order computed by summing over the radial orders for fixed $m \in (1, 6)$. The colors correspond to the harmonic order as indicated. Any single azimuthal harmonic is not clearly associated with the growth of distinct orbit families. However, we can see signs of the three qualitative phases of evolution.

As expected, the trends in $m = 2$ azimuthal power correlate with the trapped fraction and with each of the three observed phases. The assembly phase lags the $m = 2$ feature that is traditionally associated in the literature with the formation of the bar. A rapid increase and then decrease of the $m = 2$ amplitude at $T = 0.3$ is clearly associated with significant

transfer of angular momentum to the outer disc via the two-armed spiral that precedes the formation of the trapped bar[4]. Whether measured by bar mass or $m = 2$ amplitude, the bar strength grows consistently over time. However, when measured by Fourier amplitude, the bar appears to assemble quickly and strengthen more slowly than the trapped orbits indicate. An examination of the radial coefficients for $m = 2$ reveals that the spiral arms and not the bar are responsible for the initial growth of the A_2 component. Unfortunately, the trapped component is difficult to distinguish observationally, though we offer a possible method in Section 5.5.

In the cusp simulation, the overall value of the amplitude of the $m = 2$ harmonic subspace differs from the trapped fraction by 50 per cent during the phases where the bar is clearly established (growth and steady-state). This cautions against using Fourier techniques alone to quantify the strength of the bar, particularly during the assembly phase. Further, the $m = 1$ amplitude is greater than that of $m = 2$ at two key points in the simulation: during the assembly phase and also at the harmonic–coupling phase, a nonlinear power transfer between two harmonics, between $m = 1$ and $m = 2$ at $T \approx 3$. We briefly comment on the observed phenomena in this section, and will analyze the harmonic subspace coupling in much more detail in later sections. Apart from these two times, the $m = 1$ harmonic subspace is subdominant in amplitude, often lower than the $m = 4$ amplitude. As with the even harmonics, the higher-order odd harmonics ($m = 3, 5$) qualitatively resemble the evolution of the $m = 1$ harmonic. Analysis of the even–harmonic–only cusp simulation, where $\hat{a}_m = 0$ is artificially enforced for all radial subspaces $m \in \{1, 3, 5\}$ suggests that: (1) the $m = 1$ harmonic subspace is important for the formation of the bar, and (2) the $m = 1$ harmonic subspace is necessary for the long-term stability of the bar, particularly as it grows. In the even–harmonic–only cusp simulation, the bar that forms is only 75 per cent as strong as the bar in the fiducial simulation, despite having identical initial conditions,

[4] A lower disc-to-halo mass ratio or a warm disc leads to a less significant initial rearrangement.

and after $T \approx 2$ the bar decorrelates owing to a growing $m = 1$ amplitude that cannot be followed in the simulation.

The bottom panel of Figure 5.3 shows the pattern speed for the $m = 1$ (Ω_1) and $m = 2$ (Ω_2) harmonic orders, color–coded as in the middle panel. The higher–order harmonic orders exhibit the same pattern speed as the $m = 1$ and $m = 2$ orders for the odd and even harmonic orders, respectively. The $m = 2$ pattern can be interpreted as the pattern speed of the bar (Ω_p), particularly during the growth and steady-state phases. The assembly phase is moderately contaminated by outer disc activity, evident in the mis-match between the relatively large $m = 2$ amplitude and the relatively small trapped fraction during the assembly phase. The $m = 1$ pattern passes through the center of the simulation during the beginning of the simulation (up until $T = 3$), exhibiting a radial 'sloshing' or seiche mode where the phase angle of the $m = 1$ amplitude becomes zero. Near $T = 3$, the $m = 1$ pattern becomes locked to the phase of $m = 2$, and begins rotating with the bar rather than oscillating radially. The locking of the phases reveals a new mechanism for the bar to transfer angular momentum: the bar pattern transfers power to the $m = 1$ pattern imbuing net rotation on a previously seiche mode, causing the entire bar to orbit the center of mass of the combined disc-halo system.

The core simulation behaves similarly (compare Figure 5.4 to Figure 5.3). However, as discussed in Chapter 3 and Chapter 4, the onset of the growth phase occurs after an extended, semi-stable steady-state phase. For this reason, the evolutionary phases in the core simulation proceed as assembly, steady-state, and finally growth, as shown in the top panel of Figure 5.4. The x_1 family dominates the growth phase, as a new class of orbits related to a bifurcation of the standard x_1 track. Detailed orbit analyses show that it is these bifurcated x_1 orbits that are preferentially trapped. The ratio of A_4/A_2 increases with time just prior to and during the growth phase, which signals the appearance the x_1 bifurcation that drives the growth phase (see Chapter 3). In the core model, the $m = 1$ amplitude

has comparable maximum values to that of the $m = 2$ harmonic subspace during both the assembly and steady-state phases. However, the amplitude is significantly more volatile.

The bottom panel of Figure 5.4 shows the pattern speed of the $m = 2$ and $m = 1$ harmonics, color–coded as in the middle panel. The $m = 2$ pattern speed evolves as expected from standard secular evolution. During the growth phase, the pattern speed slows significantly and during the steady-state phase, the pattern speed is roughly constant, with a small decrease. The assembly phase is unlikely to be informative for bar evolution, as in the cusp simulation, owing to contamination by the outer disc $m = 2$ amplitude. In contrast to the cusp simulation, the $m = 1$ pattern begins at a much lower pattern speed and begins as a seiche mode, passing back and forth through the center. During the steady-state phase, the $m = 1$ pattern rotates about the center, as in the cusp simulation.

In contrast to many previous studies, we fully capture the different phases of bar evolution. The largest difference is that the bar stops slowing. It is an open question as to what determines the final pattern speed of the bar in these models. However, it is intriguing that in both models the asymptotic value of the $m = 2$ pattern speed (Ω_2) is some low integer fraction of the $m = 1$ pattern speed, Ω_1 ($\frac{1}{2}$ in the cusp model, 1 in the core model). In the cusp model, it appears that as the $m = 2$ harmonic subspace pattern speed approaches a low-integer commensurability with the non-evolving pattern speed of the $m = 1$ harmonic subspace. This commensurability breaks the secular evolution channel by causing Ω_2 to oscillate, inhibiting resonance passage. In the cusp model Ω_2 asymptotes to $0.5\Omega_1$, which means that the bar is displaced from the center in a rotating pattern such that when the bar completes a half rotation the $m = 1$ pattern has completed a full rotation. Visually, this appears as a constant offset of the bar from the center of the galaxy. The maximum displacement of the center is $0.3a$, which would be approximately 1 kpc in the MW. In the core model Ω_2 approaches Ω_1, but there is no obvious phase locking. We discuss the implications for studies of galaxy evolution in Section 5.4.3.1.

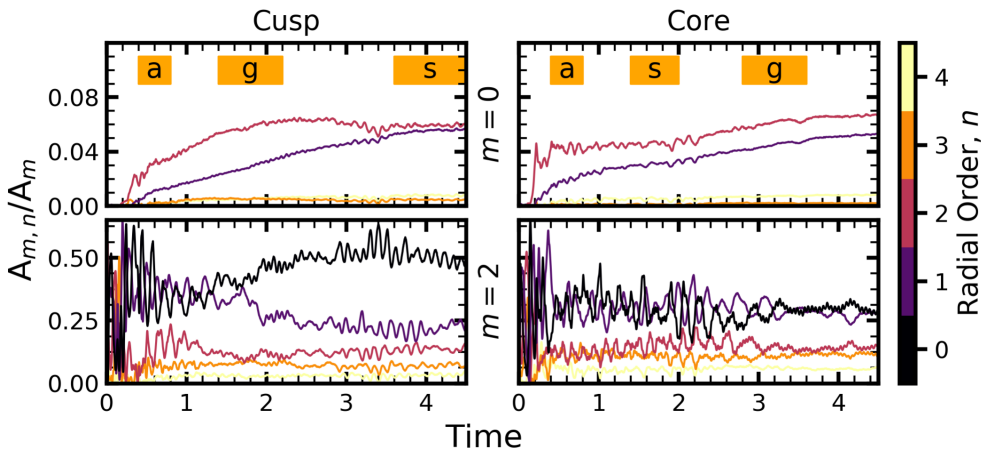

Figure 5.5. Amplitude in the first five radial subspaces (n) of the $m=0$ and $m=2$ azimuthal harmonic subspaces, normalized by the total amplitude in the corresponding harmonic subspace. The left panels are for the cusp simulation, and the right panels are for the core simulation. The upper row is $m=0$ and the bottom row is $m=2$.

5.3.2 Radial Subspaces

For any azimuthal subspace m, the amplitude of the radial harmonics indicate the radial scale of feature or response, as we described in Section 5.2.1. Radial and azimuthal orders together provide more detailed information than total azimuthal power, e.g. A_2. Throughout the section, we use the nomenclature (m,n) to refer to the specific radial subspaces n of a given harmonic order m. For example, the $m=2, n=2$ function will be denoted by $(2,2)$. When we discuss an entire harmonic subspace, for example the $m=2$ harmonic subspace, we denote that as $(2,n)$.

Consider, for example, the monopole $(0,n)$. The $m=0$ subspace has no phase information, and the amplitude is simply set by the total mass in the model (which we use as a normalization in the previous section). However, the partitioning of the $m=0$ harmonic subspace into ranges by radial order can reveal the scale of any changes in the galaxy model. In Figure 5.5, we show the first five radial orders for the $m=0$ subspace (top row) and $m=2$ subspace (bottom row). The left column corresponds to the cusp simulation, and the right column corresponds to the core simulation. In each row, the individual lines have

been normalized by the total amplitude in the corresponding harmonic subspace, e.g. for the $m = 2, n = 2$ amplitude we plot $A_{m,n}/A_m$, using the notation described in Section 5.2.1.

The $(0, 0)$ amplitude always dominates as one would expect by construction since the lowest-order basis function is exactly the initial model. The total amplitude of the $(0, n > 0)$ radial subspaces does not exceed 13 per cent during the entire integration and has been omitted from the figure. Additionally, throughout the simulation, the ordering of the radial harmonics largely stays intact (i.e. $A_{m,n} > A_{m,n+1}$ for all n orders) for the $m > 0$ harmonic subspaces. Further, the radial orders are all in phase, except for the harmonic subspace locking that occurs at $T = 3.0$ in the cusp simulation, where the radial orders may be misaligned by up to $\pi/4$. Considering the $(0, n)$ radial subspaces for both simulations (the upper row of Figure 5.5), we see that the initial radial ordering does not apply. For $m = 0$, the $n = 2$ radial harmonic ($R_{\rm firstnode} = 0.6a$) describes the rearrangement of the disk mass when the bar forms. The $(0, 1)$ subspace ($R_{\rm firstnode} = 1.2a$) grows nearly linearly in both simulations, suggesting a gradual rearrangement of the disc by the presence of the bar. The higher order ($(0, n > 2)$, $R_{\rm firstnode} < 0.4a$) harmonics of the $m = 0$ subspace play a completely subdominant role, never exceeding more than 1 per cent *in total* of the $m = 0$ amplitude, suggesting that there is little small-scale rearrangement of the disc, and that the evolution is driven by the lowest-order radial harmonics.

The $m = 2$ harmonic subspace, which is responsible for the bar feature, may also be decomposed into radial orders. Here we see stark differences between the cusp and core simulations. Comparing the radial decomposition of the $m = 2$ order to the overall $m = 2$ amplitude in Figure 5.3, we see that the assembly phase is composed of equal parts $(2, 0)$ and $(2, 1)$ amplitude. The growth phase results in the $(2, 0)$ amplitude increasing while the $(2, 1)$ amplitude decreases in relative importance, before all n orders more-or-less stop evolving by the steady-state phase. The increase in the $(2, 0)$ amplitude is consistent with the lengthening of the bar, such that the order with the largest node spacing will gain proportionally more amplitude. Additionally, all n orders appear to participate in the harmonic-

locking at $T \approx 3$, exhibiting higher variance over the interaction phase described above. The $n > 4$ orders combine to have less than 5 per cent of the total $m = 2$ amplitude. In contrast, the core simulation reveals a bar composed of significantly different distribution in the radial subspaces. At all times, the $(2, 0)$ and $(2, 1)$ amplitude are comparable, even as the bar lengthens throughout the simulation. Further, the amplitudes of the $(2, n > 2)$ harmonics are larger than the analogous harmonics in the cusp simulation. The bar is thus supported by a wider spectrum of harmonics in the cored simulation than the cusp simulation. We cite this as evidence for the steady evolution of the bar in the cusp simulation, whereas the evolution bar in the core simulation is punctuated by periods of transformation, owing to the high variance in the $m = 2$ radial orders destabilizing the evolution and prohibiting coninued bar growth. When the variance in the radial harmonics of $m = 2$ decreases at $T \approx 3$ in the core simulation (lower right panel of Figure 5.5), the bar then begins its secular growth phase.

5.3.3 Summary

While the previous two sections describe particular features of the bar evolution that have clear signatures in the harmonic analysis, the overall trends help us classify and identify the dynamical mechanisms at work in the simulation.

Our key interpretations are as follows:

1. The $m = 2$ total amplitude correlates with the evolution in fully-formed bars, i.e., the $m = 2$ total amplitude traces bar growth in a bar-dominated galaxy, but is mixed with strong spiral arm activity when it exists. This is also true for the pattern speed; the total pattern speed of $m = 2$ is the bar pattern speed at late times, but during assembly may be biased by large-scale $m = 2$ arm activity in the model.

2. The $m = 1$ total amplitude plays a dynamically important role, and its presence should not be ignored. It both captures formation scenarios (as evidenced by the

instability of the even–harmonic–only simulation comparison), and slows the evolution in the cusp simulation through harmonic interaction (discussed further below).

3. The $m = 0, n = 2$ function appears to have a special correspondence with the bar, suggesting that this term may be directly associated with the bar monopole in simulations generally.

These interpretations are generally true between the two models, and provide a set of diagnostics with which to interpret additional simulations. We will make use of these results in future work.

5.4 Analysis

In this section, we use the basic findings from the previous section to offer a more nuanced look at the coefficients that make up the bar and how we can use these harmonics to learn about bar evolution. In Section 5.4.1, we extract the coefficients that pertain to the bar only both as a means of verification of the orbit methodology, and also as a means to examine harmonic function expansion analysis in more depth. In Section 5.4.2, we discuss the lack of buckling observed in our simulations, including physical and numerical reasons for why a vertical instability may not be present. In Section 5.4.3, we look at two effects that are not typically included in linear analyses of potentials and discuss their importance for galaxy evolution.

5.4.1 Bar Coefficients

In Section 5.3, we described the correlations between the bar trapped fraction and the directly measured coefficient amplitudes. In this section, we use the trapped fraction to partially accumulate the coefficients for the bar to characterize the bar in coefficient amplitude. We then use this information to examine the evolution of the bar at each of the three epochs. In Figure 5.6, we decompose the three strongest azimuthal harmonic orders

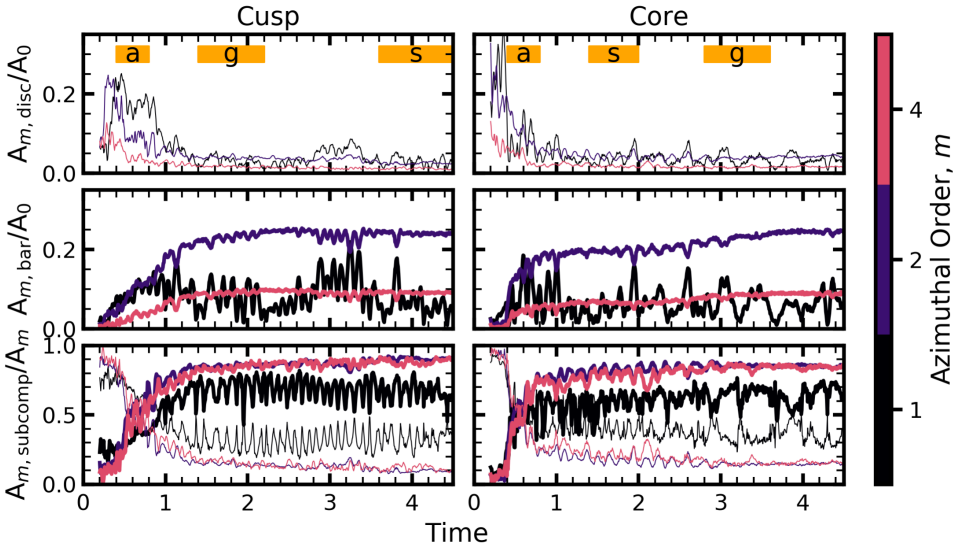

Figure 5.6. Decomposition of power in azimuthal harmonics by contribution to the bar feature. The left column corresponds to the cusp simulation, and the right column corresponds to the core simulation. Upper panels: the amplitude per harmonic order, for the untrapped disc only, normalized by the amplitude in the monopole. Middle panels: the amplitude per harmonic order, for the bar only, normalized by the amplitude in the monopole. Lower panels: the amplitude per harmonic order, subdivided by bar membership (thick solid lines) or non–bar membership (thin solid lines), normalized by the amplitude in the corresponding harmonic order. We show only the three strongest azimuthal orders by power normalized to the monopole, $m \in [1, 2, 4]$. The evolutionary epochs in each column are labeled: assembly (a), growth (g), and steady-state (s).

($m = 1, 2, 4$) into coefficients accumulated from bar particles (thick solid lines) and coefficients accumulated from particles not in the bar (thin dashed lines). The upper two rows of panels show the coefficients normalized to the monopole amplitude, and the lowest row of panels show the coefficients normalized to the total amplitude in the corresponding azimuthal harmonic order. The left column is the cusp simulation and the right column is the core simulation.

As expected, the $m = 2$ amplitude for particles in the cusp simulation that correspond to the bar strongly resembles the trapped fraction, growing rapidly during the assembly phase (a), linearly growing during the growth phase (g), and remaining constant during the steady-state phase (s). The $m = 2$ amplitude in the core simulation behaves similarly with its respective assembly (a), steady-state (s), and growth (g) phases. In both simulations, the $m = 4$ components of the bar strongly resembles those of $m = 2$. As discussed in Chapter 3, the A_4/A_2 ratio does not remain constant in either simulation, particularly in the core simulation, where the A_4/A_2 ratio increases during the growth phase and particles that are part of the bar dominate A_2 and A_4 for all the distinct evolutionary phases. A_1 is strongly affected by the bar with the exception of during the assembly phase in the cusp simulation, where A_1 is attributable to the untrapped disc particles rather than to the bar particles. It is also particularly evident in the upper panels that $m = 1$ trades amplitude with the $m = 2$ harmonic, and to a lesser extent with the $m = 4$ harmonic. We clearly see that the initial burst of $m = 2$ and $m = 1$ power in the simulations is a rearrangement that relates to the initial conditions rather than the true formation of the bar, which happens at a more modest pace. The bar increases rapidly in strength until $T \approx 0.5$, in contrast to the initial peak in $m = 2$ power, which occurs at $T \approx 0.1$.

The lower row of panels of Figure 5.6 is a different presentation of the upper two rows of panels, which confirms that the bar is the dominant source of amplitude in all harmonic orders (though not shown, this is true for $m = 3, 5, 6$ as well). At the end of both simulations, the bar accounts for greater than 80 per cent of the $m = 2, 4$ coefficient amplitude.

Not only does this confirm that the bar itself is the major source of non-axisymmetric disc distortion, it also serves as an implicit check of the orbit determination method, described in Chapter 3. It confirms that orbits may be efficiently and unambiguously attributed to the bar, as well as that we are not missing any significant population of bar-supporting orbits. The importance of the bar in $m = 1$ amplitude relative to the untrapped disc is surprising, but a subsequent orbit analysis shows that the bifurcated x_1 family, the x_{1b} family, is asymmetric with respect to the center and can sustain an $m = 1$ disturbance (Chapter 3). This same family is responsible for the strong 'beating' as the bar pattern speed approaches the natural $m = 1$ frequency (see below). It appears that the bar controls the majority of the $m = 1$ amplitude at all times after assembly, in both simulations.

5.4.2 Vertical Modes

We begin with a brief review of the low order ($m = 0, 1$) bending modes. The lowest-order mode for a disc embedded in a halo is the sloshing or 'seiche' mode (e.g. Weinberg, 1991). Subsequent works divided this response into multiple classes[5]: Sparke (1995) presents a 'bowl-shaped' $m = 0$ bending mode that results from the disc sloshing through the halo midplane, flexing into a bowl shape[6]. This mode is neutrally stable, meaning that it neither grows nor decays, in the case of a displacement from the vertical midplane. Merritt & Sellwood (1994) describe a 'bell' $m = 0$ mode, which is similar to the bowl mode except with radial nodes.

The allowed eigenfrequencies of a stellar disc are related to the 'stiffness' of the stellar disc (Sellwood et al., 1998). A stiff disc would have only very high eigenfrequencies and thus act like a rigid plate, where the tilt and translation of the disc are the primary drivers of $m = 1$ power. Lynden-Bell (1965) suggested that the mode supporting the Milky Way's

[5]The $m = 0$ 'breathing' mode is not likely to be a mode of interest in this case, so we ignore it here, but acknowledge that it may be important in other ways during the initial bar formation phase.

[6]This may also be the 'banana' mode that is sometimes used to describe polar ring galaxies.

integral sign warp could be a discrete mode of vertical vibration, similar to the Eulerian nutation of a coin thrown spinning into the air (a modification of the rigid-tilt mode of the disc). Later works (e.g. Hunter & Toomre 1969; Weinberg 1991) discuss this $m = 1$ mode as an outwardly propagating bending wave excited by some perturber. The exact modes are highly dependent on the halo model, with flattened halos providing support for such a warping mode. Further, the $m = 1$ modes have not been shown to result in lasting heating of the stellar disc (Sellwood et al., 1998), so we will assume that owing to the lack of persistent $m = 1$ vertical power in our simulations during the secular growth epoch that those modes are not driving buckling instabilities.

Sellwood & Debattista (2009) point out that the buckling mode depends on a variety of factors (some physical and some numerical), en route to their main point that the buckling mode can be exacerbated by stochasticity effects. Their simulations show prominent, but variable, buckling. This results in a rapid weaking of the bar-measuring A_2/A_0. In their Appendix B, Sellwood & Debattista (2009) examine the effect of their choice of some basic numerical parameters. If a sudden drop in A_2/A_0 is to be believed as a hallmark of buckling, then both the grid resolution and softening length appear to profoundly affect the buckling instability. As pointed out by Sellwood (2006), the vertical resolution in a softened simulation will weaken the vertical forces and, therefore, increase the vertical oscillation period of disc particles. When the bar buckles, the in-plane motion of particles are coupled to vertical motions, meaning that a buckling mode can have a back reaction on the formation of the bar. Whether this implicates numerical problems at large is a subject of debate.

The excitation of a vertical instability, or 'buckling', which is commonly observed in simulations of barred galaxies, has recently been proposed to be a generic part of the bar-formation process in disc galaxies. The buckling instability has been implicated as the primary cause of observed 'peanut' bulges (see Sellwood 2014 for a review), though the peanut shape in barred simulations has been observed since Combes & Sanders (1981).

The original explanation of bar buckling in a simulation comes from Raha et al. (1991), which they attribute to the firehose instability in the sense of Toomre (1966) and Araki (1985). The vertical disturbance in Raha et al. (1991), is a $m = 2$ buckling instability with a characteristic saddle shape. However, other instability explanations exist, such as the presence of a strong resonance (as argued in theory by Pfenniger (1998) and shown in simulations by Saha et al. (2013)) rather than a strong gradient in the velocities, as in a fire-hose instability.

In Debattista et al. (2006), the description of bar buckling describes what seems to be the brief ($\Delta t < 100$ Myr) formation and dissipation of bending modes during the violent bar formation phase. The bending modes, when inspected by eye, appear to be a mixture of $m = 0$ and $m = 2$ modes, where the $m = 2$ modes have a different pattern speed than the bar. These are long-wavelength disturbances $\lambda > 2R_{\rm bar}$ that may persist, resulting in a peanut shape. In Martinez-Valpuesta et al. (2006b), the bending modes are even more extreme, with the wavelength of the (presumably) $m = 2$ modes increasing with each of three subsequent buckling events. They argue that the two primary explanations: the fire-hose instability (Toomre, 1966; Raha et al., 1991; Merritt & Sellwood, 1994) and resonance heating (Pfenniger & Friedli, 1991) can be reconciled if buckling is merely viewed as shortening the secular timescale for particle diffusion out of the plane. Sellwood & Debattista (2009) run simulations with symmetry imposed about the midplane and find that the bar strength (measured as A_2/A_0) continues to grow throughout the entire simulation. This leads to an interpretation of the buckling instability as a self-regulating mechanism. Additionally, if $m = 1$ is disabled, Sellwood & Debattista (2009) find that all simulated bars buckle violently as a result of an instability resulting from the inability of the potential to respond to a mildly lopsided distribution[7]. Their conclusion is that it 'seems unlikely that

[7]We do not find this in our even–harmonic–only cusp simulation.

such small offsets could have such a large effect on the saturation of the buckling mode, we think it is possible that an antisymmetric mode competes'.

Saha et al. (2013) studies the meridional tilt of the velocity ellipsoid in model barred galaxies, finding that the tilt reaches a peak that triggers the onset of bar buckling. They argue that the meridional tilt is a better indicator of the onset of buckling than the σ_z/σ_r ratio. After the bending modes are excited, the amplitude gradually increases and drifts out to larger radii. However, Saha et al. (2013) finds that a bar which grows slowly does not experience a buckling instability. They attribute the slow growth of the bar to the selection of Toomre Q for the disc. Lastly, Erwin & Debattista (2016) makes a claim for observing a bar in the act of buckling, i.e., when the $m=1$ vertical power is largest, finding that all observed bars are consistent with having gone through a buckling phase.

Given these previous findings, one might naturally look at the strongest non-axisymmetric disturbance in the simulation as evidence for buckling. However, an inspection at the peak point of the A_2/A_0 in the cusp model shows that amplitude in the vertically asymmetric terms is still weak. To identify bending modes, we isolate the vertically asymmetric terms in the basis and examine their power as a function of time. In our basis, we include three vertically asymmetric functions, $(0,9)$, $(1,10)$, and $(2,11)$[8]. The $(2,11)$ function is shown in the lower panel of Figure 5.2.

We find mild bending modes at early times with no apparent lasting effects. The cusp and core models both exhibit mild $m=2$ bending after a more powerful $m=0$ bending mode, as indicated by the amplitude in vertically-asymmetric harmonics. The core model exhibits a peak $m=2$ power that is larger than that of the fiducial model. The cusp model shows a stronger $m=1$ harmonic subspace that is likely a consequence of the visible seiche mode. The amplitude of all the bending modes has a $|z|_{\max}$ of approximately $0.05a = 0.5h$

[8]The inclusion of vertically asymmetric terms is related to the disc scaleheight and number of radial terms included. Thus, a thick disc would naturally admit more vertically–asymmetric functions, while a very thin disc would admit none in the first 12 radial orders.

during the $m = 0$ dominated phase, while $|z|_{\max} = 0.025a = 0.25h$ when the A_2/A_0 ratio is largest in the cusp model and $|z|_{\max} = 0.066a = 0.66h$ in the core model. Our observed buckling modes are bisymmetric with respect to the disc plane, along the bar, and are confined to be within a bar radius. The modes observed in Debattista et al. (2006) extend past the end of the bar along the bar major axis, but are confined to be within the bar along the bar minor axis. In both our simulations, the disc does not exhibit any bending modes after $T = 0.5$. However, at $T = 0.5$, the disc is still quite thin, thickening only at late times after the bar has formed, and is far removed from any possible bending mode. We do observe a peanut shape for the inner region of the galaxy in both models at late times, but it does not result from a bending mode. Thus, the persistence of the peanut shape in other simulations remains a mystery. If the wavelength of the bending mode is greater than $R_{\rm bar}$, as in Debattista et al. (2006), it is difficult to see how it is the parent of the peanut shape. In a key difference from our work, the length of the bar and the peanut bulge are often $> 2a$ in other works, suggesting that at the very least, potential differences are at play, most likely attributable to the halo model. We will defer a discussion of bulge formation and disc thickening to Chapter 6.

5.4.3 Nonlinear Modes

In this section, we highlight two relevant planar mode features for their importance to bar evolution that are not explicitly captured in a linear analysis of bar evolution: the importance of $m = 1$ for the bar (Section 5.4.3.1) and short-timescale beating modes in the bar (Section 5.4.3.2).

5.4.3.1 Dipole ($m = 1$) Modes

The existence of $m = 1$ modes in both the real universe and simulations has been discussed and presented many times in the literature. Colin & Athanassoula (1989) demonstrated that offset bars would have a deforming effect on the morphology of galaxies, relocating the Lagrange points that are crucial for parenting stable orbits just outside of the

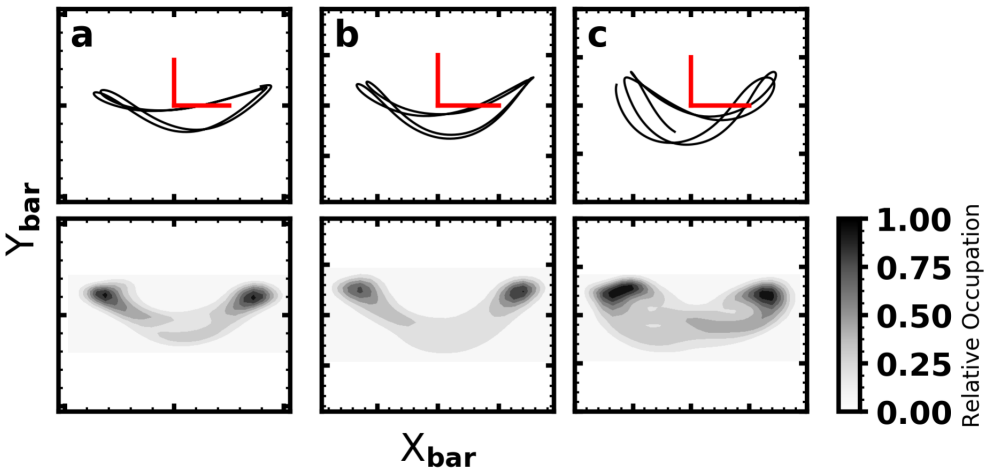

Figure 5.7. Example asymmetric x_{1b} orbits that support the increase in $m=1$ power at $T=3$ in the cusp simulation. The upper panels are orbit trajectories and the bottom panels are time-averaged densities. For scale, the red lines are half a scalelength.

bar radius. However, our post-simulation orbit analysis forces the bar and halo wake to have the same pattern speed for several rotation periods, which is not true in self-consistent simulations[9]. Athanassoula (1996) reproduced one-armed spiral morphology in simulations and noted the importance of the impact position with respect to the bar. In the following year, Athanassoula et al. (1997) found that the displacements of the centers are accompanied by changes in the bar pattern speed and bar size.

On the observational side, Zaritsky et al. (2013) studied $m=1$ distortions in 167 galaxies from the S^{4}G sample of nearby galaxies to determine the origin of lopsidedness in galaxies. While $m=1$ largely increased with radius, the $m=1$ strength was not related to the presence or absence of a bar, or bar strength if a bar is present. Saha & Jog (2014) examined angular momentum transport in lopsided galaxies through the paradigm of Lynden-Bell & Kalnajs (1972). An extreme example of $m=1$ power might be the Large Magellanic Cloud

[9]The pattern speed of the $m=1$ and $m=2$ components do in fact reach an equilibrium in our fiducial simulation, as we discuss below.

(LMC) (Pardy et al., 2016), which exhibits both a one-armed spiral and a bar offset from the dynamical center of mass. The Milky Way and Small Magellanic Cloud have long been implicated in the formation of structure in the LMC, and it stands to reason then that the MW or SMC would be the cause of the $m = 1$ disturbance. Pardy et al. (2016) modeled the LMC-MW interaction and found that the stellar disc of the LMC was shifted away from the dynamical center of the galaxy, rather than the bar itself being shifted to being off-center.

Despite the clear contribution of the bar to the $m = 1$ harmonics and a non-zero amplitude during our simulations, the orbit analysis in Chapter 3 completely ignored the existence of the $m = 1$ harmonics and still created orbital structures that matched the structure observed in the self-consistent simulations (both cusp and core). Therefore, we are left wondering whether the $m = 1$ effect is a true physical effect, or merely excited by noise in the simulations with little true effect on the evolution. Both could be true, in the sense that noise in the simulation may be physical in origin rather than numerical (and thus aphysical), where the $m = 1$ harmonics are required to adequately resolve this effect. Evidence bolstering this conclusion comes from the cusp simulation run using only even azimuthal harmonics, where late-time $m = 1$ amplitude growth substantially weakens the bar. Further, the bar that forms in the even–harmonic–only cusp simulation is appreciably different from that in the full simulation: it reaches only half the maximum amplitude of the cusp bar, and is more compact. Given that the $m = 1$ amplitude during the assembly phase is not attributable to the bar itself, the initial $m = 1$ likely relates to a readjustment of the disc, which enables the bar to grow further.

The excitation of $m = 1$ at early times clearly relates to the formation of the bar, and damps before $T = 1$ in both models (upper panel of Figure 5.6). At $T = 3$ in the cusp simulation, we see oscillations in both $m = 2$ and $m = 1$ power that appear to mirror each other, which probably is a sign of power exchange: 'harmonic–locking', which we labeled as 'interaction' in Figure 5.3. The harmonic locking appears to be a feature of the specific cusp model and is in fact not observed in the core model, but there is likely a class of

models with a combined disc and halo that have a higher $m = 1$ pattern speed (cf. bottom panel of Figure 5.3). A slightly different model may not result in this harmonic locking. In this sense, it is not 'coincidental' that the asymptotic value of Ω_2 is half that of Ω_1.

Such harmonic coupling is a nonlinear process, which makes the study of harmonic coupling in simulations the only clear path forward to understanding its dynamical implications. In the cusp simulation, we conclude that harmonic coupling results from the bar attempting to transfer angular momentum into any reservoir available, and finding the $m = 1$ harmonic—an extra dynamical degree of freedom, even while the disc transfers $L_{\rm z}$ to the combined $m = 1$ and $m = 2$ system.

Whether the two patterns may phase lock and still exchange $L_{\rm z}$ is still an open question that begs more study. A cursory analysis of the torque τ induced during the proposed harmonic-locking phase at $T = 3$ of the cusp simulation (Chapter 4) reveals a changing character with an increase in $m = 1$ amplitude, leading us to conclude that the $m = 1$ harmonic is being torqued by the outer disc as it attempts to transport angular momentum inward. The $m = 1$ bar feature is supported by the phase coherence of the asymmetric x_{1b} orbits[10]. Examples of asymmetric x_{1b} orbits are shown in Figure 5.7. Taken together, the determination of orbits reinforcing the $m = 1$ amplitude and the reduction of torque on the bar to zero supports our conclusion that the $m = 1$ amplitude is a real dynamical effect with evolutionary importance.

If systems can exhibit harmonic locking with low-level integer commensurabilities, the exchange of power will have wide-ranging implications for the dynamics. The frequency range for the $m = 1$ pattern is narrow (e.g. Weinberg, 1994) and the bar pattern speed changes by a factor of 2-3 during its evolution (see Figures 5.3 and 5.4). Therefore, it seems likely that the frequency of $m = 2$ (bar) will be commensurate with that of

[10]In principle, the symmetric x_{1b} orbits could also reproduce this effect, and indeed we note considerable family switching between the symmetric and asymmetric x_{1b} orbits, but in the particular case outlined here, the $m = 1$ amplitude is supported by the x_{1b} orbits.

$m = 1$ (seiche) at some point during its evolution. For a system with weakly damped $m = 1$ modes, an interaction with $m = 2$ would be expected. Unfortunately, the method used in Weinberg (1994) to determine the frequency of the allowed $m = 1$ modes, calculating the dispersion relation for the halo-disc system, only applies to weak perturbations and not a strongly barred galaxy like we have here. We, therefore, must resort to a larger suite of barred galaxy models (Chapter 7) to predict the importance of this harmonic–locking in nature.

We find that the coupling between the $m = 1$ and $m = 2$ harmonic subspaces exists well above the Poisson noise level by a factor of 100 in amplitude. We also track the center-of-mass for both the disc and halo expansion, finding that the offset of the two is never larger than 5 per cent of a disc scalelength. Therefore, force errors caused by basis incompleteness is unlikely to be an issue, thereby alleviating the concern that harmonic locking is numerical in origin.

5.4.3.2 Beating Modes

Some responses are identified in the basis coefficients through their amplitudes beating between two different harmonic subspaces, which may be either azimuthal (as above between $m = 1$ and $m = 2$), or between radial orders in the same azimuthal subspace. We observe the responses to trade power on a bar rotation timescale. Beating occurs when two oscillators have similar, but not exact, frequencies. In particular, this indicates nonlinear behavior that is not easily captured via other methods, so we study the possible contributions of beating to our models here, specifically asking whether beating affects the bar evolution.

As an example, we consider the $(2, 1)$ and $(2, 2)$ terms in the cusp model (the lower left panel of Figure 5.5). We see that the amplitude of a given $m = 2$ order can change by 20 per cent in opposing directions as a result of high-frequency variation in the coefficients (beating) while the overall amplitude of the entire m order does not exhibit any higher-order

variation (cf. A_2/A_0 in Figure 5.3). One may naturally question whether this rapid variation has an effect on the resultant potential that would bias a detailed analysis of the orbit structure. For example, selecting a snapshot of the potential at $T = 1.75$ versus $T = 1.8$, less than a bar rotation later, would result in a different n spectrum of amplitudes. However, the radial harmonics appear to be matched in phase, suggesting that the amplitude variation is related to changing structure in the bar rather than the presence of harmonic–locking (as in the case of $m = 1$ and $m = 2$ above). Ideally, one would study the spatial correlations between basis features and the coefficient time series, but such a study is beyond the scope of this chapter. We find that the small scale beating does not change the overall quality of the orbital structure on short timescales, such that one may confidently analyze the evolution of the bar over the $\Delta T \approx 1$ phases we identify.

A second example of higher-frequency beating is illustrates that we are not likely merely capturing numerical artifacts. In the $m = 2$ amplitude at $T > 3$ in the core simulation, as shown in the lower right panel of Figure 5.5, the amplitude of variations suddenly shifts from of order 5 per cent to of order 1 per cent. The frequency of the beating changes to a higher order multiple of the bar period as the pattern speed decreases, as expected, suggesting that this interaction is dynamical in nature and not a numerical artifact. We also find that the bar pattern is the main driver of the beating response with a 1:1 frequency ratio. This suggests that the bar beats with the outer disc, which is corroborated by the semi-periodic variations in the bottom panels of Figure 5.6, where the fraction of amplitude in the bar trades off with that in the untrapped disc on roughly a bar period in both simulations.

Thus, we have alleviated our two main concerns resulting from evident beating in the coefficients: (1) interpretations of bar structure from linear, fixed potential analysis (e.g. Chapter 3) are not strongly affected by amplitude beating between radial orders within a harmonic order, and (2) amplitude exchange between radial orders corresponds to resolvable dynamical processes, not artifacts in the basis.

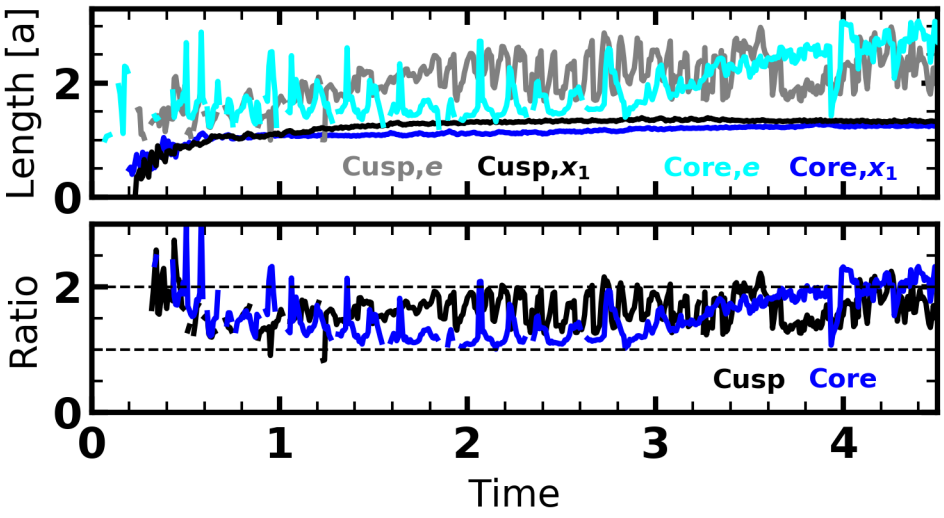

Figure 5.8. Upper panel: The length of the bar in disc scalelengths, measured in both simulations (cusp and core), using two different techniques: maximal x_1 extent and ellipse fits, versus time. The cusp simulation ellipse–fit derived length is shown in gray, while its x_1-derived length is in black. The core simulation ellipse–fit derived length is shown in cyan, while its x_1–derived length is in blue. Lower panel: The ratio of the ellipse–fit derived length to the x_1–derived length versus simulation time for the cusp (black) and core (blue) simulations.

5.5 Observational Diagnostics

In this section, we discuss two different avenues with which to observationally interpret bars. In Section 5.5.1, we describe orbits that bias ellipse fits of bars and demonstrate how ellipses may overestimate the length of the bar. In Section 7.3.4, we present a kinematic method to determine the maximal length of the bar-parenting x_1 orbit in real galaxies.

5.5.1 Dressing Orbits

In this section, we discuss relevant observational diagnostics and the possible pitfalls inherent in attempting to measure bars from surface density measurements. We describe how the standard ellipse–fitting approach gives biased quantities (length, mass, pattern speed) when compared to the maximal extent of true trapped bar orbits in the x_1 'backbone' family. In practice, the maximal extent of the x_1 family is never truly reached, as demonstrated in the orbit analysis of Chapter 3, so methods that parameterize the length

of the bar as the maximal theoretical x_1 extent may also overestimate the actual bar length (Martinez-Valpuesta et al., 2006b).

We refer to orbits that are not trapped by the bar, but are still in the physical vicitinity of and are affected by the bar as 'dressing' orbits. Dressing orbits confuse the normal metrics by which bars are measured, in particular ellipse fits and Fourier-derived strengths. A standard ellipse fit to the bar may overestimate the mass and length of the bar by a factor of two during the formation phase! At later times, the length of the bar may be overestimated by 50 per cent. One needs an accurate length for the true bar orbits to observationally determine the pattern speed (see e.g. Pérez et al. 2012). The dimensionless parameter $\mathcal{R} = R_{\rm CR}/a_{\rm bar}$ where $R_{\rm CR}$ is the corotation radius and $a_{\rm bar}$ is the semi-major axis of the bar, as given in Binney & Tremaine (2008), denotes the 'slowness' of the pattern speed. As discussed in Binney & Tremaine (2008), this parameter can be hard to measure in real galaxies for two reasons: (1) the bar does not have a sharp end, and (2) corotation does not have a clear definition for strong non-axisymmetric disturbances, e.g. a strong bar. However, several studies have attempted to measure either the pattern speed or the dimensionless parameter to characterize the bar. Thus, an overestimate for the true dynamical length of the bar overestimates the pattern speed, sometimes significantly.

Assuming a constant mass–to–light ratio, we apply the standard ellipse-fitting analysis to our simulations. We compute the face-on surface density at a resolution of $0.025a$, which for a MW–like galaxy corresponds to 75 pc[11]. We measure the length of the bar using a standard method: determine best-fit ellipses at many different surface densities and assign as the bar length to the semi-major axis value, a, where the ellipticity drops below a certain threshold or has a discontinuity. Here, we choose the semi-major axis where the ellipticity $e \equiv 1 - \frac{b}{a}$, and b is the semi-minor axis value, first drops below 0.5, which in practice is also the same location as the discontinuity in e that corresponds to the transition between

[11]In practice, the ellipse fits do not turn out to be highly dependent on the resolution, introducing approximately a 10 per cent error.

bar–dominated contours and disc–dominated contours. In addition, we have a dynamically-informed metric for the length of the bar: the maximum extent of the x_1 family (Chapter 3). Figure 5.8 shows a comparison of the maximum x_1 extent versus ellipse–fit derived bar lengths. In the upper panel, we show the measured bar lengths for the cusp and core simulation measured using both techniques. The ellipse fit length in the cusp simulation (gray line) grows steadily at $T < 2.5$. This roughly mirrors the trapped fraction growth, but when compared to the maximal extent of the x_1 orbits (black), we see that this is an extreme overestimate for the length of the trapped component. The periodicity in the ellipse measurements results from the outer disc $m = 2$ disturbances coincidentally aligning with the bar. At early times when the bar is forming, this can result in variations of nearly a factor of two. Even at later times in the cusp simulation, the variation in ellipse–fit length is 25 per cent over short ($\delta T = 0.1$) timescales owing to the $m = 2$ alignment.

For the core simulation, the ellipse measurements oscillate during the assembly epoch (cyan in Figure 5.8), as spiral arms align and anti-align with the bar on bar-period timescales. As the simulation progresses, the variations from the outer disc $m = 2$ features weaken, and the ellipse–fit appears to largely agree with the maximal x_1 (blue for the core simulation). However, as the core simulation enters the growth phase near $T = 3$, the two measurements begin to diverge. After some growth in the trapped fraction (cf. Figure 5.4), the shallow surface density profile at the end of the bar conspires with the lengthening bar to find new ellipse contours and the ellipse–fit length increases rapidly. While this scenario may not occur in every model, it is not an artifact of tuning; as we adopted a standard implementation of ellipse fitting procedues and parameters. There is little reason to suspect that similar effects could not be at play in real galaxies. We conclude that the length of a bar as measured from ellipse fits should not be interpreted as an age indicator.

The lower panel of Figure 5.8 summarizes the overall results of our comparison. We plot the ratio of the ellipse–fit length to the maximal x_1 length for the cusp (black) and core (blue) simulations. The ellipse–fit length is a large overestimate for the length of the

x_1 orbits at all times in the cusp simulation, typically by a factor of two, except during the assembly phase when the overestimate is a factor of 1.5. In the core simulation, the ellipse–fit length is a reasonable estimate for the maximum extent of the x_1 orbits during the steady-state phase near $T = 2$, but overestimates the length during assembly by a factor of 1.5, and is a considerable overestimate for the length at late times ($T > 3.4$), after the bar stars to grow by trapping. Taken together, the cusp and core simulations reveal the ambiguity in ellipse–fit determinations of bars. Ellipse–fits should be taken as a measure of the total mass distribution of the galaxy, not as the mass directly associated with a bar.

5.5.2 Kinematic Signatures

In this section, we describe an observational technique that can measure the maximal extent of x_1 orbits using a kinematic diagnostic that can be produced with current and future generation integral field units (IFUs). The technique works by exploiting the velocity tangential to the bar axis, which for trapped x_1 bar orbits, will be low compared to disc orbits. The signal will be largest where the discrepancy between bar orbits and disc orbits is largest: at the 'four corners' of the bar. This suggests that a kinematic metric using four–fold $m = 4$ symmetry will reveal the largest difference between bar and disc velocities. The difference between the velocities of bar and disc orbits will be negative at the corners of the bar, and so we expect the $m = 4$ velocity moment tangential to the bar, $v_{4\perp}$, to be appreciably negative. As the bar slows, we expect this quantity to become even more extreme, since the velocity between the untrapped disc orbits and the bar pattern speed becomes more discrepant (Chapter 3). To test the significance of the signal relative to that of the bar, we compare the $m = 2$ and $m = 4$ velocity moments, $v_{4\perp}$ to $v_{2\perp}$.

The procedure to observationally determine the maximal extent of x_1 orbits is as follows:

1. Compute the *magnitude* of the velocity perpendicular to the bar, $v_\perp$.

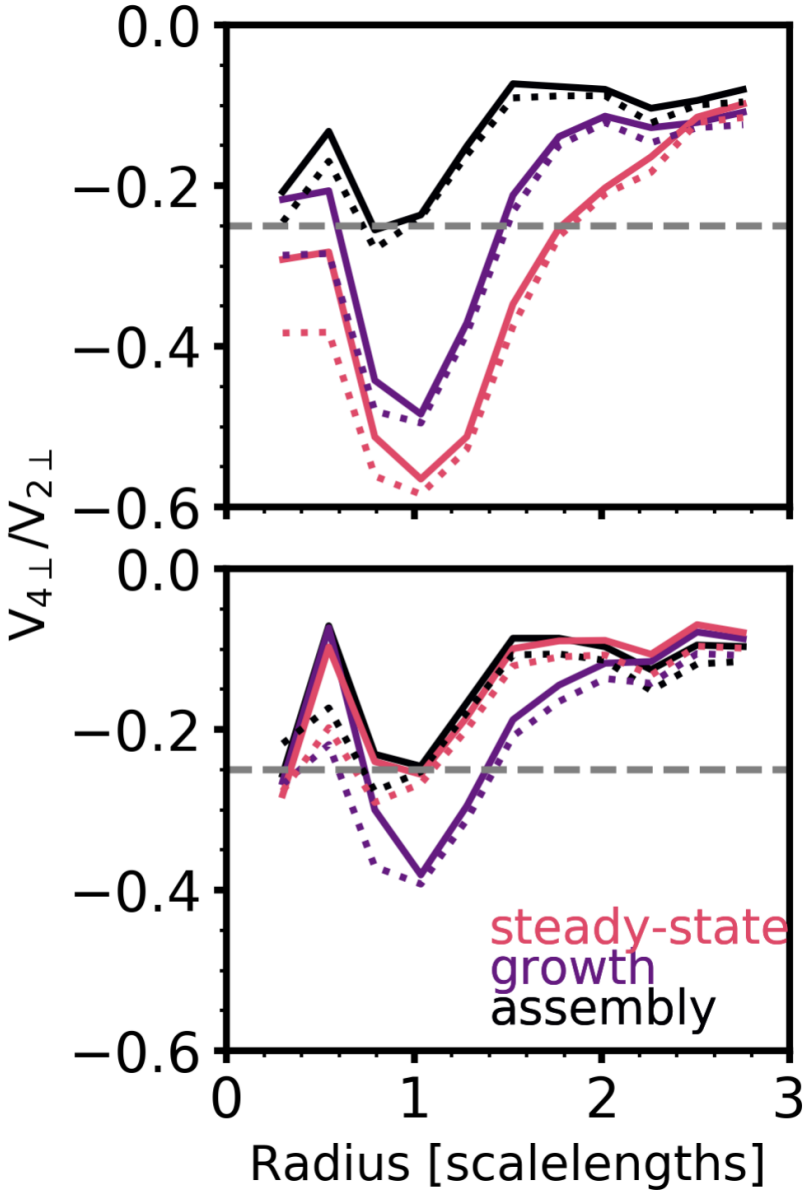

Figure 5.9. $v_{y\perp}/v_{2\perp}$, as a function of radius in annular bins, computed from the magnitude of the velocity tangential to the bar, $v_\perp$. The solid lines are computed from images degraded to $\delta v = 0.05$ resolution, and the dotted lines are from images degraded to $\delta v = 0.02$ resolution. The radius minimizing $v_{4\perp}/v_{2\perp}$ corresponds to the approximate maximal extent of the x_1 family of orbits present in the model. The value of the minimum indicates the strength of the measurement. The dashed line at $v_{y4}/v_{y2} = -0.25$ is our empirically–determined threshold for a trustworthy measurement.

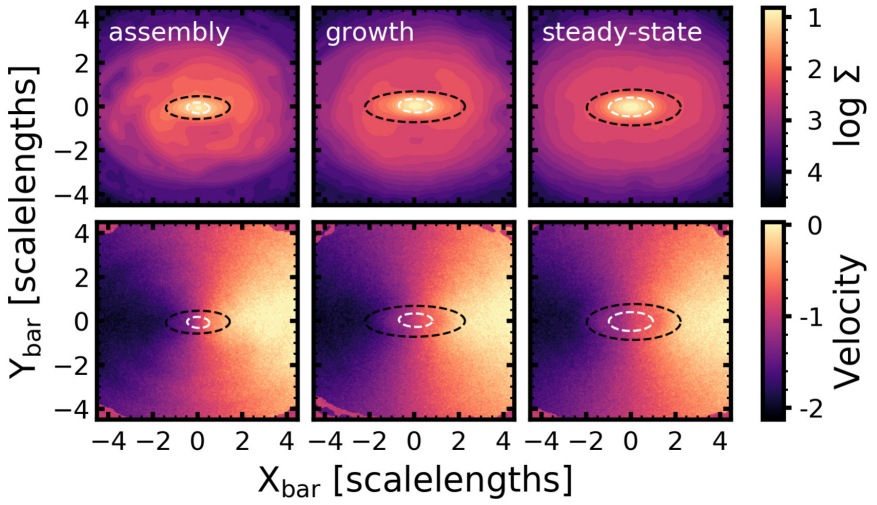

Figure 5.10. Upper panels: Log surface density, in normalized units, for three phases in the cusp simulation, where the simulation has been rotated so it is viewed at a 45° angle: assembly, growth, and steady-state. Lower panels: Velocity field in the direction tangential to the bar, for the three phases in the upper panels, degraded to a velocity resolution of $0.1v$. The white dashed ellipses show the maximum extent of the trapped x_1 orbits, which coincides with the dimple in the velocity field of the growth and steady-state phases, as calculated from $v_{4\perp}/v_{2\perp}$ for the velocity field tangential to the bar (see text). The black dashed ellipses show the best-fit ellipse fit to the bar from the surface density plot alone.

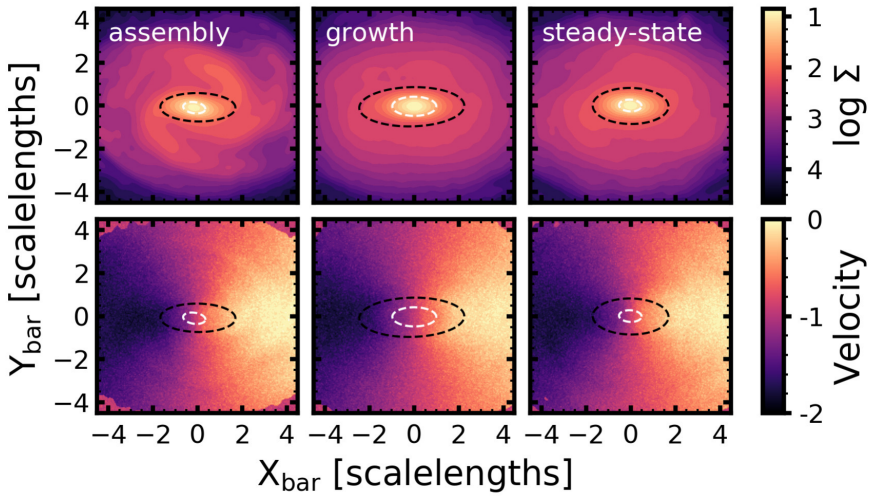

Figure 5.11. The same as Figure 5.10 but for the core simulation. The three columns correspond to the phases of evolution, preserving the order as in Figure 5.10, though in time, the steady-state comes before the growth phase in the core simulation.

2. Compute the $m=2$ and $m=4$ Fourier velocity components as a function of radius, $v_{2\perp}(r_j), v_{4\perp}(r_j)$, where the $\{r_j\}$ are annular radii. One must take care not to reduce the S/N by choosing annuli that are too small relative to the spatial resolution. We suggest a minimum annular radius of $\delta r = 10\delta x$, where δx is the pixel scale.

3. Locate the radius for the $\min\left\{v_{4\perp}(r_j)/v_{2\perp}(r_j)\right\}_j$. As long as $\min\left\{v_{4\perp}(r_j)/v_{2\perp}(r_j)\right\}_j < -0.25$, this method is reliable and the minimum approximately equals the maximal extent of the x_1 orbits.

To use this metric, one requires high spatial and velocity resolution, coupled with a modest inclination. As a general guideline, the spatial resolution required to determine the $v_{y\perp}/v_{2\perp}$ metric is $\delta x = 0.05a$, where a is the disc scalelength, for a galaxy at an inclination of 45°. The velocity resolution required is $0.05v_{\rm max}$, where $v_{\rm max}$ is the maximum circular velocity. For a MW-like galaxy, this translates to $\approx$10km s^{-1} velocity resolution and 150 pc spatial resolution. We determine the threshold $\min\left\{v_{4\perp}(r_j)/v_{2\perp}(r_j)\right\}_j < -0.25$ empirically by executing the method on galaxies during the assembly phase, for which we do not expect the velocity field to recover the bar feature, and compute the $\min\left\{v_{4\perp}(r_j)/v_{2\perp}(r_j)\right\}_j$ value obtained spuriously, finding this value to be approximately -0.25. Current image–slicing instruments such as MUSE should be able to look for this effect. For example, the data published in Gadotti et al. (2015) featured 12 pc spatial resolution with $\approx$10km s^{-1} velocity resolution in the nearby barred galaxy NGC 4371 ($d = 16.9$ Mpc) using MUSE. While the spectral resolution is at the limit of what is needed to discern the $v_{y\perp}/v_{2\perp}$ effect, the superior spatial resolution provides an excellent opportunity to look for velocity features directly attributable to a particular orbit family.

In Figure 5.9, we show results using the method, for both the cusp (upper panel) and core simulations (lower panel). As expected, both simulations show negative $v_{y\perp}/v_{2\perp}$ values, driven by the effect at the corners of the bar. The solid lines are computed from velocity images degraded to $0.05v_{\rm max}$, in annular bins that are $0.15a$ in width, for a galaxy

inclined[12] at 45° and with a bar position angle of 0°. We compute the dotted lines with velocity images degraded to $0.02v_{\max}$. We have tested the metric for a range of inclination angles, position angles, velocity resolutions, and spatial resolutions to develop the observational rules-of-thumb presented above. In the cusp simulation (upper panel), the signal is very strong during the growth and steady-state phases, with no discernable signature in the assembly phase. One expects a low signal in the assembly phase as the kinematic feature results from trapped, evolved orbits that develop at the start of the growth phase. In the core simulation (lower panel), the signal is only particularly strong during the growth phase, although we are able to tease out accurate lengths in the assembly and steady-state phases that are marginally significant. Higher velocity and spatial resolution, not feasible using current instruments, makes a modest difference, particularly in the case of the core simulation. Comparison with maximal x_1 extents (computed in Chapter 4, as shown in Figure 5.8) shows that the minima of $v_{y\perp}/v_{2\perp}$ is within 10 per cent of the maximal x_1 orbit radius, making this technique a powerful descriminator of the dynamically-relevant maximal x_1 orbit.

In Figures 5.10 and 5.11, we compare our velocity moment method with standard ellipse fits. The upper panels of Figure 5.10 show the face-on surface density for the three identified phases of bar evolution, and the lower panels show the y-component of the velocity (perpendicular to the bar) for each of the three phases. The velocity resolution has been degraded to a velocity resolution of $10\mathrm{km\ s^{-1}}$ by injecting random noise into the measured velocity field. In each phase, we plot the standard technique (ellipticity drop) best-fit ellipse in dashed black, while the ellipse that corresponds to the minimum of $v_{y\perp}/v_{2\perp}$ is shown in dashed white. As shown in Figure 5.9, while we may compute a minima in the $v_{y\perp}/v_{2\perp}$ value for the assembly phase, it is too small to say anything about the orbit struc-

[12] In practice, the inclination of the galaxy merely weakens the signal; if the minima satisfies $\min\left\{v_{4\perp}(r_j)/v_{2\perp}(r_j)\right\}_j < -0.25$, the result is trustworthy.

ture with certainty[13]. However, during the growth and steady-state phases, strong signals are observed in A_4/A_2 which show the maximal extent of the x_1 orbit family. As described in Section 5.5.1, the discrepancy between ellipse-fit lengths and maximal x_1 orbits can be significant. In the core simulation (Figure 5.11) we see much the same effect as in the cusp simulation, and we are able to calculate a relevant x_1 bar length during the assembly phase owing to the rapid construction of the x_1 family (cf. Figure 5.4). Again, the best-fit ellipses and the maximal x_1 extent are appreciably different, as in Figure 5.8.

This technique is a simple, albeit observationally expensive, way to search for the dominant barred galaxy orbit, the x_1 family. Determining the maximal extent of the x_1 family is the first step to determining a dynamically-relevant length for the bar, and a more accurate measure of the trapped fraction in galaxies.

5.6 Conclusions

We studied two bar-forming, initially exponential disc models with equal mass dark-matter halos with harmonic analysis using the biorthogonal basis intrinsic to the potential solver in the BFE implementation of EXP. The initial disc profiles are identical while one halo profile is cuspy and one is cored. We describe the two barred galaxy models in terms of azimuthal and radial harmonics, correlating previously obained features of orbits families and evolutionary phases with the radial and azimuthal harmonics.

The main results are as follows:

1. Decomposition of barred galaxy models using orthogonal functions can provide a qualitative description of evolutionary phases for barred galaxies, and provide computationally inexpensive predictive power for the underlying structure of model evolution. The 'summary' nature of BFE, where the three-dimensional potential of the

[13]With the omniscience provided by simulations and the true calculation of the maximal x_1 orbits, we see that the x_1 track is not yet fully formed (the apsis precession which assembles the bar is an ongoing process), and thus the technique will not, by definition, be informative.

total disc-halo system is described by eigenfunctions and ≈ 1000 coefficients in azimuthal and radial harmonics (m and n respectively), enables fixed potential studies as in Chapter 3.

2. The bar is responsible for the vast majority of the $m=2$ and $m=4$ amplitude in the simulation (> 80 per cent), rather than the observed spiral arms. Additionally, the bar is responsible for exciting a significant amount of the $m=1$ amplitude in the cusp model (≈ 75 per cent), and somewhat less in the core model (≈ 60 per cent), owing to the lower central density of the cored halo.

3. We provide an analysis of the successes and failures of observational techniques meant to characterize bars. We compare harmonic analysis measures to the true trapped fraction of the bar, finding that while the harmonic analysis reproduces the qualitative evolutionary trends when the bar is established, harmonic function expansion analysis does not elucidate the bar assembly phase, and thus cannot be used to understand the formation of bars in a straightforward manner.

4. We emphasize that observational techniques currently employed on both real galaxies and simulated galaxies are not measuring true dynamical quantities. We perform ellipse fits on our simulations, finding that typical ellipse–fit techniques systematically overestimate the maximal extent of the trapped bar orbits. We describe why ellipses will overestimate the length (and therefore mass) of the bar. However, while ellipse-fit methods do not accurately represent the radial extent nor mass of orbits trapped in the bar, they may reproduce the trends in evolution seen in simulations *after* the bar has fully formed.

5. We show that the remaining percentage of nonaxisymmetric amplitude is responsible for significantly biasing observations of barred galaxies. 'Dressing' orbits, those which are spatially coincident with the visual bar feature, but are untrapped, can appreciably change the perceived and/or measured strength of the bar, but can be

mitigated through the inclusion of velocity data to determine the location of orbits trapped in the bar feature.

6. The dipole $m = 1$ response is a consequence of reaching a steady-state equilibrium in the cusp simulation, and is related to both the orbital structure (from Chapter 3) and angular momentum transfer or torque (as in Chapter 4). The signature of this event is harmonic coupling (or interaction) between the $m = 1$ and $m = 2$ azimuthal harmonics.

7. We do not find any evidence for a buckling instability in our simulations and explain that the physical reasons for why we do not find such a vertical instability to be a surprise, principally the slow growth of the bar. However, the galaxies still grow bulges, suggesting that bars do not need to buckle to produce observed boxy or peanut bulges.

8. Fixed potential analysis may be used, even in the presence of nonlinear effects such as harmonic coupling or beating, to get a reasonably characterized description of the orbit structure, but cannot describe the evolution of bar phases on their own: one needs BFE-based harmonic analysis to resolve these nonlinear evolutionary scenarios.

Our BFE methods reveal new avenues for studying the evolution of bars that are not possible using simple Fourier analyses. Fourier decomposition methods do not give an accurate physical description of the influence of the bar, as characterized by orbit classification, as in Chapter 3. In a companion work, we have shown the physical influence of the bar on the evolution of the system during the bar phases (Chapter 4). Future work will extend the harmonic analysis techniques to a larger suite of model initial conditions. We hope to answer whether the phases of bar evolution seen in these simulations are ubiquitous, and hope to understand the underlying dynamical causes of the phases of evolution. Additionally, we eventually hope to invert the problem and make predictions about the evolution of

galaxies from harmonic function expansion analysis alone, or even specify evolution using a defined set of known harmonics. While we have learned a considerable amount from this BFE-based harmonic analysis, it is clear that the true power to understand model galaxy evolution comes from a hybrid suite of analyses, including trapping analysis (Chapter 3), torque analysis (Chapter 4), and harmonic function expansion analysis (this work).

CHAPTER 6

USING THE BAR TO DRIVE RADIAL MIXING AND BULGE FORMATION IN A MILKY-WAY-LIKE GALAXY

6.1 Introduction

The Gaia satellite (Gaia Collaboration et al., 2016, 2018) will enable detailed dynamical tests of secular processes based on the explicit position-velocity phase-space structure of the Milky Way (MW). Coupled with spectroscopic surveys that contain information about the ages of stars such as RAVE (Steinmetz et al., 2006), APOGEE (Allende Prieto et al., 2008), and SEGUE Yanny et al. (2009), constraints on the evolutionary history of the MW (see Bland-Hawthorn & Gerhard 2016 for a review) will emerge. Metallicities for stars near the solar location have already revealed elemental abundance ratio gradients with radius that seem inconsistent with in situ star formation (Cheng et al., 2012; Hayden et al., 2014). A picture has emerged, informed by both analytic theory (Sellwood & Binney, 2002) and simulations (Roškar et al., 2008; Schönrich & Binney, 2009b; Minchev & Famaey, 2010), of dynamical redistribution inward or outward from their birth radius, creating a mixture of ages at each radius, caused by spiral patterns with overlapping resonances. Some models include a bar similar to that in the MW to generate an additional pattern (Minchev et al., 2012).

Observationally, such overlapping pattern-induced 'radial migration' appears to be supported by analysis of different generations of stars, which show that the highest metallicity stars are the most radially compact. This may be evidence of outward radial mixing: the oldest stars have moved outward, leading to an extended, relatively metal-poor stellar disc. Observations of age-metallicity spread observed in a sample of G-dwarfs in the solar neighborhood (Bovy et al., 2012) and red-clump stars (Bovy et al., 2016) at larger distances have

determined that enhanced $[\alpha/\mathrm{Fe}]$ stars have an exponential radial distribution with a scale length of 2.2±0.2 kpc, with constant scale height for high-$[\alpha/\mathrm{Fe}]$ stars and flaring scale heights for low-$[\alpha/\mathrm{Fe}]$ stars. The scale height of stars with consistent abundance populations changes with time (Bovy et al., 2016). Two competing theoretical explanations exist: (1) the MW was originally thicker and has become thinner over time (Navarro et al., 2018), such that subsequent generations of star formation have smaller vertical velocity dispersions, σ_z, and/or (2) the MW was originally thin, and dynamical effects have gradually caused populations to thicken over time by increasing σ_z (see e.g. Rix & Bovy 2013 and references therein). Both have the same observable, namely that older generations of stars have larger σ_z. Thus, a dynamical mechanism that can simultaneously explain the observed radial and vertical trends is attractive, and many studies have sought simple dynamical explanations to connect the two.

Additionally, study of vertical structure in the disc invites a natural extension to the central region of the MW, which may host a classical bulge, so-called pseudobulge, or a combination of the two. Independent of a dynamical explanation, 'pseudobulge' has become a maligned term, and has several definitions without a clear consensus. Most agree that pseudobulges are a class of bulges that do not resemble traditional dispersion-supported 'hot' stellar systems (e.g. ellipticals or spheroidal galaxies). As elliptical galaxies may be the end product of mergers, it is generally assumed that 'classical' bulges are those structures in the center of disc galaxies formed by minor mergers or other accretion events. Pseudobulges, generally, are those that both do not fit the classical bulge definition. Their formation is commonly attribued to dynamical secular processes (see Erwin et al. (2015) for recent observations of bulges and discussion). Kormendy & Kennicutt (2004) summarize the properties and observational evidence for the formation mechanisms of different bulges. In their paradigm, secular evolution in the inner parts of the galaxy is able to transform the stellar disk into a comparatively hot structure which is energetically favored via dynamical processes.

We address the following three questions in this chapter: (1) Can an evolving bar rearrange stellar orbits radially?; (2) What is the maximum bulge mass that can form from secular processes alone?; and (3) How do the radial and vertical changes observed in the simulation correspond to physical processes in the galaxy? The questions do not have simple answers, and each depend on a variety of factors and may be addressed in a number of ways.

The term 'radial migration' has become a catch-all in the literature to describe any redistribution of material observed during simulations. We provide clarification of the conceptual space for mechanisms responsible for driving radial evolution, and additionally vertical evolution, by dividing the known mixing mechanisms into four classes: (1) *secular mixing* (or redistribution) caused by changes in actions during resonance passage (e.g. classic secular evolution Lynden-Bell & Kalnajs, 1972; Tremaine & Weinberg, 1984b) or changes in action owing to resonance capture or trapping (e.g. nonlinear secular evolution Binney & Tremaine, 2008); (2) *chaotic acceleration* (or stochastic acceleration), caused by overlapping resonances from one or more simultaneous patterns, which is the basis for the 'radial migration' of Sellwood & Binney (2002), called 'churning' in Schönrich & Binney (2009a); (3) *heteroclinic motion* or weak chaos, the signature of which is orbit family switching at heteroclinic points when two regular orbits overlap in phase space (Weinberg, 2015a,b); (4) the *stochastic web*, where a single strong perturbation causes resonance overlap such that orbits may diffuse quickly from one island of regular orbits to another (Touma & Tremaine, 1997)[1].

We will analyze a single simulation in detail, and cannot therefore explore the trends within different radial migration and bulge formation scenarios. However, our model is a reasonable approximation for the MW, including a bar of modest mass (≈30 per cent of the

[1]There is some conceptual overlap between (2) and (4), where chaotic acceleration is 'one-shot' strong chaos, where the perturbation exists for only a short period of time, while (4) is persistent strong chaos, such that the system experiences $\mathcal{O}(1)$ perturbations over long times.

stellar mass which between 1-2 scale lengths long Bland-Hawthorn & Gerhard 2016). The model has a corotation (CR) radius between 2 and 4 scalelengths.

This chapter is organized as follows. In the next section, we describe our methods, including the n-body simulations, mixing calculation, and the decomposition the galaxy into dynamical components. In Section 6.3, we present an overview of the simulation evolution, including the evolution of separate components in both two-dimensional and one-dimensional views. In Section 6.4, we analyze the radial and vertical redistribution of orbits in the simulation. In Section 7.5, we discuss the implications of our model for the relative importance of dynamical processes and the intersection with other interpretations of simulations. We also discuss implications for observations. We conclude in Section 7.6.

6.2 Methods

6.2.1 n-body Simulations

The simulation analyzed in this chapter was presented in Chapter 3; Chapter 4; Chapter 5 as the cusp simulation. The main goal here is to elucidate dynamical mechanisms, and to that end the simulation presented here (1) do not include gas and (2) do not including ongoing accretion and growth expected from a cosmological simulation. The simulation consists of a stellar disc and dark matter halo. The disc is exponential in radius and is an isothermal vertical distribution such that the three-dimensional density is initially given by

$$\rho_d(R,z) = \frac{M_{\rm d}}{8\pi z_0 a^2} e^{-R/a} \mathrm{sech}^2(z/z_0) \tag{6.1}$$

where M_d is the disc mass, a is the disc scale length, and z_0 is the disc scale height. We set $M_d = 0.025 M_{\rm vir}$, $a = 0.01 R_{\rm vir}$, and $z_0 = 0.001 R_{\rm vir}$ throughout. For comparison to the MW, we offer the following scalings: $M_{\rm vir} = 1.3 \times 10^{12}$ $\mathrm{M}_\odot$, $R_{\rm vir} = 300$ kpc, $v_{\rm vir} = 150$ km s^{-1}, and $T_{\rm vir} = 2$ Gyr. We will often report the scaled MW value throughout this chapter. When a value has been calculated for the MW, we will add a $_{\rm MW}$ subscript.

We embed the stellar disc in a responsive Navarro-Frank-White (NFW; Navarro et al. 1997) radial profile dark matter halo such that $\rho(r) \propto (r_s^3)\,(r+r_c)^{-1}\,(r+r_s)^2$ where r_s is the scale radius, here set to be $r_s = 0.04R_{\rm vir}$, where $R_{\rm vir}$ is the virial radius, and r_c is a radius that sets the size of the core, here set to be $r_c = 0.2a(= 2z_0)$ for numerical convenience. Choices for the initial conditions, as well as the procedure to realize the full phase-space for each component, are described in Chapter 1 and Chapter 3.

We evolve the system using EXP (Weinberg, 1999), a self-consistent field expansion code that solves the Poisson equation for basis functions whose lowest orders exactly match the density profiles of the halo (expanded in spherical harmonics) and the disc (expanded in a custom cylindrical basis conditioned on the density function of the disc, see Chapter 5, for a detailed description).

6.2.2 Calculating Radial Mixing

Secular evolution is driven by angular momentum (action) exchange between orbits and mean field during resonance passage. As a resonance sweeps through phase space, orbits both increase and decrease their net actions. This leads to both positive and negative energy changes in the orbital apocenters. The existence of a strong bar adds a new dynamical twist: the possibility of orbit trapping as an orbit approaches a resonance. The bar perturbation is typically strong enough that orbits linger for many orbits near resonance. Rather than passing *through* the resonance, an orbit has the probability of *falling into* the bar potential; this is orbit trapping. Orbits trapped into the bar potential lose angular momentum overall as the bar slows and tend to decrease their apocenters. In summary, evolution of a galaxy under a strong bar will have a particular pattern of secularly- and trapping-driven and mass redistribution.

We analyze the simulation to quantify this orbital rearrangement by sampling the simulation at various times: $T = \{0, 0.5, 1.0, 2.0, 3.0, 4.0\}$ ($T_{\rm MW} = \{0, 1, 2, 4, 6, 8\}$ Gyr). At each time, and for each orbit, we select a window of $\delta T = \pm 0.1$, over which we com-

pute the apocenter radius $R_{\rm apo}$, the corresponding apocenter velocity $V_{\rm apo}$, the maximum excursion off of the $z = 0$ plane $|z|_{\rm max}$, and the ellipticity $\kappa \equiv L_{\rm z}/L_{\rm z,circ}$, where $L_{\rm z}$ is the angular momentum of the particle and $L_{\rm z,circ}$ is the angular momentum of a circular orbit at the same $R_{\rm apo}$, calculated from the monopole potential.

We choose to sample only these coarsely-sample times and window to achieve accurate phase averaging and provide time for noticable secular evolution. We could have calculated the quantities in fixed potentials. However, we opt to perform the analysis *in vivo* to preserve the non-linear effects such as orbit trapping (Chapter 3).

6.2.3 Structure Decomposition

We described the bar decomposition of this model in Chapter 3. In that chapter, we used a clustering algorithm on the physically-motivated apsides (radial turning points) of orbits in order to detect coherence with the global bar pattern (Chapter 1). With empirically determined parameters for the threshold values for orbit family membership, we can reach 1 per cent accuracy in classifying bar orbits. The true advantage lies in the ability to classify orbits in small time windows as the simulation is evolving. This reveals orbits that participate in the secular evolution of the system, rather than those that coincide with the bar potential feature.

As orbital analysis of the bulge is more straightforward, using the computed value $|z|_{\rm max}$, we classify orbits as bulge orbits if they exceed the threshold $|z|_{\rm max} > 4h$. Only 0.3 per cent of orbits in the initial exponential disc will exceed this threshold, which gives us a robust discrimination.

These definitions for the bar and the bulge produce largely independent components. In any given snapshot, the intersection of the set of bar orbits and the set of bulge orbits does not exceed 20 per cent of the smaller component by mass (typically the bulge). That is, at most, 20 per cent of the bulge, as defined through a naive $|z|_{\rm max}$ cut, is part of the trapped bar. As this overlap is a small fraction of the overall simulation, we choose to treat

the bar and bulge as distinct components and ignore the overlapping particles in plotting. For the purposes of the one-dimensional density profiles, we first classify bulge orbits and then classify the bar orbits from the remainder.

We will also compare to standard photometric decomposition metrics. A bulge is often parameterized by a Sersic profile with varying index $n_{\rm bulge}$, and the bar is fit by a Sersic profile with varying index $n_{\rm bar}$ and the axis ratio. The underlying disc is fit by an exponential profile, as in the radial distribution of our initial conditions. When necessary for comparision, we perform a simple χ^2 fit of a one-dimensional profile with a variable number of components.

6.3 Overview of Simulation Evolution

In this section, we benchmark direct observational measurements for our fiducial simulation. We find the dynamical principles presented here apply to a larger sample of galaxies. The simulation is evolved from an initially exponential state with no non-axisymmetric features. The disc rapidly becomes unstable and forms a variety of strong $m \leq 4$ patterns that seed a strong $m = 2$ perturbation which forms the bar. The details of bar formation are beyond the scope of this chapter, but may be found in (Chapter 3; Chapter 4; Chapter 5). Chapter 3 introduces the three phases of bar evolution that the simulation here passes through: $T < 1$ is termed 'assembly', $1 < T < 3$ is termed 'growth', and $T > 3$ is the 'steady-state'. Additionally, owing to the known dynamical instabilitity at the outset of the simulation that decays by $T \approx 0.5$, we define $T > 0.5$ as the 'secular evolution period'. The secular evolution period encompasses the bulk of the assembly of the bar, as well as a slower period of secular growth, and a steady-state (see Chapter 4, for a more detailed description of the phases). We focus on the growth for our analysis of radial mixing, acknowledging that the early evolution of the simulation is unlikely to resemble processes in the real universe.

6.3.1 On-Sky Galaxy Appearance

In this section, we describe our simulation as it might be observed with a perfect mass-to-light ratio. We consider a face-on view for analysis of the bar appearance, and an edge-on view for study of the three dimensional bulge. Figure 6.1 is organized into four blocks from top to bottom: the total stellar component, the bar component only, the bulge component only, and the remaining disc material. The decomposition of the disc takes place using the methodology in Section 6.2.3. As the simulation is evolving, and the individual components are changing in mass through time, we show the fraction of the total disc mass in each component in the upper left of each subcomponent panel.

During the evolution of the model, the galaxy is characterized by the following morphological features, following the top block of panels in Figure 6.1: (1) featureless exponential disc at $T = 0$, (2) strong multi-arm spiral at $T = 1$, (3) strong two-arm spiral at $T = 2$, (4) bulgeless barred galaxy at $T = 3$, and (5) bulge-bearing barred galaxy at $T = 4$. From an observational standpoint, the different times fill a considerable amount of parameter space, featuring examples of three-dimensional thickened structures, a variety of arm statuses, with no particularly persistent arms and a variety of bar strengths, lengths relative to disk scalelengths.

Figure 6.1 shows the bar to have a half length of one to one-and-a-half scale lengths with high surface density; it contains more than 30 per cent of the disc mass at the end of the simulation. Further, we see that the trapped bar component is confined to relatively low vertical excursions off the plane–the trapped bar material does not thicken.

As expected, removing the elevated component from the model and examing the left-over untrapped, unelevated disc (bottom block in Figure 6.1) shows that the traditional edge-on bulge feature has been removed. Detailed orbit classification (Chapter 3) shows that the central concentration owes to trapped orbit families that are known to reside at the center of barred potentials, such as the x_2, x_3, or boxlet orbits. However, a photometric fit to the face-on image of the untrapped disc would result in a $B/T = 0.05$ at late times

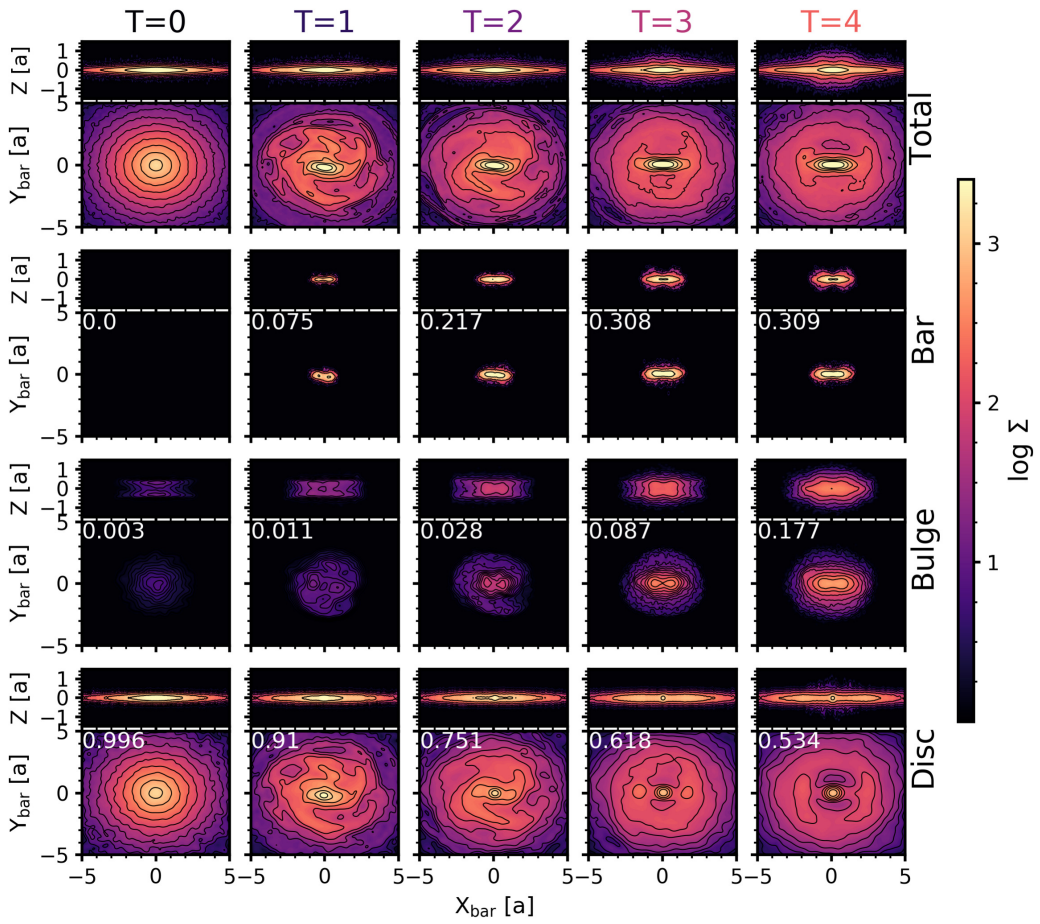

Figure 6.1. Evolution of the bar-transformed face-on ($x_{\rm bar} - y_{\rm bar}$) and edge-on ($x_{\rm bar} - z$) surface density projections in distinct model components (rows of blocks) through time (columns). Time is labeled above each column. Each panel shows the log stellar surface density, in normalized units. The figure is organized into four blocks from top to bottom: the total galaxy, the bar alone, the bulge alone, and the disc alone, found after subtracting off the bar and bulge from the total model. The blocks are labeled on the right side of the subpanels. In each of the three components (bar, bulge, disc), we list the fraction of the particles in that component at a given time. Owing to rounding and 1 per cent level contamination, the numbers do not sum to exactly unity.

using standard Sersic decomposition methods as described above, even after both the bar and elevated population have been removed. This illustrates the pitfalls of performing a photometric-only decomposition of a barred galaxy.

Although the bulge exhibits an elongated structure reminiscient of the stellar bar, an analysis of the time-integrated orbit positions reveals that on average, any given orbit is only found within the bar region 40 per cent of the time. We quantified this value by taking an ellipse appoximation for the orbits classified as part of the bar such than 90 per cent of the bar was enclosed at any given time. We then used the fit ellipse axis ratios to compute what fraction of the time bulge orbits were found in the ellipse-fit region, finding that it was only 40 per cent of the time. In other words, it is more likely than not that a true bulge orbit chosen at random will not be inside an ellipse definition of the trapped bar[2].

6.3.2 One-Dimensional Density Profiles

A straightforward way to look at radial redistribution is through the decomposition of one-dimensional projected density profiles[3]. Often, galaxy surface brightness profiles are fit using axisymmetric profiles for an exponential disc, Sersic bulge, and bar model (e.g. Gadotti, 2009). However, using our model, we demonstrate failure modes that may bias the decomposition of galaxies. Our simulation results in a rich variety of one-dimensional profiles, that may confuse a decomposition into multiple components. In particular, our bulge forms through secular processes only, but an inspection of our models reveals disc structures that may readily be fit as a bulge component. Specifically, a photometric analysis of a face-on image cannot discriminate between two and three dimensional structure, particularly if the radius of the bulge is comparable to that of the bar minor axis. For ex-

[2]The bulge orbit may be found to reside in the ellipse fit for a larger fraction of the time if a more generous and less-physically motivated description for the bar is used.

[3]Formally, our decompositions take place in two dimensions, but for ease of comparison between observations, we plot the one-dimensional density profiles, where the profile has been azimuthally averaged from the two-dimensional structure.

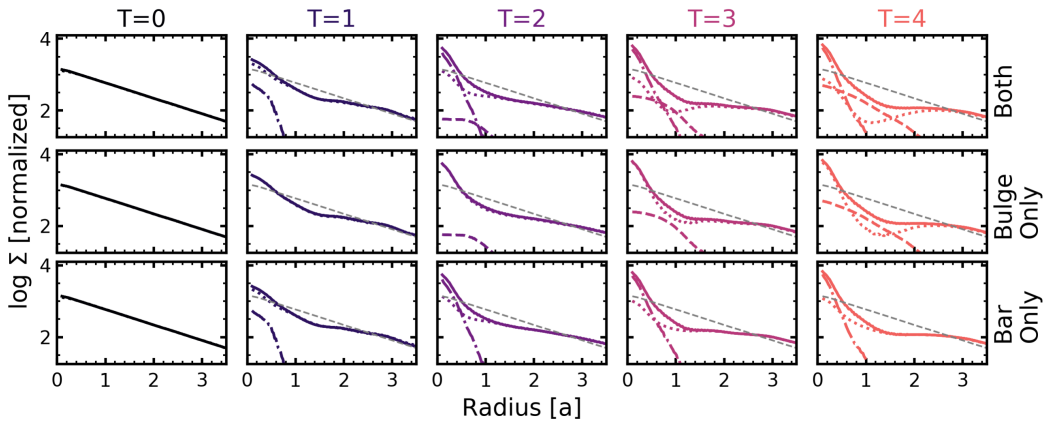

Figure 6.2. Normalized log stellar surface density as a function of radius, at different times (columns, labeled above), and for different decompositions (rows). In each panel, the total disc surface density is shown as a solid line with color corresponding to the time, and the initial disc surface density is shown as a dashed gray line. In the upper row, we perform the complete decomposition, into the bar (dash-dot line), bulge (dashed line), and disc (dotted line). In the middle row, we subtract the bulge only, showing the bulge as the dashed line identical to the upper panel, and the remaining disc found by subtracting the bulge, as a dotted line. In the lower panel, we subtract the bar only, with the bar shown as the dash-dot line identical to that in the upper panel, and remaining disc as the dotted line, found by subtracting the bar.

ample, inspection of several galaxies in Kim et al. (2014) shows that the bulge is not at all spatially distinct from the bar, and thus, a different bar structure beyond a Sersic fit may more accurately recover the bar without a bulge (see, e.g. NGC 210 in Kim et al. 2014).

Figure 6.2 shows the one-dimensional density distribution at a range of times in the model (columns). To construct the density profile, we collapse the individual panels from Figure 6.1 in azimuth, and take the mean in radial bins of width $dR = 0.02a$ ($dR_{\rm MW} = 60$ pc). We show three different decompositions in the rows of Figure 6.2 to illustrate our main point: decomposing this galaxy into a bulge, bar, and disc from the full phase-space structure will not return the same result as decomposition through standard methods (see e.g. Muñoz-Mateos et al. 2013; Kim et al. 2014; Laurikainen et al. 2014; Salo et al. 2015 for detailed fits to small samples, and Kruk et al. 2018 for a large sample of relatively low-spatial-resolution decompositions). The problem with including a bulge in our decomposition is clearly illustrated in the disc only bottom row of Figure 6.1, where a subtraction of both the dynamically-identified bar and bulge leaves a central mass that would, from a face-on image, be associated with a bulge photometrically. However, looking at the edge-on distribution of the galaxy, we see that the vertically protruding structure that one would call the bulge in the upper panel, the total, has been largely removed. Why does a central mass remain? In our case, we do not classify x_2 or box orbits as part of the bar (see the discussion regarding classification choices in Chapter 3), but they are spatially coincident with the bar and bulge, yet not vertically extended. One would only be able to discern whether the apparent central density was vertically extended for nearly edge-on images. In our tests, we determined that the bar structure is biased toward a lower Sersic index $n_{\rm bar}$ when the bulge is simultaneously fit. A comparison of the bulge-only to bar-only decomposition in Figure 6.2 demonstrates why. The truly three-dimensional bulge is a sub-dominant population in the one-(two-) dimensional fit. This motivates better priors based on bar evolution models for the two-dimensional surface decomposition of bulges in barred galaxy images.

One may notice that the leftover disc fit in Figure 6.1 is not axisymmetric, particularly at $T = 2$. However, this is not unexpected. Since our true bar is trapped orbits but the disc responds to the bar. We describe the 'dressing' orbits in detail in Chapter 5. This may explain why measurements of barred galaxies appear to show significant scatter in the fit parameters (e.g. the relationship in Kim et al. 2015 between the bar profile exponent $n_{\rm bar}$ and the mass of the host galaxy).

Additionally, some observational work has sought to implicate bars in the creation of disc 'breaks', the transition between power-law indices often seen in one-dimensional profiles of discs (e.g. Muñoz-Mateos et al., 2013). We find that our bar-induced secular mixing does not change the one-dimensional profile significantly during the periods after the bar has formed ($T > 1$). However, during the period where the bar is rapidly changing ($T < 1$), the radial mixing distribution is rearranged. That is, after the formation of the bar, even the gradual accumulation of material from 10 to 30 per cent trapped into the physical bar structure does not result in a significant change to the density profile.

6.4 Orbit Redistribution

As described in Section 6.2.2, we refer to the redistribution of orbits by secular evolution as 'radial mixing', a term which encompasses known mechanisms for radial redistribution (as discussed in Section 7.1): secular mixing, chaotic acceleration, heteroclinic motion, and a stochastic web. For the purposes of disentangling dynamical effects which may contribute either or both radial and vertical mixing, we choose to study the changes to orbits in phase-space location in an $R - z$ plane.

In Figure 6.3, we demonstrate the radial and vertical mixing of orbits in the fiducial simulation. Each panel describes the change in radius and height intervals for a subset of orbits as labeled. The early time and late time used to make each panel are noted in the format 'T_1 [early time] $<$ T $<$ T_2 [late time]' in the lower right corner. The x axis is the logarithm of the ratio of the apocenter radius at the later time to that of the apocenter

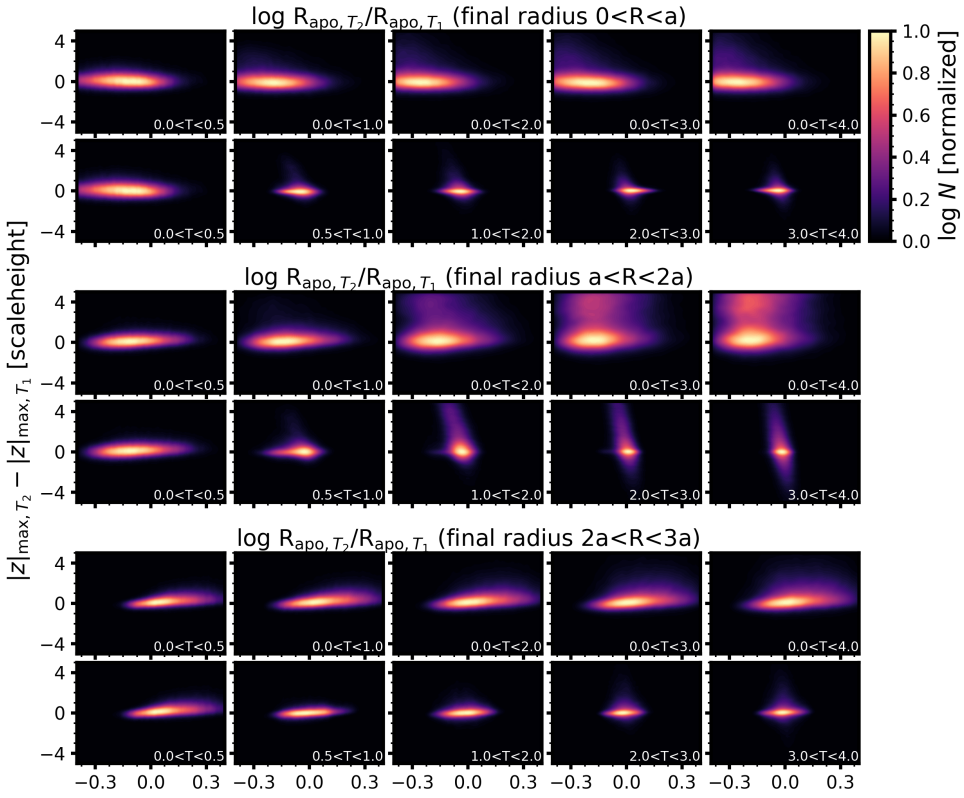

Figure 6.3. A view of radial mixing and vertical evolution in the simulation. Each panel shows the $r - z$ mixing plane, which we define as $\log R_{\mathrm{apo,T_2}}/R_{\mathrm{apo,T_1}}$ vs $|z|_{\mathrm{max,T_2}} - |z|_{\mathrm{max,T_1}}$, noting the difference in the logarithm versus the difference in the two dimenstions. The figure is divided into three blocks, the upper, middle, and lower, corresponding to three regions of the simulation, the outer disc, the end of the bar, and the inner disc (as sorted by radius at T_2), respectively. The time subscripts refer to the labels inset in each panel, where the format is $T_1 < T < T_2$. The upper row in each block is the 'cumulative mixing', where the orbits are computed against the $T = 0$ positions, and the bottom row in each block is the 'differential mixing', where the orbits are computed against a rolling time, in order to isolate mixing over shorter windows.

radius at the earlier time, $\log R_{\rm apo,T_2}/R_{\rm apo,T_1}$. The y axis is the difference of the maximum distance from the midplane of the galaxy at the later time to that of maximum distance from the midplane of the galaxy at the earlier time, $|z|_{\rm max,T_2} - |z|_{\rm max,T_1}$. To calculate the radial apocenter and vertical maximum, we choose a time window of $\Delta T = 0.2$/ This is sufficient to ensure that orbits have reached apocenter and a vertical maximum, while also being shorter than the evolutionary timescale. We further divide the sample into three radial intervals, illustrated in the three rows of Figure 6.3 as labeled. Each orbit is assigned to the radial interval by its apocenter radius at the later later. The three radial annuli describe three dynamically interesting regimes: interior to corotation ($0 < R < a$), near corotation ($a < R < 2a$), and outside of corotation ($2a < R < 3a$). Further beyond corotation, e.g. $R > 3a$, the behavior of orbits is roughly the same as the outside of corotation annulus.

In each of the three rows shows two views of the radial mixing with time. In the upper row, the apocenter and the maximum vertical extent at the later time are compared to the initial distribution at $T = 0$. In the lower row, we compare the later time to those at the earlier time. In other words, the upper row describes cumulative change, and the lower row describe differential change. We carefully inspected differential changes to verify consistency wit hthe cumulative changes. We select six time windows chosen for their correspondence with the evolutionary phases: $T = 0$, the initial conditions; $T = 0.5$, the time directly after the initial rearrangement; $T = 1.0$, the time directly after the bar assembly phase; $T = 2.0$, the primary secular evolution time; $T = 3.0$, the secondary secular evolution time; $T = 4.0$, the conclusion of the simulation.

Figure 4 reveals several distinct qualitative trends. First, for the bar region ($0 < R < a$), top panel), the orbital radii decrease overall. Most of this decrease occurs as the majority of bar orbits become trapped during the assembly phase. The redistribution of radii is biased towards smaller radii during the secular growth phase, but at a smaller magnitude then during the assembly phase. There is a small but clear trend toward increasing vertical height for a small subset of orbits. Secondly, the trend in radial redistribution in the coro-

tation region, ($0 < R < a$, middle panel), is similar to the bar region. However, secular evolution drives a strong vertically elevated population after assembly. This is the secular bulge. This growth continues out to late times ($T \approx 4$). Finally, the orbits outside of corotation are radially redistributed to larger radii on average. The width of the radial redistribution is the largest in this region of the bar-influenced disc. There is a significant trend of increasing scale height with increasing radius, consistent with the predictions of secular evolution theory and other recent simulations (Minchev et al., 2014; Grand et al., 2016; Ma et al., 2017). The magnitude of this increase is small compared to that of the pseudobulge produced in the corotation region. Although the radial redistribution is biases inward and outward depending on the initial orbital location, these figures demonstrate that apocenters for individual orbits move both inward and outward. This is also predicted by secular evolution theory and motivates our moniker: *radial mixing*.

In the next two sections, we first consider radial mixing in Section 6.4.1, before moving toward vertical mixing in Section 6.4.2. We include case studies demonstrating the dynamical mechanisms that create three-dimensional thickened structures. Motivated by the trends identified in Figure 6.3, we choose four case studies: (1) orbits that move outward, (2) orbits that move inward from CR, (3) orbits that move inward from a 3:n resonance, and (4) orbits which become part of a vertically-extended bulge distribution. We show orbits from two time windows: the outward-moving orbits from the $0.9 < T < 1.1$ window, while the inward and vertically-moving orbits come $1.9 < T < 2.1$ window. Both windows are during clear periods of strong secular evolution (cf. Chapter 3).

6.4.1 Radial Mixing

The now-classic mechanism to drive strong radial motion in galaxies is the multi-pattern spiral structure and subsequent *stochastic acceleration* caused by resonant overlap of Sellwood & Binney (2002). To summarize, Sellwood & Binney (2002) demonstrated that stars can be scattered outward via overlapping spiral patterns, showing that the radial action

of a star, J_R, could be altered by a passing spiral wave (or other pattern, such as a bar): $\Delta J_R = \frac{\Omega_p - \Omega_\phi}{\Omega_r} \Delta L_z$ where Ω_ϕ is the azimuthal frequency of the star, and Ω_r is the radial frequency. However, the radial motion in our simulation is unlikely to result from overlapping spiral patterns during the secular evolution phase. During this phase, $T > 1$, the bar contributes 90 per cent of the non-axisymmetric perturbation (Chapter 5) and distince spiral patterns are weak. In simulations with discrete pattern speeds and long-lived spiral structure, the radial mixing process is shown to be quite efficient (Minchev & Famaey, 2010; Roškar et al., 2012).

To verify this, we attempt to identify the mechanism by directly examining the dynamics for several classes of orbits identified from regions on Figure 6.3:

1. Orbits which move outward to CR or OLR and become more eccentric (Figure 6.4).

2. Orbits which move inward from CR to either x_1 orbits, higher-order bar orbits, or 3:n orbits (Figure 6.5).

3. Orbits which move inward from 3:n orbits and become either bar orbits or boxlet orbits (Figure 6.6).

In practice, and in contrast to the findings of earlier radial mixing studies, we find that a change in radius (set by J_R) has a corresponding change in eccentricity (set by L_z) at all bar-driven evolution times ($T > 1$), such that orbits moving in either become more eccentric. Further, interior to corotation ($R_\mathrm{CR} = 1.5a$ at the beginning of the simulation, and is at $R_\mathrm{CR} = 2a$ by $T = 1$), orbits do not move outward at any time, in any appreciable amount. After the very early initial rearrangement of mass, $0 < T < 0.5$, the orbits do very little rearrangement, changing by $\log R_{\mathrm{apo,T_2}}/R_{\mathrm{apo,T_1}} < 0.1$, which corresponds to less than half a scalelength, on average.

Near corotation, the orbits show both inward and outward radial motion. Corotation clearly acts to split the behavior of orbits, particularly if one looks at the evolution for and ensemble of orbits sorted on their *initial* radius at early times ($T < 2$). We do see orbits

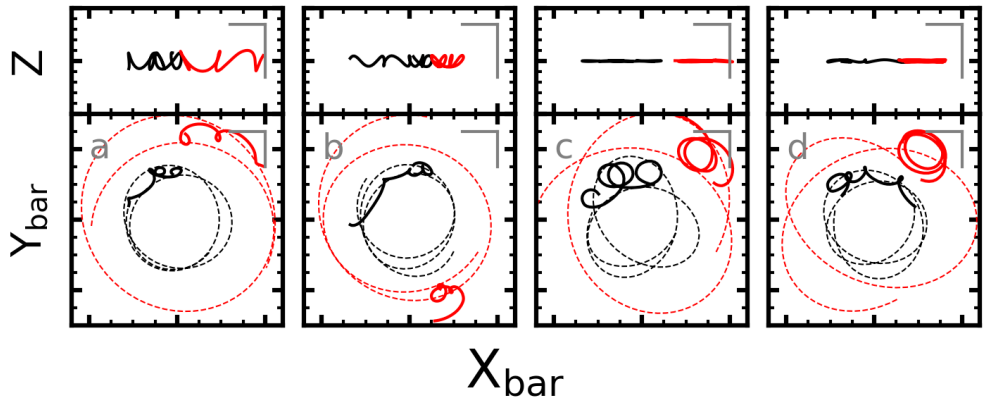

Figure 6.4. Orbits which move outward early in the simulation ($0.5 < T < 1.0$) are uniformly caught at a low-order resonance: either CR or OLR. All four orbits shown in this panel are captured at OLR. Orbits do not thicken or flare while moving outward in our study. Orbits also become more eccentric when moving outward. The gray bar is each panel is a scale length.

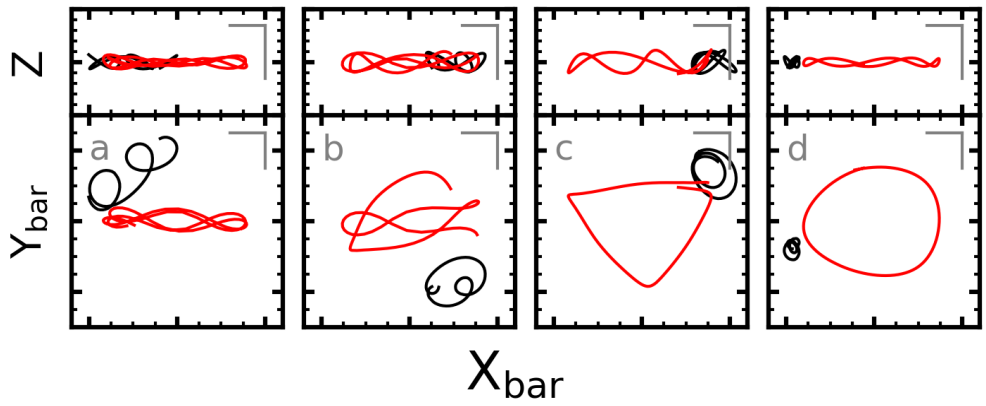

Figure 6.5. Case study orbits which move inward from CR during the simulation at intermediate times, $1.9 < T < 2.1$ (red) and $2.9 < T < 3.1$ (black). At least four different outcomes are possible. From left to right: (a) Becoming an x_1 orbit directly. (b) Becoming a dressing orbit in a higher-order pattern which is aligned with the bar. (c) Becoming a 3:1 orbit. (d) Becoming a warped circular orbit. The gray bar is each panel is a scale length.

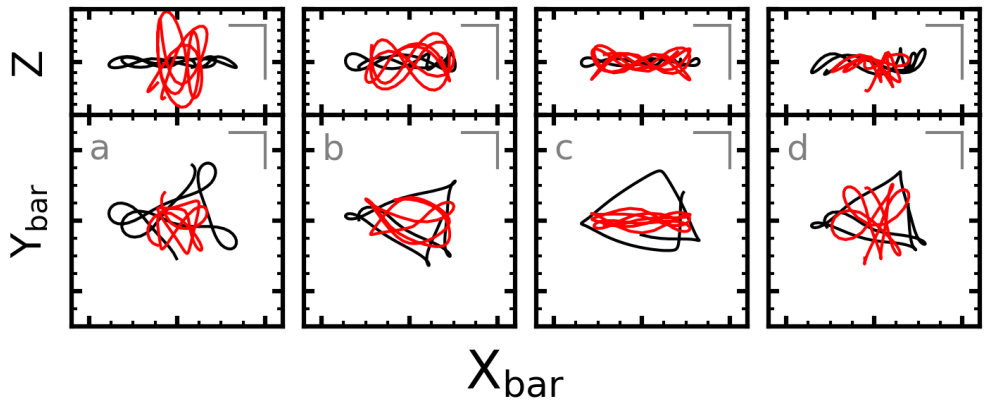

Figure 6.6. Case study orbits for the 3:n resonances at the end of the bar at intermediate simulation evolution times, $1.9 < T < 2.1$ (red) and $2.9 < T < 3.1$ (black). From left to right: (a) 3:1 ending in a classical bulge orbit. (b) Becoming a generic bar orbit. (c) Becoming an x_1 orbit. (d) Becoming a boxlet. The gray bar is each panel is a scale length.

moving outward, but they are stopped by low-order bar resonances. Perhaps in principle strong spiral activity could dominate the perturbations in the outer disc and cause the barrier imposed by the bar to be overridden, but that is not the case in our bar-dominated models. Some orbits at early times may move outward and be caught by OLR, as well. This is most likely to be the presence of a *stochastic web*, where a strong perturbation causes rapid diffusion between two stable regions of phase space.

Outward motion is accompanied by significant changes in ellipticity. For orbits moving outward, $\langle \Delta\kappa \rangle = 0.05$, the average change in ellipticity. Even with this outward motion, the flaring is negligible: $\langle \Delta|z|_{\rm max} \rangle = 0.5h$, or half a scaleheight. These numbers are true for all orbits moving outward, regardless of starting radius. Additionally, the outward mixing takes place quickly–over a single bar period. The orbit may move along the bar potential to reach an family at larger radius. This appears to be similar to the mechanism presented in Herpich et al. (2017).

In Figure 6.4, we show four example orbits which move outward at any point during the disc simulation. We find that uniformly, these orbits are emitted at CR and captured by OLR. In order to move out, the orbits *increase* their radial energy such that the eccentricity

increases. Additionally, these orbits move outward at early times only, before the bar dominates the potential. At all times after the bar has formed, we find that the channel where an orbit gains $L_{\rm z}$ at CR and is captured by OLR does not exist.

In Figure 6.5, we offer case studies of orbits which migrate inward from CR or nearly CR. These orbits uniformly move inward to bar-influenced orbits, such as the x_1 family (panel a), higher-order x_1 families (panel b), a $m = 3$ orbit (panel c), or an $m = 4$ orbit that appears nearly circular. The subsequent evolution of orbits that reach the $m = 3$ resonances at the co-located at end of the bar are shown in Figure 6.6. Several different tracks are open to orbits in the chaotic region at the end of the bar. They may become part of the bar, either as an x_1 or a generic bar orbit. They may lose all sense of net $L_{\rm z}$ and either become a boxlet or the even more specialized thickened classical bulge orbit. As shown in Chapter 3, the region with $m = 3$ multiplicity at the end of the bar is crucial for the growth of the bar. This is because the region is one of overlapping resonances, where family switching is common.

As all of the case study effects may be explained by bar features alone (even the outward mixing from CR to OLR), taken together, the radial mixing case studies suggest that the bar itself may initiate orbit switching that includes a mild amount of radial mixing–an additional source of a pattern, such as spiral arms, is not required.

6.4.2 Vertical Mixing

Kormendy & Kennicutt (2004) summarized the evidence for bulges caused by bar-driven secular evolution. In this two-step process, bars rearrange disc gas by funneling gas to small radii, and stars subsequently form and build up a central concentration. Observationally, many of these central concentrations appear to be young. The secularly-built bulges tend to be 'flatter' than classical bulges, with largely ordered motions and small velocity dispersions. Fisher & Drory (2008, 2016) defined galaxies with bulge Sersic indices $n_{\rm bulge} \leq 2$ to be pseudobulges, while $n_{\rm bulge} > 2$ are classical bulges. However, Graham

et al. (2016) demonstrated that there is no bimodality in the population, so bulges cannot be reliably separated by using a fit alone. A Sersic fit to the inner regions of our model galaxy consistently, whether with the thickened bulge included or not, return $n_{\rm bulge} \leq 2$ as the best-fit parameter. Of course, this picture does not apply to our simulation, which is purely n-body, so the buildup of the inner bulge must be explained by other dynamical processes.

Sridhar & Touma (1996) proposed forming bulges by a resonance between the vertical and radial frequencies that results in adiabatic thickening of the disc over time, which they call 'levitation'. Quillen (2002) forms bulges by coupled two-dimensional resonances using the model Hamiltonian describing the vertical ILR as in Pfenniger & Friedli (1991). The resonance between the azimuthal and vertical degrees of freedom $2(\Omega_\phi - \Omega_p) = \Omega_R$ and $2(\Omega_\phi - \Omega_p) = \Omega_z$ are simultaneously satisfied; that is, the observed vertical feature is the coincidence of *two* resonances. The second equality is called the *vertical* inner Lindblad resonance (vILR) for its relationship to the planar ILR that parents the bar (the first equality). The dynamics are distinct from a true three dimensional resonance, where the $l_1\Omega_r + l_2\Omega_\phi + l_3\Omega_z = m\Omega_p$ resonant condition is satisfied in all three dimensions simultaneously.

On the simulation side, Debattista et al. (2006) reported that vertical heating was influence most strongly by the buckling instability, a direct consequence of the bar formation phase in their models. Schönrich & Binney (2009b) and Loebman et al. (2011) argued for queiscent internal dynamical evolution that results in a thick disc, which may generally be described as the motion of stars from the inner disc to the outer disc in their models. Ma et al. (2017) argues for a natural formation of a distinct thin and thick disc in their cosmological zoom-in simulation, where the thick disc is formed from older stars that were both born at a thicker scale height, as well as some that scattered to the larger scale height owing to small-scale noise in the simlation (physical or aphysical). They also find evidence for a reversal in the metallicity gradient with height above the midplane of the galaxy, where the

metallicity gradient is negative in the midplane (more metal rich in the center), and positive at larger vertical extents (more metal rich in the outskirts), which recent observations have supported.

In our model, the initial distribution of maximum vertical extents is relatively low: 99.6 per cent of the disc does not reach more than four scale heights. The distribution changes, but *not* owing to the initial rearrangement of the disc: thickening is a secular evolution process that persists throughout the evolution. We do not find any measurable flaring from the outward radial mixing of stars. This is expected if the radial mixing mechanism is dominated by secular evolution by in-plane disc resonances in our simulation. If $L_{\rm z}$ and thereby apocenter radius increases, then the orbital inclination decreases. Specifically, if χ is the orbital inclination then $\cos\chi \equiv L_z/\sqrt{L_x^2+L_y^2+L_z^2}$. It immediately follows that $d\cos\chi/d$Ł$_x > 0$ and therefore χ decreases with increasing Ł$_z$. Conversely, inward moving orbits increase their orbital inclinations. This trend is clearly seen in Figure 4 (e.g. bottom row of the $a < R < 2a$ or central panel). Overall, since orbits move inward and outward with the mean absolute value of the change for each orbit much larger than the mean change, the net change in scale height by in-plane secular evolution is insignificantly small. Our dynamical rationale is further backed by long-standing observations that observed discs do not flare (Comerón et al., 2011). Note that this discussion does not preclude flaring caused by satellite interactions or other external sources.

The $a < R < 2a$ range in Figure 6.3 also reveals the primary radius for growing the orbits which protrude out of the plane of the disc. A clear locus is seen in the thickening orbits when considering the cumulative change in vertical extent near corotation, corresponding to a significant population of semi-resonant orbits (orbit which reside in the resonance for some period of time, then are released, and originally surfed resonances to become thickened).

We examine case studies of several interesting classes of orbits for vertical mixing, showing examples in Figure 6.7 as well as one that has already been shown in Figure 6.6:

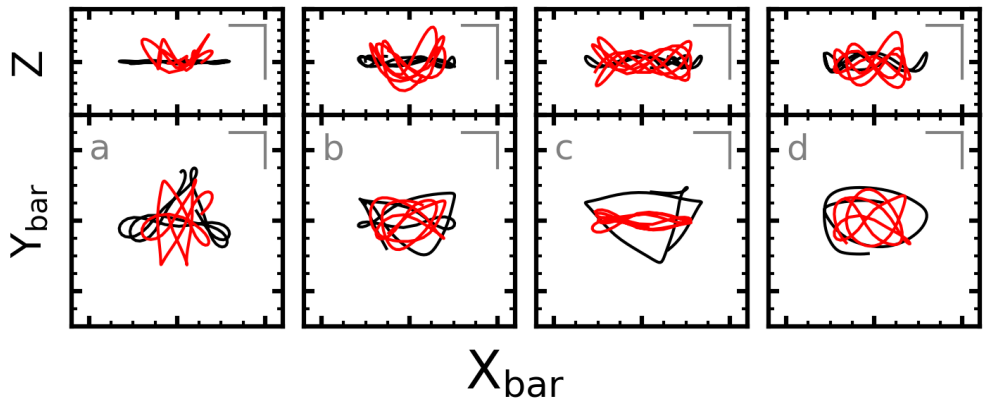

Figure 6.7. Case study orbits for vertical mixing. Orbits change from thin orbits in the black trajectory ($1.9 < T < 2.1$) to thicker orbits in the red trajectory ($2.9 < T < 3.1$). From left to right: (a) A 3:n orbit becomming an $m = 0$ trapped orbit. (b) A higher-order dressing orbit becoming an $m = 2, n = 2$ trapped banana orbit. (c) A 3:n: orbit becoming a non-vertically-resonant x_1 orbit. (d) A nearly x_1 orbit becoming a $m = 2, n = 2$ trapped orbit with dual commensurabilities. The gray bar is each panel is a scale length.

1. Orbits which move inward and upward (panels ‘a’ and ‘d’ of Figure 6.7)

2. Orbits which stay at nearly the same radius and move to larger vertical excursions (family switching, panels ‘b’ and ‘c’ of Figure 6.7).

3. Orbits which move into the ‘classical’ bulge (cf. panel ‘a’ of Figure 6.6)

We describe structure in the $x_{\rm bar} - z$ plane through a vertical commensurability equation, modeled after the vILR resonance condition described above:

$$n(\Omega_\phi - \Omega_p) = \Omega_z \tag{6.2}$$

By appearance, n corresponds to the number of maxima observed in the $x_{\rm bar} - z$ plane over some time window much longer than an orbital time. Therefore, orbits which are trapped vertically will exhibit low values of n.

As demonstrated in Figure 6.7, orbits whose vertical extent increases to three or more scaleheights have a variety of outcomes: (1) $m = 0$ bowl orbits (very asymmetric with

respect to midplane), (2) $n = 2, 3, 4$ resonant orbits (though the planar resonance must be very low order, e.g. $m = 2, 3$ in order for any structure to be apparent, and these orbits may be observed at different phases relative to the planar resonances), (3) isotropic orbits with no rotational memory (the bar can rob orbits of *all* their rotation). How the orbits got to a thickened state is also curious: the black lines in Figure 6.7 show a huge variety of morphologies. Some are loosely related to the bar, some are generically trapped, some are trapped into low-order resonances (including very curious $m = 3$ orbits). Many orbits do not show coherent structure in the $x - y$ plane, but do contributed to the thickened structures. Fewer than half of the thickened orbits are truly trapped in the z dimension at any given time.

An inspection of individual orbits shows that some orbits do satisfy the dual commensurability requirement from Pfenniger & Friedli (1991); Quillen (2002). In particular, while both Panels (b) and (d) of Figure 6.7 exhibit $2(\Omega_\phi - \Omega_p) = \Omega_r$ and $2(\Omega_\phi - \Omega_p) = \Omega_z$, the phases between r and z are different. Panel (b) has a phase shift $\phi_{rz} = 0$, and persists for considerable time, while panel (d) has a phase shift $\phi_{rz} = \frac{\pi}{2}$. We refer to $\phi_{rz} = 0$ orbits as 'U' orbits, and $\phi_{rz} = \frac{\pi}{2}$ as 'butterfly' orbits. Both may contributed to the bulge, but the peak of the z distribution will be at different radii[4]. The key difference between $\phi_{rz} = 0$ and $\phi_{rz} = \frac{\pi}{2}$ orbits is that the $\phi_{rz} = 0$ orbit may be resonant for a longer period of time than the $\phi_{rz} = \frac{\pi}{2}$ orbit.

Despite these identifications, the majority of orbits at any given time still do not show any vertical commensurability, even when considering phase shifts. The vertically-commensurate orbits do not prefer the bar or the untrapped disc, exhibiting nearly equal fractions between both. This suggests that vertical commensurability is transient. Therefore, we argue that the orbits which primarily contribute to the 'X' morphology, at any n, are incomplete sec-

[4]Similarly, $n = 3$ orbits may also play a role in setting the structure of the thickness of the disc. While $n = 3$ orbits are the most prominent vertical commensurate structure in our model, they have too large of a radial extent to support the bulge.

ular passage through corotation. One may show this result analytically using numerical perturbation theory, where a passage through ILR (or CR) leads to larger vertical excursions (Weinberg in prep). The 'partial passage' channel is particularly relevant for late times when the bar slowing has stalled; an orbit which passes through ILR will enter the separatrix region created by the bar and eventually diffuse, retaining no vertical commensurability with the bar. As both trapped and untrapped orbits pass the separatrix during mixing, the process to elevate orbits via partial resonance passage will equally efficient for both.

Lastly, an inspection of simulations that demonstrate 'buckling' undergo a rapid, *vertically asymmetric* instability. We emphasize the vertical asymmetry as a possible hint for the orbit families which may act to propagate the bending mode. We suggest that the $m = 0$ 'bowl' orbit shown in Panel (a) of Figure 6.7 may be able to support the buckling mode, which would be a new interpretation from the traditional Raha et al. (1991) interpretation of a firehose instability in the manner of Toomre (1966); Araki (1985). In our simulation, we find that the maximum number of bowl orbits in any time window is less than one per cent, and they distribution is always symmetric[5].

6.5 Discussion

6.5.1 Implications for Dynamical Interpretations

With harmonic analysis studies (as in Chapter 5), radial mixing may be informed by studying the monopole for changes, as the primary radial mixing that we identify is marked by changes to the monopole (e.g. the mixing is not symmetric in inward and outward motion). We see that during the initial assembly phase, the monopole changes significantly. As we see evidence for orbits diffusing rapidly between CR and OLR (e.g. Figure 6.4),

[5]The bowl orbits are not difficult to isolate: we have not identified any other orbits with an asymmetric signature with respect to the $x - y$ plane, so a simple cut on orbits which show an asymmetric signature (e.g. $z_{\max} - z_{\min} \neq 0$) can readily identify these orbits.

we interpret this as evidence for the stochastic web, where families which are typically isolated in phase space are connected via a strong perturbation connecting the stable islands. After the formation phase, we do not see appreciable restructuring of the monopole (cf. Figure 6.2).

Returning to the fundamental dynamical questions posed at the outset of this chapter, we find that the bar itself can be responsible for appreciable radial mixing, and all radial mixing observed during the secular evolution phase ($T > 1$) in this model can be explained by interaction with the bar. We also identify signatures of different mechanisms which lead to radial mixing during the secular evolution phase: *secular mixing*, where the orbit passes through resonance and changes its actions (e.g. Figure 6.5 and panels a, b, d of Figure 6.6), and *heteroclinic motion*, where an orbit presents a different morphology as a result of family switching near a heteroclinic point in phase space (e.g. panel c of both Figure 6.6 and 6.7). We find that during the steady-state phase of the simulation, heteroclinic motion is responsible for the majority of the radial mixing near the end of the bar. At all other times and radii, secular mixing, where orbits interact with resonances, potentially including the myriad higher-order resonances seen in the detailed decomposition of Chapter 3, induces radial mixing.

We found that significant amounts of mass (>15 per cent) may be elevated out of the plane, primarily through interaction with bar-induced potential features (chiefly resonances, e.g. secular mixing through resonant interaction). While the torque study of Chapter 4 was confined to planar forces, one could imagine extending the methodology presented in that chapter to study the vertical forces experienced by a family thickened orbits by some other component (e.g. the bar). Clearly from inspection of the vertical thickening case studies, multiple dynamical processes are interacting, including incomplete resonant passage and vertical commensurabilities, as well as secular mixing transforming orbits into classical bulge-like (non-rotating, spherical) orbits when the orbits linger near the ILR separatrix (Weinberg in prep). The presence of classical bulges is a dynamically

relevant one owing to the difficulty with which spherical components often have participating in secular evolution. However, the reactive halo in our models clearly particpates in the secular evolution processes, so the degree of pre-processing which takes place prior to a minor merger that may form a classical bulge in a disc galaxy is a particularly interesting question to study.

While the simulation presented appears to reach a steady-state bar phase, such that the observed bar is the maximum that may be created given the initial conditions, our results do not reach a steady-state bulge, as processes to form the bulge are ongoing throughout the simulation and continuing to the end of the simulation. We therefore do not know the maximum mass that a bulge could reach given these processes. The character of the bulge formation changes with time. One may notice that the mass of the bar has not increased from $3 < T < 4$, while the mass of the bulge has roughly doubled from $f_{\mathrm{bulge,T=3}} = 0.087$ to $f_{\mathrm{bulge,T=4}} = 0.177$. Additionally, the pattern speed of the bar changes by less than 5 per cent during this 'steady-state' period (Chapter 4; Chapter 5). Secular evolution theory would suggest then that orbits cannot be trapped without a change to one of these quantities. However, a hint as to what mechanisms may be active is found in the moment of inertia of the bar, I_{bar}, as well as the rate of 'untrapping', or release from the bar (Chapter 4). Though the mass of the bar does not increase, bar orbits are consistently being exchanged with dressing orbits, with a net effect of changing the moment of inertia–an example of heteroclinic motion, where bar orbits are exchanged for dressing orbits at the end of the bar, resulting in untrapping. Given the observed increase in bulge fraction, it stands to reason that this changing geometry of the bar is sufficient to drive mechanisms which elevate orbits.

We may understand the change in angular momentum that enables orbits to continue switching families using a simple dynamical argument. Given $L_{\mathrm{z,bar}} = I_{\mathrm{bar}}\Omega_p$, the angular momentum of the bar, the rate of angular momentum change may be expressed by simply taking the derivative such that

$$\dot{L}_{\mathrm{z,bar}} = I_{\mathrm{bar}}\dot{\Omega}_p + \dot{I}_{\mathrm{bar}}\Omega_p \tag{6.3}$$

Many analytic studies have ignored $\dot{I}_{\mathrm{bar}}$, which naively would appear to be a reasonable assumption during the steady-state phase, given the subtle, 10 per cent change. However, our findings in a self-consistent simulation suggest that a regime exists where subtle changes to the geometry of the bar are enough to cause resonant interaction and secular mixing which pushes orbits to larger vertical extents.

We still lack an understanding for many pieces of galaxy formation that may change the dynamics in ways not described here. For example, the mass assembly leading to present-day galactic discs is not well understood. The growth of mass in the disc from star formation may alter these results. Arguably the most complicating factor is the evolution that has occured in galaxies (both secular and merger-related), erasing memory of the initial conditions in galaxy formation. Other simulations including chemical evolution have supported the general trend where young stars in the solar neighborhood formed near the solar circle, but older stars originated in the inner galaxy (Bird et al., 2013; Minchev et al., 2013). Thus, in general, models which reproduce the observed stellar distribution in the solar neighborhood have been designed with the understanding that the young stars in the solar neighborhood formed near the solar radius, while older stars come are redistributed outward through the galaxy (originating in the inner galaxy). Whether the observations in the simulation are driven primarily by dynamical processes or other processes (perhaps related to star formation) is an open question.

6.5.2 Implications for Milky Way Observations

Given our findings of radial mixing induced by the bar secular evolution alone, one may naturally wonder how they apply to the MW. As it is generally currently accepted that the MW bar is stronger than the spiral activity, and the model has low level spiral activity persistent throughout the simulation, we take this model to be a reasonable approximation for at least the recent history of the MW. Other previous radial mixing studies have

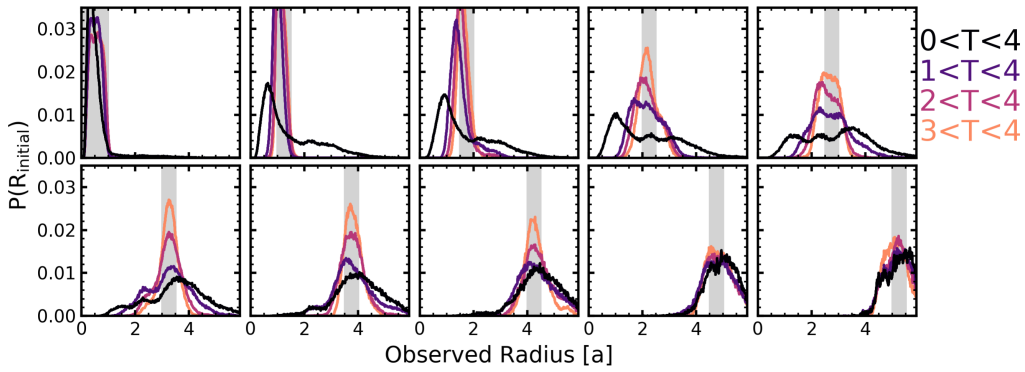

Figure 6.8. Probability distribution of final radii as a function of initial radii, separated by bins of initial radii. In each panel, we mark the bin of the initial radii with a light gray band, such that the upper left panel is the smallest initial radial bin, and the lower right panel is the largest initial bin. Additionally in each panel, we show the radial mixing distribution in four separate time windows, as labeled by color. At early times, $0 < T < 1$, the mixing is significant, as the bar forms. At late times, $3 < T < 4$, the mixing is smaller in magnitude, but still ongoing.

implicated the interaction of the bar with spiral arms as the cause of radial redistribution (Minchev et al., 2012; Di Matteo et al., 2013); we do not find evidence for spiral-induced radial mixing, finding that the bar drives all the observed radial mixing.

As several radial mixing processes have now been put forward to describe the entirety of the MW metallicity gradient and observed stellar distribution at the solar circle, we require more in-depth dynamical studies of the relative importance for the different radial mixing mechanisms outlined in order to make progress with interpreting the MW. This study is a first step in broadening the horizons as to what mixing mechanisms may be the most important, but many details remain to be ironed out, such as the location of the end of the bar (near 5 kpc according to Portail et al., 2017) and CR. Additionally, the history of the MW, and in particular the role of external perturbers, cannot be discounted from having caused radial mixing. Until radial mixing mechanisms incited by substructure and satellites is studied, the gradients in the metallicity will be difficult to interpret, though this study provides a baseline for different dynamical mixing mechanisms. Therefore, we undertake a parameterization of the radial mixing observed in our simulation.

In Figure 6.8, we show the distribution of observed final radii for particles which are initially in some radial (annular) bin. In each panel, we identify particles which are initially in some radial bin denoted by the light gray band, then observe the distribution of particles at some later time. We perform this computation over four windows, $0 < T < 4$ (the entire length of the simulation); $1 < T < 4$ (the time after the assembly of the bar to the end of the simulation); $2 < T < 4$ (the entire steady-state evolution of the bar, after the assembly of the bar has concluded to the end of the simulation) and $3 < T < 4$ (a shorter window of steady-state evolution). Comparing the distributions informs the relative magnitude of the mixing over different time windows.

The mixing related to the formation of the bar ($0 < T < 1$) is difficult, if not impossible, to parameterize, so we do not attempt to do so here. Further, during the growth of the bar ($1 < T < 2$), obvious resonances drive strong secular mixing (e.g. the secondary peaks in the lower left panel of Figure 6.8, which are a result of the end of ILR at $1 < T < 2$). Instead, we determine distributions for the steady-state evolution of the bar, from $2 < T < 4$, noting that the distributions from $2 < T < 3$ and $3 < T < 4$ in Figure 6.8 are similar in most cases.

To parameterize bar-driven radial mixing, we use a gamma distribution owing to the asymmetric nature of the distributions observed in Figure 6.8, following Wang & Zhao (2013), given by

$$f_{\rm mixing}(\alpha, \beta) = \frac{1}{\beta^{\alpha}\Gamma(\alpha)} r^{\alpha-1} \exp\left(-\frac{r}{\beta}\right) \tag{6.4}$$

where $\Gamma(\alpha) = \int_0^{\infty} t^{\alpha-1} e^{-t} dt$ is the gamma function. α is commonly called the shape parameter, and β is the scale or rate parameter. Smaller values of α mean that the distribution is more symmetrical. As β grows, the distribution becomes wider. We choose a gamma distribution owing to the observed asymmetry in the mixing at all radii, such that a tail exists toward larger radii in all annular bins. We allow the location of the peak of the fit to vary, in this case, we choose an offset, $r_{\rm offset}$, for the $f_{\rm mixing}$ function that is the minimum radius at which we observe a star from the initial distribution, relative to the center of the

bin. Thus, to apply this distribution to a population of stars born at some radius, one would first calculated the function $f_{\rm mixing}(\alpha, \beta)$, then offset the distribution from the central radius of the annular bin by $r_{\rm offset}$.

In Table 6.5.2, we use the radial mixing distributions from $2 < T < 4$ as shown in Figure 6.8, during the full steady-state evolution. We note different radii of interest in the rightmost column. During the steady-state evolution, the contributions to mixing from secular evolution and heteroclinic motion dominate over the other mechanisms (chaotic acceleration and the stochastic web). Thus, the fits provided in Table 6.5.2 are generally applicable as mixing distributions for steady-state evolution or in the presence of a slowly-changing pertrbation. We find that away from resonances, $f_{\rm mixing}(5.5 \pm 1.0, 0.22 \pm 0.02)$, along with a radial offset of $r_{\rm offset} = -0.75a$ provides a reasonable fit to the observed distribution of stars. We refer to this as the benchmark steady-state radial mixing.

Near resonances, α increases and the distribution becomes more broad as β decreases. Therefore, near resonances we estimate that $f_{\rm mixing}(14. \pm 2.0, 0.08 \pm 0.02)$, along with a radial offset of $r_{\rm offset} = -1.0a$ provides a reasonable estimate for the mixing near resonances. Within the bar, we find $f_{\rm mixing}(5.4 \pm 1.0, 0.08 \pm 0.02)$, along with a radial offset of $r_{\rm offset} = -0.1a$ to be a reasonable parameterization, as the distributions during the secular evolution period are strongly peaked within the bar, and still roughly centered on their birth radius. Wang & Zhao (2013) found that a model with similar magnitude α and β values as our findings, albeit artificially chosen, was able to reasonably approximate the trends in the MW. We therefore suggest that our parameterizations could reasonably describe the rough magnitude of radial mixing required to reproduce the MW trends.

Feuillet et al. (2018) developed a model to fit the $[\rm M/H]$, log(age), and $[\alpha/\rm Fe]$ distribution at the solar radius using a multi-zone chemical model for star formation and a prescription for radial mixing roughly informed by simulations and a theoretical desire to approximate diffusion such that the distribution of stars goes as $\propto (\Delta t)^{1/2}$. In this radial mixing model, the stars from a given birth radius are distributed at some later time as a

Center Radius $[a]$	α	β	Radial Offset $[a]$	Notes
0.75	4.4	0.09	0.05	Within the bar
1.25	5.9	0.07	-0.07	Within the bar
1.75	6.4	0.09	-0.27	End of the bar
2.25	4.7	0.23	-0.62	
2.75	6.3	0.2	-0.89	
3.25	12.5	0.12	-0.93	Secondary peak from 3:n
3.75	9.4	0.14	-0.75	
4.25	6.5	0.22	-0.72	
4.75	5.6	0.25	-0.77	
5.25	5.7	0.23	-0.74	
5.75	14.0	0.06	-1.01	Secondary peak from CR
6.25	15.3	0.06	-0.38	CR effects
6.75	6.2	0.1	-0.05	Outside of CR
7.25	8.7	0.06	0.06	

Table 6.1. Parameterization of radial mixing during the bar-driven mixing phase, $2 < T < 4$, following Equation 6.4.

Gaussian given by $P(r, R_{\rm initial}) = (2\pi\sigma^2)^{-1/2} \exp\left[-\left(r - R_{\rm initial}\right)^2 / 2\sigma^2\right]$, where the dispersion is computed as $\sigma = \sigma_0 \left(1 - t_{\rm form}/t_0\right)^{1/2}$, where $t_{\rm form}$ is the birth age of the stars (here taken to be the initial time for comparison), t_0 is the observed time, and $\sigma_0 = 2.5$ kpc is set as a fixed parameter. In our model, the choice of fixed dispersion from Feuillet et al. (2018) would be akin to $\sigma_0 = a$. The parameterization of σ in Feuillet et al. (2018) means that σ_0 is only reached as the dispersion after the maximum amount of evolution (e.g. 12 Gyr in Feuillet et al. 2018).

The gamma distribution fits contrast with the fits of Feuillet et al. (2018), where 2 Gyr after birth, the dispersion in observed radius will be $\sigma_{2\ \rm Gyr} = 1\,\rm kpc$, or $\sigma = 0.4a$ at $\Delta T = 1$ if scaled to our models. Using the benchmark radial mixing as a comparison, the Gaussian fit of Feuillet et al. (2018) will roughly match the overall dispersion, but will drastically overestimate (underestimate) the fraction of stars moving inward (outward). The outward mixing is particularly underestimated, owing to the tail. Despite the differences, in particular the symmetry of the distributions and generally smaller dispersions in Feuillet et al.

(2018), the crude Gaussian model is able to reasonably reproduce the trends in the MW. Therefore, this is further supporting evidence that if our model fits were instead applied to the chemical evolution model in Feuillet et al. (2018), they would reasonably approximate the magnitude of radial mixing in the MW.

Based solely on the model presented in this chapter, if the solar radius is assumed to be $R_{\odot} = 1.6R_{\rm bar} = 2.5a$, it would not be unexpected that the Sun could have radially moved from the dynamically-active region at the end of the bar. However, estimates for $R_{\rm CR}$ in the Milky Way range between 4.5 and 7 kpc (Bland-Hawthorn & Gerhard, 2016), which we find to be a natural barrier for outward radial mixing. Wielen et al. (1996) originally suggested that the Sun may have been born $\sim$2 kpc closer to the Galactic center, a finding bolstered by recent models (Minchev et al., 2018). Our model evolution does not discount such a scenario, but does suggest that the Sun could not have been born inside the end of the bar. However, these studies generally require that the outer disc is comprised of kinematically hot stars, in contrast to simulations such as Schönrich & Binney (2009b); Roškar et al. (2013). If the model is kinematically hot, the standard mixing process of stochastic acceleration (e.g. radial migration from Sellwood & Binney 2002) is no longer efficient (Minchev et al., 2012; Daniel & Wyse, 2018). We find that even when stochastic acceleration is not efficient, secular mixing may still drive orbits to different radii.

Lastly, our findings use the apocenter radius to compute radial mixing. This means that a comparison to observational data is missing the 'blurring' ingredient, where the phases of stars are mixed, such that stars with a guiding radius away from the solar circle could be observed near the sun owing to epicyclic motions. Blurring may be a strong effect, such that Haywood et al. (2016) argued that blurring may be sufficient to explain the observed gradient at the solar circle without any radial mixing. Our findings indicate that even in a steady-state bar model, one cannot ignore radial mixing. Antoja et al. (2018) argued for a dynamically young MW disc from Gaia results, which implies that the MW dynamical regime is more like the beginning of our simulation, where we do find rapid rearrangement

of the mass that resembles radial mixing. However, as our steady-state bar drives radial mixing which is either sufficient or nearly sufficient to resemble the stellar distribution at the solar radius, a model where the radial redistribution is abrupt as the early phase of our simulation would not reproduce the MW distribution.

6.6 Conclusion

We dissect the radial and vertical evolution of orbits in a MW-like n-body simulation. The mixing of metalliticities in galaxies is apparent in the gradients observed, and our findings suggest that bars alone, without a spiral pattern, may be strong drivers of radial mixing—contradicting previous studies which have argued that the MW metallicity gradient is a result of radial mixing which includes spirals. We also find that a bar may be a strong driver of three-dimensional bulge formation. We search for and identify standard secular evolution channels resulting in radial mixing (Sellwood & Binney, 2002) and bulge formation (Pfenniger & Friedli, 1991; Quillen, 2002), but also find that the mechanisms they outline cannot alone explain the evolution in the model, requiring standard secular evolution processes (e.g. resonant interaction changing actions) and heteroclinic motion (e.g. family switching at regions of phase space where families are coincident). We provide evidence that these other channels through which radial mixing and bulge formation take place exist, namely the bar-driven evolution presented in Chapter 3; Chapter 4; Chapter 5, identifying generic orbits that participate in the evolution.

The main results of this chapter are as follows:

(1). We decompose a barred galaxy model which has undergone considerable (≈ 8 Gyr) secular evolution, into dynamically-motivated disc, bar, and bulge components, demonstrating the bar and bulge components are distinct, and in particular, the thickened bulge component may be isolated in simulations using a simple maximum vertical excursion technique (Figure 6.1).

(2). The resulting decomposition into bar, bulge, and disc models runs counter to traditional one- or two-dimensional parameterizations of density profiles (Figure 6.2). We discuss strategies to mitigate the degeneracies with traditional fitting to obtain quantities of physical interest.

(3). Radial mixing is present in our models, at a similar level to that generally reported in the literature (Figure 6.8), despite the non-axisymmetric perturbations in our model being bar-dominated rather than spiral-arm dominated (Figure 6.3). We find that the most active region of radial mixing is the end of the bar, where the resonance density is highest such that both secular mixing and heteroclinic motion can take place (cf. Chapter 3). These are distinct mechanisms from the previous findings which required resonance overlap from transient patterns to chaotically scatter orbits (Sellwood & Binney, 2002). We provide fits to the radial mixing in our simulation based on the proximity to resonances.

(4). We find significant amounts of bulge formation in our models, which continues even after the bar appears to have reached a steady-state.

(5). We find evidence for two unique regions for *outward* orbital motion: (i) mixing inside of a bar radius, such that orbits never move outward past the end of the bar, and (ii) mixing outside of a bar radius, where orbits may increase their eccentricity (in contrast to previous findings which claimed continued circularity, Roškar et al. 2008, 2012) and become trapped at CR, or in special cases such as early times in our simulation, OLR (Figure 6.4).

(6). We find several paths for *inward* radial motion, including (i) orbits which move inward from the end of the bar (untrapped) and simultaneously elevate, (ii) orbits which move inward from CR to either being trapped in the bar or not, which do not elevate (Figure 6.5), and (iii) orbits which move inward from the 3:n resonance zone co-located at the end of the bar (Figure 6.6).

(7). We find evidence that several bulge-formation channels co-existing simultaneously: (i) partial resonance passage, (ii) dual two-dimensional resonant capture and (iii) heteroclinic motion. Each results in a different morphology of orbit (Figure 6.7). Therefore, observations of orbits or mass off the plane of galaxies may inform the secular processes, but does not provide a reliable estimate for bar mass or strength, owing to the distinct nature of the physically-motivated decomposition presented here.

In addition to work in the MW discussed in Section 6.5.2, ongoing measurements of abundance gradients in external galaxies (e.g. Ruiz-Lara et al., 2017; Sánchez-Menguiano et al., 2018) will help constrain the dynamical histories of galaxies. Laurikainen et al. (2018) recently demonstrated the power of using integral field units on external galaxies to analyze stellar populations for inferences as to the ages of the populations at a given radius, which may be a more powerful discriminator between different theories of radial redistribution. Of course, the history of any given galaxy will determinte the pattern of radial redistribution. Thus, continued study of dynamical mechanisms relating to radial redistribution, and in particular careful analysis of dynamical mechanisms is crucial to interpretation of abundance and age gradients.

We stress that although we have not presented other simulations in the same detail as this chapter, the mechanisms and discussion presented in this chapter are generally applicable to model galaxies, including the suite presented in Chapter 7. The bar-driven processes that move orbits within the galaxy are the same, and the one-dimensional density distributions have similar profiles at comparable disc-to-halo mass ratios.

CHAPTER 7

UNDERSTANDING TRENDS IN BAR FORMATION AND EVOLUTION IN VARIED n-BODY MODELS

7.1 Introduction

A key morphological feature in the classification of galaxies, stellar bars are found to be present in 70 per cent of disc galaxies in the infrared Sheth et al. (2008). Bars are diverse in length and strength, but nearby are generally 1-2 disc scalelengths long and up to 40 per cent of the stellar mass in galaxies. Some bars end in open $m = 2$ arms, while others (thought to include the Milky Way, MW) end in multiple wrapped arms, often in higher multiplicities ($m = 4$, $m = 6$). Still other galaxies exhibit multiple bars at different position angles. Understanding the physical mechanisms tha shape these features has captivated dynamicists for nearly a century.

With the advent of numerical simulations, idealized models of isolated disc galaxies have uniformly shown that bars readily form as a consequence of a cold, massive, axisymmetric disc, and are persistent features with no clear destruction mechanism (see the reviews of Sellwood & Wilkinson, 1993; Sellwood, 2014). Cosmological simulations have considerably more trouble forming a consistent sample of believable bar morphologies, presumably owing to the resolution limits (Garrison-Kimmel et al., 2018; Trayford et al., 2018; Lovell et al., 2018).

In other chapters (Chapter 3; Chapter 4; Chapter 5), we constructed an empirical, qualitative description for the evolution of barred galaxies, based on the movement of angular momentum throughout the systems, the resultant orbital structure, and the harmonic composition of high-resolution idealized disc and halo models. However, the studies were

based on a carefully selected region of galaxy model parameter space, and are too idealized to study larger questions about bar formation and evolution. Thus, while Chapter 3, Chapter 4, and Chapter 5 demonstrate the mechanisms that drive bar evolution, we had little ability to say which were rare, generic, or compulsory for evolution. Further, given the diversity in observed barred galaxies, we need an expanded parameter space to study whether we are missing important evolutionary mechanisms.

The framework with which we interpret bar-driven galaxy secular evolution is angular momentum transfer (Chapter 4), as mediated by orbits that make up the bar (Chapter 3), which may readily be represented by harmonic expansions which elucidate evolutionary phases (Chapter 5). Fundamentally, we know the angular momentum content, orbital properties, and pattern speed are related. A simple equation connects the geometry and the pattern speed to the total angular momentum of the bar:

$$L_{z,bar} = I_{\rm bar}\Omega_{\rm bar} \tag{7.1}$$

where $I_{\rm bar} = \sum_i m_i r_i^2$, m_i is the mass and r_i is the distance from the inertial center, summed for i discrete mass elements. In the case of the bar, the mass elements are the stars or star particles which make up the trapped component of the bar. We identified three phases of bar evolution in Chapter 3 that are described by the angular momentum content of the bar: the assembly phase, the growth phase, and the steady-state phase. We bolstered the physical mechanisms supporting these phases in Chapter 4. Additionally in Chapter 4, we identified the resonant transfer of angular momentum and its regulation, finding that galaxies could reach a state where the angular momentum transfer reaches a steady-state equilibrium. Prior to that equilibrium, however, the available channels to transfer angular momentum vary, controlled by the phase-space distribution.

In particular, to undergo secular evolution, orbits must be able to change their conserved quantities, energy, E, and angular momentum, $L_{\rm z}$. Unique locations in the phase-space of a galaxy where an individual orbit may change its conserved quantities control the transfer of

angular momentum, created by non-axisymmetric structure, such as bars. Those locations are resonances, where an orbit may gain or lose significant L_z over a handful of rotation periods. At these locations, low-integer commensurabilities between orbital frequencies Ω occur, where standard perturbation theory implies that collective torques on the orbit may induce changes to the conserved quantities. We parameterized the commensurabilities in the three cylindrical coordinates (r, ϕ, z), and Ω_p, the angular frequency of the dominant pattern. The most well-known resonance is corotation (CR), where the orbital frequency Ω_ϕ equals that of the pattern Ω_p. More generally, resonant (or commensurate) orbits satisfy the equation

$$l_1\Omega_r + l_2\Omega_\phi + l_3\Omega_z = m\Omega_p, \tag{7.2}$$

where (l_1, l_2, l_3) is a triple of small integers (usually $l_{1,2,3} \leq 3$) and m is the multiplicity of the pattern, such that the quadrupole $m = 2$ corresponds to a bar or two-arm spiral. The phenomena is referred to as resonant coupling, where the disc transfers angular momentum to the halo at resonances, and has been studied extensively in the literature (see e.g. Lynden-Bell & Kalnajs 1972; Tremaine & Weinberg 1984b; Hernquist & Weinberg 1992; Weinberg & Katz 2002; Ceverino & Klypin 2007; Weinberg & Katz 2007a,b). We used a basis function expansion (BFE) description of the potential in Chapter 5 to study evolutionary phases. The ability to accurately characterize the potential of the phase space enabled the orbital structure analysis in Chapter 3 and the location of important resonances.

We confirmed the importance of the inner Lindblad resonance (ILR), where orbits satisfy the equation $-\Omega_r + 2\Omega_\phi = 2\Omega_p$, for bar-driven evolution, finding that the disc could efficiently transfer angular momentum to the halo given sufficient phase space density. In the absence of sufficient halo phase space density in the vicinity of the bar, the disc would transfer angular momentum to the outer disc (Chapter 5). Further, Chapter 3 identified the importance of a bifurcation in the 'backbone' of the bar, the x_1 family. We denote this as the x_{1b} orbit. The allowed orbital structure in Chapter 3 is one picture for how orbits move throughout the galaxy and support the bar pattern changing its angular momentum: (1)

Orbits may trap into elongated orbits at the end of the bar from quasi-circular orbits previously, (2) trapped orbits may become more eccentric (though not longer) following family conversion (e.g. $x_1 \rightarrow x_{1b}$), or (3) the pattern speed of the bar may decrease. In Chapter 3, we found that the existence of x_{1b} orbits was required to grow the bar after assembly and during the slower secular growth phase.

Throughout Chapter 3, Chapter 4, and Chapter 5 comparing and contrasting a cusp and core simulation, we found hints that an additional parameter controlling the evolution was the ratio of the inner disc mass to the inner halo mass. Therefore, in this chapter, we expand our halo model parameter space to include different concentrations, such that the disc-to-halo mass ratio varies. We confirm the mechanisms in Chapter 3, Chapter 4, and Chapter 5 are valid for a suite of barred galaxy models, and find regimes in both phase-space structure and temporal evolution where different mechanisms dominate the evolution.

This chapter is organized as follows: In Section 7.2, we present our methodology, including the initial conditions, the evolution, and the analysis of the suite of simulations. In Section 7.3, we discuss the primary suite of simulations, identifying the role of different mechanisms in the evolution. Beyond the primary suite of simulations, in Section 7.4 we discuss additional variants to the models which test the persistence of mechanism and explanatory power of our findings. In Section 7.5 we discuss the results in the context of galaxy evolution as a whole. We conclude in Section 7.6.

7.2 Methodology

Before describing the methodology, a few words on the spirit of this chapter. Rather than turning to n-body simulations in an attempt to approximate nature in its entirety, we consider the simulations we need to understand an observable problem–in this case, the physical mechanisms that control bar formation and evolution–as well as how our simulations can interface with established analytic theory to both provide checks on our findings, but also to demonstrate how one must move beyond linear analytic theory into a regime of

nonlinearity and simulations to understand the physical mechanisms. We therefore carefully design our simulation suite to investigate the fundamental unknowns of galaxy evolution (such as dark matter halo profile and disc-to-halo mass ratio), while maintaining high numerical accuracy using a methodology that links well to analytic theory, the basis function expansion (BFE) technique. The inherent multiscale nature of galactic evolution (from granular interactions between stars and giant molecular clouds in real galaxies to multi-kpc length spiral arms, and from short timescale processes to a Hubble time) necessitates a move beyond analytic theory to create a global picture of observable questions. We choose to approach this research by controlling n-body simulations. This approach is necessary to study strong bars; Chapter 3, Chapter 4, and Chapter 5 provide evidence that some of key mechanisms such as trapping, untrapping, weak chaos, strong choas, and harmonic locking may be beyond the standard domain of Hamiltonian perturbation theory.

Unfortunately, an enormous list of parameters may be changed in the generation of galaxy models, emphasizing the challenging task modelers face when attempting to replicate the complex processes that make up galaxy evolution. An exhaustive study of the dependence of all parameters on one another is not tractable at this time, and may not be tractable for many years using simulations. Advancements are being made that enable the rapid execution and minimize the ambiguity in analysis (Chapter 3; Chapter 4; Chapter 5). We use the findings of those works to analyze a larger suite of models that begin to shed light on important parameters, and produce generic mechanisms that apply to broad classes of models rather than specific realizations. In this section, we first generically describe the n-body technique we use in Section 7.2.1, then describe the two types of components we include: the dark matter halo (Section 7.2.2) and the stellar disc (Section 7.2.3), including variations therein. We adopt so-called 'virial units' where $G = 1$ such that $M_{\rm vir} = 1$, $R_{\rm vir} = 1$, $V_{\rm vir} = 1$, and $T_{\rm vir} = 1$. We primarily compare to the Milky Way using $M_{\rm vir} = 1 \times 10^{12}$, $R_{\rm vir} = 300$ kpc, $V_{\rm vir} = 220$ km s^{-1}, and $T_{\rm vir} = 2$ Gyr, but the simulations may be scaled by virial mass for any galaxy to obtain physical quantities.

7.2.1 n-body Technique

We describe the intial conditions of the simulations in the following sections, but we first briefly describe the technique used to evolve the simulations. We use the BFE code EXP (Weinberg, 1999) to evolve the simulations and realize initial conditions, and BFE principles to analyze the simulations. EXP has been extensively used to study several aspects of galaxy evolution, including stellar streams (Choi et al., 2007, 2009), imposed bars (Weinberg & Katz, 2002; Holley-Bockelmann et al., 2005), and self-consistent bars (Weinberg & Katz, 2007b) and (Chapter 1; Chapter 3; Chapter 4; Chapter 5). The methodology is described in detail elsewhere, but we briefly review the salient points here for the purposes of motivating our suite of simulations.

The interaction of the bar, disc, and halo is mediated by resonances, which makes achieving the highest resolution possible a principal concern such that phase space is fully sampled (resonances may be small regions of phase space, and yet have an outsize effect on the evolution). This is particularly relevant for the halo, where the average mass of a halo particle must be approximately equal to that of the disc particles in the vicinity of the disc, in order to achieve the particle number criteria described in Weinberg & Katz (2007a). To that end, we model the disc as $N_{\rm disc} = 10^6$ equal mass particles and the halo as $N_{\rm halo} = 10^7$ multimass particles, such that the number density of particles follows $N \propto r^{-2.5}$, which is significantly steeper than the inner slope of the halos. The multimass scheme means that the effective halo particle number in the vicinity of the disc is $N_{\rm halo,eff} = 10^9$.

EXP solves the Poisson equation for biorthogonal potential-density basis functions whose lowest orders exactly match the density profiles of the halo and the disc. The halo is expanded in spherical harmonics Y_{lm} described by $l_{\rm halo} \cdot (m_{\rm halo} + 2) + 1$ azimuthal orders with $n_{\rm halo}$ radial orders. The disk is expanded in a custom cylindrical basis conditioned on the density function of the disc including $m_{\rm disc}$ azimuthal orders with sine and cosine terms and $n_{\rm disc}$ radial orders. We may truncate the formally infinite series of basis functions to $l_{\rm halo} = 6, m_{\rm halo} \leq l_{\rm halo}, n_{\rm halo=20}$ in the halo and $m_{\rm disc} = 6, n_{\rm disc=12}$. Truncating the

series acts as a low-pass spatial filter that eliminates relaxation and selects spatial scales of interest for galaxy evolution: i.e. fractions of a scale length (in the case of the disc) or scale radius (in the case of the halo). We will refer to the weights on the basis functions as 'coefficients', or the 'amplitudes' of a particular basis eigenfunction. For the purposes of this chapter, we will always sum the contributions from the disc radial orders to obtain an amplitude A_m for the entire azimuthal order m in the disc. Likewise, when we consider the $l = 2$ amplitude in the halo, we are including all $m \pm 2$ and n radial terms. A more complete description of the technique may be found in Chapter 5.

We evolve each simulation until $T = 4$, outputting the positions and velocities every $\delta T = 0.002$. The orbits are integrated at up with 16 times smaller timesteps than this, i.e. $\delta T = 1.25^{-}5$ depending upon three timestep criteria, as defined in Chapter 1. 90 per cent of the disc orbits, and all orbits at $r < 4a$, are integrated at this smallest timestep. The rest of the orbits are integrated at larger timesteps with no loss of accuracy (Chapter 1).

Our goal is a reliable determination of disc structure and kinematics for observational comparison. Therefore we extensively test the ability of the basis to resolve structure formation. We describe several tests. In one test, following the computation of the numerical significance of any expansion coefficient described in Weinberg (1996), we evolve a disc and halo system without self-gravity, e.g. the initial potential field is not allowed to evolve. Successive recomputation of the expansion coefficients provides a measure of the numerical noise inherent in the system based on the number of particles. The resultant variation in amplitude is $\mathcal{O}(10^{-6})$, while in the self-consistent simulation, the amplitudes are $\mathcal{O}(> 10^{-3})$, suggesting that we are far from a regime where numerical noise affects the evolution. To further check that the effects of Poisson noise are within tolerable limits, we perform a verification simulation with $N_{\rm disc} = 10^7$, also without self-gravity. Correspondingly, the Poisson-induced power in each m order in the high fidelity model is reduced to $\mathcal{O}(10^{-7})$, suggesting that our methdology is behaving as expected.

A second test involves increasing the radial orders in the disc to $n_{\rm disc,max} = 18$ and comparing the trace with that of the $n_{\rm disc,max} = 12$ model. We find that the differences in the orders present are of order the previously computed Poisson noise. A third set of tests involves requiring the basis to realize structures to test the translational property of spherical harmonics. We do this by realizing a basis for a disc distribution offset from the expansion centre. This tests whether the basis is missing any eigenfunctions that could bias the evolution and miss structures that are very asymmetric and distorted. We find that the computed eigenfunctions, at $n_{\rm disc,max} = 12$, do not change for a translated disc.

7.2.2 Halo Models

The initial condition realization described in this section and the next has also been discussed in Holley-Bockelmann et al. (2005) and Chapter 1. We describe the models here to motivate the variation of parameters. We choose a modified NFW (Navarro et al., 1997) dark matter halo with concentration c, whose density is given by

$$\rho_{\rm halo}(r) = \frac{\rho_0 r_s^3}{(r + r_c)\,(r + r_s)^2} \tag{7.3}$$

where ρ_0 is a normalization set by the chosen mass, $r_s = R_{\rm vir}/c$ is the scale radius, and $r_c \ll r_s$ is a radius that sets the size of the core. In this chapter, we vary c and test the effects presented in Chapter 3, Chapter 4, and Chapter 5 owing to the presence or absence of a core by testing a choice set of models with $r_c = 0.02 R_{\rm vir}$, in contrast to the standard $r_c = 0.002 R_{\rm vir}$ we set in most models for numerical consistency. We title the models using the concentration as the base of the model name, e.g. $c25$ for a halo with concentration 25. When present, the core radius is appended as γ and the core size in disc scalelengths in Table 7.1. We realize the initial positions and velocities in the halo by Eddington inversion (Binney & Tremaine, 2008) using the total monopole potential of the multi-component system.

There are many other parameters that may be adjusted in the creation of a halo which we do not explore here: triaxiality and spin are two that are addressed by others (Athanassoula et al., 2013; Aumer et al., 2016; Collier et al., 2018b,a). However, we do not expect either of these to qualitatively change the dynamical features explored in this chapter.

7.2.3 Disc Models

The simulations begin with an exponential disc with density

$$\rho_{\rm disc}(r,z) = \frac{M_{\rm d}}{8\pi h a^2} \exp\left(-\frac{r}{a}\right) \mathrm{sech}^2\left(\frac{z}{h}\right) \tag{7.4}$$

where M_d is the disc mass, $a = 0.01 R_{\rm vir}$ is the disc scale length, and $h = 0.001 R_{\rm vir}$ is the disc scale height. We choose the scale length and scale height to be fixed for all of the thin disc components. We note the ratio of the total disc mass to the total halo mass sometimes as a decimal value, but more frequently as a fraction, e.g. ξ^{-1} for a disc whose mass is ξ times less than the virial mass. We title the models using a nomenclature where ξ is appended to the model name.

We select the initial positions in the disc via acceptance–rejection algorithm using Equation 7.4. We select the velocities by the solution to the Jeans equations (Binney & Tremaine, 2008) with an axisymmetric velocity ellipsoid in the disc plane ($\sigma_r = \sigma_\phi$). We characterize the radial velocity dispersion using the Toomre Q parameter,

$$\sigma_r^2(r) = \frac{3.36 \Sigma(r) Q}{\Omega_r(r)} \tag{7.5}$$

where $\Sigma(r)$ is the disc surface density, and the radial frequency, Ω_r, is given by

$$\Omega_r^2(r) = r\frac{d\Omega_\phi^2}{dR} + 4\Omega_\phi^2. \tag{7.6}$$

where Ω_ϕ is the azimuthal frequency. In Chapter 3, Chapter 4, and Chapter 5, we set $Q = 0.9$, a dynamically 'cold' disc, to promote the rapid growth of disc structure. In this

chapter, we vary Q for some models to span a range $Q \in \{0.9, 1.2, 1.4, 1.6\}$. We append 10 times the value of Q to the model name as 'QXX'. The vertical velocity dispersion is obtained directly from the Jeans' equations for a disc,

$$\sigma_z^2(r) = \frac{1}{\rho_d(R,z)} \int_z^\infty \rho_d(R,z) \frac{\partial \Phi_{\rm tot}}{\partial z} dz \tag{7.7}$$

where $\Phi_{\rm tot}$ is the sum of the disc and halo potential (Binney & Tremaine, 2008).

We test an additional family of models by converting a fraction of the mass into a thick disc. The thick disc follows the same density distribution as the thin disc, but the disc scale length is $a = 0.02R_{\rm vir}$ and $h = 0.004R_{\rm vir}$ is the disc scaleheight. The total mass of the stellar component remains the same overall, but the thick disc now takes a fraction $f_{\rm thick} \in \{0.05, 0.1, 0.2\}$ of the formerly thin disc, such that the thick disc mass is $f_{\rm thick} M_d$ and the thin disc mass is $(1 - f_{\rm thick}) M_d$. We append 'tXX' to the model name, where XX is $100 f_{\rm thick}$, to describe each model in Table 7.3. We use a second cylindrical basis tuned to independently characterise the thick-disk evolution. We first verify that the model is stable by running the simulation to $T = 1$ without allowing the potential to evolve and inspecting the resultant noise spectrum from recomputing the potential.

In all, we vary five parameters: (1) the halo concentration c, (2) the presence or absence of a core at $r_c = 0.02R_{\rm vir}$, (3) the mass of the stellar component M_d, (4) the Toomre Q parameter, and (5) the presence or absence of a thick disc component.

Changing the concentration of the halo has a sizeable effect on the mass enclosed by the outer radii of the disc, and in particular, with a radius that the prospective bar may form. We identify the halo concentration and mass of the stellar component as the primary parameters of study, such that our primary study concerns models drawn from a grid with halo concentration as one axis and $\frac{1}{\xi}$ as the other axis. We will refer to this as the $c - \xi$ grid. We summarize the models in Table 7.1 for the $c - \xi$ grid, Table 7.2 for the models with $r_c = 0.02R_{\rm vir}$, and Table 7.3 for variations in Q and $f_{\rm thick}$.

Model	Concentration	Disk Mass M_d (ξ^{-1}) [M_{vir}]	$M_d(r < 2.2a)/M_h(r < 2.2a) \equiv \eta$ (η)	$A_2(T = 2)/A_0(T = 2) > 0.1$?	$\Omega_{p,T=0}$
			$c = 25$ models		
$c25\xi80$	25	0.0125	0.40	✗	60
$c25\xi40$	25	0.025	0.81	✓	70
$c25\xi20$	25	0.05	1.61	✓	70
$c25\xi10$	25	0.05	3.22	✓	70
			$c = 20$ models		
$c20\xi160$	20	0.00625	0.38	✗	40
$c20\xi80$	20	0.0125	0.76	✓	60
$c20\xi40$	20	0.025	1.52	✓	80
			$c = 15$ models		
$c15\xi160$	15	0.00625	0.43	✗	40
$c15\xi80$	15	0.0125	0.86	✓	60
$c15\xi40$	15	0.025	1.72	✓	60

Table 7.1. Summary of models in the concentration-disc mass grid. All models have $Q = 0.9$ and $r_c = 0.002R_{vir}$.

Model	Concentration	Core Radius	Disk Mass M_d [$\mathrm{M}_{\mathrm{vir}}$]	$\mathrm{M}_{\mathrm{d}}(r < 2.2a)/\mathrm{M}_{\mathrm{h}}(r < 2.2a) \equiv \eta$ [$\mathrm{M}_{\mathrm{vir}}$]	$A_2(T = 2)/A_0(T = 2) > 0.1$?	$\Omega_{p,0}$
$c25\gamma2\xi80$	25	0.02	0.0125	0.45	✗	70
$c25\gamma2\xi40$	25	0.02	0.025	0.90	✓	70
$c20\gamma2\xi80$	20	0.02	0.0125	0.76	✓	80

Table 7.2. Models with cores. All models have $Q = 0.9$.

Model	Disk Mass M_d (ξ^{-1}) [M_{vir}]	Notes
$c = 25$ models, vary Q		
$c25\xi80$Q16	0.0125	Q=1.6
$c25\xi40$Q12	0.025	$Q = 1.2$
$c25\xi40$Q14	0.025	$Q = 1.4$
$c25\xi40$Q16	0.025	$Q = 1.6$
Thick Disc models		
$c25\xi40$t5	0.025	5% Thick
$c25\xi40$t10	0.025	10% Thick
$c25\xi40$t20	0.025	20% Thick

Table 7.3. Additional models. All models have $r_c = 0.002R_{\rm vir}$, the same η, and the same concentration as the fiducial simulation.

Additionally in Tables 7.1 and 7.2, we report the disc-to-halo mass ratio within $r < 2.2a$: $\mathrm{M_d}(r < 2.2a)$/$\mathrm{M_h}(r < 2.2a)$. This quantity indexes comparisons across different concentrations and total disc-to-halo mass ratios as a parameter that quantifies the amount of mass available to participate in the bar formation process as a function of the enclosed halo mass. Throughout the chapter, we simplify the notation of the disc-to-halo mass ratio at $r < 2.2a$ as $M_{\rm d}(r < 2.2a)/M_{\rm h}(r < 2.2a) \equiv \eta$.

The studies of Chapter 3, Chapter 4, and Chapter 5 focus on an analysis of a model of a single disc embedded in a dark matter halo, with with $c = 25$ and $\xi = 40$. This fiducial model represents the $z = 0$ MW and is the basis for variations with Q and thick disc fraction.

7.2.4 Analysis Techniques

In this section, we briefly describe the analysis techniques used in this chapter. All techniques have been presented elsewhere. We refer the interested reader to the cited works for a more detailed introduction to each technique individually.

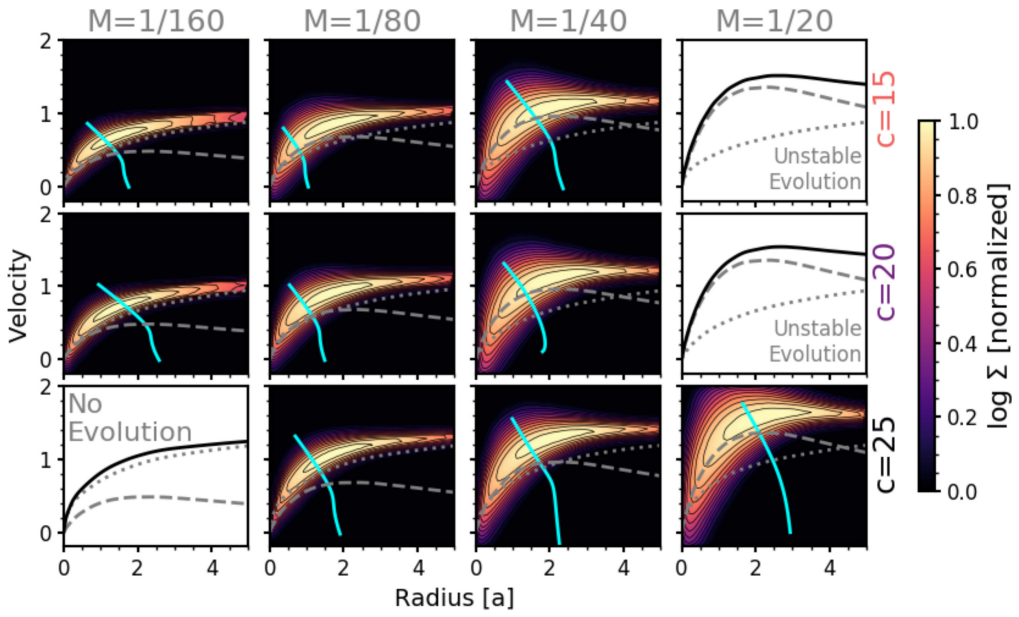

Figure 7.1. Circular velocity curves for the nine models evolved as part of the $c - \xi$ grid. The panels each show instantaneous radius versus tangential velocity for the models which were analyzed (in color). Three additional models that were not analyzed are shown in black and white and discussed in the text. Overlaid on each panel are the contribution to the circular velocity curve from the disc (dashed line) and halo (dotted line), as well as the location of corotation (cyan), computed from the monopole, using pattern speeds as estimated from the coefficient series (see 7.2.4.3).

7.2.4.1 Radius-Velocity Space

Chapter 3, Chapter 4, and Chapter 5 used the distribution of apocentric radius and tangentially velocity to represent phase space in observable quantities. Although apocentric radius is not a direct observable, orbits spend proportionally more time at apocenter than any other phase of their orbit, therefore instantaneous radius and tangential velocity tends toward the apocenter values. Further, radius and velocity are the standard rotation curve axes as well as a plane that can be fully populated using integral field units (IFUs).

In Figure 7.1, we introduce the grid of primary models analyzed in this chapter in these units. Later figures will follow this same panel arrangement to describe simulations on the $c - \xi$ grid. The rows correspond to different halo concentrations ($c = 15, 20, 25$ from top to bottom), and columns correspond to disc-to-halo mass ratios (defined by $\xi =$

$160, 80, 40, 20$ from left to right). Each panel shows the particle density in a plane defined by instantaneous tangential velocity, $v_t = (x\dot{y} - y\dot{x})/r$ and cylindrical radius r. The panels have been normalized such that the peak density in each panel is unity. We show the tangential velocity from the disc and halo separately. While the total circular velocity curve may look similar in several cases, the relative contributions may be very different. Panels in color are simulations and panels in black and white show the theoretically-computed circular velocity curve as a function of radius for simulations we do not analyze in this chapter. We discuss the reasons for choosing not to analyze the simulations in Section 7.3.2. We also estimate the initial bar pattern speed as in Section 7.3.2, and use the pattern speed to compute the location of CR. In general, we see that CR moves to larger radii toward the lower right of the grid, where η is largest.

7.2.4.2 Orbit Techniques

We use two different techniques for characterizing orbital dynamics: (1) in-situ trapped orbit tracking, and (2) commensurate structure analysis. Both techniques are described in detail in Chapter 3, including a detailed Appendix with algorithms and test examples.

To calculate trapped orbits, we rely on a clustering method which computes the apsis position angle for a given orbit in a specified time window relative to the position angle of the bar. Orbits whose apsides are coherent over several apocenters are considered to be trapped: that is, their apsides librate around the minimum of the bar potential and thus reinforce the bar feature. Our method begins with a time series of apocenters transformed into a frame corotating with the bar. We use a standard k-means implementation (Lloyd, 1982) to locate the $k = 2$ clusters in apsis angle. In this way, we identify two key families: x_1 orbits, which form the backbone of the bar, and 'other' bar-supporting orbits, which encompasses all higher-order commensurabilities that support the bar. We do not classify other standard families of orbits, e.g. $x_{2,3,4}$, finding that these orbits do not play a significant role in they dynamics described below.

Additionally, Chapter 3 presents methods to locate commensurabilities in our model galaxies: one determines the location of ILR and the trapped x_1 family, and one determines the location of CR and OLR. The method to determine the location of ILR uses a geometric technique based on Delaunay Triangulation to compute the planar area an orbit would fill in a frame corotating with the bar in the limit that $T \rightarrow \infty$. Trapped orbits, which librate around the minimum in the bar potential, fill very little area in the plane, while standard rosette orbits will fill nearly the entire plane within their apocenter radius. After finding the nearly commensurate or closed orbits which fill a small volume, we assign orbit families by inspection. This yields the ILR track. The geometric algorithm-determined commensurability tracks will be shown in white in the figures that follow.

The method to locate CR and OLR relies on mapping frequency space in the model galaxy using the monopole potential. Given the monopole potential, we can define Ω_r and Ω_ϕ in the epicyclic limit, and given a pattern speed for the bar, Ω_p, determine the location of CR and OLR. The monopole-determined resonances will be shown in cyan in the figures that follow.

7.2.4.3 Harmonic Decomposition

Chapter 5 used a harmonic decomposition based on the basis function expansion (BFE) that serves as the Poisson solver for the evolution. In Chapter 5, we found correlations between the amplitude and phase of the basis coefficients that describe the simulation (e.g. density, forces, and potential) and evolutionary scenarios. For example, the coefficients of each basis function are complex quantities that we may use to calculate the phase and the pattern speed of the bar, allowing for transformation to the bar frame during the simulation, as well as giving direct measurements for the pattern speed.

Chapter 4 introduced a tool for explicitly tracking angular momentum transfer during a simulation by calculating the instantaneous torque from the basis functions, $\tau \equiv$

$dL_{\rm z}/dt = r \times F_\theta = rF_\theta$. We used the field F_θ to quantify the importance of halo dynamics, under the assumption at late times that the evolution was roughly steady-state.

7.3 The Halo Concentration-Disc Mass Grid

In this section we describe trends in bar formation and evolution as a function of c and ξ. We compare our findings to the known mechanisms for bar formation and evolution, based on the results of Chapter 3, Chapter 4, and Chapter 5. We also present new results, including (1) evidence for a peak in bar formation efficiency as a function of c and ξ owing to the competing dynamical effects of violent bar evolution at low ξ and disc stability at high ξ, (2) evidence for a maximum efficiency in pattern speed decay, also as a function of c and ξ, and (3) the existence of clear growth phases in only roughly half of the models.

We first examine the isophotal appearance of the models (Section 7.3.1) after bar formation, finding that we cannot differentiate between different regions in parameter space using the appearance alone. A time-series analysis of a harmonic decomposition of the models (Section 7.3.2), reveals that the evolution is markedly different for all models in the $c - \xi$ grid. We analyze dynamics leading to the observed evolution in Section 7.3.3, using the tools from Chapter 4. We use the improved kinematic diagnostics from Chapter 3 to provide observational diagnostics in Section 7.3.4.

7.3.1 Final Isophotal Appearance

We show two views of the simulations at $T = 4$, the end of the simulation in Figure 7.2. Not all model galaxies will form a bar. The lower color panels show the surface density of the galaxy models at $T = 4$, rotated so that the bar aligns with the x axis. The bars that do form all seem to have lengths of $R_{\rm bar} \approx 2a$, only weakly dependent on either the disc mass, halo concentration, or η. The ratio $\frac{b}{a}$ of semi-minor to semi-major axis lengths increases, i.e. the bars become rounder as η increases. The roundness is attributable to two factors; the presence of a larger number of x_2 orbits and boxlets (Chapter 6), and a lack of

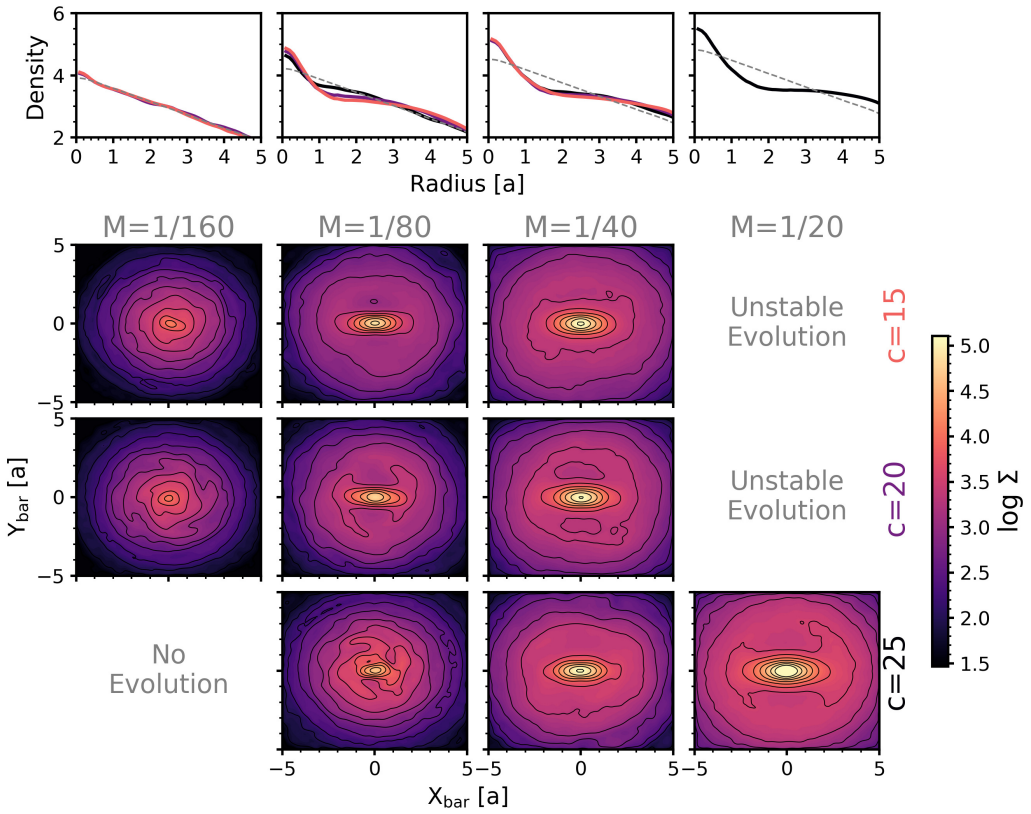

Figure 7.2. Grid of nine simulations at $T = 4$. The lower gridded panels show the face-on appearance of the galaxy in surface density. Columns in ξ^{-1} are labeled above the panels, and correspond to different disc-to-halo mass ratios. Rows are labeled on the right, with different values of halo concentration. The upper row of panels shows the azimuthally-averaged density, color coded by concentration, as labeled. The initial exponential disc is shown as a dashed gray line for comparison.

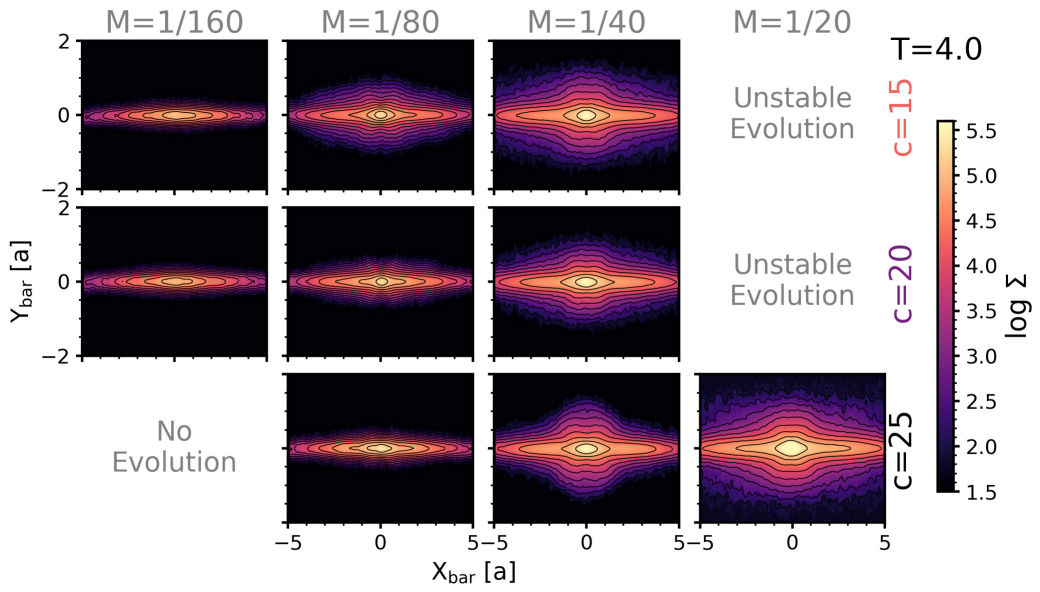

Figure 7.3. Grid of nine simulations at $T = 4$, shown edge-on parallel to the bar. Columns in ξ^{-1} are labeled above the panels, and correspond to different disc-to-halo mass ratios. Rows are labeled on the right, with different values of halo concentration.

x_{1b} orbits, which are highly eccentric (Chapter 3). Kruk et al. (2018) found a measured axis ratio for the bar of $b/a = 0.31 \pm 0.12$, which corresponds well to canonical value of 0.2-0.4 from Kormendy & Kennicutt (2004). This constrasts with the finding of $b/a = 0.24 \pm 0.07$ from Hoyle et al. (2011), in which bar axes were measured by eye, but compares favorably with Gadotti (2011), who found $b/a = 0.37 \pm 0.10$ when using a generalized ellipse fit. Our models are all in the range $\frac{b}{a} = (0.25, 0.4)$, consistent with observations.

The uppermost row of Figure 7.2 shows the azimuthally-averaged density as a function of radius for each of the models in the column. We find negligible dependence on halo concentration; the shape of the disc density relative to that of the initial exponential disc is qualitatively similar for all models that form a bar. The density profiles all show the characteristic shape of nearby barred galaxies (e.g. Kim et al., 2014), namely a central high density region, a shallow exponential density profile or plateau just outside of the isophotal bar radius, and an outer exponential, which in all our models is steeper than the inner exponential. The uniformity of these models in both face-on surface density and

density profile across a range of parameters suggesting that instability-formed bars have a characteristic structure.

In Figure 7.3, we show the edge-on projected surface density of the models. Here we see a diversity of morphologies. The models with no bar do not form a bulge, while the models with bars for bulges of various strength. The bars vary in their 'peanut' or 'X-shape' morphology, with the most obvious bulges showing more spherical isophotes, and the less pronounced bars showing a clearer boxy isophotal structure. We have described mechanisms for secular bulge formation in Chapter 6; the mechanisms which elevate orbits out of the plane, are the driver in all models in the $c - \xi$ grid. The primary mechanism to elevate orbits is partial resonance passage, where orbits are pushed to higher elevations as a result of passing through the separatrix from some resonance, in this case ILR or CR. We discuss this mechanism in Chapter 6, and a more thorough treatment will be in Weinberg (in prep). Some bulges appear to have more spherical isophotes: this supports our conjecture in Chapter 6 that subsequent evolution after the initial peanut/X-shape formation will act to decorrelate the bulge orbits that once supported the peanut shape, resulting in a structure that resembles what is traditionally referred to as a 'classical bulge'. Given the diversity of morphologies in the $c - \xi$ plane, the bulge morphology implies a value for η. However, this assumes that the elevated struture was the result of secular evolution and not accreted material. In subsequent sections, we will apply our understanding of dynamical mechanisms responsible for bar evolution to differentiate between the models where isophotal analysis falls short.

7.3.2 Harmonic Evolution

Following the analysis of Chapter 5, we analyze the basis function coefficients, identifying the evolutionary phases in each model. We summarize our findings as (1) not all bars have the same values of the ratio of total amplitude in the $m = 2$ harmonic to the $m = 0$ harmonic, A_2/A_0, despite their apparent photometric similarity, (2) model galax-

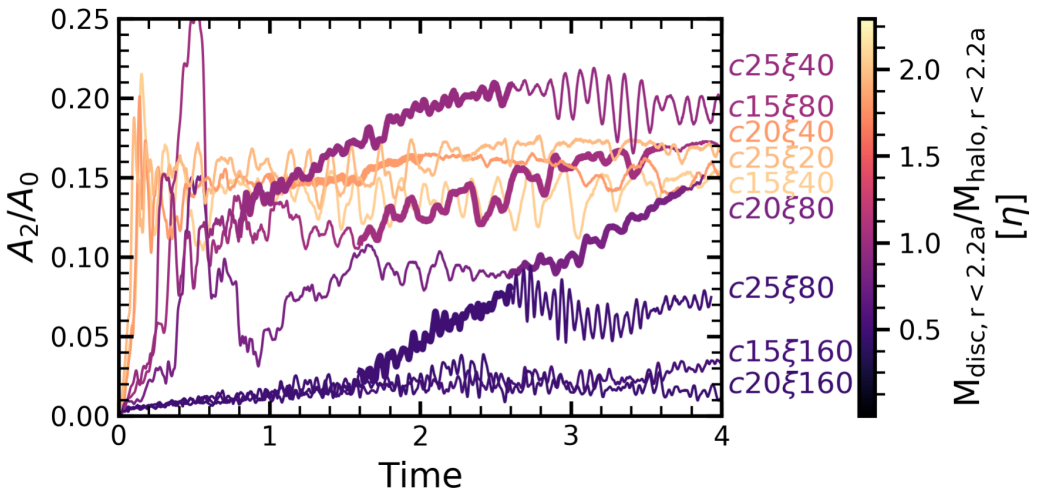

Figure 7.4. The $m = 2$ amplitude normalized by the $m = 0$, A_2/A_0, versus time in nine simulations. Simulations are labeled and color-coded by the disc-to-halo ratio interior to 2.2 disc scalelengths, η. In each panel, if a simulation is in a growth phase, we double the line thickness.

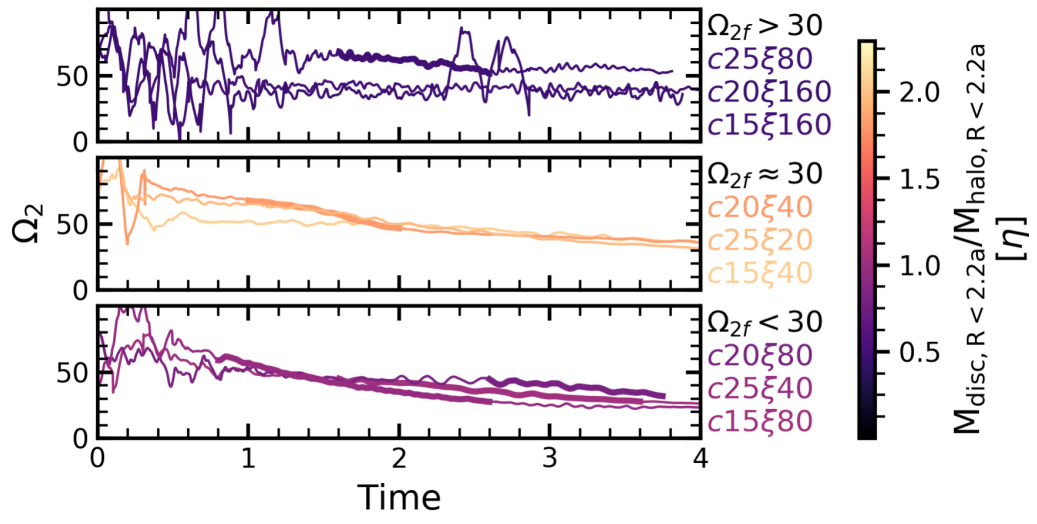

Figure 7.5. Ω_2 versus time, where Ω_2 is computed from the phase of the coefficients. The panels are separated by late-time values of Ω_2. In each panel, if a simulation is in a growth phase, we double the line thickness.

ies with similar A_2/A_0 ratios may have taken different evolutionary paths with different mechanisms, and (3) the formation and assembly epochs of bars from axisymmetric discs is strongly dependent on η which also affects the later evolution of the system.

In Figure 7.4, we show the evolution of A_2/A_0 versus time for the nine models in the $c-\xi$ grid. The models in the grid are color-coded by η, the disc-to-halo mass ratio interior to 2.2 disc scale lengths. We highlight the growth phases, when present, in each model, and increasing the line width correspondingly to highlight these epochs.

We may broadly partition the models into three groups by η: $\eta \approx 0.5$, ($c15\xi160$, $c20\xi160$, $c25\xi80$); $\eta \approx 1.0$, ($c15\xi80$, $c20\xi80$, $c25\xi40$); and $\eta \approx 2.0$, ($c15\xi40$, $c20\xi40$, $c25\xi20$). All models with $\eta > 1$ exhibit an assembly phase, which takes place very quickly for those models ($\Delta T < 1$; a scaling to the Milky Way gives $\Delta T_{\rm MW} = 2$ Gyr). The models with $\eta \approx 2$ quickly saturate and reach a steady-state, similar to the observed behavior of the cusp simulation in Chapter 3, Chapter 4, and Chapter 5. The average peak of $m=$ during formation is at $T_{m=2\ peak} = 0.15$, or less than two rotation periods. We parameterize the rapidity of the bar formation process by roughly describing the the increase in A_2/A_0 at early times with an exponential as a function of time from the beginning of the simulation to the peak of A_2/A_0, such that $A_2/A_0 \propto \exp(\alpha t)$. α is largest for the simulations with $\eta \approx 2$.

Only one of the models, $c20\xi40$, proceeds to have a bona fide growth period (shown as a heavy line segment in Figure 7.4) where the bar mass increases with any appreciable rate. The evolution scenarios in these models is best defined as a rapid assembly phase followed by steady-state evolution, punctuated by possible growth phases if the orbital structure of the model allows for bar-growing mechanisms. During the steady-state evolution phase the bar geometry is changing owing to slow orbital rearrangement, such that $\dot{I}_{\rm bar} \neq 0$ and thus $\dot{L}_{z,{\rm bar}} \neq 0$. During the growth phase, x_{1b} orbits and higher-order resonances feed the zone at the end of the bar, such as $3n$.

The models with $\eta \approx 0.5$ do not form a bar at the outset of the simulations. However, the $c25\xi80$ model is unique in its formation sequence from all the other models: the bar grows smoothly from some seed disturbance, jumping directly into a growth phase. Given the linear growth in A_2/A_0, this is a prime candidate to be the slow growth mechanism of Lynden-Bell (1979). However, the evolution reaches only a fraction of the A_2/A_0 ratio of other models which form a bar.

The models with $\eta \approx 1$ show the largest diversity in A_2/A_0 outcomes. While the models are the strongest bars as measured by A_2/A_0, and each of the simulations show a clear growth period, the models follow different evolutionary paths during the simulation. In particular, while model $c25\xi40$ does not show a steady-state phase after assembly, both $c15\xi80$ and $c20\xi80$ have some steady-state evolution prior to their growth phase. Model $c20\xi80$ does not undergo a true bar assembly phase until $T = 1$, as the initial $m = 2$ evolution was highly unstable and could not form a stable bar. In Tables 7.1, 7.2, and 7.3, we report whether A_2/A_0 is above 0.1 at $T = 4.0$, a measure of whether the simulation has a persistent, evolving bar. In simulations with $\eta \approx 1$, $\alpha \approx 1$ in our units.

We also estimate the initial pattern speed of the bar from the extrapolation of the trends in Ω_2 to $T = 0$ and report it in the tables. In Figure 7.5, we plot Ω_2, the bar $m = 2$ pattern (which is equivalent to the bar pattern after assembly) versus time. We separate the models into three panels by the asymptotic value of Ω_2 at the end of the simulations. In some cases, we were forced to continue the evolution of the simulation to be certain that the evolution had reached the asymptotic value, but all simulations showed a clear asymptotic value of Ω_2 before $T = 5$, which is $T_{\rm MW} = 10$ Gyr if scaled to the MW. The η classes we defined above have relevance for the final pattern speed in the models: the strongest bars, with $\eta \approx 1$, slow the most. We attribute this slowdown to the efficiency of coupling to the halo, which we discuss below.

It is well known that a massive, cold axisymmetric disc is prone to bar instability, and we exploit that to produce bars for study. Our initial conditions are close to but not in

perfect equilibrium. For the most massive discs in our grid, the instability is seeded by features produced as the inner disc settles into equilibrium for $\eta > 0.5$. For unstable disc, any noise will be enough to produce the instability and the time to produce the bar will depend on the noise. In addition, the experiment itself is not natural: a true galaxy would accrete mass slowly over cosmic time. Therefore, we focus on the evolution of bar after formation, and not the time of formation, for the grid of simulations.

As the bar forms, we identify two distinct scenarios of bar formation from our grid of models. The first is the *dynamical* instability: the initial conditions seed physical instabilities which give way to bar formation. In this scenario, the natural self-gravitating modes of the combined disc and halo system (e.g. the frequencies allowed by the dispersion relation wavenumbers, Weinberg, 1994) is excited by noise or some external disturbance. For a cold disc, this growth appears to run away. The final bar formation scenario is driven by a gradual precession of orbits toward a bisymmetric disturbance that is self reinforcing (e.g. Lynden-Bell & Kalnajs, 1972). Dynamical instabilities are characterized by exponential growth, while secular instabilities feature linear growth. After formation for both mechanisms, the bar grows by self-trapping of orbits which is distinct secular processs. Therefore, we look to the obviously linear growth phases in our models to learn about the secular evolution that may be driven by bars.

We may summarize the three η regimes as (1) weak bar formation at $\eta \approx 0.5$, (2) a sweet spot for bar formation in our models when $\eta \approx 1$, and (3) over-massive violent bar formation when $\eta \approx 2$. We have described models which fit each of the regimes, finding that they may exist for different combinations of halo concentration and disc-to-halo mass ratio. We also find evidence for a peak in bar formation efficiency, as the $c25\xi40$ model produces the strongest bar as measured by A_2/A_0. **The establishment of such thresholds to bar evolution regimes, if well-understood, may hold valuable information for cosmological simulations as they approach resolutions and sizes where morphological comparisons to the real universe may reasonably be undertaken.**

7.3.2.1 Non-quadrupole Evolution

The $m = 2$ or quadruople component of the bar is the strongest non-axisymmetric feature in our models. However, Chapter 3 demonstrates the importance of $m = 4$ power to the x_1 bifurcation and x_{1b} family. We also found in Chapter 5 that the $m = 1$ or dipole may play a role in the transition between the growth and steady-state phases. The time evolution of the $m = 4$ pattern generally follows the qualitative features of the $m = 2$ pattern, particularly after formation. However, in the highest η models, $c25\xi20$, we see continued $m = 4$ activity, which modulates the $m = 2$ pattern.

Additionally, models $c25\xi80$, $c25\xi40$ (the fiducial simulation), and $c20\xi40$ all show signs of mode-locking between the $m = 2$ and $m = 1$ patterns, which acts to halt bar evolution in all three cases. However, while the coupling identified in $c25\xi40$ by Chapter 5 was $\Omega_2 = 2\Omega_1$, we find that for $c25\xi80$, the mode locking is $2\Omega_2 = \Omega_1$, and in $c20\xi40$, the mode-locking is $\Omega_2 = \Omega_1$. This suggests that the mode-locking mechanism is a common, but not necessary, part of bar evolution, which acts to inhibit bar growth possibly by preventing the slow secular change in the pattern speed or bar amplitude that is necessary for secular growth.

7.3.2.2 Parameter Space Limits

We do not show the results from a simulations with $\xi = 160$, instead marking this regions of $c - \xi$ grid as 'no evolution'. At this mass ratio and concentration, the disc is stable to non-axisymmetric perturbations in the 9 Gyr of evolution, and does not develop harmonic amplitudes above the Poisson noise level that we require to interpret evolution.

Additionally, we do not show the results from two simulations with $\xi = 20$, instead marking these regions of $\xi - c$ space as 'unstable evolution'. While bars readily form in these simulations, the initial formation phase is very strong and affected by the initial non-equilibrium mixing. We therefore cannot draw accurate conclusions about the final status of bars in simulations with these parameters. The initial unstable evolution is marked by

strong aphysical $m = (1, 3, 5)$ amplitudes and strongly peaked A_2/A_0 as a function of time[1]. Extending the $c = 25$ row to $\xi = 10$ yields a model with unstable evolution, leading to our discovery of a threshold in $c - \xi$ space for bar evolution that may be studied from an initially axisymmetric initial condition. Models with halo concentration of $c = 10$ are unstable above $\xi = 80$. Therefore, we believe that our parameter space in $c - \xi$ roughly covers the range of interest for secular bar evolution.

We acknowledge that bars may exist in galaxies with $\xi > 20$ and $c < 25$, but it is highly unlikely, given our simulations, that the bar formed in initially axisymmetric discs. The initial conditions simply do not resemble any real galaxies. Thus, if barred galaxies with $\xi > 20$ and $c < 25$ exist, they are more likely to be the result of mass accretion after the bar has formed, making the formation and early evolution of the bar a more apt comparison to our grid of models. However, $\xi = 20$ is not an abnormal initial ratio for the disc and halo in many seminal bar-formation studies in the literature (Debattista & Sellwood, 2000; Athanassoula & Misiriotis, 2002). Additionally, in a recent cosmological zoom-in simulation, Debattista et al. (2018) analyzed the bar formation in a model galaxy with $\xi = 20$, arguing that the model was an appropriate comparison to the MW. However, we find that both bar formation and evolution proceed differently in $\xi = 20$ and $\xi = 40$ models, with an additional dependence on c, so interpreting models that are significantly more massive than the MW may not probe the dynamical regime of the MW.

7.3.3 Dynamical Description

We have identified trends in the evolution of models in the $c - \xi$ grid and have described some dynamical processes, but have not yet described the controlling mechanisms that drive evolution in each model. To understand the role of different mechanisms in the models, we identify resonant structure and associate the commensurate families with

[1] As we demonstrate in Chapter 5, the initial peak in A_2/A_0 is not related to the actual mass or strength of the bar, but rather the global $m = 2$ response the assists the formation of the bar.

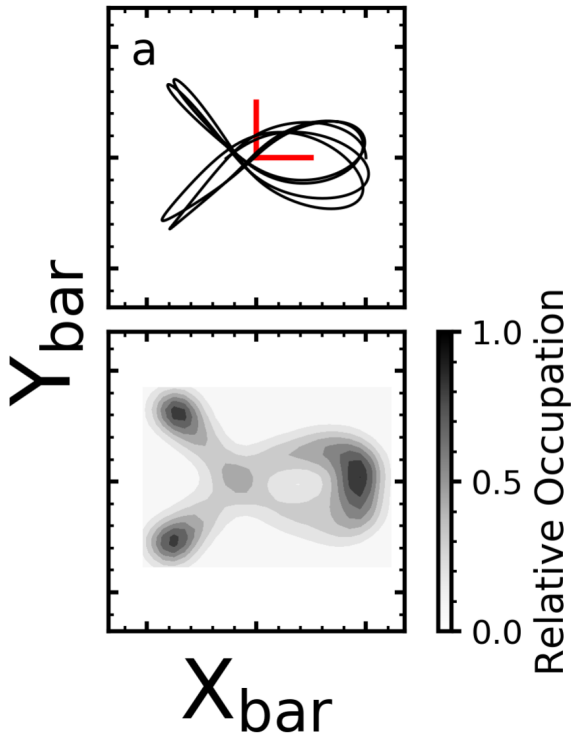

Figure 7.6. An example of a higher-order x_{1b} orbit present only in the strongest bars. The upper panel shows the trajectory of the orbit. The lower panel shows the time-averaged position of the orbit. The red lines are half a scale length.

evolution as described in Chapter 3. Therefore, we first locate the dynamically-important resonances, then quantify the role of the angular momentum transfer channels as described in Chapter 4.

7.3.3.1 Where are the resonances?

We use our geometric algorithm (Chapter 3) to empirically locate ILR. This allows us to find the maximal extent of orbits in the x_1 family. We find that the maximal length of x_1 orbits generally increases with both the concentration of the halo for models which form a bar as well as the total disc mass.

The presence of the growth phase in A_2/A_0 amplitude correlates with pattern speed decline. This is expected from the secular evolution theory: continued growth of the bar

through trapping requires that the bar change its angular momentum through resonant transport. If the bar strength and pattern were fixed, trapping could not occur. The ILR identification using the geometric algorithm also reveals that the in all models with a growth phase, the growth is accompanied by the presence of the x_{1b} subfamily of orbits. The x_{1b} family is particularly difficult robust such that further evolution does not cause the family to become unstable again, and thus is an important element in building bars.

Once ILR has been identified, we look for subfamilies that may be important for the evolution. In Chapter 3, we found that the x_{1b} orbit family promites the growth of bars. The geometric method from Chapter 3 successfully identified the orbit families for our entire model grid. Moreover it found one key addition to the orbital pantheon described in Chapter 3: an additional bifurcation of the x_1 family, shown in Figure 7.6. This orbit family is only present in strong bars. The effect is to increase the axis ratio of the bar, in contrast to the x_{1b} orbits presented in Chapter 3. The orbits in this family exist at larger $V_{\rm apo}$ than the bar, but is spatially coincident and stable over a long period of time. However, this orbit family is only observed in $c25\xi20$, suggesting that η must be very large before this orbit is observable. However, when it is observable, it may have implications for the long-term evolution of the bar, as discussed below in Section 7.5.3.

Outside the bar where the orbits remain nearly circular, the geometric algorithm is ambiguous, so we use monopole-derived frequencies to locate CR in our models. CR plays an important role in keeping the bar supplied with new orbits to trap by driving orbits inward to smaller radii (Chapter 6), but the location of CR is largely unimportant for the evolution of the overall system after the bar has reached its maximal A_2/A_0 ratio[2]. As with ILR, the location of CR generally increases with both disc mass (ξ^{-1}) and halo concentration. Despite the late-time pattern speeds being generally similar, the location of CR and the character of ILR is appreciably different for the models in the $c-\xi$ grid. The

[2]In the fiducial simulation, $c25\xi40$, CR moves out to such large radii so as to be unimportant for the evolution of the model.

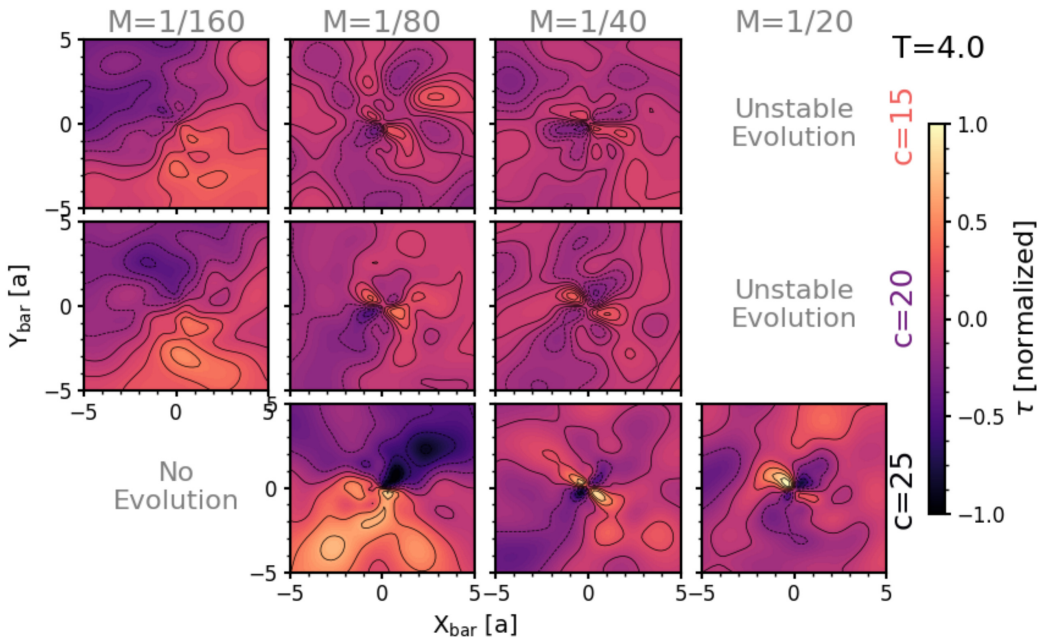

Figure 7.7. The $F_{\theta,\mathrm{halo}}$ field in $x-y$ space in the $c-\xi$ grid of simulations. Positions have been oriented such that the stellar bar is aligned with the x axis. All panels are normalized such that the color map may be compared across panels.

location of CR in the models which do not form a bar is particularly illuminating. We find that CR is at approximately a scalelength, which we will see below is too small of a radius to organize a self-consistent bar response.

7.3.3.2 The role of the halo

We use the BFE method to derive instantaneous torques between the disc, halo, and subcomponents of the disc in Chapter 4. In the cusp simulation, the halo controlled the transfer of angular momentum by applying larger torque, while in the core simulation, the halo was unable to supply significant torque, and thus the bar transported angular momentum to the outer disc. Secular angular momentum transfer by resonant interaction is dual with the torque applied by the response of component accepting angular momentum. From the resonance point of view, orbits cross the resonance in both directions, gaining and losing angular momentum , respectively. The net change depends on a phase-space gradient.

An orbit passing through resonance also changes its phase. The asymmetry caused by the gradient causes a trailing or leading feature in the distribution depending on the net sign of the change. For the bar–halo interaction the halo response to the bar lags the bar position at early times, and thereby applies significant torque. The continued torque tends to remove the gradient. Therefore, the response becomes aligned with the bar position at late times, reducing the torque to zero. In this section, we measure the role of the halo in applying torque to the bar and driving its evolution.

The detailed torque analysis from Chapter 4 is expensive. However, we can use the dual nature of the secular transport mechanism to qualitatively interpret the role of the halo in the evolution of the bar. Specifically, we use the amplitude of the F_θ field in Figure 7.7 to estimate the role the halo played in the evolution of the bar, i.e. through accepting angular momentum. As the wake forms owing to the acceptance of angular momentum from the bar, a higher-amplitude wake, particularly at fixed disc mass, indicates a strong secular evolution channel. We see that in the case of the $c = 25$ halo, the magnitude of the torque is much larger than that of the other halo models, consistent with our interpretation that the evolution in the $c = 25$ models is dominated by the torque from the halo and the angular momentum deposition, whereas the $c = 20$ and $c = 15$ models are progressively more dominated by the angular momentum sink of the outer disc. Thus, a more concentrated halo plays a larger role in applying torque to the disc and encouraging evolution. When a bar does not form, the halo response is dominated by $m = 1$ amplitude.

At a certain point in the self-consistent evolution, these assumptions will break down, as the halo wake, saturated, will no longer lag the bar and thus no longer exert a torque as described above. We see that all simulations in a steady-state phase in the $c - \xi$ grid have the F_θ field aligned with the bar major axis. We will assume that when the wake has aligned with the bar that halo-driven secular evolution is complete. The exceptions are the high halo-to-disc mass ratio models. In the case of the $c = 15$ and $c = 20$ models, this is simply because a bar has not formed. However, in the $c25\xi80$ model, a bar has formed, but

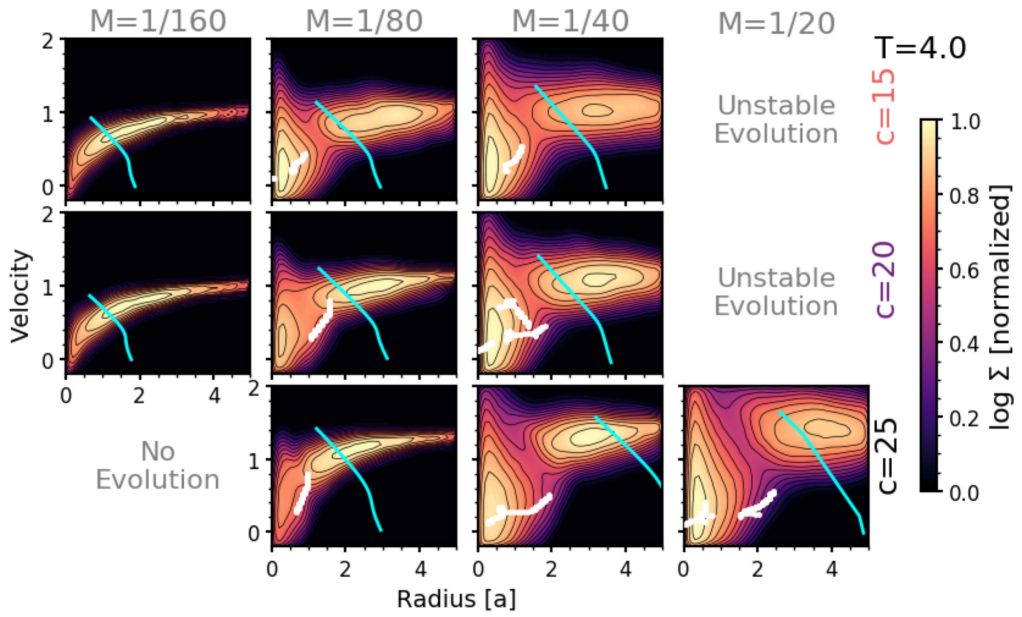

Figure 7.8. Tangential velocity as a function of radius diagrams for the grid of nine simulations at $T = 4$. The ILR is shown in white, and CR is shown in cyan.

has not sufficiently evolved to transfer angular momentum to the halo and align the wake with the bar major axis. Making a similar grid to examine wake at $T = 2$ shows that the wake has not fully aligned with the bar major axis in any model.

At high enough disc mass, the transport of angular momentum to the outer disc may dominate that to the halo. For example, the value of A_2/A_0 reaches a large value for $\eta \approx 2$ models despite lower halo influence. Specifically, the outer disc accepts angular momentum when the halo channels are weak or unavailable. Thus, we conclude that for the models at with $c < 25$, the primary driver of the angular momentum transfer is the outer disc, whereas in the $c = 25$ model, the inner is the primary channel controling angular momentum transfer.

7.3.4 Kinematic Appearance

With a clearer dynamical understanding of the processes that drive evolution, we wish to connect the dynamics to features which may be observable. For this, we return to $r - v_t$ space (as in Figure 7.1). In Figure 7.8, we plot the density of the galaxy models in

instantaneous $r - v_t$ space. The bar-hosting models bear little resemblence to the initial conditions inside of two scalelengths, and in particular, a spur of particles at small radii have a large tangential velocity: these are the boxlets and x_2 orbits. The trapped bar orbits are found in the vicinity of ILR, which we mark in white for all models where we are able to calculate the pattern speed. We also place CR, calculated from the monopole frequencies, on each panel, including for those models without a bar. The two $\xi = 160$ models do not form a bar in either isophotal appearance or A_2/A_0, and placing CR on the phase space density shows us why: the location of CR for all realistic pattern speeds is located at too small of radii to seed a self-gravitating $m = 2$ response. See Table 7.1 for the initial pattern speed estimates of all models, including models without an apparent isophotal bar that still show coherent $m = 2$ phases.

We have shown in previous chapters (Chapter 3; Chapter 4) that the location of resonances relative to the phase-space density is important for controlling the evolution of a barred galaxy. The location of CR plays a strong role in moving orbits into the vicinity of the bar where they can be trapped into ILR. (Chapter 6), as well as affecting the L_z reservoir in the outer disc. Further, if the CR radius is very large, there is only small amount of density available for resonant transfer but if the CR radis located near a region of high disc density, significant resonant transfer is possible. This is the case for the fiducial simulation $c25\xi40$, where the initial pattern speed from the extrapolation of Ω_2 places CR at the peak of the exponential distribution. In general, for other models, CR is always interior to the peak of the circular mass distribution in Figure 7.1, marking a clear difference between the strongest bar in our $c - \xi$ grid and the others.

7.4 Models to Test Additional Parameter Space

In this section, we vary the three parameters held fixed in the $c - \xi$ grid: r_c, $f_{\rm thick}$, and Q. We find that the dynamical mechanisms governing bar evolution discussed above are all still applicable. The limitations imposed by the available halo density and the orbital

structure allowed by the potential apply in intuitive ways: including a halo core results in less inner halo density, effectively changing the angular momentum transfer, and a thick or kinematically warmer disc results in different orbital structure that variously promotes or supress bar growth. Unfortunately, variation of these parameters do not lead to unique patterns of bar morphology or evolution. From this, we infer that a unique prediction of the underlying disc and halo model based on observed diagnostics may be difficult or impossible.

7.4.1 Effect of the Core

Our companion works compared and contrasted a cusp simulation (the fiducial simulation of this chapter) and a core simulation, which is the cusp simulation with $r_c = 0.02R_{\rm vir}$. While the core changes η by only 25 per cent, the existence of the core causes the inner halo density to be unable to accept angular momentum as the bar forms. Thus, in a cored halo at fixed concentration and disc mass, the disc is more likely to transfer angular momentum to the outer disc than the inner halo. As shown in Section 7.3.3, the ability of the disc to couple with the halo is contingent on sufficient phase-space density at the ILR of the halo where the disc can most efficiently couple (Chapter 5).

From Chapter 3, the orbital structure is different in the central regions of the core simulation at the outset. The cored model has less central density and weaker phase-space gradients near the primary resonances (ILR and CR) and therefore slower angular momentum transport. This slower angular momentum transport yields less evolution of the azimuthally-averaged density profile in the vicinity of the disk, and the bars themselves are less elongated (larger $\frac{b}{a}$ axis ratio). We demonstrated in Chapter 3 that the orbit structure of cusp and core models at the same mass ratio can be appreciably different, including the presence or absence of entire families, with effects on the evolution of models by altering the efficiency of angular momentum transport.

For the three core models we test here (see Table 7.2), designed to span a range of barred strengths in the cusp equivalent models, we find that the evolution proceeds to the same final state as that of the equivalent cusp model, but, the formation of the bar was parameterized by a larger value of α in $A_2/A_0 \propto \exp(\alpha t)$, i.e., the formation is more rapid, a hallmark of higher η models. By and large, coring the halo profile has the same effect as reducing the halo concentration. Thus, the $c - \xi$ grid may be useful to interpret cored versions of the cusp models: one may approximate the strength of the bar and evolutionary states by choosing a model at fixed ξ and lower c.

7.4.2 Effect of the Thick Disc

Aumer & Binney (2017); Aumer et al. (2017) study the dynamics of a co-existing thin and thick disc. However, in their studies, they treat numerous other processes and may not be able to distinguish the effects of secular evolution and resonant coupling. Therefore, to isolate the dynamical features directly attributable to the thin-thick disc superposition, we perform pure n-body simulations without any star formation (neither artificially-added stellar mass or gas prescription).

In Figure 7.9, we illustrate the evolution of models with thick discs added. The bottom row shows the fiducial $c25\xi40$ simulation, from which we modify the stellar component to have progressively more thick disc (bottom to top). The columns correspond to times, incremented by $\Delta T = 0.5$ from left to right. Bar length at $T = 2$ increases with increasing thick disc fraction. Also, increasing the thick disc fraction decreases the arm activity and promotes trapping by the bar. In addition, the thick disk increases the rate of secular evolution: the model reaches the same evolutionary phase as described in Chapter 4 sooner.

A fixed potential analysis as in Chapter 3 reveals that when the same pattern speed is imposed on the models, the radius of the maximal x_1 orbit increases. This suggests that the presence of the thick disc acts to shepherd orbits near the end of the bar that might otherwise remain dressing orbits into actual trapped orbits. Further evidence comes from

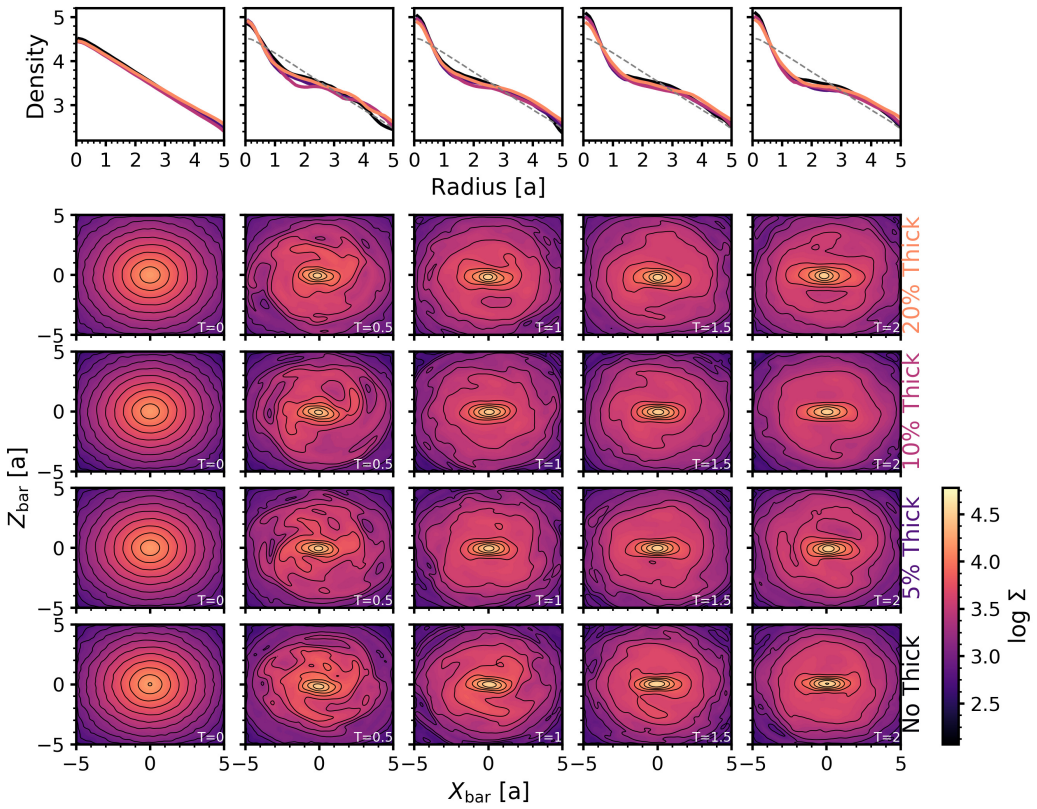

Figure 7.9. Evolutionary illustrations for the thick disc simulations, as compared to the fiducial simulation, $c25\xi40$. The lower panels show the face-on surface density, where the bar has been rotated to align with the x axis. The upper row of panels shows the projected density. The amount of thick disc is noted at the right edge of the face-on panels. The columns correspond to different times, increasing by $\Delta T = 0.5$ from left to right.

inspecting the vertical distribution of the thin disc. We found in Chapter 6 that orbits that are important for growing the bar by moving inward often change their vertical action on account of secular resonance passage.

Further, an examination of the thin and thick disc components separately reveals that not only does the length of the bar get longer in the thin disc, but the thick disc adds a substantial dressing component to the isophotal appearance of the bar, such that the bar appears even longer than the already-increased maximal x_1 orbit. As we have only tested the inclusion of a thick disc on the fiducial simulation, which we already know is unique in the strength of the resultant bar, we caution against overinterpretation of our findings, but suggest the findings warrant further focused study of the interaction between a thin and a thick disc.

7.4.3 Effect of varying Q

Figure 7.10 illustrates the evolution of models with increasing values of Toomre Q (see equation 7.5) from our fiducial value of $Q = 0.9$ to $Q = 1.6$. We choose the value $Q = 0.9$ to promote rapid bar formation, even though this is an unnatural initial condition. Saha et al. (2012) suggested that a cool disk ($Q \leq 1.4$) is a condition under which bars will rapidly form. We have demonstrated here that the relative mass of the disc and halo direct affects the bar formation timescale and strength. A study of both parameters has not been undertaken, leaving a blind spot in the understanding of the formation of bars, which may have real applications in the high redshift universe, where disks are expected to form in an unstable state (Genzel et al., 2006).

We find that the rate of evolution decreases with increasing Q, but the models have the same end state. The bar assembly phase takes twice as long for $Q = 1.6$ than in the fiducial $Q = 0.9$ simulation. The slower evolution allows more untrapped orbits to precess towards and align with the bar. Thus, the bar appears to be much longer than in the fiducial model. We find no evidence for significantly longer maximal x_1 values using the fixed potential

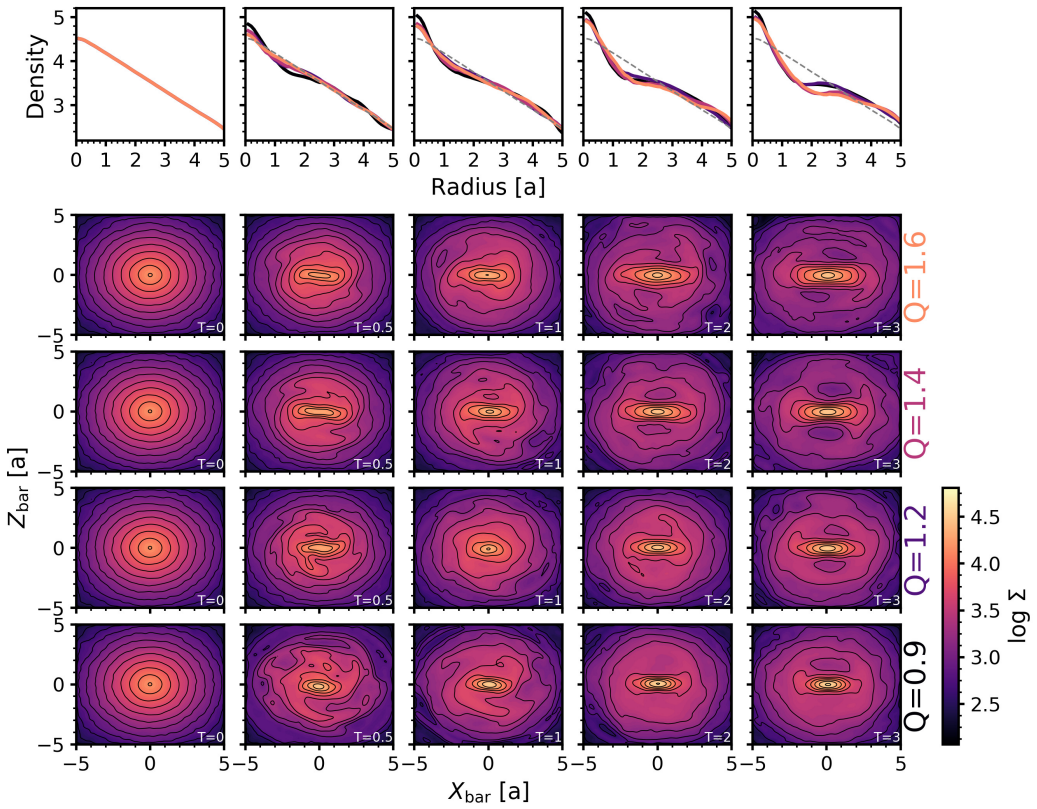

Figure 7.10. Evolutionary illustrations for the Toomre Q-varying disc simulations, as compared to the fiducial simulation, $c25\xi40$, which has $Q = 0.9$ (the bottom row). The lower panels show the face-on surface density, where the bar has been rotated to align with the x axis. The upper row of panels shows the projected density. The amount of thick disc is noted at the right edge of the face-on panels. The columns correspond to different times, increasing from left to right.

analysis (Chapter 3). We conclude the appearance of the bar is being biased by the dressing orbits.

The upper row of Figure 7.10 shows that the mass is rearranged somewhat differently. In particular, considering the one-dimensional density profile at $T = 3$, we see that the $Q = 1.4$ and $Q = 1.6$ models have a lower 'plateau' of density between two and three scalelengths, corresponding to a larger break radius. This suggests that dressing orbits, while not trapped by the bar, are still influenced enough by the bar to secularly rearrange in radius a modest amount.

7.5 Discussion

In this section, we discuss the findings of the various models in the larger context of galaxy evolution. We first summarize the important mechanisms that distinguish bar evolution in various models in Section 7.5.1, before discussing the maximal strength of bars and evolutionary timescales in Section 7.5.2, and inferences we may draw about bar destruction in Section 7.5.3.

7.5.1 Mechanism Census

Chapter 3, Chapter 4, and Chapter 5 presented a range of dynamical mechanisms controlling bar evolution. In this chapter, we have tested the mechanisms against a larger, more generic suite of disc galaxy models. We find that the same mechanisms presented in Chapter 3, Chapter 4, and Chapter 5 explain the observed evolution: (1) We identify no new families of orbits that were not seen in the detailed study of Chapter 3, (2) the F_θ (torque) maps at late times show the same evolution-asymptotic values as in Chapter 4, and (3) the evolutionary scenarios in A_2/A_0 are clearly different, but in understandable fashion in the context of Chapter 5.

Other results from Chapter 3, Chapter 4, and Chapter 5 also hold true for the larger suite of models: for example bar strength and lengths can easily be overestimated by a factor of

two in the presence of dressing orbits. Adding to the complexity of interpreting bars from isophotes, the fraction of dressing orbits changes with different model parameters in ways that are not easily understood. We will return to the presence of dressing orbits in a future work. The harmonic–locking discovered in Chapter 5 is found in models in our $c - \xi$ grid, albeit at different frequency ratios between Ω_1 and Ω_2, suggesting that interaction between different azimuthal harmonics is more common than previously thought.

The additional coverage in model parameter space reveals a continuum of trends dependent on η. We are able to explain the trends using the mechanisms presented previously, and do not new mechanisms particular to mass ratio, halo model shape, or velocity dispersion. For the models presented here, we are satisfied that we can explain the evolution both qualitatively and quantitatively. Chapter 3, Chapter 4, and Chapter 5 provide a framework for understanding of the physical mechanisms that control evolution in bared galaxies. Specifically, a wider range of initial conditions are described by the same mechanisms in different combinations. Bar evolution is explained by determining the location and strenght of angular momentum transport. This is determined by the joint phase-space structure of the halo and disc.

7.5.2 Bar Maximality and Timescales

Although the most massive discs for the most massive bar, the most massive bars relative to the halo are not the most massive bars relative to their disc. Instead, our fiducial model forms the strongest bar as measured by A_2/A_0 of the entire suite of simulations. Further, the fiducial model reaches the maximum more quickly than other models reach their maximum amplitude. We find that A_2/A_0 does not exceed 0.2 for instability bars, suggesting a possible avenue for determining whether a bar was triggered through an interaction, if measurements of real galaxies exhibit $A_2/A_0 > 0.2$.

Increasing the value of Q slows the evolution but leaves the character of the end state unchanged. A larger Q implies that less disc material is near key resonances (and especially

ILR) at any one time so the trapping rate is proportionately less, even though the trapping probability may be the same. This results in slower bar growth.

We naturally wonder whether the timescales observed in other models are inherent to the model in some predictive sense, or are the product of an exceedingly complex blend of mechanisms. As the mechanisms identified in Chapter 3, Chapter 4, and Chapter 5 are common to the model grid presented here and can explain the evolutionary phases, it is natural to test whether the differences in model details change the rates of the various processes, and therefore change the time scales, but not the underlying explanations.

The phases observed in the $c - \xi$ model grid have the same character as the phases studied in the models of Chapter 3, Chapter 4, and Chapter 5. Therefore, prediction of the exact timescales are difficult because the timescales depend on the rates of angular momentum transport which in turn depend on the details of the phase-space structure. the mechanisms are universal to some extent. Taken together, we have developed an intuitive picture where secular evolution depends on bar strength and the evolutionary timescale scales with bar strength, driven by universal mechanisms (Chapter 3; Chapter 4; Chapter 5).

We find that bars grow quickly when angular momentum transport channels exist in the halo and outer disk to promote secular processes. Similarly, the secular growth changes the phase-space distribution near the resonance, so a period of growth may be self limiting by itself. Growth phases in our grid of models have $\Delta T = 1$ or approximately 2 Gyr in MW units.

7.5.3 Bar Destruction

The models we study in detail in this chapter do not show any signs of dissolving. Each model reaches a roughly steady-state pattern speed at the conclusion of the simulation. This is not surprising; previous studies determined that an additional mechanism is required to destroy the bar. For instance, Hasan & Norman (1990) found that a central mass may

dissolve the bar in a fixed potential owing to the interaction of orbits with a sufficiently strong ILR. Friedli & Pfenniger (1991) found that only 1-2 per cent of the total disc mass residing in a central structure was sufficient to destroy the bar, owing to the presence of a resonance zone with $\Omega_R \simeq \Omega_z$ being unavoidable for a potential which changes from spherical symmetry, such as near the central mass ($\Omega_R = 2\Omega_z$), to a perfectly flat disc ($\Omega_z = 0$), a reasonable limit in which to consider the stellar disc.

However, although we have not managed to successfully destroy any bars as the result of secular evolution, we identify mechanisms that weaken the bar, and under different scenarios, may be able to fully destroy the bar. In Figure 7.6, we show a higher-order x_{1b} orbit, bifurcated from the x_1 family, but instead of being symmetric with respect to the bar minor axis, as the x_{1b} orbit identified as crucial for growth in Chapter 3, this bifurcated orbit is not symmetric about either bar axis. This $m = 3$ bifurcated orbit visually contributes to the decrease in bar axis ratio, and is only present in strong bars, such as the late-time $c25\xi20$ model and a similar model with double the disc mass $c25\xi10$, not shown. As the simulation evolves and more orbits join the $m = 3$ x_{1b} family, the bar becomes more round. One could imagine a scenario where enough orbits reinforce the potential causing the bar to be round through secular evolution, before eventually the bar decorrelates and a central lens is left, as may be observationally observed (Kormendy, 1979; Laurikainen et al., 2014).

7.6 Conclusions

We analyze a suite of disc and halo models to further shed light on the parameter space of instability bar formation and evolution. In the previous chapters (Chapter 3; Chapter 4; Chapter 5), we developed three distinct tools with which to analyze simulations of disc and halo models: orbit analysis, torque diagrams, and harmonic decomposition. The three techniques pointed to a range of processes and mechanisms that are all active in careful, high-resolution simulations, including growth of the bar driven by x_{1b} orbits,

steady-state evolution owing to resonance saturation, and the phenomenon of $m = 1$, $m = 2$ mode-locking.

The suite of simulations confirm the general applicability of the findings in Chapter 3, Chapter 4, and Chapter 5. We find regions of model parameter space delineated by halo concentration and disc-to-halo mass ratio where previously identified mechanisms are absent, present, or dominant. Our main findings are:

(1). We find a threshold to excite instability bar formation as a function of halo concentration and disc-to-halo mass ratio. The threshold falls between disc-to-halo mass ratios of 1/160 and 1/80, depending on the halo concentration. We find a trend between the disc-to-halo mass ratio inside of 2.2 scale lengths and the final pattern speed.

(2). We find a second threshold for interpretable instability bar evolution as a function of disc-to-halo mass ratio, given the assumption of an initially axisymmetric disc, i.e. above a certain disc-to-halo mass ratio, the resulting bar is unrealistic and does not evolve according to bar formation mechanisms presented in Chapter 3, Chapter 4, and Chapter 5. We conjecture that other models for bar formation in disc galaxies found in the literature may be in this regime, and caution against drawing direct conclusions about the bar that result from initial conditions above this threshold.

(3). A 'sweet spot' for bar formation exists, where the balance between being massive enough to be unstable to bar formation and having enough halo density to accept angular momentum and thereby drive secular evolution. This maximum occurs along a continuum dependent on the mass ratio of the disc to the halo and the halo concentration, with MW-like galaxies residing near the maximum in bar strength. We find the maximum A_2/A_0 at each concentration ($c \in \{15, 20, 25\}$), further finding that the ($c = 25$,$\xi = 40$) model has the largest A_2/A_0 of all models.

(4). We show that not all galaxy models have a strong secular bar growth phase. The appearance of the secular bar growth phase is mediated by the orbital structure, in

particular, the presence of a bifurcated x_1 family. The secular growth phase is always accompanied by slowing of the bar. However, the bar may slow, even without clear growth in the A_2/A_0 ratio. The pattern speed evolution alone is insufficient to determine the presence or absence of a growth phase.

(5). Adding a core to a halo model changes the dynamics of the model system in the same qualitative manner as either reducing the concentration or increasing the disc mass. Angular momentum transfer previously controlled by the cuspy halo is controlled by the outer disc in a corresponding cored halo.

(6). Adding a thick disc component to model galaxies results in a longer bar and shortens the timescale for evolution, but does not result in a different final pattern speed for the bar.

(7). Changing the velocity dispersion of the disc by increasing the Toomre Q parameter causes the bar evolution to proceed more slowly, but does not result in final strengths or slowdowns that are appreciably different.

Our suite of models by no means provides an exhaustive look at all parameters that could be varied to describe galaxy models. Rather, we find that in a suite of models where we do vary parameters, often considerably, we are still able to describe the evolution using mechanisms understood in detail (Chapter 3; Chapter 4; Chapter 5; Chapter 6). The analysis tools of Chapter 3, Chapter 4, and Chapter 5 used here can be applied to cosmological simulations, which are approaching resolutions where nuanced dynamical processes may be observable. Specifically, basis function expansion tools can be used to study and summarize general n-body simulations.

BIBLIOGRAPHY

Aalseth C. E., Barbeau P. S., Colaresi J., Collar J. I., Diaz Leon J., Fast J. E., Fields N. E., Hossbach T. W., Knecht A., Kos M. S., Marino M. G., Miley H. S., Miller M. L., Orrell J. L., Yocum K. M., 2013, PhysRevD, 88, 012002

Agnes P., Agostino L., Albuquerque I. F. M., Alexander T., Alton A. K., Arisaka K., Back H. O., Baldin B., et al., 2016, Phys. Rev. D, 93, 081101

Agnese R., Ahmed Z., Anderson A. J., Arrenberg S., Balakishiyeva D., Basu Thakur R., Bauer D. A., Borgland A., Brandt D., Brink P. L., Bruch T., Bunker R., et al., 2013, PhysRevD, 88, 031104

Agnese R., Ahmed Z., Anderson A. J., Arrenberg S., Balakishiyeva D., Basu Thakur R., et al., 2013, Physical Review Letters, 111, 251301

Agnese R., Anderson A. J., Aramaki T., Asai M., Baker W., Balakishiyeva D., Barker D., Basu Thakur R., Bauer D. A., Billard J., Borgland A., Bowles M. A., Brink P. L., Bunker R., Cabrera B., et al., 2016, Phys. Rev. Lett., 116, 071301

Aguerri J. A. L., Méndez-Abreu J., Falcón-Barroso J., Amorin A., Barrera-Ballesteros J., Cid Fernandes R., García-Benito R., García-Lorenzo B., González Delgado R. M., Husemann B., 2015, ArXiv e-prints

Allende Prieto C., Majewski S. R., Schiavon R., Cunha K., Frinchaboy P., Holtzman J., Johnston K., Shetrone M., Skrutskie M., Smith V., Wilson J., 2008, Astronomische Nachrichten, 329, 1018

Allgood B., Flores R. A., Primack J. R., Kravtsov A. V., Wechsler R. H., Faltenbacher A., Bullock J. S., 2006, MNRAS, 367, 1781

Amole C., Ardid M., Arnquist I. J., Asner D. M., Baxter D., Behnke E., Bhattacharjee P., Borsodi H., Bou-Cabo M., et al., 2016, Phys. Rev. D, 93, 061101

Angloher G., Bento A., Bucci C., Canonica L., Defay X., Erb A., von Feilitzsch F., Iachellini N. F., Gorla P., et al., 2016, European Physical Journal C, 76, 25

Antoja T., Helmi A., Dehnen W., Bienaymé O., Bland-Hawthorn J., Famaey B., Freeman K., et al., 2014, A&A, 563, A60

Antoja T., Helmi A., Romero-Gómez M., Katz D., Babusiaux C., Drimmel R., Evans D. W., Figueras F., Poggio E., Reylé C., Robin A. C., Seabroke G., Soubiran C., 2018, Nature, 561, 360

Araki S., 1985, Ph.D. thesis, MIT

Arthur D., Vassilvitskii S., 2007, in Proceedings of the Eighteenth Annual ACM-SIAM Symposium on Discrete Algorithms SODA '07, K-means++: The advantages of careful seeding. Society for Industrial and Applied Mathematics, Philadelphia, PA, USA, pp 1027–1035

Athanassoula E., 1992, MNRAS, 259, 328

Athanassoula E., 1996, in Buta R., Crocker D. A., Elmegreen B. G., eds, IAU Colloq. 157: Barred Galaxies Vol. 91 of Astronomical Society of the Pacific Conference Series, Evolution of Bars in Isolated and in Interacting Disk Galaxies. p. 309

Athanassoula E., 2003, MNRAS, 341, 1179

Athanassoula E., 2007, MNRAS, 377, 1569

Athanassoula E., Machado R. E. G., Rodionov S. A., 2013, MNRAS, 429, 1949

Athanassoula E., Misiriotis A., 2002, MNRAS, 330, 35

Athanassoula E., Morin S., Wozniak H., Puy D., Pierce M. J., Lombard J., Bosma A., 1990, MNRAS, 245, 130

Athanassoula E., Puerari I., Bosma A., 1997, MNRAS, 286, 284

Aumer M., Binney J., 2017, MNRAS, 470, 2113

Aumer M., Binney J., Schönrich R., 2016, MNRAS, 459, 3326

Aumer M., Binney J., Schönrich R., 2017, MNRAS, 470, 3685

Babusiaux C., Gilmore G., 2005, MNRAS, 358, 1309

Babusiaux C., Katz D., Hill V., Royer F., Gómez A., Arenou F., Combes F., Di Matteo P., Gilmore G., Haywood M., Robin A. C., Rodriguez-Fernandez N., Sartoretti P., Schultheis M., 2014, A&A, 563, A15

Barbanis B., 1976, Celestial Mechanics, 14, 201

Barnes J., Hut P., Goodman J., 1986, ApJ, 300, 112

Bernabei R., Belli P., Cappella F., Caracciolo V., Cerulli R., Dai C. J., d'Angelo A., d'Angelo S., Di Marco A., He H. L., Incicchitti A., Ma X. H., Montecchia F., Prosperi D., Sheng X. D., Wang R. G., Ye Z. P., 2014, Nuclear Instruments and Methods in Physics Research A, 742, 177

Bernabei R., Belli P., Cappella F., Cerulli R., Dai C. J., D'Angelo A., He H. L., Incicchitti A., Kuang H. H., Ma X. H., Montecchia F., Nozzoli F., Prosperi D., Sheng X. D., Wang R. G., Ye Z. P., 2010, European Physical Journal C, 67, 39

Bertone G., Hooper D., Silk J., 2005, Physical Reports, 405, 279

Bienaymé O., Famaey B., Siebert A., Freeman K. C., Gibson B. K., Gilmore G., et al., 2014, A&A, 571, A92

Billard J., Riffard Q., Mayet F., Santos D., 2013, Physics Letters B, 718, 1171

Binney J., 2018, MNRAS, 474, 2706

Binney J., Gerhard O. E., Stark A. A., Bally J., Uchida K. I., 1991, MNRAS, 252, 210

Binney J., McMillan P. J., 2016, MNRAS, 456, 1982

Binney J., Spergel D., 1982, ApJ, 252, 308

Binney J., Spergel D., 1984, MNRAS, 206, 159

Binney J., Tremaine S., 2008, Galactic Dynamics: Second Edition. Princeton University Press

Bird J. C., Kazantzidis S., Weinberg D. H., Guedes J., Callegari S., Mayer L., Madau P., 2013, ApJ, 773, 43

Bissantz N., Gerhard O., 2002, MNRAS, 330, 591

Bland-Hawthorn J., Gerhard O., 2016, ARA&A, 54, 529

Blitz L., Spergel D. N., 1991, ApJ, 379, 631

Bournaud F., Combes F., 2002, A&A, 392, 83

Bournaud F., Combes F., Semelin B., 2005, MNRAS, 364, L18

Bovy J., 2015, ApJS, 216, 29

Bovy J., Allende Prieto C., Beers T. C., Bizyaev D., da Costa L. N., Cunha K., Ebelke G. L., Eisenstein D. J., Frinchaboy P. M., et al., 2012, ApJ, 759, 131

Bovy J., Rix H.-W., 2013, ApJ, 779, 115

Bovy J., Rix H.-W., Liu C., Hogg D. W., Beers T. C., Lee Y. S., 2012, ApJ, 753, 148

Bovy J., Rix H.-W., Schlafly E. F., Nidever D. L., Holtzman J. A., Shetrone M., Beers T. C., 2016, ApJ, 823, 30

Boylan-Kolchin M., Bullock J. S., Sohn S. T., Besla G., van der Marel R. P., 2013, ApJ, 768, 140

Bozorgnia N., Calore F., Schaller M., Lovell M., Bertone G., Frenk C. S., Crain R. A., Navarro J. F., Schaye J., Theuns T., 2016, JCAP, 5, 024

Breddels M. A., Helmi A., 2013, A&A, 558, A35

Bruch T., Read J., Baudis L., Lake G., 2009, ApJ, 696, 920

Bullock J., Dekel A., Kolatt T., Kravtsov A., Klypin A., Porcianai C., Primack J., 2001, ApJ, 555, 240

Cabrera-Lavers A., González-Fernández C., Garzón F., Hammersley P. L., López-Corredoira M., 2008, A&A, 491, 781

Cappellari M., 2008, MNRAS, 390, 71

Ceverino D., Klypin A., 2007, MNRAS, 379, 1155

CGAL Project 2018, CGAL User and Reference Manual, 4.11.1 edn. CGAL Editorial Board

Chatzopoulos S., Fritz T. K., Gerhard O., Gillessen S., Wegg C., Genzel R., Pfuhl O., 2015, MNRAS, 447, 948

Cheng J. Y., Rockosi C. M., Morrison H. L., Schönrich R. A., Lee Y. S., Beers T. C., Bizyaev D., Pan K., Schneider D. P., 2012, ApJ, 746, 149

Cheung E., Athanassoula E., Masters K. L., Nichol R. C., Bosma A., Bell E. F., Faber S. M., Koo D. C., Lintott C., Melvin T., Schawinski K., Skibba R. A., Willett K. W., 2013, ApJ, 779, 162

Chirikov B. V., 1979, Physics Reports, 52, 263

Choi J.-H., Weinberg M. D., Katz N., 2007, MNRAS, 381, 987

Choi J.-H., Weinberg M. D., Katz N., 2009, MNRAS, 400, 1247

Clutton-Brock M., 1972, APSS, 16, 101

Clutton-Brock M., 1973, APSS, 23, 55

Clutton-Brock M., Innanen K. A., Papp K. A., 1977, APSS, 47, 299

Colin J., Athanassoula E., 1989, A&A, 214, 99

Colín P., Valenzuela O., Klypin A., 2006, ApJ, 644, 687

Collier A., Shlosman I., Heller C., 2018a, ArXiv e-prints

Collier A., Shlosman I., Heller C., 2018b, MNRAS, 476, 1331

Combes F., Sanders R. H., 1981, A&A, 96, 164

Comerón S., Elmegreen B. G., Knapen J. H., Salo H., Laurikainen E., Laine J., Athanassoula E., Bosma A., Sheth K., et al., 2011, ApJ, 741, 28

Considere S., Athanassoula E., 1988, AAPS, 76, 365

Contopoulos G., 1978, A&A, 64, 323

Contopoulos G., 1988, A&A, 201, 44

Contopoulos G., Grosbol P., 1989, AApR, 1, 261

Contopoulos G., Papayannopoulos T., 1980, A&A, 92, 33

Daniel K. J., Wyse R. F. G., 2015, MNRAS, 447, 3576

Daniel K. J., Wyse R. F. G., 2018, MNRAS, 476, 1561

de Vaucouleurs G., 1964, in Kerr F. J., ed., The Galaxy and the Magellanic Clouds Vol. 20 of IAU Symposium, Interpretation of velocity distribution of the inner regions of the Galaxy. p. 195

de Zeeuw P. T., Lynden-Bell D., 1985, MNRAS, 215, 713

Debattista V., Mayer L., Carollo C., Moore B., Wadsley J., Quinn T., 2006, ApJ, 645, 209

Debattista V. P., Gonzalez O. A., Sanderson R. E., El-Badry K., Garrison-Kimmel S., Wetzel A., Faucher-Giguère C.-A., Hopkins P. F., 2018, ArXiv e-prints

Debattista V. P., Moore B., Quinn T., Kazantzidis S., Maas R., Mayer L., Read J., Stadel J., 2008, ApJ, 681, 1076

Debattista V. P., Sellwood J. A., 1998, ApJL, 493, L5

Debattista V. P., Sellwood J. A., 2000, ApJ, 543, 704

Dehnen W., 2000, AJ, 119, 800

Dehnen W., 2009, MNRAS, 395, 1079

Dekel A., Devor J., Hetzroni G., 2003, MNRAS, 341, 326

Di Matteo P., Haywood M., Combes F., Semelin B., Snaith O. N., 2013, A&A, 553, A102

Earn D. J. D., 1996, ApJ, 465, 91

Elmegreen B. G., Elmegreen D. M., Seiden P. E., 1989, ApJ, 343, 602

Erwin P., 2005, MNRAS, 364, 283

Erwin P., Debattista V. P., 2016, ApJL, 825, L30

Erwin P., Saglia R. P., Fabricius M., Thomas J., Nowak N., Rusli S., Bender R., Vega Beltrán J. C., Beckman J. E., 2015, MNRAS, 446, 4039

Feuillet D. K., Bovy J., Holtzman J., Weinberg D. H., García-Hernández D., Hearty F. R., Majewski S. R., Roman-Lopes A., Rybizki J., Zamora O., 2018, MNRAS, 477, 2326

Fisher D. B., Drory N., 2008, AJ, 136, 773

Fisher D. B., Drory N., 2016, in Laurikainen E., Peletier R., Gadotti D., eds, Galactic Bulges Vol. 418 of Astrophysics and Space Science Library, An Observational Guide to Identifying Pseudobulges and Classical Bulges in Disc Galaxies. p. 41

Fitts A., Boylan-Kolchin M., Bullock J. S., Weisz D. R., El-Badry K., Wheeler C., Faucher-Giguère C.-A., Quataert E., Hopkins P. F., Kereš D., Wetzel A., Hayward C. C., 2018, MNRAS, 479, 319

Fornasa M., Green A. M., 2014, PhysRevD, 89, 063531

Frandsen M. T., Kahlhoefer F., McCabe C., Sarkar S., Schmidt-Hoberg K., 2013, JCAP, 7, 23

Freese K., Gondolo P., Newberg H. J., Lewis M., 2004, Physical Review Letters, 92, 111301

Freese K., Lisanti M., Savage C., 2013, Reviews of Modern Physics, 85, 1561

Friedli D., Pfenniger D., 1991, in Combes F., Casoli F., eds, Dynamics of Galaxies and Their Molecular Cloud Distributions Vol. 146 of IAU Symposium, Destruction of Bars by Dissipative Processes. p. 362

Gadotti D. A., 2009, MNRAS, 393, 1531

Gadotti D. A., 2011, MNRAS, 415, 3308

Gadotti D. A., Seidel M. K., Sánchez-Blázquez P., Falcón-Barroso J., Husemann B., Coelho P., Pérez I., 2015, A&A, 584, A90

Gaia Collaboration Brown A. G. A., Vallenari A., Prusti T., de Bruijne J. H. J., Babusiaux C., Bailer-Jones C. A. L., 2018, ArXiv e-prints

Gaia Collaboration Prusti T., de Bruijne J. H. J., Brown A. G. A., Vallenari A., Babusiaux C., Bailer-Jones C. A. L., et al., 2016, A&A, 595, A1

Garrison-Kimmel S., Boylan-Kolchin M., Bullock J. S., Lee K., 2014, MNRAS, 438, 2578

Garrison-Kimmel S., Hopkins P. F., Wetzel A., El-Badry K., Sanderson R. E., Bullock J. S., Ma X., van de Voort F., Hafen Z., Faucher-Giguère C.-A., Hayward C. C., Quataert E., Kereš D., Boylan-Kolchin M., 2018, MNRAS, 481, 4133

Genzel R., Tacconi L. J., Eisenhauer F., Förster Schreiber N. M., Cimatti A., Daddi E., Bouché N., et al., 2006, Nature, 442, 786

Gerhard O., 2002, in Da Costa G. S., Sadler E. M., Jerjen H., eds, The Dynamics, Structure & History of Galaxies: A Workshop in Honour of Professor Ken Freeman Vol. 273 of Astronomical Society of the Pacific Conference Series, The Galactic Bar. p. 73

Gilmore G., Randich S., Asplund M., Binney J., Bonifacio P., Drew J., Feltzing S., Ferguson A., Jeffries R., Micela G., et al. 2012, The Messenger, 147, 25

Governato F., Zolotov A., Pontzen A., Christensen C., Oh S. H., Brooks A. M., Quinn T., Shen S., Wadsley J., 2012, MNRAS, 422, 1231

Graham A. W., Ciambur B. C., Savorgnan G. A. D., 2016, ApJ, 831, 132

Grand R. J. J., Springel V., Kawata D., Minchev I., Sánchez-Blázquez P., Gómez F. A., Marinacci F., Pakmor R., Campbell D. J. R., 2016, MNRAS, 460, L94

Green J. A., Caswell J. L., McClure-Griffiths N. M., Avison A., Breen S. L., Burton M. G., Ellingsen S. P., Fuller G. A., Gray M. D., Pestalozzi M., Thompson M. A., Voronkov M. A., 2011, ApJ, 733, 27

Hammersley P. L., Garzón F., Mahoney T. J., López-Corredoira M., Torres M. A. P., 2000, MNRAS, 317, L45

Hasan H., Norman C., 1990, ApJ, 361, 69

Hayden M. R., Holtzman J. A., Bovy J., Majewski S. R., Johnson J. A., Allende Prieto C., Beers T. C., Cunha K., Frinchaboy P. M., et al., 2014, AJ, 147, 116

Haywood M., Lehnert M. D., Di Matteo P., Snaith O., Schultheis M., Katz D., Gómez A., 2016, A&A, 589, A66

Hernquist L., Ostriker J. P., 1992, ApJ, 386, 375

Hernquist L., Weinberg M. D., 1992, ApJ, 400, 80

Herpich J., Stinson G. S., Rix H.-W., Martig M., Dutton A. A., 2017, MNRAS, 470, 4941

Herrera-Endoqui M., Díaz-García S., Laurikainen E., Salo H., 2015, A&A, 582, A86

Holley-Bockelmann K., Weinberg M., Katz N., 2005, MNRAS, 363, 991

Hoyle B., Masters K. L., Nichol R. C., Edmondson E. M., Smith A. M., Lintott C., Scranton R., Bamford S., Schawinski K., Thomas D., 2011, MNRAS, 415, 3627

Hunt J. A. S., Bovy J., 2018, MNRAS, 477, 3945

Hunt J. A. S., Hong J., Bovy J., Kawata D., Grand R. J. J., 2018, MNRAS, 481, 3794

Hunter C., Toomre A., 1969, ApJ, 155, 747

Jeans J. H., 1915, MNRAS, 76, 70

Jeans J. H., 1922, MNRAS, 82, 122

Jungman G., Kamionkowski M., Griest K., 1996, Physical Reports, 267, 195

Jurić M., Ivezić Ž., Brooks A., Lupton R. H., Schlegel D., Finkbeiner D., Padmanabhan N., Bond N., et al., 2008, ApJ, 673, 864

Kalnajs A. J., 1971, ApJ, 166, 275

Kalnajs A. J., 1976, ApJ, 205, 745

Kamionkowski M., Koushiappas S. M., 2008, PhysRevD, 77, 103509

Kelso C., Savage C., Valluri M., Freese K., Stinson G. S., Bailin J., 2016, ArXiv e-prints

Kim T., Gadotti D. A., Sheth K., Athanassoula E., Bosma A., Lee M. G., Madore B. F., Elmegreen B., Knapen J. H., Zaritsky D., Ho L. C., Comerón S., Holwerda B., Hinz 2014, ApJ, 782, 64

Kim T., Sheth K., Gadotti D. A., Lee M. G., Zaritsky D., Elmegreen B. G., Athanassoula E., Bosma A., Holwerda B., Ho L. C., et al., 2015, ApJ, 799, 99

Kormendy J., 1979, ApJ, 227, 714

Kormendy J., Kennicutt Jr. R. C., 2004, ARA&A, 42, 603

Kravtsov A. V., 2013, ApJL, 764, L31

Kruk S. J., Lintott C. J., Bamford S. P., Masters K. L., Simmons B. D., Häußler B., Cardamone C. N., Hart R. E., Kelvin L., Schawinski K., Smethurst R. J., Vika M., 2018, MNRAS, 473, 4731

Kuhlen M., Diemand J., Madau P., 2007, ApJ, 671, 1135

Kuhlen M., Lisanti M., Spergel D. N., 2012, PhysRevD, 86, 063505

Kuhlen M., Weiner N., Diemand J., Madau P., Moore B., Potter D., Stadel J., Zemp M., 2010, JCAP, 2, 30

Kuijken K., Dubinski J., 1994, MNRAS, 269, 13

Laskar J., 1993, Celestial Mechanics and Dynamical Astronomy, 56, 191

Laurikainen E., Salo H., Athanassoula E., Bosma A., Herrera-Endoqui M., 2014, MNRAS, 444, L80

Laurikainen E., Salo H., Laine J., Janz J., 2018, A&A, 618, A34

Lavalle J., Magni S., 2015, PhysRevD, 91, 023510

Lee S. K., Lisanti M., Safdi B. R., 2013, JCAP, 11, 33

Lees J. F., Schwarzschild M., 1992, ApJ, 384, 491

Lewin J. D., Smith P. F., 1996, Astroparticle Physics, 6, 87

Ling F.-S., Nezri E., Athanassoula E., Teyssier R., 2010, JCAP, 2, 12

Lisanti M., Spergel D. N., 2012, Physics of the Dark Universe, 1, 155

Lloyd S., 1982, IEEE Transactions on Information Theory, 28, 2

Loebman S. R., Roškar R., Debattista V. P., Ivezić Ž., Quinn T. R., Wadsley J., 2011, ApJ, 737, 8

Lovell M. R., Pillepich A., Genel S., Nelson D., Springel V., Pakmor R., Marinacci F., Weinberger R., Torrey P., Vogelsberger M., Alabi A., Hernquist L., 2018, MNRAS, 481, 1950

LUX Collaboration Akerib D. S., Araújo H. M., Bai X., Bailey A. J., Balajthy J., Beltrame P., Bernard E. P., Bernstein A., Biesiadzinski T. P., Boulton E. M., Bradley A., Bramante R., Cahn S. B., et al., 2016, Physical Review Letters, 116, 161301

Lynden-Bell D., 1965, MNRAS, 129, 299

Lynden-Bell D., 1979, MNRAS, 187, 101

Lynden-Bell D., Kalnajs A. J., 1972, MNRAS, 157, 1

LZ Collaboration Akerib D. S., Araújo H. M., Bai X., Bailey A. J., Balajthy J., Beltrame P., Bernard E. P., Bernstein A., Biesiadzinski T. P., Boulton E. M., Bradley A., Bramante R., Cahn S. B., et al., 2015, ArXiv e-prints

Ma X., Hopkins P. F., Wetzel A. R., Kirby E. N., Anglés-Alcázar D., Faucher-Giguère C.-A., Kereš D., Quataert E., 2017, MNRAS, 467, 2430

Mao Y.-Y., Strigari L. E., Wechsler R. H., Wu H.-Y., Hahn O., 2013, ApJ, 764, 35

Martinet L., 1984, A&A, 132, 381

Martinez-Valpuesta I., Shlosman I., Heller C., 2006a, ApJ, 637, 214

Martinez-Valpuesta I., Shlosman I., Heller C., 2006b, ApJ, 637, 214

Martinsson T. P. K., Verheijen M. A. W., Westfall K. B., Bershady M. A., Andersen D. R., Swaters R. A., 2013, A&A, 557, A131

Mashchenko S., Couchman H. M. P., Wadsley J., 2006, Nature, 442, 539

Masters K. L., Nichol R. C., Haynes M. P., Keel W. C., Lintott C., Simmons B., Skibba R., Bamford S., Giovanelli R., Schawinski K., 2012, MNRAS, 424, 2180

McCabe C., 2010, PhysRevD, 82, 023530

McCabe C., 2011, PhysRevD, 84, 043525

McCabe C., 2014, JCAP, 2, 27

McMillan P. J., 2017, MNRAS, 465, 76

Merritt D., Sellwood J. A., 1994, ApJ, 425, 551

Merritt D., Valluri M., 1999, AJ, 118, 1177

Minchev I., Anders F., Recio-Blanco A., Chiappini C., de Laverny P., Queiroz A., et al., 2018, MNRAS, 481, 1645

Minchev I., Chiappini C., Martig M., 2013, A&A, 558, A9

Minchev I., Chiappini C., Martig M., Steinmetz M., de Jong R. S., Boeche C., Scannapieco C., Zwitter T., et al., 2014, ApJL, 781, L20

Minchev I., Famaey B., 2010, ApJ, 722, 112

Minchev I., Famaey B., Quillen A. C., Di Matteo P., Combes F., Vlajić M., Erwin P., Bland-Hawthorn J., 2012, A&A, 548, A126

Miralda-Escude J., Schwarzschild M., 1989, ApJ, 339, 752

Molloy M., Smith M. C., Shen J., Evans N. W., 2015, ApJ, 804, 80

Monari G., Famaey B., Siebert A., 2016, MNRAS, 457, 2569

Monari G., Famaey B., Siebert A., Duchateau A., Lorscheider T., Bienaymé O., 2017, MNRAS, 465, 1443

Morganti L., Gerhard O., 2012, MNRAS, 422, 1571

Moster B. P., Naab T., White S. D. M., 2013, MNRAS, 428, 3121

Muñoz-Mateos J. C., Sheth K., Gil de Paz A., Meidt S., Athanassoula E., Bosma A., Comerón S., Elmegreen D. M., Elmegreen B. G., Erroz-Ferrer S., Gadotti D. A., Hinz J. L., Ho 2013, ApJ, 771, 59

Navarro J. F., Frenk C. S., White S. D. M., 1997, ApJ, 490, 493

Navarro J. F., Yozin C., Loewen N., Benítez-Llambay A., Fattahi A., Frenk C. S., Oman K. A., Schaye J., Theuns T., 2018, MNRAS, 476, 3648

Nelson D., Pillepich A., Springel V., Weinberger R., Hernquist L., Pakmor R., Genel S., Torrey P., Vogelsberger M., Kauffmann G., Marinacci F., Naiman J., 2018, MNRAS, 475, 624

Nikolaev S., Weinberg M. D., 1997, ApJ, 487, 885

O'Hare C. A. J., Green A. M., 2014, PhysRevD, 90, 123511

Papayannopoulos T., Petrou M., 1983, A&A, 119, 21

Pardy S. A., D'Onghia E., Athanassoula E., Wilcots E. M., Sheth K., 2016, ApJ, 827, 149

Pérez I., Aguerri J. A. L., Méndez-Abreu J., 2012, A&A, 540, A103

Petersen M. S., Katz N., Weinberg M. D., 2016, PhysRevD, 94, 123013

Petersen M. S., Weinberg M. D., Katz N., 2016, MNRAS, 463, 1952

Petersen M. S., Weinberg M. D., Katz N., 2019a, in prep

Petersen M. S., Weinberg M. D., Katz N., 2019b, in prep

Petersen M. S., Weinberg M. D., Katz N., 2019c, in prep

Petersen M. S., Weinberg M. D., Katz N., 2019d, in prep

Petersen M. S., Weinberg M. D., Katz N., 2019e, in prep

Petrou M., Papayannopoulos T., 1986, MNRAS, 219, 157

Pfenniger D., 1998, Celestial Mechanics and Dynamical Astronomy, 72, 37

Pfenniger D., Friedli D., 1991, A&A, 252, 75

Piffl T., Binney J., McMillan P. J., Steinmetz M., Helmi A., Wyse R. F. G., Bienaymé O., Bland-Hawthorn J., Freeman K., et al., 2014, MNRAS, 445, 3133

Piffl T., Scannapieco C., Binney J., Steinmetz M., Scholz R.-D., Williams M. E. K., de Jong R. S., Kordopatis G., Matijevič G., et al., 2014, A&A, 562, A91

Pillepich A., Kuhlen M., Guedes J., Madau P., 2014, ApJ, 784, 161

Polyachenko E. V., Berczik P., Just A., 2016, MNRAS, 462, 3727

Polyachenko V., Polyachenko E., 1996, AstL, 22, 302

Portail M., Gerhard O., Wegg C., Ness M., 2017, MNRAS, 465, 1621

Portail M., Wegg C., Gerhard O., Martinez-Valpuesta I., 2015, MNRAS, 448, 713

Purcell C. W., Bullock J. S., Kaplinghat M., 2009, ApJ, 703, 2275

Purcell C. W., Bullock J. S., Tollerud E. J., Rocha M., Chakrabarti S., 2011, Nature, 477, 301

Purcell C. W., Zentner A. R., Wang M.-Y., 2012, JCAP, 8, 27

Quillen A. C., 2002, AJ, 124, 722

Raha N., Sellwood J. A., James R. A., Kahn F. D., 1991, Nature, 352, 411

Read J. I., Lake G., Agertz O., Debattista V. P., 2008, MNRAS, 389, 1041

Read J. I., Mayer L., Brooks A. M., Governato F., Lake G., 2009, MNRAS, 397, 44

Reid M. J., Menten K. M., Brunthaler A., Zheng X. W., Dame T. M., Xu Y., Wu Y., Zhang B., Sanna A., Sato M., Hachisuka K., Choi Y. K., Immer K., Moscadelli L., Rygl K. L. J., Bartkiewicz A., 2014, ApJ, 783, 130

Rix H.-W., Bovy J., 2013, AApR, 21, 61

Rojas-Arriagada A., Recio-Blanco A., Hill V., de Laverny P., Schultheis M., Babusiaux C., Zoccali M., Minniti D., Gonzalez O. A., 2014, A&A, 569, A103

Rossi L. J., Ortolani S., Barbuy B., Bica E., Bonfanti A., 2015, MNRAS, 450, 3270

Roškar R., Debattista V. P., Loebman S. R., 2013, MNRAS, 433, 976

Roškar R., Debattista V. P., Quinn T. R., Stinson G. S., Wadsley J., 2008, ApJL, 684, L79

Roškar R., Debattista V. P., Quinn T. R., Wadsley J., 2012, MNRAS, 426, 2089

Ruiz-Lara T., Pérez I., Florido E., Sánchez-Blázquez P., Méndez-Abreu J., Sánchez-Menguiano L., Sánchez S. F., Lyubenova M., Falcón-Barroso J., van de Ven G., Marino R. A., et al., 2017, A&A, 604, A4

Saha K., Jog C. J., 2014, MNRAS, 444, 352

Saha K., Martinez-Valpuesta I., Gerhard O., 2012, MNRAS, 421, 333

Saha K., Naab T., 2013, MNRAS, 434, 1287

Saha K., Pfenniger D., Taam R. E., 2013, ApJ, 764, 123

Saha K., Tseng Y.-H., Taam R. E., 2010, ApJ, 721, 1878

Salo H., Laurikainen E., Laine J., Comerón S., Gadotti D. A., Buta R., Sheth K., Zaritsky D., Ho L., Knapen J., Athanassoula E., et al., 2015, ApJS, 219, 4

Sánchez-Menguiano L., Sánchez S. F., Pérez I., Ruiz-Lara T., Galbany L., Anderson J. P., Krühler T., Kuncarayakti H., Lyman J. D., 2018, A&A, 609, A119

Savage C., Freese K., Gondolo P., 2006, PhysRevD, 74, 043531

Schönrich R., 2012, MNRAS, 427, 274

Schönrich R., Binney J., 2009a, MNRAS, 396, 203

Schönrich R., Binney J., 2009b, MNRAS, 399, 1145

Schönrich R., Binney J., Dehnen W., 2010, MNRAS, 403, 1829

Schwarzschild M., 1979, ApJ, 232, 236

Schwarzschild M., 1993, ApJ, 409, 563

Sellwood J., 2014, RevModPhys, 86, 1

Sellwood J. A., 1980, A&A, 89, 296

Sellwood J. A., 1981, A&A, 99, 362

Sellwood J. A., 2006, ApJ, 637, 567

Sellwood J. A., 2014, Reviews of Modern Physics, 86, 1

Sellwood J. A., Binney J. J., 2002, MNRAS, 336, 785

Sellwood J. A., Debattista V. P., 2006, ApJ, 639, 868

Sellwood J. A., Debattista V. P., 2009, MNRAS, 398, 1279

Sellwood J. A., Nelson R. W., Tremaine S., 1998, ApJ, 506, 590

Sellwood J. A., Wilkinson A., 1993, Reports on Progress in Physics, 56, 173

Sevenster M. N., 1999, MNRAS, 310, 629

Sheth K., Elmegreen D. M., Elmegreen B. G., Capak P., Abraham R. G., Athanassoula E., Ellis R. S., Mobasher B., Salvato M., Schinnerer E., Scoville N. Z., Spalsbury L., Strubbe L., Carollo M., Rich M., West A. A., 2008, ApJ, 675, 1141

Skokos C., Patsis P. A., Athanassoula E., 2002, MNRAS, 333, 847

Sloane J. D., Buckley M. R., Brooks A. M., Governato F., 2016, ArXiv e-prints

Smith M. C., Ruchti G. R., Helmi A., Wyse R. F. G., Fulbright J. P., Freeman K. C., Navarro J. F., Seabroke G. M., et al., 2007, MNRAS, 379, 755

Soto M., Zeballos H., Kuijken K., Rich R. M., Kunder A., Astraatmadja T., 2014, A&A, 562, A41

Sparke L. S., 1995, ApJ, 439, 42

Sridhar S., Touma J., 1996, MNRAS, 279, 1263

Steger C., 1998, IEEE Transactions on Pattern Analysis and Machine Intelligence, 20, 2

Steinmetz M., Zwitter T., Siebert A., Watson F. G., Freeman K. C., Munari U., Campbell R., Williams M., Seabroke G. M., Wyse R. F. G., Parker Q. A., Bienaymé O., Roeser S., Gibson B. K., Gilmore G., Grebel E. K., Helmi 2006, AJ, 132, 1645

SuperCDMS Collaboration Agnese R., Anderson A. J., Asai M., Balakishiyeva D., Basu Thakur R., Bauer D. A., et al., 2015, PhysRevD, 92, 072003

Syer D., Tremaine S., 1996, MNRAS, 282, 223

Tan A., Xiao X., Cui X., Chen X., Chen Y., Fang D., Fu C., Giboni K., Giuliani F., et al., 2016, Phys. Rev. D, 93, 122009

Tiret O., Combes F., 2007, A&A, 464, 517

Toomre A., 1966, in Goephys. Fluid Dyn., pp 111–114

Touma J., Tremaine S., 1997, MNRAS, 292, 905

Trayford J. W., Frenk C. S., Theuns T., Schaye J., Correa C., 2018, MNRAS

Tremaine S., Ostriker J. P., 1999, MNRAS, 306, 662

Tremaine S., Weinberg M. D., 1984a, ApJL, 282, L5

Tremaine S., Weinberg M. D., 1984b, MNRAS, 209, 729

Undagoitia T. M., Rauch L., 2016, Journal of Physics G: Nuclear and Particle Physics, 43, 013001

Valluri M., Debattista V. P., Quinn T. R., Roškar R., Wadsley J., 2012, MNRAS, 419, 1951

Valluri M., Shen J., Abbott C., Debattista V. P., 2016, ApJ, 818, 141

van der Marel R. P., Cretton N., de Zeeuw P. T., Rix H.-W., 1998, ApJ, 493, 613

Villa-Vargas J., Shlosman I., Heller C., 2009, ApJ, 707, 218

Villa-Vargas J., Shlosman I., Heller C., 2010, ApJ, 719, 1470

Vogelsberger M., Genel S., Springel V., Torrey P., Sijacki D., Xu D., Snyder G., Nelson D., Hernquist L., 2014, MNRAS, 444, 1518

Vogelsberger M., Helmi A., Springel V., White S. D. M., Wang J., Frenk C. S., Jenkins A., Ludlow A., Navarro J. F., 2009, MNRAS, 395, 797

Wang Y., Zhao G., 2013, ApJ, 769, 4

Wegg C., Gerhard O., Portail M., 2015, MNRAS, 450, 4050

Weinberg M. D., 1985, MNRAS, 213, 451

Weinberg M. D., 1991, ApJ, 368, 66

Weinberg M. D., 1994, ApJ, 421, 481

Weinberg M. D., 1996, ApJ, 470, 715

Weinberg M. D., 1998, MNRAS, 297, 101

Weinberg M. D., 1999, AJ, 117, 629

Weinberg M. D., 2004, ArXiv Astrophysics e-prints

Weinberg M. D., 2015a, ArXiv e-prints

Weinberg M. D., 2015b, ArXiv e-prints

Weinberg M. D., Katz N., 2002, ApJ, 580, 627

Weinberg M. D., Katz N., 2007a, MNRAS, 375, 425

Weinberg M. D., Katz N., 2007b, MNRAS, 375, 460

Wielen R., Fuchs B., Dettbarn C., 1996, A&A, 314, 438

Williams M. J., Bureau M., Kuntschner H., 2012, MNRAS, 427, L99

XENON100 Collaboration Aprile E., Arisaka K., Arneodo F., Askin A., Baudis L., Behrens A., Bokeloh K., Brown E., Cardoso J. M. R., et al., 2010, Physical Review Letters, 105, 131302

XENON100 Collaboration Aprile E., Arisaka K., Arneodo F., Askin A., Baudis L., Behrens A., Bokeloh K., Brown E., Cardoso J. M. R., et al., 2012, Physical Review Letters, 109, 181301

XENON100 Collaboration Aprile E., Arisaka K., Arneodo F., Askin A., Baudis L., Behrens A., Bokeloh K., Brown E., Cardoso J. M. R., et al., 2014, Journal of Instrumentation, 9, P11006

Yanny B., Rockosi C., Newberg H. J., Knapp G. R., Adelman-McCarthy J. K., Alcorn B., Allam S., Allende Prieto C., An D., Anderson K. S. J., Anderson S., et al., 2009, AJ, 137, 4377

Zaritsky D., Salo H., Laurikainen E., Elmegreen D., Athanassoula E., Bosma A., Comerón S., Erroz-Ferrer S., Elmegreen B., Gadotti D. A., Gil de Paz A., Hinz 2013, ApJ, 772, 135